skb.se

SKB TR-25-07

ISSN 1404-0344
ID 2080838
September 2025

Climate and climate-related issues for Forsmark

State of knowledge report 2025

Johan Liakka, Jens-Ove Näslund
Svensk Kärnbränslehantering AB

Keywords: Climate, Climate change, Global warming, Ice sheets, Permafrost, Sea level, Denudation, Forsmark, Deep geological repository, Post-closure safety, Operational safety.

Summary

This report presents the current state of knowledge on climate and climate-related issues of relevance for post-closure safety assessments for the existing repository for short-lived radioactive waste (SFR) and the repository for spent nuclear fuel (hereafter referred to as the "spent fuel repository"), both located at Forsmark, Sweden. Its primary purpose is to provide a scientific foundation for selecting and describing future climate developments ("climate cases") used in post-closure safety assessments for both repositories. Additionally, the report includes climate-related information relevant to the construction and operational phases of the repositories, such as projections of climate change and sea-level rise up to the year 2100. The report will serve as a reference for upcoming safety assessments for both SFR and the spent fuel repository.

Aside from an introductory and a concluding chapter, this report consists of six chapters, each focussing on a specific Feature, Event and Process (FEP) relevant to SFR and the spent fuel repository: climate forcing (Chapter 2), climate evolution (Chapter 3), ice-sheet development (Chapter 4), relative sea-level change (Chapter 5), permafrost (Chapter 6) and denudation (Chapter 7). Each chapter provides an overview of the process, its historical and projected future development, as well as present-day conditions and trends.

This report builds on the most recent climate reports published by SKB, specifically those supporting the Preliminary Safety Analysis Reports (PSAR) for both SFR and the spent fuel repository. It incorporates information from the PSAR climate reports alongside new findings. Key updates include for instance: (i) an updated assessment of future climate change and sea-level rise in Forsmark until the year 2100 and over the coming millennia, based on the latest (sixth) assessment report from the Intergovernmental Panel on Climate Change (IPCC) and subsequent studies; (ii) an analysis of the frequency and duration of ice coverage and permafrost in Forsmark over the next one million years; and (iii) a revised estimate of denudation in Forsmark over the next one million years, incorporating new results from the analysis of future ice duration.

Sammanfattning

Denna rapport presenterar det aktuella kunskapsläget om klimat och klimatrelaterade frågor av relevans för analyser av säkerhet efter förslutning av det befintliga slutförvaret för kortlivat radioaktivt avfall (SFR) samt det planerade slutförvaret för använt kärnbränsle, båda belägna i Forsmark, Sverige. Rapportens huvudsakliga syfte är att tillhandahålla vetenskapligt underlag för att välja och beskriva framtida klimatutvecklingar ("klimatfall") som används i analyser av säkerhet efter förslutning för båda förvaren. Därutöver innehåller rapporten klimatrelaterad information som är relevant för förvarens byggnads- och driftsfaser, såsom uppskattningar av klimatförändringar och havsnivåhöjning fram till år 2100. Rapporten kommer att utgöra en referens för kommande säkerhetsanalyser för både SFR och kärnbränsleförvaret.

Utöver ett inledande och ett avslutande kapitel består denna rapport av sex kapitel, som var och en fokuserar på en/ett specifik/specifikt förhållande, händelse eller process (Feature, Event and Process – FEP) av relevans för SFR och kärnbränsleförvaret: klimatdrivning (kapitel 2), klimatutveckling (kapitel 3), inlandsisutveckling (kapitel 4), förändringar i relativ havsnivå (kapitel 5), permafrost (kapitel 6) samt denudation (kapitel 7). Varje kapitel ger en översikt över processen, dess historiska och projicerade framtida utveckling, samt dagens förhållanden och trender.

Rapporten bygger på de senaste klimatrapporterna publicerade av SKB, särskilt referenserna för den preliminära säkerhetsredovisningen (PSAR) för både SFR och kärnbränsleförvaret. Rapporten inkluderar information från PSAR-rapporterna samt nya forskningsresultat. Viktiga uppdateringar omfattar exempelvis: (i) en uppdaterad bedömning av framtida klimatförändringar och havsnivåhöjning i Forsmark fram till år 2100 samt under de kommande årtusendena, baserat på den senaste (sjätte) sammanställningsrapporten från FN:s klimatpanel (IPCC) och efterföljande studier; (ii) en analys av frekvensen och varaktigheten av is- och permafrostförekomst i Forsmark under de kommande en miljon åren; samt (iii) en reviderad uppskattning av denudation i Forsmark under samma tidsperiod, där de nya resultaten kring isens framtida varaktighet i Forsmark har beaktats.

Content

1 Introduction

1.1 Role and motivation of the report

This report presents the current state of knowledge on climate and climate-related issues for Forsmark, Sweden (Figure 1-1), the site of the existing repository for short-lived radioactive waste (SFR) and the repository for spent nuclear fuel (hereafter referred to as the "spent fuel repository"). Its primary purpose is to provide a scientific foundation for selecting and describing future climate developments ("climate cases") used in post-closure safety assessments for both repositories (Figure 1-2). Additionally, the report includes climate-related information relevant to the construction and operational phases, such as projections of climate change and sea-level rise up to the year 2100.

Climate science is constantly evolving, for instance regarding anthropogenic climate change and its impacts, such as sea-level rise. Therefore, it is essential to keep this documentation updated for each step of the licensing procedure of SKB's repositories. Previously, climate and climate-related issues were fully described in separate climate reports for SFR and the spent fuel repository. These reports provided all necessary information, including the scientific foundation and the selection and description of climate cases. However, since both repositories are located in Forsmark, the scientific content in those reports was largely similar, leading to significant overlap. The present report consolidates the scientific information into a single document as a reference for future safety assessments for both SFR and the spent fuel repository.

The scientific information in this report supports the selection of climate cases in the post-closure safety assessments. These need to be tailored to each repository and the specific questions that are addressed in the safety assessment at hand. Therefore, they will continue to be selected and described separately within each safety-assessment project, and not in this report.

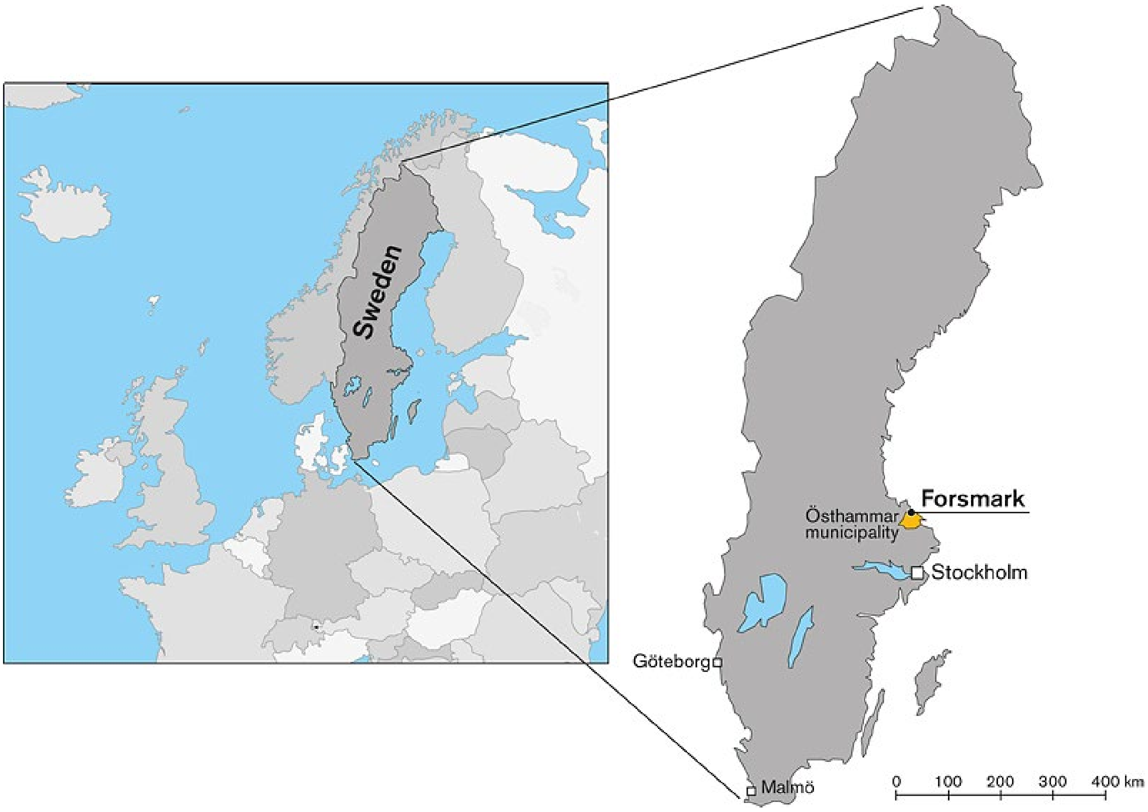

__Figure 1-1.__ Location map.

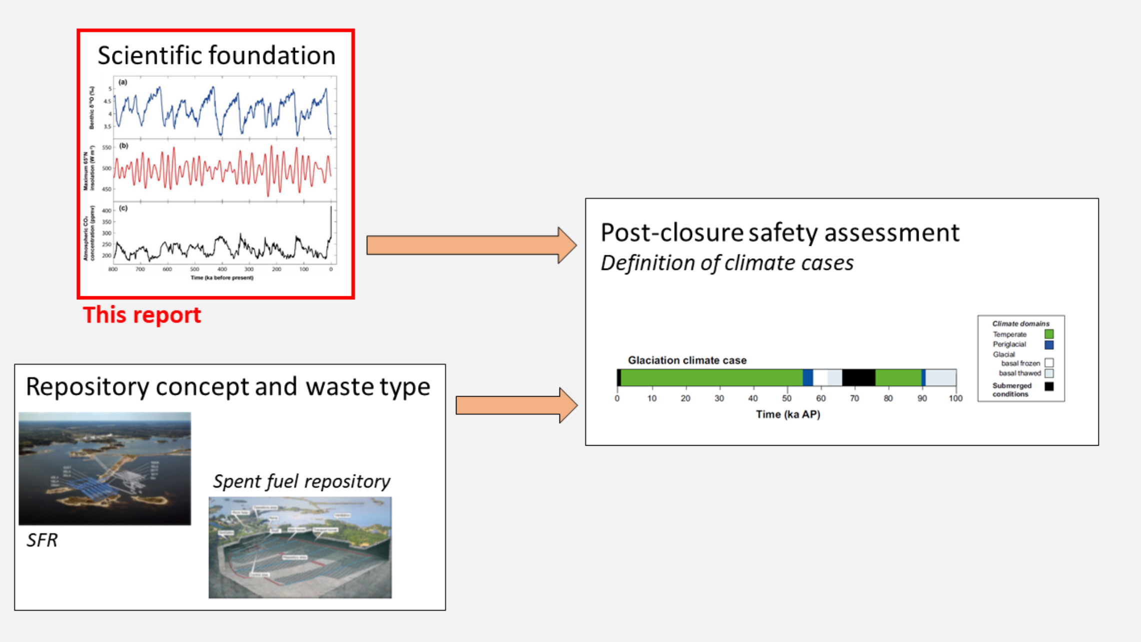

Figure 1-2. *Schematic overview of the role of this report in the context of post-closure safety assessments at SKB. In these assessments, uncertainty in future climate evolution is represented by a few climate developments, so-called climate cases. The selection and description of these cases are defined based on the current state of knowledge on climate and climate-related issues (i.e. the scientific foundation), and the repository concept and waste type to be analysed in the safety assessment. This report describes the current scientific foundation on climate and climate-related issues in Forsmark that will serve as input for the upcoming safety assessments for both SFR and spent fuel repository.*

1.2 Context – licensing of SKB's repositories and post-closure safety assessments

This section provides background information on SKB's repositories, including their stepwise licensing procedure and post-closure safety assessments. This information helps provide context for the scientific questions discussed in later chapters.

1.2.1 SFR

SFR consists of the existing part, SFR1, and an extension, SFR3, which is currently under construction. SFR1 is designed for disposal of short-lived low- and intermediate-level waste produced during operation of the Swedish nuclear power reactors, as well as waste generated during the application of radioisotopes in medicine, industry, and research. This part became operational in 1988. SFR3 is designed primarily for disposal of short-lived low- and intermediate-level waste from decommissioning of nuclear facilities in Sweden. SFR is currently estimated to be closed by year 2075.

The SFR waste vaults are at present located beneath the Baltic Sea. SFR1 consists of five waste vaults, covered by about 60 metres of bedrock, and SFR3 consists of six waste vaults, covered by about 120 metres of bedrock. The barrier design is adapted to the waste form and the characteristics and radiotoxicity of the radionuclides in the waste. The waste that constitutes the main part of the radiotoxicity is deposited in the vaults with the highest protective capability. For waste that contributes with less relative radiotoxicity, the barriers are adapted accordingly with a simpler design.

The license application for SFR3 was granted permit and permissibility by the Swedish government in December 2021. The construction license application for SFR3, which included a Preliminary Safety Analysis Report (PSAR), was approved by Swedish Radiation Safety Authority (SSM) in November 2024. The next step will be an updated safety analysis report (SAR) that needs to be approved by SSM before trial operation of the facility may commence.

1.2.2 Spent fuel repository

The spent fuel repository uses the so-called KBS-3 method for the final stage of spent nuclear fuel management. In this method, copper canisters with a cast iron insert containing spent nuclear fuel are surrounded by bentonite clay and deposited at approximately 500 m depth in granitic rock. The purpose of the KBS-3 repository is to isolate the nuclear waste from humans and the environment for very long times. Around 12 000 tonnes of spent nuclear fuel is forecasted to arise from the currently approved Swedish nuclear power programme, corresponding to roughly 6000 canisters in a KBS-3 repository. In contrast to SFR, most of the area above the planned spent fuel repository is presently above sea level.

The license application for the spent fuel repository was approved by the Swedish government in January 2022. The construction license application, including the PSAR, is currently (Feb 2025) under review by SSM.

1.2.3 Post-closure safety assessments

Post-closure safety assessment is a central part of the SAR and thus needs to be updated for each step in the licensing procedure. The most recent assessments of post-closure safety are included in the PSAR for SFR (SKB TR-23-01) and the PSAR for spent fuel repository (SKB TR-21-01). The corresponding previous assessments for the license applications were the so-called SR-PSU assessment for SFR (SKB TR-14-01) and the SR-Site assessment for the spent fuel repository (SKB TR-11-01).

The main role of the post-closure safety assessment in a license application is to demonstrate that the repository is radiologically safe for humans and the environment after closure. This is done by evaluating compliance with respect to SSM's regulations concerning post-closure safety and the protection of human health and the environment. The safety assessment covers a period of 100 000 years (100 kyr) after repository closure for SFR (e.g. SKB TR-23-01) and 1 000 000 years (1 Myr) for the spent fuel repository (e.g. SKB TR-21-01).

Handling of climate and climate-related issues

Defining the evolution of climate and climate-related issues is an essential part of any safety assessment as they affect both the surface and subsurface conditions, and hence potentially also the engineered repository barriers, over the assessment period. In summary, the methodology for handling the future evolution of climate and climate-related issues in the safety assessments consists of the following steps.

- As a first step, based on the contemporary scientific information (i.e. this report), we identify and describe a range within which future climatic conditions and climate-related processes may vary at the repository site. Within these limits, characteristic climate-related conditions of importance for repository safety can be identified. The conceivable climate-related conditions are represented as climate-driven process domains (Boulton et al. 2001), where such a domain is defined as "a climatically determined environment in which a set of characteristic processes of importance for repository safety appear". In the following parts of this report, these climate-driven process domains are referred to as *climate domains*. At a Swedish Baltic Sea coastal site, such as Forsmark, characteristic climate-related conditions can be represented by the *temperate*, *periglacial* and *glacial* climate domains. In short, the temperate climate domain is defined as a region without the presence of permafrost or ice sheets, the periglacial climate domain as regions that contain permafrost without the presence of ice sheets, and the glacial climate domain as regions that contain ice sheets (for further details, see e.g. SKB TR-23-05, Section 1.4.3). In addition to these three domains, the climate cases also describe whether or not the area above the repository is submerged below the sea. An example of a climate case featuring an evolution of climate domains can be seen in Figure 1-2 (in the box "Definition of climate cases").

- As a second step, we identify and describe a few possible representative climate developments, so-called *climate cases*, as a basis for assessing repository safety and the repository's protective capabilities (see e.g. SKB TR-23-05, Chapter 5). These climate cases are selected so that they together illustrate the most important and reasonably foreseeable sequences of future climate states and their impact on the protective capability of the repository and their environmental consequences. The set of climate cases for a specific safety assessment is chosen to represent conditions covering the range of possible future climate development at the repository site that may influence post-closure safety for the specific repository (Näslund et al. 2013). The selection of climate cases is based on (i) the identified range within which future climatic conditions and climate-related processes may vary at the repository site (see bullet point above) and (ii) the knowledge of those processes that are of importance for the functioning of the repository concept under consideration. The latter has been obtained from the iterative process of having performed several safety assessments for a specific repository concept.

Furthermore, the climate cases support the selection of the scenarios in the safety assessment. Based on the regulatory advice (SSMFS 2008:21, SSMFS 2008:37), three types of scenarios are considered in the safety assessments: (i) a *main scenario*, which takes into account the most probable changes in the repository and its environs over the assessment time frame, based on probable climate developments; (ii) *less probable scenarios*, which consider uncertainties that are not accounted for in the framework of the main scenario, including climate evolutions that are reasonably foreseeable, yet less likely to occur within the assessment period; and (iii) *residual scenarios*, which include analyses of highly unlikely or hypothetical events or developments that could have a severe impact on individual barriers and barrier functions. Consequently, to support the scenario selection, the definition of each climate case should also consider its likelihood in relation to other, potential, climate developments. To this end, climate cases representing likely or typical developments over the assessment time frame are handled in the main scenario, while cases representing less likely, extreme or hypothetical developments are handled in less probable or residual scenarios.

1.3 Structure of the report

1.3.1 Chapters and appendices

The climate and climate-related issues of relevance for post-closure safety have been identified in the analysis of Features, Events and Processes (FEPs) for each repository. In general, the same six Climate FEPs have been identified as relevant for both SFR and the spent fuel repository; these are summarised in Figure 1-3. Chapters 2–7 in this report are devoted to each of these FEPs. Figure 1-3 also shows an overview on how the Climate FEPs influence each other. The sequence of the chapters is based on these interactions. To this end, the FEP "Climate forcing" is described first, in Chapter 2, because it is not dependent on any of the other FEPs, while the FEPs "Permafrost" and "Denudation" are described at the end of the report (Chapters 6 and 7) as they depend on several other Climate FEPs (Figure 1-3). The report concludes with Chapter 8, which synthesizes future projections from the preceding chapters into a set of examples illustrating transitions between climate domains at Forsmark over the next 1 Myr.

In addition to eight report chapters, the report comprises numerous appendices. These contain supplementary results or analyses that were judged to be too detailed to be included in the main report. The appendices are cited from the main text where appropriate.

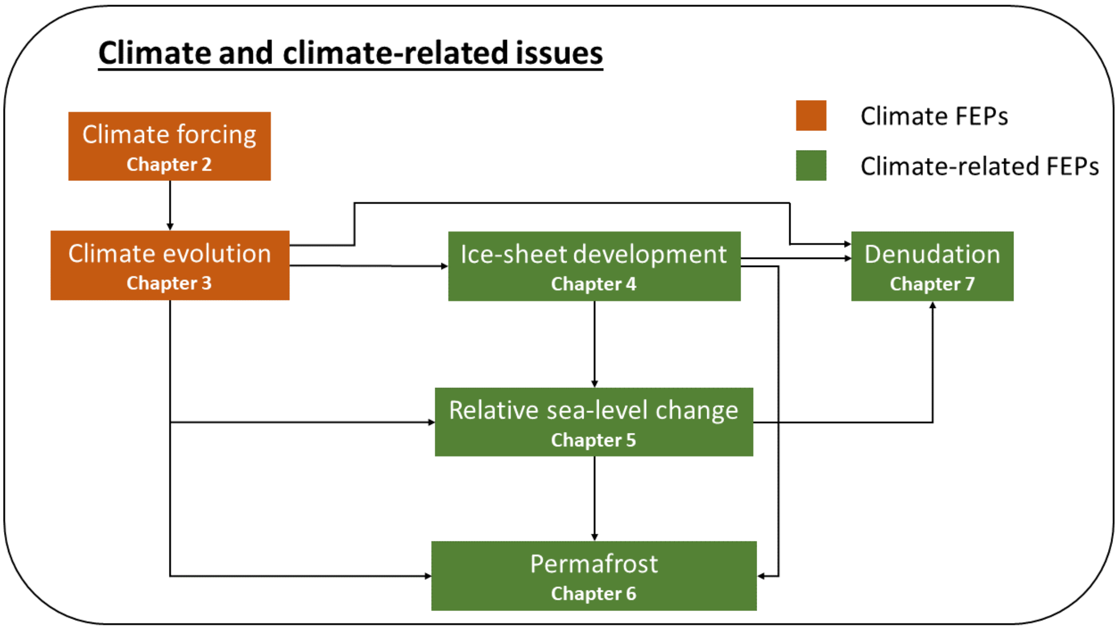

Figure 1-3. *Climate (orange) and climate-related issues (green), i.e. FEPs, of relevance for post-closure safety of SFR and spent fuel repository. In this report, a chapter has been devoted to each FEP as indicated. The figure also gives an overview on how the FEPs influence each other.*

1.3.2 Structure within each chapter

In discussing each of the climate and climate-related issues in Chapters 2–7, the following standardised structure has been adopted within each chapter.

Introduction

Definitions

In this subsection, the climate or climate-related issue is briefly introduced and important concepts and terms are defined.

Importance for post-closure safety (and operational safety) for SKB's repositories

This subsection summarises the relevance of the issue to the post-closure safety of SFR, the spent fuel repository, or both. For relative sea-level change (Chapter 5), its significance for the operational safety of both facilities is also discussed.

Previous documentation

This subsection references previously published SKB-related documents on climate and climate-related issues. These documents serve as starting point for the descriptions provided in the remainder of the chapter (see Section 1.3.3 for more details).

Controlling variables and conditions

Under this heading, the most important variables and conditions that control each issue are discussed. These can be both external or internal to the issue of interest.

Historical evolution

This subsection describes the historical development of the issue. Depending on the issue, the focus may be global, local specific to Forsmark, or a combination of both. For example, the climate forcing agents discussed in Chapter 2 generally have a global influence, so their historical evolution is presented on a global scale. In contrast, permafrost is relevant to post-closure safety only at a local or regional scale, so the discussion is limited to Forsmark.

For all issues, the historical evolution spans at least the last glacial cycle (the *Weichselian* glacial and the *Holocene* interglacial), covering the past 120 kyr. However, for certain issues – such as ice-sheet development (Chapter 4) and denudation (Chapter 7) – earlier periods are also described, as they provide insights that broaden the understanding of the potential future evolution of these issues.

Present-day conditions and trends

Under this heading, present conditions or trends of the issue are discussed. This section is mostly relevant for issues that are of relevance for operational safety of SKB's repositories, i.e. most notably relative sea-level change (Chapter 5), but also to some extent climate forcing (Chapter 2) and climate evolution (Chapter 3). However, it is also relevant for defining the initial state regarding climate and climate-related conditions in post-closure safety assessments.

Future evolution

This section presents and discusses potential future developments of the issue. Rather than outlining deterministic trajectories, the focus is on capturing relevant uncertainty ranges based on current knowledge. For most issues, future uncertainty is derived from climate modelling, particularly the long-term projections by Lord et al. (2019) and Williams et al. (2022), which span the next 1 Myr and form the basis for analyses in Chapters 3, 4, 6, and 7. Additionally, for issues related to operational safety, a dedicated subsection about the projected evolution up to the year 2100 is included.

Safety assessment-specific questions

This subsection is included only in certain chapters. It presents information relevant to safety assessments that do not fit within the overall structure of the other sections. Examples include likelihood assessments of various future climate scenarios (Chapters 2 and 3), the possibility of an ice-marginal stillstand over Forsmark (Chapter 4), and analyses of how long after closure SFR and the spent fuel repository could be submerged beneath the sea (Chapter 5).

1.3.3 Approach and conventions

This report has been written using the PSAR climate reports for SFR (SKB TR-23-05) and the spent fuel repository (SKB TR-20-12) as starting point. As a result, descriptions, results, and conclusions from these reports are summarised here, with citations to the relevant sections in the PSAR reports. In most cases where new analyses, results and conclusions are presented, the corresponding status in the PSAR reports is first summarized, followed by a description of the new developments since those reports were prepared.

This approach of building on previous reports is inspired by the Intergovernmental Panel on Climate Change (IPCC), which follows a similar approach when updating its assessments with the latest scientific understanding of climate and climate change. The main advantage of this strategy is that it highlights new developments since the last report, rather than presenting all information with equal detail. We hope this makes it easier for readers to track progress through each update of this report. However, a drawback is that readers may need to consult multiple reports for full details on certain issues. To mitigate this, we have aimed to provide precise citations to relevant sources.

When summarising descriptions, results, and conclusions from previous climate reports, significant effort has been made to review and, when necessary, update references with more recent sources. However, the need for updates varies by topic. In general, issues related to human-induced climate change (i.e. global warming) and its impacts (primarily Chapters 2, 3, and 5) require a more extensive literature review than those concerning colder climate conditions (primarily Chapters 4, 6, and 7). This is due to the larger volume of scientific research focused on current climate change compared to topics related to colder climates.

Since the preparation of the PSAR climate reports, the IPCC has published its Sixth Assessment Report (AR6) on the physical science of climate change (IPCC 2021a). The IPCC AR6, along with more recent publications, forms the basis for the updated descriptions in Chapters 2, 3, and 5. Additionally, the definitions and conventions used here closely follow those of the IPCC, including the adoption of the Shared Socioeconomic Pathways (SSPs) as emissions scenarios, replacing the Representative Concentration Pathways (RCPs) used in the PSAR climate reports.

1.4 Summary of key updates since the PSAR climate reports

The key updates made in this report since the PSAR climate reports (SKB TR-20-12, SKB TR-23-05) are summarised in the following.

Chapter 2 – Climate forcing

- General descriptions of climate-forcing processes most relevant for post-closure safety have been included (Section 2.2).
- Greenhouse-gas (GHG) emission scenarios have been updated based on the new SSP scenario framework (Section 2.5).
- The likelihood assessment of different emissions scenarios has been updated based on the latest forecasts of CO_2 emissions from fossil fuels and industry at the time of writing (Section 2.6.1).

Chapter 3 – Climate evolution

- A description of the key factors influencing climate evolution in Forsmark has been added (Section 3.2).
- The historical climate of Fennoscandia over the past 120 kyr has been updated based on SKB-funded research (Helmens et al. 2024) published after the PSAR reports were prepared (Section 3.3.2).
- Projections of surface air temperature (SAT), precipitation, and potential evapotranspiration (PET) in Forsmark – both up to 2100 AD and over the coming tens of thousands of years – have been updated using SSP scenarios and more recent climate modelling results (Section 3.5). The methodology for estimating long-term climate change has also been revised to a more simplified approach (Appendix A2).
- Climate analogues – regions with present-day conditions similar to Forsmark's future projected SAT and precipitation – have been identified for different SSP scenarios (Section 3.5.2 and Appendix A4).
- An evaluation of the potential collapse of the Atlantic Meridional Overturning Circulation (AMOC) and its possible consequences for Forsmark has been included (Section 3.6.1 and Appendix A1).
- The likelihood assessment of periglacial and glacial conditions in Forsmark over the next 100 kyr has been updated (Section 3.6.1) based on new analyses of future periglacial and ice-sheet variability (see further subsections "Chapters 4 – Ice-sheet development" and "Chapter 5 – Relative sea-level change" below).

Chapter 4 – Ice-sheet development

- The frequency and duration of ice-sheet coverage in Forsmark over the next 1 Myr has been assessed using conceptual global climate modelling (Lord et al. 2019), calibrated with historical data on global ice variations (Section 4.5.2). This analysis has also been published in a scientific article (Liakka et al. 2024).
- The analysis of ice-marginal stillstands has been expanded to include a theoretical assessment of potential stillstands during maximum ice-sheet extents (Section 4.6.2).

Chapter 5 – Relative sea-level change

- The processes and conditions influencing relative sea-level (RSL) change in Forsmark have been thoroughly described (Section 5.3).
- Current sea-level trends in the Baltic Sea and at Forsmark have been analysed (Section 5.4.1).
- The sea-level rise projections for Forsmark by 2100 AD, included in the PSAR reports, have been evaluated against more recent projections from IPCC AR6 and subsequent studies (Section 5.5.1).
- Projections of future RSL change at Forsmark over the next few millennia have been updated using results from IPCC AR6 (Section 5.5.2). These projections have been used to estimate the duration during which the areas above the SFR and spent fuel repository could be submerged after closure (Section 5.6).
- A simplified isostacy model (LLRA – "Local Lithosphere and Relaxing Asthenosphere") has been implemented to estimate submerged periods following ice coverage in Forsmark over the next 1 Myr (Section 5.5.3).

Chapter 6 – Permafrost

- The frequency and duration of periglacial conditions in Forsmark over the next 1 Myr have been assessed based on projected periods of ice coverage and SAT based on climate modelling (Lord et al. 2019, Williams et al. 2022) as well as projected periods of submerged conditions based on the LLRA model (Section 6.5.1).
- The likelihood of permafrost reaching the depth of SFR and spent fuel repository over the next 100 kyr and 1 Myr, respectively, has been further evaluated using results from the future permafrost variability analysis (point above), combined with findings from previous sensitivity permafrost simulations (Section 6.5.2).

Chapter 7 – Denudation

- The assessment of past denudation in the Forsmark area has been updated with findings from recent SKB studies (Goodfellow et al. 2023, 2024; Hall et al. 2022, 2023; Krabbendam et al. 2022, 2023) (Section 7.3.1).
- The estimated total denudation depth over the next 1 Myr at the location of the spent fuel repository has been revised based on future ice-sheet variability analyses (see subsection "Chapter 4 – Ice-sheet development" above) and the potential effects of the erosion process glacial ripping (Section 7.5.2).

1.5 Contributing experts, review and timeline

All report chapters and appendices have been authored by Johan Liakka (SKB). However, some text has been adapted from previous climate reports (SKB TR-20-12 and SKB TR-23-05), which were also authored by others. The report has undergone an internal review process by the following SKB employees: Jenny Brandefelt (Chapters 1–3 and 7), Johannes Johansson (Chapters 1, 4 and 5), Georg Lindgren (Chapters 2, 3 and 7), Kent Werner (Chapters 2, 3, and 7), Albin Nordström (Chapters 4 and 5), Jean-Marc Mayotte (Chapter 3), Frederic Wagner (Chapter 4), Jan-Olof Selroos (Chapter 4), Juri Palmtag (Chapter 5) and Peter Saetre (Chapter 7). Additionally, Jacob Heyman (Gothenburg University) conducted an internal review of Chapter 6.

The report was factually reviewed by Jens Becker (Nagra, Switzerland), Koen Beerten (SCK CEN, Belgium) and Lauri Parvainen (Posiva, Finland).

Each chapter was written sequentially over a period of two and a half years, which is reflected in the state of knowledge and the most recent citations used. Table 1-1 indicates the year and month when the internal review for each chapter was completed. In general, citations of more recent publications than the dates featured in the table should not be expected, though some may appear due to revisions made after internal review or in response to comments from factual reviewers.

Table 1-1. Month and year of completed internal review for each report chapter

Chapter	Date (Month Year) of completed internal review
1. Introduction	April 2025
2. Climate forcing	January 2024
3. Climate evolution	January 2024
4. Ice-sheet development	December 2024
5. Relative sea-level change	July 2023
6. Permafrost	March 2025
7. Denudation	November 2024

1.6 Abbreviations

List of abbreviations, except expressions in equations, chemical expressions and common units.

1D	One dimensional
2D	Two dimensional
3D	Three dimensional
AD	Anno Domini
AMOC	Atlantic Meridional Overturning Circulation
AOGCM	Atmosphere-Ocean General Circulation Model
AP	After Present
APS	Announced Policy Scenario (scenario used by the IEA)
ASL	Absolute Sea Level
BP	Before Present
CGM	Conceptual Global Model
CMIP5	Coupled Model Intercomparison Project Phase 5
CMIP6	Coupled Model Intercomparison Project Phase 6
CPS	Current Policies Scenarios (scenario used by the IEA)
CRU	Climate Research Unit
DEM	Digital Elevation Model
DJF	December, January and February
DO event	Dansgaard-Oeschger event
EBM	Energy Balance Model
ECS	Equilibrium Climate Sensitivity
ELA	Equilibrium Line Altitude
EMIC	Earth Model of Intermediate Complexity
ESM	Earth System Model
FEPs	Feature, Events and Processes
GHG	Greenhouse gases
GIA	Glacial Isostatic Adjustment
GRIP	Greenland ice core project

GRISLI	GRenoble Ice Shelf and Land Ice model
IEA	International Energy Agency
IPCC	Intergovernmental Panel on Climate Change
- AR5	Fifth assessment report of IPCC
- AR6	Sixth assessment report of IPCC
JJA	June, July and August
Kyr	Thousands of years
LGM	Last Glacial Maximum
LHS	Latin Hypercube Sampling
LLRA	Local Lithosphere and Relaxing Asthenosphere
MAM	March, April and May
MICI	Marine Ice Cliff Instability
MIS	Marine Isotope Stage
MISI	Marine Ice Sheet Instability
MPT	Mid-Pleistocene Transition
Myr	Millions of years
NAO	North Atlantic Oscillation
P	Precipitation
PDF	Probability Density Function
PET	Potential Evapotranspiration
Pg C	Petagrams of carbon
PP2004 model	PET model of Pereira and Pruitt (2004)
Ppbv	Parts per billion by volume
Ppmv	Parts per million by volume
PSAR	Preliminary Safety Analysis Report
RCP	Representative Concentration Pathway (emissions scenario in IPCC AR5)
RMSE	Root Mean Square Error
RSL	Relative Sea Level
SAR	Safety Analysis Report
SAT	Surface Air Temperature
SEJ	Structured Expert Judgement
SIA	Shallow Ice Approximation
SMHI	The Swedish Meteorological and Hydrological Institute
SON	September, October and November
SSP	Shared Socioeconomic Pathway (emissions scenario in IPCC AR6)
STEPS	Stated Policies Scenario (scenario used by the IEA)
UMISM	University of Maine Ice-sheet Model
UNFCCC	United Nations Framework Convention on Climate Change

2 Climate forcing

2.1 Introduction

2.1.1 Definitions

Climate forcing refers to any factor that influences the Earth's climate system and causes it to change. Such a factor is typically referred to as a climate forcing *agent*; it can be either natural or anthropogenic and can include both internal and external factors. Internal forcing agents on the climate act within the Earth, while external agents act outside the Earth. The term "forcing" in this context refers to *radiative* forcing, and implies that the agent forces the climate system to move away from its current state, either by increasing or decreasing the flux of energy that enters or leaves the Earth system. Examples of climate forcing agents are incoming solar radiation (insolation), greenhouse gases (GHGs) and atmospheric particles (aerosols).

2.1.2 Importance for post-closure safety

There are three main reasons as to why climate forcing is relevant to post-closure safety.

1. The temporal evolution of climate and climate-related issues of importance for post-closure safety are primarily controlled by the variation in climate forcing. For example, changes in insolation and atmospheric concentrations of GHGs play important roles to control the timing of the onset of the next glaciation in the Northern Hemisphere, the maximum warming that can be expected up until that glaciation, and the variability of subsequent glacial-interglacial cycles.
2. The likelihood of a climate case (Section 1.2.3) is largely determined by future levels of anthropogenic GHG emissions. Despite the inherent deep uncertainty in these projections, it is feasible to qualitatively estimate the likelihood of different future GHG emissions based on current trends, plans and ambitions.
3. The conditions of terrestrial ecosystems are impacted by atmospheric carbon dioxide (CO_2). As a result, typical concentrations of atmospheric CO_2 under different climate conditions are used as input for the parameterisation of terrestrial ecosystems in the biosphere transport and exposure model (SKB TR-23-06, Section 8.3.1).

2.1.3 Previous documentation

Climate forcing agents have previously been described in the climate reports included in SKB's safety assessments for the spent fuel repository and SFR (e.g. SKB TR-10-49, SKB TR-13-05, SKB TR-20-12 and SKB TR-23-05). Whilst the latest climate report for the spent fuel repository (PSAR) did not include a dedicated section for climate forcing, the most relevant aspects related to climate forcing were included in sections describing the future evolution of climate and climate-related issues (e.g. SKB TR-20-12, Sections 5.1 and 5.2). In the latest climate report for SFR (PSAR), the forcing agents were primarily described in SKB TR-23-05, Section 3.4. The climate report for PSAR SFR also included a likelihood assessment of future climate developments as well as associated future anthropogenic GHG emissions (SKB TR-23-05, Chapter 4).

Most of the information about climate forcing compiled in previous SKB documents will only be briefly summarised in this chapter. Instead of repeating previously published information, this chapter focuses on the evaluation of new developments since the publication of the safety assessment climate report (PSAR SFR). In particular, this concerns implementation of new information and data provided by the sixth assessment report (AR6) of the Intergovernmental Panel on Climate Change (IPCC), in particular a new set of emission scenarios. Furthermore, this chapter includes process descriptions of climate forcing agents that are of relevance for post-closure safety; such descriptions have not been included in previous climate reports.

2.2 Controlling variables and conditions

The relative importance of each climate forcing agent for the climate evolution depends strongly on the timescale considered. On sub-annual to multi-annual timescales, for instance, volcanic eruptions can temporarily cool the Earth's surface by injecting large amounts of aerosols into the atmosphere that reflect sunlight back into space (e.g. Gulev et al. 2021). On even shorter timescales (typically several days), aerosols emitted by humans can have significant direct or indirect effects on Earth's radiative balance as well as global and regional surface air temperature (SAT) and precipitation (Gulev et al. 2021, Quaas et al. 2022). On geologic timescales (several tens to hundreds of millions of years), plate tectonics influence the climate by altering the carbon cycle and the distribution of continents and oceans (Ruddiman 2001).

The most relevant climate forcing agents for post-closure safety assessments are those with characteristic timescales ranging from millennia to hundred thousand of years. This includes mainly changes in the Earth's orbit (Milankovitch cycles) and concentrations of atmospheric GHGs. CO_2 is of particular concern for post-closure safety because, unlike other prominent GHGs with atmospheric residence times on the order of 10–100 years, CO_2 can remain in the atmosphere over the long timescales considered in the safety assessments. However, since the climate evolution and relative sea-level change during this century is also of interest for the definition of the initial state in the safety assessments (e.g. SKB TR-23-01, Section 4.5) and climate adaptation purposes during construction and operation of SKB's facilities (Chapters 3 and 5), human-induced changes in climate forcing agents of relevance on centennial timescales are also briefly discussed in this section, the most relevant of which (besides CO_2) are the GHGs methane (CH_4) and nitrous dioxide (N_2O).

2.2.1 Solar radiation

The latitudinal and seasonal distribution of solar radiation (insolation) that reaches the Earth's surface is affected by the sunspot cycle, which refers to the periodic variation in the number of sunspots on the Sun's surface, occurring approximately every 11 years. These variations have only a small contribution to the global climate forcing, and can be neglected in the safety assessments. For example, the maximum contribution to radiative forcing from these variations is less than 10 % of the corresponding contribution from anthropogenic CO_2 emissions until the year 2020 (see e.g. Figure 2.10 in Gulev et al. 2021).

Over timescales of 10–100 kyr the latitudinal and seasonal insolation distribution is affected by Earth's orbital variability, also known as *Milankovitch cycles*, through changes in the amount and distribution of solar radiation (insolation) that reaches the Earth's surface. The three main components of Milankovitch forcing are variations in the eccentricity of Earth's orbit, changes in the tilt of the Earth's axis (obliquity) and variations in the precession of the Earth's axis (e.g. Berger 1978).

Variations in the eccentricity of Earth's orbit occur over periods of approximately 100 kyr and 400 kyr. When the eccentricity is high, the Earth's orbit becomes more elliptical, which causes seasonal differences in solar radiation to become more pronounced. Variations in Earth's eccentricity are small and, as a result, annual insolation variations due to eccentricity are also small (only 0.18 % according to Paillard 2010). Consequently, eccentricity variations have only a negligible effect on climate.

Variations in the tilt of the Earth's axis occur over a period of about 41 kyr and affects the amount of solar radiation that reaches different latitudes on the Earth's surface. When the tilt is greater, the polar regions receive more solar radiation in the summer, leading to warmer conditions and increased melting of ice sheets and permafrost. When the tilt is lower, the polar regions receive less solar radiation in the summer, which can lead to colder conditions and growth of ice sheets and permafrost. At 60ºN, variations in obliquity can lead to insolation variations of up to 5 % during summer solstice (Bosmans et al. 2015).

Variations in the precession of the Earth's axis occur over a period of about 23 kyr and affect the timing of the seasons. When the Earth's axis is oriented towards the Sun during the Northern Hemisphere summer, more solar radiation reaches the Arctic region, which generally leads to warmer conditions and increased ice sheet and permafrost melting. Conversely, when the Earth's axis is oriented away from the Sun during the Northern Hemisphere summer, less solar radiation reaches the Arctic region, which can cause colder conditions favouring ice-sheet and permafrost growth.

Whilst the growth and decay of ice sheets are primarily controlled by the insolation conditions in the summer (see further Section 2.3), variations in annual insolation may help to explain differences between past warm periods and the present one (see further Section 3.3). Precession may affect the seasonal insolation for a certain latitude but, by design, it does not alter the annual-mean insolation. In contrast, an increase in obliquity also translates into an increase of the annual-mean solar radiation received at high latitudes, and a decrease in the tropics. Specifically, if the axial tilt increases from a low-end value (22°) to a high-end value (24.5°), the annual-mean insolation increases by about 1 % at the poles and decrease by 0.4 % at the equator (Paillard 2010). At present, the obliquity is approximately 23.5° and it exhibits a decreasing trend.

The components of the Milankovitch cycles can be predicted with high accuracy over timescales considered in the safety assessments, i.e. 100 kyr to 1 Myr (e.g. Berger 1978, Laskar et al. 2004).

2.2.2 Greenhouse gases

GHGs affect the climate by trapping heat in the Earth's atmosphere, which leads to a warming effect known as the *greenhouse effect*. When sunlight reaches the Earth's surface, it is absorbed and re-emitted as infrared radiation, some of which is trapped by the GHGs in the atmosphere. This trapped heat warms the atmosphere and the Earth's surface, resulting in an increase in the global-mean SAT. The most important GHGs in Earth's atmosphere are water vapour, CO_2, CH_4 and N_2O (Schmidt et al. 2010, IPCC 2021b).

Water vapour

Water vapour is the most abundant greenhouse gas and accounts for about half of Earth's natural greenhouse effect (e.g. Schmidt et al. 2010). The amount of water vapour in the atmosphere is largely controlled by the climate, making it a positive feedback mechanism that amplifies any warming/cooling perturbation of the Earth (e.g. Held and Soden 2000). The current state of knowledge about the water vapour feedback, and how much it contributes to amplify a certain climate change perturbation is relatively high (Forster et al. 2021). Consequently, water vapor feedback is incorporated into nearly all numerical models used to reconstruct past climates and project future climate changes.

Carbon dioxide (CO_2)

Following water vapour, CO_2 is the most abundant greenhouse gas in Earth's atmosphere (e.g. Schmidt et al. 2010). The radiative forcing of CO_2 increases logarithmically with the atmospheric concentrations, implying that a certain unit of increase from relatively low atmospheric CO_2 levels will have a larger effect on the radiative forcing, and thereby the climate, than an equivalent increase from high CO_2 levels (e.g. Figure 2 in Etminan et al. 2016).

Concentrations of CO_2 in the atmosphere are affected by both natural and anthropogenic factors. Naturally, CO_2 is exchanged between the atmosphere, the oceans and the land through a process known as the *carbon cycle*. The strength of the carbon cycle in turn depends on the climate, and this has resulted in generally higher atmospheric CO_2 concentrations during *interglacials* (warmer periods with limited ice cover) than during *glacials* (colder periods with abundant ice cover) of the past 800 kyr (see further Section 2.3). Since the Industrial Revolution, the carbon cycle has been strongly influenced by anthropogenic activities, particularly due to the burning of fossil fuels such as coal, oil and natural gas, with smaller contributions from land use, cement production and industrial processes. These anthropogenic activities have resulted in a 50 % increase of the atmospheric CO_2 concentration since the Industrial Revolution (e.g. Friedlingstein et al. 2022), and constitute the main cause for the observed warming of the Earth's surface and atmosphere since then (IPCC 2021a), see further Chapter 3.

CO_2 is removed from the atmosphere by a range of processes acting over centennial timescales to several 100 kyr (e.g. Lord et al. 2016). Over centennial timescales, CO_2 equilibrates between various carbon reservoirs in the atmosphere, the ocean surface and the terrestrial biosphere (e.g. Archer et al. 2009). Further amounts of CO_2 are removed from the atmosphere over millennial timescales by which CO_2-rich waters on the ocean surface are mixed into the deep ocean, where the calcium carbonate in the sediments is dissolved and CO_2 is transformed into bicarbonate (e.g. Lord et al. 2016). Following a complete cessation in anthropogenic emissions, it is projected that 20–35 % of the anthropogenic CO_2 remains in the atmosphere after several thousands of years until the ocean uptake has equilibrated (e.g. Archer et al. 2009, Lord et al. 2016). The remaining concentrations are removed primarily by chemical weathering processes on land acting on timescales of more than 10 kyr. Specifically, carbonate rock weathering is the dominant removal process over timescales of 10 kyr, and silicate rock weathering provides a permanent transfer of CO_2 to the geologic reservoir over timescales of 100 kyr (e.g. Lord et al. 2016).

The long lifetime of (some of the) CO_2 implies that the atmospheric concentrations resulting from the anthropogenic emissions are *cumulative*, i.e. the concentrations can approximately be expected to continue to increase (and thus global warming will continue) as long as the net anthropogenic emissions are greater than zero. As atmospheric CO_2 concentrations continue to rise, the logarithmic nature of CO_2 radiative forcing causes its climate impact to be gradually lowered. At the same time, natural sinks of CO_2 in the ocean and terrestrial biosphere are projected to weaken in a warming climate (e.g. Canadell et al. 2021; see also Section 2.5.1), leaving a larger fraction of emissions in the atmosphere. Overall, these two effects largely compensate each other such that the global-mean warming is projected to increase approximately linearly with the cumulative CO_2 emissions (Canadell et al. 2021). IPCC AR6 estimates that this linear increase is likely in the range 1.0–2.3 °C per 1000 petagrams of carbon (Pg C) with a best estimate of 1.65 ºC per 1000 Pg C (Section 5.5.1.4 in Canadell et al. 2021). The validity of the linear relationship is uncertain for higher emissions. However, the IPCC estimates that it is valid at least until the cumulative emissions reaches 3000 Pg C, but possibly also with even higher cumulative emissions.

Methane (CH_4) and nitrous dioxide (N_2O)

Similar to CO_2, both CH_4 and N_2O exist naturally in the atmosphere and their atmospheric concentrations are also strongly affected by human activities. Natural sources of CH_4 are e.g. wetlands and thawing permafrost. However, in recent centuries the atmospheric concentrations of methane have increased due to human activities, most notably from livestock farming, rice cultivation and leaks from fossil fuel production (e.g. UNEP-CCAC 2022). Natural sources of N_2O include nitrogen in soils and oxidation of ammonia in the atmosphere, while anthropogenic sources are mostly agriculture and industry (e.g. Tian et al. 2020).

Although CH_4 and N_2O are greenhouse gases with about 20 and 300 times[1] stronger greenhouse effect than CO_2, respectively (Table 7.15 in Forster et al. 2021), they contribute significantly less to the natural and anthropogenic greenhouse effect. The reason is that there is much more CO_2 in the Earth's atmosphere than there is CH_4 and N_2O, and that anthropogenic emissions of CO_2 exceed that of CH_4 and N_2O by several orders of magnitude (e.g. IPCC 2021a). Furthermore, while a significant portion of anthropogenic CO_2 is expected to remain in the atmosphere for several millennia and longer, CH_4 and N_2O are destroyed by chemical reactions, and so the average lifetime of these gases in the atmosphere are limited to approximately 10 and 100 years, respectively (e.g. Table 2.2 in Gulev et al. 2021). Thus, when evaluating changes in the greenhouse effect over typical timescales relevant for the post-closure safety assessment (10 kyr–1 Myr), potential effects of current CH_4 and N_2O emissions are of negligible importance compared to CO_2.

---

[1] These global warming potentials are estimated over a 100-year period. For shorter periods than 100 years, the effective potentials of these gases would be even higher relative to CO_2, whereas they would be lower for longer periods.

2.3 Historical evolution

This section describes the variations of Milankovitch forcing and CO_2 over the last 800 kyr. During this period, Earth's climate has repeatedly alternated between warm interglacials and cold glacials over a characteristic timescale of approximately 100 kyr. Before this time, from approximately 2.5 Ma to 800 kyr ago, glaciations were generally less intense and glacial-interglacial cycles occurred on a shorter timescale of about 40 kyr. The shift in the periodicity between 40- and 100-kyr cycles is referred to as the Mid-Pleistocene Transition (MPT). In this report, we focus on the period after the MPT, as it represents the most recent climate history and offers a significantly greater abundance of reliable data compared to earlier periods.

To illustrate the climate variations over the last 800 kyr, stacked $\delta^{18}O$ measured in marine sediment records, which is a proxy for global ice volume, is displayed in Figure 2-1a. In general, high $\delta^{18}O$ values in marine sediments correspond to cold glacial periods because isotopically ligher water is stored in continental ice sheets (resulting in a relatively low global sea level), while low values

correspond to warm interglacial periods with considerably less water stored in ice sheets (resulting in a relatively high global sea level).

Milankovitch cycles, which determine the latitudinal and seasonal insolation distribution (Section 2.2.1), play an important role for the observed variability in ice volume. Although these variations influence the insolation over the entire year, the summer insolation is generally considered to be more important for pacing glacial-interglacial cycles than the winter insolation (e.g. Liakka et al. 2021). This is because ice-sheet growth and decay are largely controlled by changes in the ice-sheet ablation (Section 4.2.1), which is primarily determined by the surface energy balance in the summer season.

Figure 2-1b shows the variations in maximum summer insolation at 65°N over the last 800 kyr. The insolation variability at high latitudes is dominated by the 41-kyr obliquity and 23-kyr precession cycles, whereas the 100-kyr eccentricity cycles have negligible influence on the seasonal insolation changes (Section 2.2.1). Thus, variations in summer insolation alone cannot explain the dominant 100-kyr periodicity of glacial-interglacial cycles over this period. Understanding the dynamics of the 100-kyr glacial-interglacial cycles was subject to numerous investigations a few decades ago (e.g. Oerlemans 1980, Pollard 1982, Imbrie et al. 1993, Berger et al. 2005). A more recent and comprehensive effort to investigate this matter was undertaken by Abe-Ouchi et al. (2013). They used comprehensive climate and ice-sheet models to simulate the ice-sheet variability over the past 400 kyr forced by the insolation and atmospheric CO_2 concentration. Their model successfully simulated the saw-tooth characteristic 100-kyr periodicity of glacial cycles (similar to that shown in Figure 2-1a), the timing of the terminations and the amplitude of the Northern Hemisphere ice-volume variations. An important conclusion of Abe-Ouchi et al. (2013) is that the 100-kyr periodicity of glacial-interglacial cycles is primarily caused by the combination of insolation and internal feedbacks between the climate, ice sheets and the lithosphere–asthenosphere system.

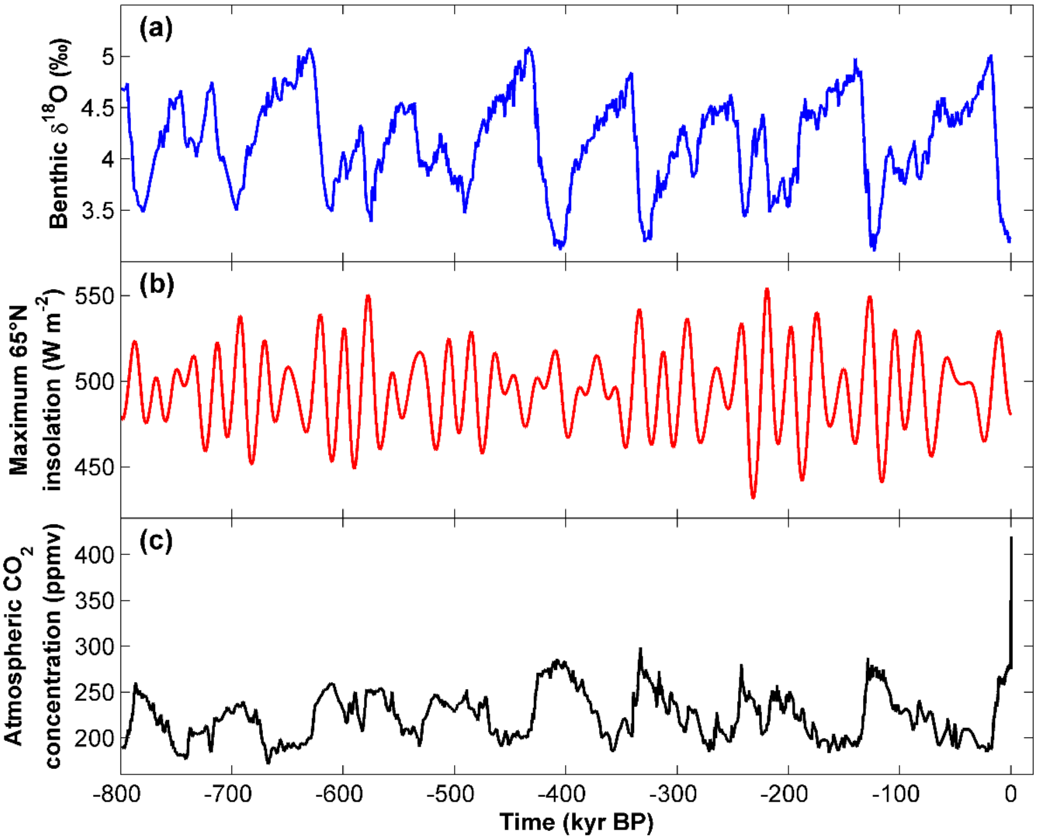

Figure 2-1. *(a) Proxy data for global ice volume from the stack of benthic $\delta^{18}O$ records of Lisiecki and Raymo (2005). High $\delta^{18}O$ values correspond to cold glacial periods whereas low values correspond to warm interglacial periods. (b) Maximum (solstice) summer insolation at 65°N from 800 kyr BP until present day (Laskar et al. 2004). (c) CO_2 variations over the past 800 kyr. Composite record from Lüthi et al. (2008) complemented with the observed atmospheric CO_2 concentration in 2022 (419 ppmv; NOAA 2023).*

In addition to the insolation, concentrations of GHGs have also experienced a high variability during past glacial-interglacial cycles. The variability of atmospheric CO_2 over the last 800 kyr, as inferred from Antarctic ice core records, is illustrated in Figure 2-1c. The changes in atmospheric CO_2 exhibit a high correlation with the changes in global ice volume over the same time period (cf. Figure 2-1a). This co-variation illustrates a positive feedback between atmospheric CO_2 and the climate on glacial-interglacial timescales. The feedback arises from a wide range of processes associated with e.g. ocean biogeochemistry and physics, terrestrial vegetation and peatlands (e.g. Canadell et al. 2021, Khatiwala et al. 2019). The combination of these processes gives rise to lower atmospheric CO_2 concentrations during glacials (typically in the range 180–200 parts per million by volume (ppmv)) and higher concentrations during interglacials (260–300 ppmv). Abe-Ouchi et al. (2013) found that the CO_2-climate feedback serves to increase the amplitude of the glacial-interglacial oscillations. Thus, the CO_2-climate feedback contributes to more extensive glacials and to warmer interglacials.

2.4 Present-day conditions and trends

An intriguing feature of Figure 2-1b is that the summer insolation is at present approaching a local minimum. This means that current insolation conditions, in theory, are favourable for large-scale glaciation. This has also been discussed in several studies (e.g. Tzedakis et al. 2012, Ganopolski et al. 2016). Ganopolski et al. (2016), for example, concluded that the onset of the next glaciation was narrowly missed before the Industrial Revolution. Since the Industrial Revolution, however, human activities have served to move the Earth system further away from a glacial state due to anthropogenic greenhouse-gas emissions. The effect of the anthropogenic emissions on the atmospheric concentrations are clearly visible in the CO_2 records; in 2022, annual-mean atmospheric CO_2 concentration amounted to 419 ppmv (NOAA 2023), which is approximately 40 % higher than peak values (~300 ppmv) during previous interglacials.

In general, global anthropogenic CO_2 emissions have gradually increased over the last century, in particular since the 1950s (e.g. Figure 3 in Friedlingstein et al. 2022). However, the increase in emissions has flattened somewhat in recent years (cf. black line in Figure 2-3). Between 2012 and 2021, the average increase in annual CO_2 emissions was 0.6 Pg C yr^{-1}, which is notably lower than the corresponding increase (2.2 Pg C yr^{-1}) between 2002 and 2011. However, the observed slowdown in the increase of emissions over the last decade is hardly visible in the atmospheric concentrations, which have continued to increase at a steady rate of approximately 2 ppmv yr^{-1} over the last two decades (Figure 2-2).

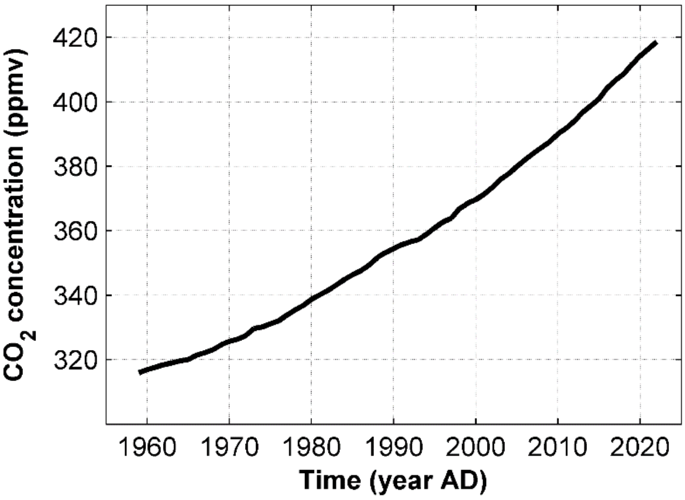

Figure 2-2. *Annual mean atmospheric CO_2 concentration from 1959 to 2022, derived from measurement at the Mauna Loa Observatory (Hawaii, USA). Data acquired from NOAA (2023).*

In addition to CO_2, notable anthropogenic increases of CH_4 (150 %) and N_2O (25 %) have also occurred since the Industrial Revolution (Canadell et al. 2021). However, these increases have started from much lower levels than for CO_2. Pre-industrial concentrations of CH_4 and N_2O were only about 700 parts per billion by volume (ppbv) and 270 ppbv, respectively (IPCC 2021b), thus about three orders of magnitude lower than the corresponding concentrations of CO_2. Consequently, even if accounting for the higher GHG potentials of these gases (Section 2.2.2), their contributions to the total radiative forcing balance of the Earth remain considerably smaller than that of CO_2.

Owing to the slow removal of CO_2 from the atmosphere (Section 2.2.2), the global-mean SAT can only be stabilised if net-zero anthropogenic emissions are reached. This can be achieved either if all CO_2 emissions are eliminated completely, or if the amount of CO_2 emitted to the atmosphere is also removed by natural or technical measures. A crucial step towards achieving net-zero anthropogenic emissions is the implementation of the so-called Paris Agreement, which was adopted by the United Nations Framework Convention on Climate Change (UNFCCC) in 2015. The Paris Agreement has been ratified by the European Union (EU) and 194 nations, and one of its most prominent goals is to "limit global warming to well below 2 °C above pre-industrial levels, and to pursue efforts to limit the temperature increase to 1.5 °C above pre-industrial levels" (UNFCCC 2015). To meet the 1.5 °C target, global CO_2 emissions must be reduced to net zero before the middle of this century (IPCC 2018). Therefore, the EU and several individual nations have pledged to achieve net-zero CO_2 emissions by 2050 AD or around this time. However, as of December 2023, taking the latest initiatives of the 28th United Nations climate conference (COP28) into account, world-wide pledges and targets are projected to limit the warming to only around 2 °C by 2100 AD (Climate Action Tracker 2023). Thus, they still fall short from meeting the 1.5 °C target (see also Section 2.6.1).

2.5 Future evolution

In this section, the future evolution of insolation and GHGs, especially CO_2, is described. The discussion primarily revolves around the long timescales relevant for post-closure safety, i.e. the next 100 kyr to 1 Myr. On these timescales, changes in insolation are controlled by the Milankovitch cycles (Section 2.2.1) and the atmospheric CO_2 concentrations will change as a result of both natural variability and anthropogenic influences (Section 2.2.2). Owing to its slow removal from the atmosphere, future atmospheric concentrations of CO_2, even after 10 kyr and 100 kyr, will be influenced by historical and present anthropogenic emissions (Sections 2.3–2.4) as well as anthropogenic emissions that will occur in the future.

Plausible trajectories of future CO_2 emissions are often described by so-called emission scenarios. While these scenarios typically only cover the first few centuries after present, they also collectively describe a wide range of cumulative CO_2 emissions within known limits of current fossil-fuel reserves (Global Registry of Fossil Fuels 2022). Thus, the emission scenarios are also of interest for the analysis of climate and climate-related issues in the safety assessments, even if they are defined over much shorter timescales that those considered in the safety assessments. The emission scenarios are introduced in Section 2.5.1, including a discussion about uncertainties associated with the global carbon cycle. This is then followed by assessments of how the climate forcing agents will evolve over the next 100 kyr to 1 Myr. The evolution of climate forcing over these longer timescales determine the timing of the onset of the next glaciation, i.e. the next *glacial inception*, after which a glacial-interglacial climate variability similar to that of the past 800 kyr can be expected to re-emerge (see further Sections 3.5.3 and 3.5.4). The evolution of climate forcing over the next 1 Myr is described in Section 2.5.2.

2.5.1 Until 2100 AD

In this section, the evolution of climate forcing agents until 2100 AD is presented. Since no significant variation in insolation is expected on this timescale, only changes in atmospheric GHGs are described.

Emission scenarios

An emission scenario is a representation of how GHG emissions may evolve over time, based on assumptions about various driving forces that influence these emissions, such as population growth, economic development and technological change. These scenarios are used in climate modelling to explore the potential impacts of future GHG emissions on the climate. Emission scenarios have constituted an essential part of climate change since the publication of the first assessment report by the IPCC (IPCC 1990). However, a new set of scenarios have been developed in preparation for each IPCC assessment report (Girod et al. 2009). The scenarios used in the vast majority of the climate literature are adopted from the most recent IPCC assessment report (AR6).

In preparation of the IPCC fifth assessment report (AR5), emission scenarios were replaced by Representative Concentration Pathways (RCPs) (van Vuuren et al. 2011). Specifically, four RCPs were analysed in IPCC AR5 representing different amounts of greenhouse gas emissions: RCP2.6, RCP4.5, RCP6.0 and RCP8.5. The number associated with each RCP (2.6, 4.5, 6.0 and 8.5) indicates the anthropogenic forcing (in W m^{-2}) by 2100 AD relative to pre-industrial times, with 2.6 W m^{-2} corresponding to a low emission scenario (net-zero emissions within this century), 4.5 and 6.0 W m^{-2} to medium emission scenarios (emissions similar to present-day levels for most of this century) and 8.5 W m^{-2} to a high emission scenario (significantly higher emissions than present levels for the remainder of this century), see van Vuuren et al. (2011).

One of the main advantages of the RCPs was that they provided standardised GHG concentration inputs for climate models. This ensured that different numerical models were driven by the same set of anthropogenic forcing, which in turn facilitated comparison between models without involving the large uncertainty associated with the global carbon cycle (see further subsection *Carbon cycle feedbacks* below). One of the shortcomings of using RCPs, on the other hand, was that they lacked a consistent set of socioeconomic descriptions, or “narratives”, corresponding to each radiative forcing level (Moss et al. 2010). Therefore, in preparation for IPCC AR6 a new set of scenarios was developed.

In these new scenarios, entitled Shared Socioeconomic Pathways (SSPs), the radiative forcing targets from the RCPs are accompanied with broad descriptions of different global socioeconomic trends (Riahi et al. 2017). The SSPs describe different ways the world might develop in absence of climate policy, and how different levels of climate change mitigation could be achieved when combined with different RCP targets. A total of five SSP narratives have been developed, which describe a wide range of socioeconomic pathways, ranging from a world shifting towards renewable energy (SSP1) to a world dominated by an accelerated use of fossil fuels (SSP5), see Table 2-1.

Each SSP can be used with different levels of climate change mitigation (so-called *mitigation scenarios*), or in absence of climate mitigation policies (so-called *baseline scenarios*). Consequently, several 2100 AD radiative forcing targets can be achieved within the same SSP. For example, 6.0 W m^{-2}, which approximately corresponds to the 2100 AD baseline radiative forcing of SSP1 and SSP4 (Table 2-1), can also be reached under the other SSPs for different levels of climate change mitigation. Likewise, 4.5 W m^{-2} can also be achieved with every SSP. The same is however not true for 2.6 W m^{-2}, which was not possible to reach under SSP3 (Fujimori et al. 2017), and 8.5 W m^{-2}, which can only be achieved in SSP5 (Table 2-1 and Riahi et al. 2017).

Table 2-1. Summary of the Shared Socioeconomic Pathways (SSPs) (Riahi et al. 2017). The baseline radiative forcing corresponds to the total anthropogenic forcing in the absence of climate policies. However, each SSP can also be combined with some level of climate change mitigation to reach lower radiative forcing targets, see the text. The radiative forcing targets used by the core set of scenarios in IPCC AR6 are also indicated; these are also most extensively analysed in the present report

Scenario	Short description	Approximate 2100 AD baseline radiative forcing (W m^{-2})	Radiative forcing targets used by core scenarios (W m^{-2})
SSP1	Sustainability – Taking the Green Road	6.0	1.9, 2.6
SSP2	Middle of the Road	7.0	4.5
SSP3	Regional Rivalry – A Rocky Road	7.0	7.0
SSP4	Inequality – A Road Divided	6.0	-
SSP5	Fossil-fueled Development – Taking the Highway	8.5	8.5

The radiative forcing targets from IPCC AR5 (2.6, 4.5, 6.0 and 8.5 W m^{-2}) are also included in the new SSP framework, together with some additional targets (1.9, 3.4, 7.0 W m^{-2}), see Table 2-1 and O'Neill et al. (2016). The naming of the new SSP scenarios follows the convention developed for the RCPs, with the exception that the corresponding number of the socioeconomic narrative is also included. For example, RCP8.5 corresponds to SSP5-8.5 in the new scenario framework.

The RCP scenarios, in particular RCP2.6, RCP4.5 and RCP8.5, were used as basis for the analysis of future climate evolution and relative sea-level change at Forsmark in the PSAR for both the spent fuel repository and SFR (SKB TR-20-12 and SKB TR-23-05). Given the overall strategy for this report to follow conventions and definitions of the most recent IPCC assessment report (Section 1.3.3), SSPs will be used in this report rather than the RCPs. Exceptions to this general rule include, for instance, discussions of literature and results in previous safety assessments that were published before the SSP scenarios were introduced.

In IPCC AR6, the SSP scenarios SSP1-1.9, SSP1-2.6, SSP2-4.5, SSP3-7.0 and SSP5-8.5 are selected as the core set of scenarios and are most extensively analysed, whereas SSP4-3.4 and SSP4-6.0 are not as extensively analysed. IPCC's selection of core scenarios is also reflected in this report, where SSP4-3.4 and SSP4-6.0 receive less attention than the other SSP scenarios. Among the five core scenarios, SSP3-7.0 and SSP5-8.5 are explicit baseline 'no-climate-policy' scenarios (Gidden et al. 2019), resulting in a global-mean warming of approximately 4 °C and 5 °C by the end of this century compared to pre-industrial SAT. The scenarios SSP1-1.9, SSP1-2.6 and SSP2-4.5 assume some level of climate change mitigation. The SSP1-1.9 and SSP1-2.6 scenarios limit global warming to approximately 1.5 °C and 2 °C, respectively, whereas the SSP2-4.5 scenario leads to approximately 3 °C warming by the end of the century.

The fossil-fuel CO_2 emissions from the SSP scenarios until 2100 AD are shown in Figure 2-3. The grey shading illustrates the non-policy baseline range from the SSP database (IIASA 2018). The CO_2 emissions under the SSP5-8.5 scenario are close to the upper end of the baseline range, whereas the emissions under SSP3-7.0 falls approximately in the middle of that range. The remaining core set of scenarios assume some level of climate-change mitigation, and so their emissions fall below the baseline range (Figure 2-3). As expected, the strong mitigation scenarios SSP1-1.9 and SSP1-2.6 describe the lowest emissions until 2100 AD among all SSPs. Toward the end of this century, these scenarios even exhibit net-negative emissions, characterised by a global-mean removal of CO_2 from the atmosphere by means of natural and technical solutions[2]. These net-negative emissions thereby lead to a reduction of the atmospheric CO_2 concentrations in the SSP1-1.9 and SSP1-2.6 scenarios.

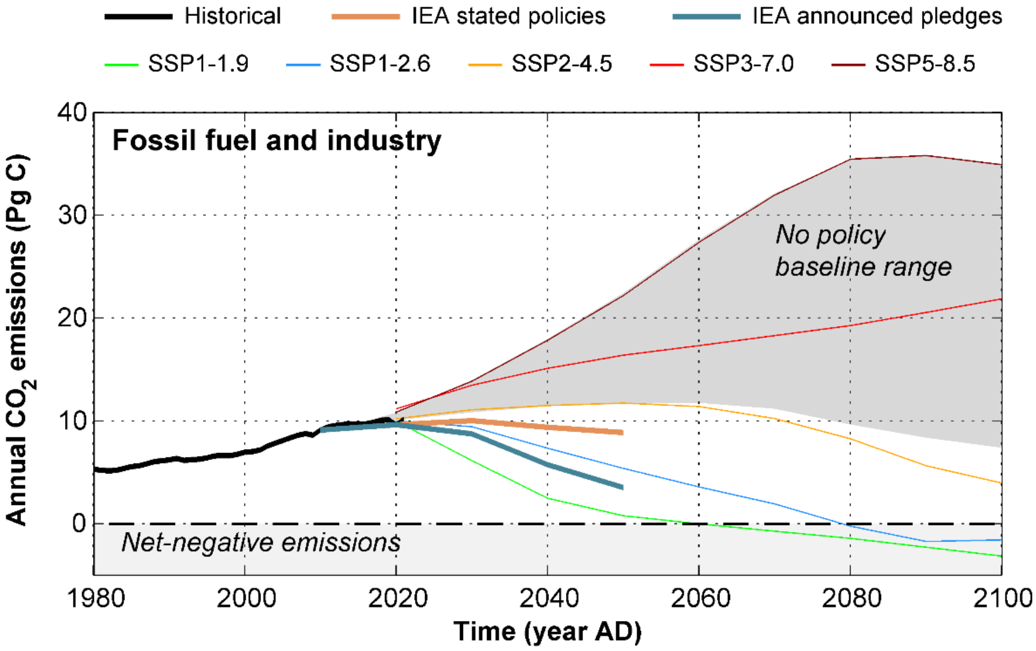

Figure 2-3. *Annual CO_2 emissions from fossil fuels (Pg C yr^{-1}) until 2100 AD in all SSP no-policy baseline scenarios (grey shading), and the core set of SSP scenarios used in IPCC AR6 (thin solid lines). Also shown are the corresponding CO_2 emissions in the "stated policies" (STEPS) and "announced pledges" (APS) scenarios from IEA (2022), as well as historical emissions since 1980 from the Global Carbon Project (Friedlingstein et al. 2022). The SSP data were downloaded from IIASA (2018) (see also Riahi et al. 2017).*

Cumulative emissions

In evaluating the climate impact of CO_2, it is often sufficient to consider only the cumulative emissions up to a certain point in time rather than the temporal evolution as described by the SSP scenarios (Figure 2-3). This is especially true when considering timescales that extend over millennia and beyond, because anthropogenic influences over these longer timescales are characterised by an increased dominance of CO_2 in comparison to other human-induced climate forcing agents. For instance, after 1000 years following the cessation of anthropogenic GHG emissions, virtually all CH_4 and N_2O emitted by humans will have been removed from the atmosphere by chemical processes, whereas more than 20 % of the emitted CO_2 will remain (Section 2.2.2). Consequently, cumulative CO_2 emissions are a key factor in assessing the anthropogenic impact on climate over timescales relevant to post-closure safety.

To estimate cumulative CO_2 emissions in the SSP scenarios, the extensions of the scenarios to 2300 AD are used (Meinshausen et al. 2020). These extensions assume that all scenarios reach net-zero emissions at the latest by 2250 AD. Under SSP1-1.9 and SSP1-2.6, which describe net-negative emissions by the end of this century (Figure 2-3), emissions are assumed to gradually return to zero by approximately 2200 AD (Meinshausen et al. 2020).

Up until the present, anthropogenic activity has emitted about 700 Pg C of CO_2 to the atmosphere (Table 2-2), and this number is currently increasing by more than 10 Pg C each year (Figure 2-3). According to the extended SSP scenarios, the total CO_2 emitted by humans until 2020 AD will more than double under the SSP2-4.5 scenario and increase five-fold under the SSP5-8.5 scenario between 2020 AD and 2300 AD (Table 2-2). Under the SSP1-1.9 and SSP1-2.6 scenarios, the net-positive

---

[2] Natural solutions for achieving net-negative emissions include e.g. afforestation and reforestation, whereas bioenergy with carbon capture and storage (BECCS) and direct air capture are two examples of technical solutions.

emissions during most of this century will be compensated by net-negative emissions from about 2080 to 2200 AD (Meinshausen et al. 2020), resulting in close to zero future cumulative emissions under these scenarios (Table 2-2).

Table 2-2. Historical and future cumulative CO_2 emissions (Pg C) based on the data from the Global Carbon Project (Friedlingstein et al. 2022) and extended SSP scenarios (Meinshausen et al. 2020), respectively. Note that all values are approximate

Time period	Dataset/scenario	Cumulative CO_2 emissions (Pg C)
1850 – 2020 AD	Global carbon project	700
2020 – 2300 AD	SSP1-1.9	0
	SSP1-2.6	0
	SSP2-4.5	1000
	SSP3-7.0	3000
	SSP5-8.5	4500

Carbon cycle feedbacks

As mentioned above, a major advantage of the IPCC scenario framework is that it provides standardised CO_2 concentration inputs for climate models. Thus, future climate projections are primarily driven by prescribed concentrations of atmospheric CO_2 rather than by the emissions underlying the scenarios. The CO_2 concentrations in the scenarios are typically derived from a standard set of parameters in a carbon cycle model. Accounting for uncertainties in those parameters may result in lower or higher CO_2 concentrations than those currently assumed in the scenarios. The study of Friedlingstein et al. (2014), for example, found that running the IPCC AR5 models with emissions underlying RCP8.5 leads to an average of 0.25 W m^{-2} higher 2100 AD radiative forcing across the models than when using a fixed set of concentrations. A similar conclusion was reached by Booth et al. (2017) who performed several carbon-cycle sensitivity experiments in a climate model. They found that CO_2 concentration under RCP6.0 was on average 8 % higher across the sensitivity experiments than in the prescribed RCP-representation.

It is important to note that the range of carbon-cycle feedback estimates in Friedlingstein et al. (2014) and Booth et al. (2017) may still be relatively narrow as many contemporary carbon-cycle models lack a number of processes, including dynamic vegetation and permafrost thaw.

Changes in vegetation due to global warming may have a large effect on the global carbon cycle. While the carbon storage in vegetation is projected to increase in high-latitude regions (Canadell et al. 2021), the situation in the tropics, where approximately half of the terrestrial carbon is stored (e.g. Hubau et al. 2020), is much more uncertain due to primarily uncertainties in tropical rainfall patterns (Jupp et al. 2010, Rammig et al. 2010) and how the vegetation will respond to climate change (Galbraith et al. 2010). Taking all these uncertainties into account, IPCC AR6 estimates that the upper limit of the overall loss of tropical land carbon to the atmosphere is around 50 Pg C per °C of tropical warming (Canadell et al. 2021). This implies that the release to the atmosphere of tropical land carbon will likely be less than 150 Pg C under the SSP2-4.5 scenario.

Thawing of permafrost at high-latitudes has the potential to release large amounts of buried carbon to the atmosphere. Current estimates suggest that carbon release from thawing permafrost soils range from 3.1 to 41 Pg C per °C by 2100 AD (Canadell et al. 2021). Thus, permafrost carbon releases will likely be less than 200 Pg C if the Arctic region warms by 5 °C, which roughly corresponds to the maximum warming under the SSP2-4.5 scenario.

In conclusion, while processes related to vegetation changes and thawing permafrost may result in additional carbon releases due to global warming, they are still considerably smaller than the difference in cumulative emissions between the individual SSP scenarios (Table 2-2). The same conclusion was also reached in IPCC AR6 (see e.g. the executive summary of Canadell et al. 2021). Thus, it is unlikely that GHG emissions corresponding to SSP scenarios with a lower radiative forcing will result in similar atmospheric CO_2 concentrations as in scenarios with higher forcings, e.g. that CO_2 emissions under the SSP2-4.5 scenario will result in CO_2 concentrations similar to those described by SSP3-7.0.

2.5.2 Until 1 Myr

In this section, the evolution of climate forcing agents over the next 1 Myr is presented. The evolution of each Milankovitch component during this period is shown in Figure 2-4a, and the resulting summer insolation is shown in Figure 2-4b. During the first 100 kyr, the Earth's orbit will be characterised by a low eccentricity (Figure 2-4a), resulting in a low-amplitude variability of the summer insolation compared to, for instance, the last 100 kyr (Figures 2-1b and 2-4b). Combined with the present insolation minimum (Section 2.3), this low variability implies that summer insolation will be higher than at present for the next 50 kyr, at which point the insolation is expected to start declining towards a major minimum at 54 kyr AP (Laskar et al. 2004). The summer insolation between 50 kyr and 1 Myr AP is mostly characterised by a higher variability compared to the first 50 kyr (Figure 2-4b).

The atmospheric CO_2 over the next 1 Myr is expected to be influenced by natural variability (Section 2.2.2 and 2.3) as well as the historical, present, and near-future[3] anthropogenic emissions. The anthropogenic influence is particularly noticeable in the beginning of the 1 Myr period. For example, it is estimated that 15–30 % and 5–10 % of the anthropogenic emissions will remain in the atmosphere after 10 kyr and 100 kyr, respectively (Archer and Ganopolski 2005, Archer et al. 2009, Colbourn et al. 2015, Lord et al. 2016, 2019), resulting in notably elevated CO_2 concentrations over the next 100 kyr under medium emissions, and over the next 500 kyr under high emissions (Figure 2-4c).

The variability in summer insolation and the amount of anthropogenic CO_2 are key factors in determining the timing of the next glacial inception. This is further discussed in Section 3.5.3.

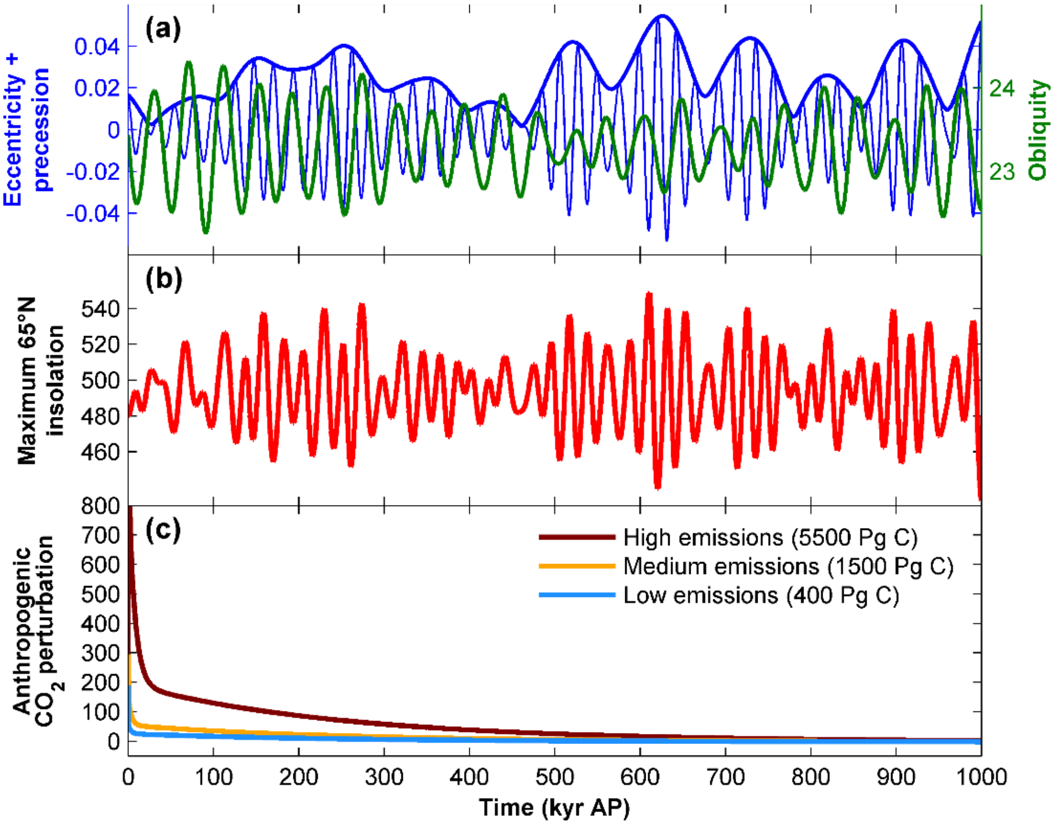

Figure 2-4. *Summary of the evolution of climate forcing agents over the next 1 Myr. (a) Time series of orbital variations (Laskar et al. 2004), showing eccentricity (blue thick line) and precession (blue thin line) on the left axis, and obliquity (degrees; green) on the right axis. (b) Maximum (solstice) summer insolation at 65°N (Laskar et al. 2004). (c) Anthropogenic* CO_2 *perturbation in the atmosphere in scenarios with low (blue line), medium (yellow line) and high (red line) cumulative* CO_2 *emissions, calculated using a carbon-cycle impulse response function (Lord et al. 2019). To obtain the total* CO_2 *concentrations used in the scenarios, the anthropogenic perturbations should be added to the pre-industrial concentration (280 ppmv). The amount of carbon released to the atmosphere in each scenario is provided by the legend. All emissions are assumed to occur within the first 1000 years after present.*

---

[3] "Near-future" here refers to approximately the first 1000 years.

2.6 Safety assessment-specific information

2.6.1 Likelihood assessment of future greenhouse-gas emissions

In the safety assessments, the main scenario is based on the probable climate evolution, whereas less probable scenarios account for scenario uncertainties (i.e. also those related to climate) that are not handled in the framework of the main scenario (Section 1.2.3). Since future climate evolution is influenced by anthropogenic GHG emissions (Sections 2.5 and 3.5), the likelihood of different cumulative emissions is a relevant input for selecting climate cases for the safety assessment scenarios.

A likelihood assessment of future emissions was first introduced in the climate report of PSAR SFR (SKB TR-23-05, Chapter 4). In that report, the likelihood of low (comparable to RCP2.6), medium (comparable to RCP4.5/RCP6.0) and high (comparable to RCP8.5) future emissions was evaluated using a qualitative likelihood scale. The same likelihood scale is used also in the present work (Table 2-3). The assessment of qualitative likelihoods in the present work uses the corresponding assessment in PSAR SFR as a starting point.

Because CO_2 is the most relevant human-induced GHG over the long timescales relevant for post-closure safety, and because the effect of CO_2 on the climate is cumulative (Section 2.2.2), the likelihood assessment focuses primarily on the cumulative anthropogenic CO_2 emissions as described by the core set of SSP scenarios (Table 2-2).

It is important to note that the present likelihood assessment contains a number of limitations. First, uncertainties in carbon cycle feedbacks (Section 2.5.1) are not considered in the assessment. Thus, potential additional carbon releases (caused by e.g. environmental changes), which were not included in the derivation of the SSP scenarios, are not considered in the likelihood assessment. Second, the likelihood assessment is only based on the assumption that net-zero anthropogenic emissions will prevail indefinitely into the future once they have been achieved. Thus, the possibility of sudden increases in emissions beyond the period covered by the emission scenarios are not considered. This choice is motivated by that it is not meaningful, or even possible, to account for details in human behaviour and socioeconomic developments in the far future.

Table 2-3. Qualitative likelihood scale used in the likelihood assessment of emission scenarios

Likelihood	Description
Very low	Highly unlikely to occur. Very little to no scientific evidence.
Low	Unlikely to occur. Not supported by most scientific evidence.
Moderate	Possible to occur. Scientific evidence is ambiguous. This category is also used when the likelihood assessment is highly uncertain.
High	Likely to occur. Supported by most scientific evidence.
Very high	Highly likely to occur. Scientific consensus.

Assessment in PSAR SFR (SKB TR-23-05, Section 4.2)

A future development comparable to RCP2.6 (i.e. that the 2 °C goal of the Paris Agreement will be met) was given a *moderate* likelihood in PSAR SFR (SKB TR-23-05, Section 4.2.2). It was assessed that meeting the goals of the Paris Agreement solely by means of substantial emission reductions within the coming decades is not a likely outcome. The *moderate* likelihood was however motivated by a deep uncertainty related to the potential future development of technologies that may be employed at a massive scale to remove CO_2 from the atmosphere.

In PSAR SFR, the development characterised by medium emissions (i.e. similar to RCP4.5/RCP6.0) was assigned a *high* likelihood (SKB TR-23-05, Section 4.2.2). This assessment was based primarily on projections of likely CO_2 emissions from fossil fuels and industry. Such projections are compiled in the World Energy Outlook published annually by the International Energy Agency (IEA). In preparation for PSAR SFR, the IEA had published two projections representing “business as usual” emissions until the year 2040: the current policies scenario (CPS) and the stated policies scenario (STEPS) (IEA 2019). In both CPS and STEPS, it was assumed that all climate policies that had been implemented until that point in time will remain in the future. The only difference between the scenarios was that in CPS, it was assumed that no new policies will be implemented, whereas in STEPS it was assumed that also stated climate policy commitments by the nations are met, but that no new policies are added beyond that. Both scenarios were considered "business as usual" developments because the underlying assumption is that current global energy and emissions trajectories will continue in the future. The difference in the projected CO_2 emissions between the scenarios was however small due to a small contribution by the nations' stated policy commetments. As a result, both CPS and STEPS described emissions comparable to the RCP4.5/RCP6.0 scenarios in IPCC AR5.

The scenario describing high-end emissions with no climate policy implementation (RCP8.5) was assigned a *low* likelihood in PSAR SFR (SKB TR-23-05, Section 4.2.2). This assessment was based on multiple sources of information, most importantly the successful implementation of policies to mitigate climate change (which was supported by the IEA projections) as well as the fact that a several-fold increase in coal use, which is necessary for achieving emissions comparable to RCP8.5, has become increasingly unlikely in light of substantially cheaper renewables in recent decades.

Assessment in the present report

The IEA projections constitute a key input when assessing the likelihood of cumulative emissions also in the present report. The most recent IEA projections at the time of writing (IEA 2022) are shown in Figure 2-3. These projections present a few notable differences compared to that used in the PSAR SFR (IEA 2019). First, the projections in IEA (2022) are made until the year 2050 as opposed to 2040 in IEA (2019). Second, CPS has been removed in IEA (2022), so "business as usual" emissions are represented only by STEPS in that publication. While the projected emissions from STEPS is slightly lower in IEA (2022) compared to IEA (2019), it is still roughly consistent with SSP2-4.5 (RCP4.5 in the previous analysis, see further Section 2.5.1) and below any baseline development that assumes no climate policy (Figure 2-3). Based on this result, the likelihood of achieving emissions comparable to SSP2-4.5 is assessed to be *high* in the present report (Table 2-4), thus the same as in PSAR SFR.

Another important update in IEA (2022) is the inclusion of the announced policy scenario (APS), which assumes that all pledged ambitions and climate mitigation targets by all countries are met. Thus, APS shows the extent by which current ambitions deviate from achieving net-zero emissions by 2050 AD, which is frequently used as benchmark for meeting the 1.5 °C target the Paris Agreement (Section 2.4). Although it fails to achieve net-zero emissions by 2050 AD (Figure 2-3), the APS illustrates a plausible path toward lower emissions based on current ambitions. If all announced policies of today were to be implemented, the warming by 2100 AD would be around 2 °C, which is roughly consistent with the projections for 2100 AD under the SSP1-2.6 scenario. However, whether all pledged ambitions and targets included in APS will be met is judged to be highly uncertain. Therefore, a future development comparable to the SSP1-2.6 scenario is assigned a *moderate* likelihood in the present report (Table 2-4). The likelihood of limiting the warming to 1.5 °C, i.e. consistent with the SSP1-1.9 scenario, is assessed to be lower than for the SSP1-2.6 scenario. On the other hand, the uncertainty related to potential large-scale employment of technological solutions to reduce emissions has not changed since PSAR SFR. Thus, it cannot be excluded that the atmospheric CO_2 concentrations will be significantly reduced even if the anthropogenic emissions remain considerably above zero. Therefore, following the approach in PSAR SFR, the likelihood of the SSP1-1.9 scenario is also assessed to be *moderate* due to a deep uncertainty in future technological developments.

Table 2-4. Assessed likelihood of cumulative CO_2 emissions in the five core SSP scenarios. The likelihoods are assessed according to the qualitative likelihood scale in Table 2-3

Emission scenario	Qualitative likelihood
SSP1-1.9	Moderate
SSP1-2.6	Moderate
SSP2-4.5	High
SSP3-7.0	Moderate
SSP5-8.5	Low

Given that global emissions have not increased substantially since the preparation of PSAR SFR (Figure 2-3), the conclusion in PSAR SFR that the likelihood of SSP5-8.5 is *low* still holds. Since the assessment in PSAR SFR, also the IPCC, who traditionally has abstained from assigning individual probabilities to their emission scenarios, has also explicitly stated that SSP5-8.5 is an unlikely development until 2100 AD in light of recent developments in the energy sector (Section 1.6.1.4 in Chen et al. 2021). In addition to SSP5-8.5, IPCC AR6 also includes SSP3-7.0 as an alternative high emission scenario (Section 2.5.1). Similar to SSP5-8.5, this scenario assumes a world without any climate policy, which is clearly at odds with current trends. However, achieving cumulative emissions comparable to SSP3-7.0 is still considered more likely than SSP5-8.5. This is, for example, illustrated by the possibility to achieve a radiative forcing of about 7 W m^{-2} for several SSP-narratives as opposed to only one for 8.5 W m^{-2}. Furthermore, there is a great uncertainty related to when net-zero emissions are reached under business-as-usual developments. If this were to occur significantly later than the beginning of the next century, as suggested by SSP2-4.5, the total emissions could end up being close to SSP3-7.0 (while still being far from SSP-8.5). Therefore, the likelihood of SSP3-7.0 is assessed to be *moderate* (Table 2-4).

2.6.2 Typical atmospheric CO_2 concentrations under different SSP scenarios and climate domains

In this section, typical atmospheric CO_2 concentrations for present-day (year 2020) conditions, for the five core SSP scenarios and for colder climate domains are presented (Table 2-5). These are used in the parameterisations of terrestrial ecosystems in the biosphere transport and exposure model (Section 2.1.2). Best estimates close to the maximum concentrations for each SSP scenario are selected (IPCC 2021b), as well as ranges based on uncertainties in the global carbon cycle. These uncertainties are based on the interquartile range of CO_2 concentrations in the carbon-cycle sensitivity experiments of Booth et al. (2017) (see further Section 2.5.1). For the highest emissions explored in Booth et al. (2017), the resulting median CO_2 concentration in the simulations was approximately 1000 ppmv with an interquartile range of approximately 20 % of the median value. For lower emissions, the uncertainty was found to be smaller, with an interquartile range amounting to approximately 10 % of the resulting median concentrations. These results are adopted to the definitions of the uncertainty ranges in Table 2-5. Thus, for the SSP3-7.0 and SSP5-8.5 scenarios, which exhibit maximum concentrations well above 1000 ppmv, it is assumed that the interquartile range is 20 % of the best estimate, whereas for SSP1-1.9, SSP1-2.6 and SSP2-4.5, the corresponding range is assumed to be only 10 %. For periglacial/glacial conditions, the typical concentrations and uncertainty ranges are inferred from the Antarctic ice core records (Section 2.3).

Table 2-5. Best-estimate (outside brackets) and uncertainty (inside brackets) of atmospheric CO_2 concentrations for the five core SSP scenarios (Section 2.5.1) and for colder climate domains. The present-day (year 2020) CO_2 concentration is also included for comparison.

Climate domain	Scenario	Atmospheric CO_2 concentration (ppmv)
Temperate	Present-day	419
	SSP1-1.9	440 [418 to 462]
	SSP1-2.6	470 [447 to 493]
	SSP2-4.5	640 [608 to 672]
	SSP3-7.0	1500 [1350 to 1650]
	SSP5-8.5	2200 [1980 to 2420]
Periglacial	-	200 [180 to 220]
Glacial	-	200 [180 to 220]

3 Climate evolution

3.1 Introduction

3.1.1 Definitions

Climate evolution comprises the evolution of SAT, precipitation (P) and potential evapotranspiration (PET) that follows from the climate forcing agents described in Chapter 2 as well as intrinsic climate-system processes and feedbacks. The difference between precipitation and potential evapotranspiration, defined as P–PET, is also of particular interest as it measures the excess, or deficit, of water provided by the atmospheric conditions. The climate evolution also determines the timing of transitions between climate domains (Section 1.2.3). In particular, the timing of the onset of the next glaciation in the Northern Hemisphere, referred to as the next glacial inception, is of particular interest for post-closure safety.

3.1.2 Importance for post-closure safety

Climate evolution affects post-closure safety both *directly* and *indirectly*.

Climate evolution *directly* impacts post-closure safety primarily through changes in P–PET during future temperate and terrestrial (i.e. when the Forsmark area is not submerged beneath the sea) conditions. These changes in P–PET are largely governed by the anticipated future SAT changes. P–PET influences hydro(geo)logical gradients and groundwater composition in both the soil and bedrock which, consequently, affects groundwater flow. Accounting for potential changes in groundwater composition and flow is important for several aspects of the safety assessments, including the analyses of radionuclide containment for the spent fuel repository (SKB TR-21-01).

Changes in P–PET may also alter the depth to the groundwater table, which can affect the depth of alluvial wells (i.e. wells installed in the soil) and, consequently, the distance travelled by repository-derived radionuclides before they may be accessed by humans. Finally, P–PET controls the availability of excess surface water for crops and, thereby, also the extent with which crops must satisfy their water demands via groundwater uptake and/or artificial irrigation (SKB TR-23-06, Section 10.2). This water availability can, in turn, affect the radionuclide doses to humans that cultivate these crops. Potential radionuclide uptake by crops is more likely to occur during the *vegetation period*, which is the period of the year warm enough for plants to grow. Changes in the length of this period are also controlled by climate evolution.

As a whole, direct effects of climate evolution on post-closure safety are most relevant during temperate conditions and generally less important during periglacial and glacial conditions, when the surface is frozen (periglacial) or covered by an ice sheet (glacial). Moreover, during periglacial and glacial conditions, human exploitation of the land surface around Forsmark is generally marginal or non-existent. This is not the case during temperate conditions. Therefore, descriptions and analyses included in this chapter focus mainly on the climate evolution during temperate conditions.

Indirect effects of climate evolution primarily include impacts on other climate-related processes relevant to post-closure safety, such as ice-sheet development (Chapter 4), relative sea-level change (Chapter 5) and permafrost development (Chapter 6). Thus, climate evolution determines the timing of transitions between, and the temporal extent of, climate domains (Section 1.2.3) at Forsmark on timescales of 100 kyr to 1 Myr, as well as the possibility and temporal extent of periods during which the region is submerged by the sea. The evolution of climate domains is based both on the historical and the projected future climate in Forsmark.

In general, at some point within the next 1 Myr, the climate is expected to return to the dynamics as observed over the past 800 kyr, i.e. recurrent 100-kyr long glacial–interglacial cycles (Section 2.3). However, as discussed later in this chapter (Section 3.5.3), the timing of this return is highly dependent on anthropogenic GHG emissions. Over the next 100 kyr, these emissions are projected to have an even stronger influence on the climate evolution at Forsmark than over longer timescales. A key question for SFR, therefore, is the likelihood of transitions to colder climate domains (periglacial or glacial, see Section 1.2.3) at Forsmark within the next 100 kyr, taking scenarios of future anthropogenic emission into account. These likelihoods, in turn, support the selection of scenarios in the safety assessment (Section 1.2.3).

3.1.3 Previous documentation

Climate evolution at Forsmark has previously been described primarily in the climate reports produced for SKB's safety assessments for the spent fuel repository and SFR (e.g. SKB TR-10-49, SKB TR-13-05, SKB TR-20-12 and SKB TR-23-05). The latest climate reports (PSAR) for the spent fuel repository and SFR both included a dedicated section on the historical climate evolution of the last glacial cycle and the Holocene (SKB TR-20-12, Section 4.2 and SKB TR-23-05, Section 3.2), based on several publications on this topic (Helmens 2009, 2013, 2019, Helmens et al. 2021, Schenk and Wohlfarth 2019, Wohlfarth 2009, 2013). Both climate reports also included extensive summaries of regional climate modelling for past periglacial and glacial as well as warmer temperate conditions based on Kjellström et al. (2009). In the climate report for PSAR SFR, a dedicated section of the future climate evolution at Forsmark on timescales ranging from 100 years to 100 kyr was also included (SKB TR-23-05, Section 3.4) as well as a likelihood assessment of these future climate developments (SKB TR-23-05, Chapter 4).

Most of the information about climate evolution compiled in previous SKB documents will only be briefly summarised in this chapter. Instead of repeating previously published information, this chapter focuses on the evaluation of new developments since the publication of the most recent safety assessment climate report. In particular, this concerns implementation of new information and data provided by the recent literature, in particular IPCC AR6.

3.2 Controlling variables and conditions

The discussion about controlling variables and conditions in this chapter is divided into two parts. The first part focuses on the impact of the climate forcing agents described in Chapter 2 by introducing simplified, yet physically consistent, models on how the global-mean SAT can be computed from these climate forcing agents. The second part has a more regional focus; it describes processes and conditions of importance for maintaining the present-day climate at Forsmark, and regional factors that are important to consider in a changing climate.

3.2.1 Global-mean SAT response to climate forcing

The simplest model to describe the Earth's climate and its response to climate forcing is the zero-order energy balance model (EBM) (e.g. North and Stevens 2006):

$$C\frac{\partial \overline{T}_s}{\partial t} = \frac{S}{4}\left(1-\alpha_p\right) - \varepsilon\sigma\overline{T}_s^4, \qquad \text{Equation 3-1}$$

where t is time [s], $\overline{T}_s$ the global and annual mean SAT [K], and C a numerical constant describing the global average heat capacity [J m^{-2} K^{-1}]. In this model, the change in $\overline{T}_s$ is a function of the difference between the flux of energy reaching the Earth's atmosphere and the outgoing energy flux escaping Earth's atmosphere back to space. The energy flux to the Earth is controlled by the solar irradiance at the top of the atmosphere (S [W m^{-2}]) as well as the planetary albedo (α_p [-]), which represents the reflection of the solar flux back to space by clouds, particles in the atmosphere and the Earth's surface. On multi-millennial timescales or longer, the solar irradiance is primarily controlled by the Milankovitch cycles, described in Section 2.2.1.

The net outgoing radiation from Earth is a function of the global mean SAT according to Stefan Boltzmann's law for thermal radiation (σ is the Stefan-Boltzmann constant and approximately equals 5.7×10^{-8} W m^{-2} K^{-4}). The dimensionless parameter ε represents the effective emissivity and is included to account for atmospheric effects. If the thermal radiation emitted by the Earth surface were to escape directly to space, without being absorbed in the atmosphere, then $\varepsilon = 1$. However, due to the greenhouse effect (Section 2.2), the thermal radiation emitted from the surface is absorbed in the atmosphere, resulting in a lowering of the effective emissivity. For current conditions, ε is estimated to be around 0.6 (e.g. McGuffie and Henderson-Sellers 2014). This value will gradually decline with increasing atmospheric GHG concentrations which, all else being equal, results in an increase of $\overline{T}_s$ to satisfy Equation 3-1.

For a climate in equilibrium (i.e. incoming = outgoing energy flux), $\partial\overline{T}_s/\partial t = 0$ and the global mean SAT is governed by:

$$\overline{T}_s = \sqrt[4]{\frac{S(1-\alpha_p)}{4\varepsilon\sigma}} \qquad \text{Equation 3-2}$$

Inserting estimated values of the model parameters based on current climate conditions (S = 1360 W m^{-2}, α_p = 0.3 and ε = 0.6) yields $\overline{T}_s \approx 289$ K $\approx$ 16 °C, which approximately corresponds to the present-day observed global mean SAT (NASA 2023).

Equation 3-1 can be further simplified to illuminate the effect on the climate of anthropogenic GHG forcing (see e.g. McGuffie and Henderson-Sellers 2014). As a first step, owing to the small range of global-mean SAT that can realistically be observed at Earth (typically in the range 280–300 K), the outgoing thermal radiation can be approximated as a linear dependency on SAT, i.e. $\varepsilon\sigma\overline{T}_s^4 \approx F + B\overline{T}_s$, where F is the radiative forcing [W m^{-2}] and B is the climate-sensitivity parameter [W m^{-2} K^{-1}]. If considering only incremental changes of the radiative forcing (ΔF) and, again, assuming steady state, the equilibrium global-mean SAT change ($\Delta\overline{T}_s$) in response to anthropogenic forcing can be expressed as:

$$\Delta\overline{T}_s = ECS\frac{\Delta F}{\Delta F_{2xCO_2}} \qquad \text{Equation 3-3}$$

where ECS is the *equilibrium climate sensitivity*, defined as the equilibrium global-mean SAT response to doubling of the atmospheric CO_2 concentration ($ECS \equiv \Delta\overline{T}_{s,2\times CO_2} = \Delta F_{2xCO_2}/B$). Owing to the logarithmic dependence on the atmospheric CO_2 concentration of its radiative forcing (Section 2.2.2), any doubling of the atmospheric CO_2 will result in approximately the same increase in radiative forcing (ΔF_{2xCO_2}). The magnitude of this parameter is relatively well constrained and amounts to approximately 3.9 W m^{-2} (Myhre et al. 1998, Meinshausen et al. 2020). The magnitude of ECS has been estimated to be 3 °C, or close to 3 °C, since the publication of the first IPCC assessment report. In the latest IPCC assessment report (AR6), the best estimate of ECS is also assessed to be 3 °C, with a likely range between 2.5 °C and 4 °C, and a very likely range between 2 °C and 5 °C. (Forster et al. 2021). This assessment is based on multiple lines of evidence, including evidence from process understanding, instrumental records and paleoclimate data.

An important limitation of ECS is that it does not account for changes in the planetary albedo (note that potential changes in α_p were dropped in the derivation of Equation 3-3). Thus, contributions to the global mean SAT from albedo changes due to, for instance, changes in Earth's ice sheets need to be calculated separately. It is also important to emphasise than any GHG-induced SAT change inferred from Equation 3-3 describes only the *global mean*, and this may differ significantly from the associated SAT change in a certain region. In northern Europe, for example, three additional aspects must be considered when describing the climate in the region: (i) the land-ocean warming contrast, (ii) Arctic amplification and (iii) changes in the atmosphere and ocean circulation. These are further discussed in the following subsections.

3.2.2 Land-ocean warming contrast

IPCC AR6 concludes that it is virtually certain that future warming will be higher over land than over the oceans. This land-ocean-warming contrast is also clearly visible in observational records. For example, between 1979 and 2016, the average SAT increase was approximately 40 % higher over land than over the oceans (Byrne and O'Gorman 2018). A similar contrast is also found in future climate projections (Lee et al. 2021). The warming contrast occurs because air over land is drier than air over oceans, and this contrast is greater over drier land regions than over moister ones. For example, the ratio of land-to-ocean warming over dry subtropical continents is about 1.5, while it is only 1.2 over moister regions such as the midlatitudes (e.g. Byrne and O'Gorman, 2013). Thus, the land-to-ocean warming ratio in Forsmark is in the lower end of the 1.2–1.5 range.

3.2.3 Arctic amplification

The Arctic surface is projected to warm more than the global average in response to increased GHG forcing (Lee et al. 2021). This phenomenon, known as *Arctic amplification*, has also been observed over recent decades concurrent with Arctic sea ice loss (e.g. Serreze and Barry 2011). A combination of processes contributes to the Arctic amplification, including feedbacks associated with the loss of sea ice and snow as well as radiative feedbacks associated with the temperature in the Arctic atmosphere and increases in the poleward heat transport by the atmosphere and oceans (Lee et al. 2021). The Arctic-to-global average warming ratio is estimated to be between 2 and 4 (e.g. Nummelin et al. 2017). Located south of the Arctic, at around 60ºN, the enhanced warming at Forsmark is projected to be slightly smaller. Projections using coupled atmosphere-ocean circulation models suggest that the ratio of warming at this latitude to the global-average warming is between 1 and 2 (Nummelin et al. 2017).

3.2.4 Atmosphere and ocean circulation

In general, the SAT in northern Europe, including Forsmark, is significantly higher than the average SAT of comparable latitudes (Figure 3-1). This warm anomaly is most pronounced in the winter season (December–February; DJF), when it reaches almost 10 °C above the latitudinal average, while it is smaller (less than 5 °C above the latitudinal average) during the summer season (Figure 3-1). These warmer conditions are maintained by the atmosphere and ocean circulation, both of which contribute to a net transport of heat and moisture from lower latitudes to the region. In the atmosphere, heat and moisture are transported primarily through synoptic-scale weather systems, which travel along narrow zones over the oceans, referred to as storm tracks. Over the North Atlantic, the storm tracks have on average a southwest-northeast direction, resulting in a net transport of relatively mild and humid air to northern Europe.

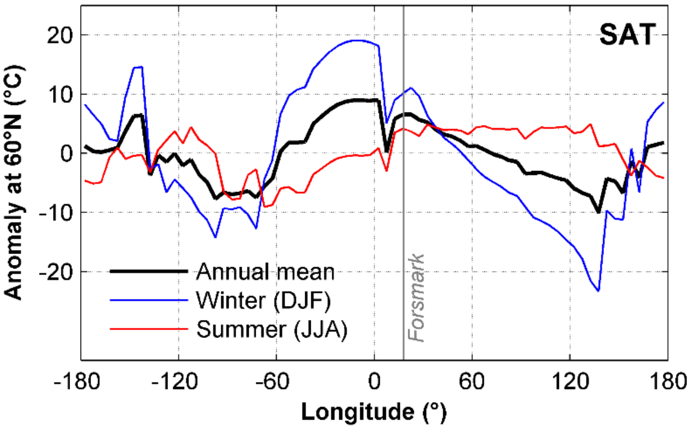

Figure 3-1. *Differences from the average conditions at 60ºN of present-day SAT for the annual mean (black) as well as the winter (blue) and summer (red) seasons. The figure is based on monthly-mean ERA5 reanalysis data*[4] *between the years 1991 and 2020 (Hersbach et al. 2020). The longitude of Forsmark is indicated by the vertical grey line.*

---

[4] Reanalysis data comprise a mixture of observations with past short-range weather forecasts rerun with modern weather forecasting models.

The extent by which the atmospheric circulation over northern Europe will change in a warmer climate is associated with large uncertainty; this is mirrored by a high variability in projected future changes of the average wind speed in the region (Christiansen et al. 2022). In general, however, most models project that the latitudinal position of the storm tracks will shift poleward as the climate becomes warmer, resulting in increased precipitation in northern Europe, especially during the winter season (Lee et al. 2021, Christiansen et al. 2022).

The relatively warm conditions in Forsmark are also maintained by the ocean circulation, in particular the Atlantic Meridional Overturning Circulation (AMOC). The AMOC is characterised by warm and saline waters that move northward in the upper ocean by the Gulf Stream and the North Atlantic current (e.g. Buckley and Marshall 2016). As they travel north, these waters become more dense due to a loss of heat and, thus, buoyancy to the atmosphere. Once they reach a critical density threshold, the waters will sink and, ultimately, return southward in the deep ocean (Broecker 1991).

In a warmer world, rising water temperatures along with increased precipitation and meltwater forcing from the Greenland ice sheet are projected to make the North Atlantic surface waters less dense, resulting in a weakening of the AMOC. Direct measurements of the AMOC, which began in the year 2004, show that the AMOC strength has declined in recent years (Robson et al. 2013, Smeed et al. 2014, 2018). However, the internal temporal variability is large, and so it is not yet possible to establish whether the recent decline is caused by anthropogenic warming or if it reflects natural variability (e.g. Frajka-Williams et al. 2019). Nonetheless, projections with coupled atmosphere-ocean models collectively show that the AMOC strength will decline until 2100 AD due to increased GHG forcing (Fox-Kemper et al. 2021).

Depending on the magnitude of the atmospheric warming and the freshwater input, the AMOC may potentially also shut down completely into a collapsed state (e.g. Wang et al. 2023). Such collapse may result in several degrees of cooling over Scandinavia, but its effects are likely limited in time (see further Appendix A1). The magnitude of the atmospheric warming and freshwater input required for transitioning into a collapsed state of the AMOC are highly uncertain. Whilst the magnitude of the AMOC response to global warming varies greatly across state-of-the-art atmosphere-ocean models, none of the models project a complete collapse of the AMOC before the end of this century (Bellomo et al. 2021). This result can partially be explained by that the models neglect meltwater release from the Greenland ice sheet. In addition, it has been argued that the models have systematic biases that considerably affect the sensitivity of the modelled AMOC to freshwater forcing (e.g. Liu et al. 2017). By correcting for existing biases, it has been found that the AMOC behaviour may change dramatically on centennial to millennial time scales, and that the probability of a collapsed state increases (Liu et al. 2017). Along the same lines, recent process studies suggest that a collapse of AMOC can be induced, even by small changes in freshwater forcing (Lohmann and Ditlevsen 2021, Ditlevsen and Ditlevsen 2023).

Taken together, the possibility of a collapse of the AMOC over the next centuries and millennia cannot be excluded. However, the IPCC argues (albeit with reduced confidence) that the AMOC will not collapse before 2100 AD under any emission scenario (Fox-Kemper et al. 2021). In their special report on the ocean and cryosphere in a changing climate, the IPCC assessed that a collapse of the AMOC before 2300 AD is “as likely as not” (IPCC 2019). Although the exact threshold of an AMOC collapse is not known, the probability of such event increases with increasing freshwater forcing and, thus, with increasing human-induced warming. The impact of an AMOC collapse on the future climate at Forsmark is further discussed in Sections 3.5.2 and 3.6.1 as well as in Appendix A1.

3.3 Historical climate

In this section, the historical climate evolution of the Middle and Late Quaternary (approximately the last 800 kyr) is discussed. This period is characterised by large global climate fluctuations resulting in recurrent glacial-interglacial cycles of periods of about 100 kyr (Figure 2-1a). In particular, the climate evolution during the last of these cycles, i.e. the *Weichselian* glaciation and the subsequent *Holocene* interglacial, is described in more detail as more data is available from these periods compared to preceding glacials and interglacials.

3.3.1 Late Quaternary

As discussed in Section 2.3, the later part of the Quaternary is characterised by recurring glacial-interglacial cycles lasting approximately 100 kyr. Throughout each cycle, ice sheets grow gradually in a stepwise manner, advancing during colder phases (stadials) and retreating during warmer phases (interstadials). This pattern of ice-sheet expansion and contraction gives rise to the characteristic saw-tooth shape of late Quaternary global ice volume evolution (Figure 2-1a), with prolonged (typically 80–90 kyr) periods of stepwise ice growth followed by shorter (10–20 kyr) interglacial phases. During these extended periods of ice-sheet growth, the climate was significantly colder than today, with global mean surface air temperatures estimated to have been 1–5 °C below pre-industrial levels (Snyder 2016).

During the shorter interglacial periods, global-mean SAT was generally comparable to pre-industrial levels. However, variations in insolation, GHG concentrations, and remaining ice extents meant that not all interglacials of the past 800 kyr were equally warm (e.g. PAGES 2016). Marine paleo-proxy records suggest that the previous interglacial, the Eemian (~130–115 kyr BP), was among the warmest – if not the warmest – of this period (PAGES 2016, Snyder 2016). During this interglacial, atmospheric CO_2 concentrations were higher than during most preceding interglacials (Figure 2-1c). In the early Eemian, Northern Hemisphere summer insolation was relatively high but gradually declined toward the end of the interglacial (Figure 2-1b). This high summer insolation was primarily driven by a greater obliquity (axial tilt; see Section 2.2.1) than at present.

Paleo-proxy data suggest that the average global-mean SAT during the Eemian was comparable to present-day levels, with an early peak reaching about 1 °C above current temperatures, coinciding with the maximum in Northern Hemisphere summer insolation (Turney et al. 2020). However, recent coordinated climate modelling experiments estimate that early Eemian global mean SAT was similar to pre-industrial levels (Otto-Bliesner et al. 2021), thus indicating slightly cooler conditions than those inferred from paleo-proxy data.

The modelling experiments further suggest that during the early Eemian, annual-mean SAT in Scandinavia was 1–2 °C higher than pre-industrial levels due to increased obliquity (Otto-Bliesner et al. 2021). The simulations also indicate that this warming was primarily a summer phenomenon. Specifically, the average summer SAT (June–August; JJA) is estimated to have been 3–4 °C above pre-industrial levels (2–3 °C warmer than at present), while winter (DJF) SAT remained similar to pre-industrial temperatures (Otto-Bliesner et al. 2021). In contrast to SAT changes, early Eemian precipitation rates in Scandinavia were likely similar to pre-industrial levels in both summer and winter (Otto-Bliesner et al. 2021).

3.3.2 Weichselian glacial cycle and the Holocene

The declining summer insolation towards the end of the Eemian interglacial eventually resulted in the growth of ice sheets over the Northern Hemisphere continents. This is estimated to have occurred around 115 kyr BP (e.g. Clark et al. 1993, Waelbroeck et al. 2002) following a relative minimum in the summer insolation. The last glacial inception also marks the onset of the Weichselian glacial cycle, which represents the last glacial cycle in the Northern Hemisphere. The Weichselian ended at the transition to the Holocene approximately 11 kyr ago. The different warm interstadial and cold stadial phases of the last glacial cycle are often divided into numbered so-called Marine Isotope Stages (MIS). To facilitate the discussions in this section and in subsequent chapter, these stages are summarised and described in Table 3-1 for the Weichselian and the Holocene as well as for the Eemian and the penultimate glacial period.

Table 3-1. Summary and description of Marine Isotope Stages, ages, stadials and interstadials of the Eemian, Weichselian and Holocene. Regional variations from the denoted warm/cold state occur and there is a wide range of regional names used for each of the stadials/interstadials, see e.g. Helmens (2013, 2019) and Wohlfarth (2013)

Marine Isotope Stage	Age (kyr BP)	Interglacial /glacial	Name of interglacial/phase of Weichselian	Stadial/Interstadial	Warm/Cold
MIS 6	190–130	Glacial	Late Saalian		Cold
MIS 5e	130–115	Interglacial	Eemian		Warm
MIS 5d	115–105	Glacial	Early Weichselian	Stadial	Cold
MIS 5c	105–93	Glacial	Early Weichselian	Interstadial	Warm
MIS 5b	93–85	Glacial	Early Weichselian	Stadial	Cold
MIS 5a	85–74	Glacial	Early Weichselian	Interstadial	Warm
MIS 4	74–59	Glacial	Middle Weichselian	Stadial	Cold
MIS 3	59–24	Glacial	Middle Weichselian	Interstadials/Stadials	Warm/cold
MIS 2	24–11	Glacial	Late Weichselian, including the Last Glacial Maximum	Stadial	Cold
MIS 1	11–0	Interglacial	Holocene		Warm

The climate evolution during the Weichselian and Holocene has been extensively studied in numerous SKB publications (Helmens 2009, 2013, 2019; Helmens et al. 2021; Schenk and Wohlfarth 2019; Wohlfarth 2009, 2013). Key findings from these studies are summarised in the PSAR climate reports (e.g., SKB TR-20-12, Section 4.2). Many of the findings are based on interpretations of late Quaternary environmental and climate-proxy data from lake sediments in Sokli, located close the Arctic circle in northern Finland. However, as each study has focused on different phases of the Weichselian, a comprehensive picture of climate evolution throughout the entire glacial cycle, based on the Sokli data, has not emerged. To address this, all proxy studies from the Sokli site have been summarised concisely and coherently in Helmens et al. (2024).

The multi-proxy analyses on the Sokli sediments provide an unprecedented wealth of environmental data for the late Quaternary of Fennoscandia. Most importantly, it has resulted in an environmental/climate record that significantly revises earlier concepts of glaciation, vegetation, and climate in Fennoscandia over the last 130 kyr. The Sokli sequence reveals a highly dynamic Fennoscandian ice sheet with significantly less ice-cover over Fennoscandia in both time and space than previous reconstructions. According to the previous reconstructions, Sokli was mostly glaciated for nearly 100 kyr, from the start of MIS 5d to the start of the Holocene.

In contrast, analyses of Sokli sediments show that the summer SAT during the three warm stages of MIS 5, i.e. MIS 5a, 5c and 5e as well as part of MIS 3 (Table 3-1), were similar, or in some cases even higher, compared the present temperatures in region. These periods were also dominated largely by boreal forests. The data also suggest that the Sokli basin was not glaciated during the cold MIS 5d stage (centred at 110 kyr BP). Instead, the proxy analysis suggests that steppe-tundra vegetation prevailed during this time with relatively high summer temperatures, indicating a strong continental climate regime with the possibility of deep continuous permafrost. Only during MIS 5b, MIS 4 and MIS 2 was Sokli fully glaciated.

The results obtained from Sokli enhance our understanding about the Weichselian climate in Forsmark. Since summer SATs as high, and even higher, than at present existed in the Sokli region north of Forsmark during the warm stages of MIS 5 and parts of MIS 3, it is likely that south–central Sweden, including the Forsmark region, experienced similar warm summer climates during these periods. Another conclusion is that since Sokli was not fully glaciated for most of the glacial cycle, this must have also been the case for Forsmark. Indeed, this notion is also supported in the Weichselian ice-sheet reconstruction, which is described in Section 4.3.1.

3.4 Present-day climate at Forsmark

3.4.1 SAT, precipitation, potential evapotranspiration and P–PET

As weather patterns may deviate significantly from their average on seasonal to annual timescales, typically 20 or 30 years of data are used when defining present-day climate at a certain location. Here we use the reference period 1995–2014, which is also used in IPCC AR6. SKB's meteorological measurements at the Forsmark site were initiated in year 2003. Therefore, the Forsmark SAT and precipitation data for the 1995–2014 period are estimated using both local meteorological measurements from the site and data from nearby stations operated by the Swedish Meteorological and Hydrological Institute (SMHI), following the methodology described in SKB (TR-23-05, Appendix C). The calculated mean seasonal and annual SAT and precipitation at Forsmark for the 1995–2014 period are shown in Table 3-2.

For comparison, we have also included SAT and precipitation from the period October 1st 2014–September 30th 2017. These data are considered representative in a long term, average sense, for the present climate in Forsmark. They are used as upper boundary condition in the quantitative hydrological modelling of Baseline Forsmark (Lampinen 2025), which is a multidisciplinary description of environmental conditions at the Forsmark repository sites prior to the start of above ground and underground contract works. In contrast to the 1995–2014 period, the Baseline Forsmark data (2014–2017) are acquired entirely from SKB's own meteorological measurements. The mean seasonal and annual SAT and precipitation estimated for the Baseline Forsmark period are in general similar to those estimated for the IPCC reference period (Table 3-2). This supports continued use of these data as "typical" Forsmark climate in the hydrological modelling, despite only consisting of three years instead of the 20 or 30 years which are traditionally used.

It is important to note that it is not possible to calculate Forsmark PET accurately for the IPCC reference period. This is because calculating PET accurately requires abundant local meteorological data, such as SAT, humidity, wind speed and net radiation (e.g. Gustafsson 2022). Since these data are only available for Forsmark since 2003, estimates of PET for the entire 1995–2014 reference period are not provided here. In contrast to the 1995–2014 period, however, it is possible to calculate PET for the Baseline Forsmark period (2014–2017). These calculations were initially carried out using the Penman equation as described in Eriksson (1981). However, it has been demonstrated that these calculations overestimate PET in Forsmark, as the methodology used in Eriksson (1981) was designed for short-cut grass. If taken boreal forests into account, which are abundant in the Forsmark area, the estimated PET becomes considerably lower (Gustafsson 2022). The overestimation of the PET using the Eriksson (1981) methodology has also been demonstrated by the hydrological modelling in Forsmark. In this modelling, the original PET values are reduced by 15 % during model calibration in order to accurately reproduce observed present-day runoff rates in discharge areas (e.g. Bosson et al. 2008). Therefore, the PET values shown in Table 3-2, based on the Baseline Forsmark data, reflects the calibrated PET values used in the hydrological modelling rather than the original ones. As can be seen in Table 3-2, the calculated Forsmark PET for this period exhibits a strong seasonality, with more than half of the annual PET occurring in the summer season (JJA). As a result, precipitation exceeds PET during autumn and winter, while the opposite is true during spring and summer (Table 3-2). Annually, precipitation exceeds PET by approximately 60 mm (Table 3-2).

Table 3-2. Mean seasonal and annual SAT and precipitation estimated for the IPCC AR6 reference period (1995–2014). Mean seasonal and annual SAT, precipitation, PET and P-PET based on local data (Oct 2014–Sep 2017) used in the hydrological modelling of Baseline Forsmark (Lampinen 2025) are also shown. SAT and precipitation estimated for the IPCC AR6 baseline period (1995–2014) are also shown for comparison. Abbreviations refer to different seasons: DJF refers to December–February, MAM to March–May, JJA to June–August and SON to September–November

Variable	Reference period	Winter (DJF)	Spring (MAM)	Summer (JJA)	Autumn (SON)	Annual
SAT (ºC)	1995–2014	–1.8	4.8	16.1	7.3	6.6
	Baseline Forsmark	–0.5	5.5	15.2	7.4	6.9
Precipitation (mm)	1995–2014	136	106	194	170	606
	Baseline Forsmark	132	103	187	140	563
PET (mm)	Baseline Forsmark	15	154	273	62	504
P–PET (mm)	Baseline Forsmark	117	–50	–86	78	59

3.4.2 Köppen-Geiger classification

The Köppen-Geiger system classifies climate into five main groups (A to E, see Table 3-3). These are subdivided, with additional letters again used to designate the various subtypes. For some of the B, C and D subtypes, also a third letter is introduced to differentiate between hotness/coldness of different seasons. The classification is based on monthly-mean SAT and precipitation. It aims to empirically map biome distributions around the world as different regions in a similar class share common vegetation characteristics. The first version of this classification was developed in the late 19th century (Köppen 1884), but has been further updated and refined since then. Here we apply the classification decribed by Peel et al. (2007) (Table 3-3) for Forsmark using climate data from both Baseline Forsmark (2014–2017) and the IPCC reference period (1995–2014).

All Köppen-Geiger parameters listed in Table 3-3 are computed for the present-day Forsmark climate (Table 3-4). The resulting Köppen-Geiger classification is *Dfb* for both the IPCC and the Baseline Forsmark reference periods. Thus, according to this classification, Forsmark is currently charactersied by a cold temperate climate with warm summers but without a dry season.

Table 3-3. Description of Köppen-Geiger climate classification symbols and defining criteria. Temperatures have unit ºC and precipitation mm. The table has been adopted from Peel et al. (2007)

1st	2nd	3rd	Description	Criteria*
A			Tropical	$T_{cold} > 18$
	f		-Rainforest	$P_{dry} > 60$
	m		-Monsoon	Not (Af) & $P_{dry} \geq$ 100–MAP/25
	w		-Savannah	Not (Af) & $P_{dry} <$ 1 00–MAP/25
B			Arid	MAP < 10×$P_{threshold}$
	W		-Desert	MAP < 5×$P_{threshold}$
	S		-Steppe	MAP ≥ 5×$P_{threshold}$
		h	-Hot	MAT ≥ 18
		k	-Cold	MAT < 18
C			Warm temperate	$T_{hot} >10$ & $0<T_{cold}<18$
	s		-Dry summer	$P_{sdry}< 40$ & $P_{sdry}< P_{wwet}/3$
	w		-Dry winter	$P_{wdry}<P_{swet}/10$
	f		-Without dry season	Not (Cs) or (Cw)
		a	-Hot summer	$T_{hot} \geq 22$
		b	-Warm summer	Not (a) & $T_{mon10} \geq 4$
		c	-Cold summer	Not (a or b) & $1 \leq T_{mon10} < 4$
D			Cold temperate	$T_{hot} > 10$ & $T_{cold} \leq 0$
	s		-Dry summer	$P_{sdry} < 40$ & $P_{sdry} < P_{wwet}/3$
	w		-Dry winter	$P_{wdry} < P_{swet}/10$
	f		-Without dry season	Not (Ds) or (Dw)
		a	-Hot summer	$T_{hot} \geq 22$
		b	-Warm summer	Not (a) & $T_{mon10} \geq 4$
		c	-Cold summer	Not (a, b or d)
		d	-Very cold winter	Not (a or b) & $T_{cold} < –38$
E			Polar	$T_{hot} < 10$
	T		-Tundra	$T_{hot} > 0$
	F		-Frost	$T_{hot} \leq 0$

* MAP = mean annual precipitation, MAT = mean annual SAT, T_{hot} = SAT of the hottest month, T_{cold} = SAT of the coldest month, T_{mon10} = number of months where the SAT is above 10 °C, P_{dry} = precipitation of the driest month, P_{sdry} = precipitation of the driest month in summer, P_{wdry} = precipitation of the driest month in winter, P_{swet} = precipitation of the wettest month in summer, P_{wwet} = precipitation of the wettest month in winter, $P_{threshold}$ = varies according to the following rules (if 70 % of MAP occurs in winter then $P_{threshold}$ = 2 × MAT, if 70 % of MAP occurs in summer then $P_{threshold}$ = 2 × MAT + 28, otherwise $P_{threshold}$ = 2 × MAT + 14). Summer (winter) is defined as the warmer (cooler) six month period of October–March and April–September.

Table 3-4. Köppen-Geiger parameters (Table 3-3) computed for Forsmark using the IPCC AR6 and Baseline Forsmark reference periods

	Reference period	
Köppen-Geiger parameter	**IPCC AR6 (1995–2014)**	**Baseline Forsmark (Oct 2014 – Sep 2017)**
MAT	6.6 °C	6.9 °C
T_{hot}	17.5 °C	16.2 °C
T_{cold}	–2.5 °C	–2.1 °C
T_{mon10}	4	4
MAP	606 mm	563 mm
P_{dry}	33 mm	25 mm
P_{sdry}	35 mm	25 mm
P_{wdry}	33 mm	25 mm
P_{swet}	74 mm	74 mm
P_{wwet}	62 mm	59 mm
$P_{threshold}$	27.2 mm	27.8 mm

3.4.3 Length of the vegetation period

According to SMHI (2022), the start of the vegetation period in a given year is defined as the first day in a period of at least six successive days when the daily-mean SAT is at least +5.0 °C. Similarly, the last day of the vegetation period is defined as the day before the first period of at least six successive days after 1 July, with a daily-mean SAT below +5.0 °C. If no such period occurs after 1 July, the vegetation period is defined to end on 31 December according to SMHI's definition (SMHI 2022).

In this report, the definition of vegetation period is approximated using monthly means instead of daily means. Thus, the start of the vegetation period is defined as the first month of a given year when the monthly-mean SAT is above +5.0 °C, whereas the end of the vegetation period is defined as the last month of that year when the monthly-mean SAT is above +5.0 °C. Using this definition, the vegetation period at Forsmark is between May and October for both the IPCC AR6 and Baseline Forsmark reference periods (Table 3-5).

Table 3-5. Length of the vegetation period as estimated from the normal year data and in the IPCC baseline period 1995–2014

Baseline	**Vegetation period**
Baseline Forsmark (2014-2017)	May to October
IPCC AR6 (1995–2014)	May to October

3.5 Future climate evolution

This section provides an overview of the projected future climate evolution in Forsmark. The discussion begins with the projected climate change until 2100 AD (Section 3.5.1), a period that roughly aligns with the construction and operation phases of SKB's repositories. The climate change projections for this period benefit from a comprehensive set of climate modelling simulations. These simulations are also used to derive key relationships between relevant climate variables (SAT, precipitation and PET). These relationships then serve as important elements for extending the projections beyond 2100 AD until the next glacial inception (Section 3.5.2). The timing of the next glacial inception is thoroughly discussed in Section 3.5.3, whereas the climate variability beyond this event is discussed in Section 3.5.4.

3.5.1 Until 2100 AD

In this section, the projected future climate evolution until 2100 AD is assessed. The section begins with a brief description of the modelling work supporting the projections, after which the projected global and regional changes in SAT, based on IPCC AR6, are presented for each SSP emission scenario (Section 2.5.1). The section ends with a description of how future precipitation and PET (and thereby also the P–PET) may change in response to the projected changes in SAT.

Climate modelling and projections of SAT

The future climate projections are carried out using a range of models of varying complexity which are forced using different scenarios of anthropogenic GHG emissions (Section 2.5.1). The most comprehensive of these models, the global Earth System Models (ESMs), constitute mathematical formulations of the natural laws that govern the evolution of the atmosphere, ocean, cryosphere, land, and biosphere, as well as the carbon cycle (Flato 2011)[5]. Less complex models that are often used to evaluate future climate change include Earth Models of Intermediate Complexity (EMICs) and so-called climate emulators, which are forced by various climate-sensitivity metrics, including ECS (Section 3.2.1).

In preparation of each IPCC assessment report, coordinated experiments are conducted in which several ESMs from different modelling centres are run under a fixed set of input data. In general, several experiments are conducted with each ESM to account for uncertainties in the modelled scenario, initial conditions and in the mechanics of the model itself. The most recent of these activities is the Coupled Model Intercomparison Project Phase 6 (CMIP6; Eyring et al. 2016), coordinated by the World Climate Research Programme. The CMIP6 experiments are used in support of the assessments of future climate change in IPCC AR6. The CMIP6 models thereby replace the previous ESMs, participating in CMIP5, that were used in support of IPCC AR5.

In IPCC AR5, the average ECS across the CMIP5 models (3.2 °C) fell approximately in the middle of the likely range (1.5 °C– 4.5 °C) based on multiple lines of evidence (e.g process understanding, instrumental records and paleoclimate data) (Collins et al. 2013, Flato et al. 2013). Because of this, the projections featured in IPCC AR5 relied heavily on the CMIP5 models.

In preparation for IPCC AR6, the CMIP6 models underwent several improvements compared to the CMIP5 versions, in particular with regard to the model grid resolution, the representation of physical and chemical processes, and biogeochemistry including the carbon cycle (Chen et al. 2021). In spite of (or because of) these improvements, the spread in the ECS across the CMIP6 models increased significantly compared to the CMIP5 models (Section 7.4.6 in Forster et al. 2021; see also Hausfather 2019). The increased spread in ECS is caused by some of the CMIP6 models producing a remarkably high ECS, which even extends beyond the very likely range (5 °C) estimated from multiple lines of evidence (Section 3.2.1). As a result, the simulated global-mean SAT increase from the 1970s until present day in these models is significantly overestimated compared to the observed warming during this time (Section 7.4.6 in Forster et al. 2021). Furthermore, another outcome of these high-ECS models is that, on average, the ECS values projected by the CMIP6 models surpass both the ECS estimates based on multiple lines of evidence (e.g. instrumental and paleoclimate data; see further Section 3.2.1), and the ECS values estimated by the CMIP5 models.

In light of the high ECS across the CMIP6 models, the approach of projecting the global-mean SAT change until 2100 AD was updated in IPCC AR6. Instead of relying solely on the CMIP experiments, the global-mean SAT change under different SSP scenarios was projected using a climate emulator. The emulator was forced by the ECS (based on multiple lines of evidence) along with other climate-sensitivity metrics[6] in order to ensure consistency between the reported global-mean SAT and climate sensitivities. Owing to the difference in ECS, the average projected global-mean SAT until 2100 AD, as estimated by the climate emulator, is consistently lower than that of the CMIP6 models (Table 3-6).

---

[5] If the carbon cycle is not included in the models, the ESMs are often referred to as atmosphere-ocean general circulation models, or AOGCM for short.

[6] An example of such a metric is the "transient climate response", which is defined as the global-mean SAT for the hypothetical scenario in which CO_2 increases at 1% yr^{-1} from a pre-industrial reference state to the time of a doubling of atmospheric CO_2 concentration (year 70), see further Forster et al. (2021).

It is important to recognise that metrics like the ECS and other climate-sensitivity measures are specifically defined in relation to global-mean SAT. Consequently, the climate emulator is exclusively applied for projections concerning global-mean SAT. While the CMIP6 models are employed by the IPCC for regional climate change projections, it is important to acknowledge that the regional SAT projections in these models may be biased due to the high average ECS, similar to the global projections. Hence, rather than directly utilising regional SAT projections from CMIP6, it is more useful to assess the projected SAT change in Forsmark by considering the ratio of projected regional to global-mean SAT change in the models (see further Section 3.5.2). This ratio can then be applied to the global-mean SAT change projected by the emulator to estimate the regional warming until 2100 AD.

Table 3-6. Projected mid-century (2041–2060) and end-of-century (2081–2100) global-mean and regional SAT change from IPCC AR6 under different SSP scenarios relative to the 1995–2014 reference period. The projected global-mean SAT changes are shown both from projections using a climate emulator, that was constrained with likely ranges of ECS and other climate sensitivity metrics (Table 4.5 in Lee et al. 2021), and from the CMIP6 projections (Table 4.2 in Lee et al. 2021). CMIP6-projected SAT changes for IPCC reference region "northern Europe" are also shown, together with ratio of the projected warming in northern Europe to that of the global mean. Data for the regional projections are derived from the IPCC Interactive Atlas (Gutiérrez et al. 2021, Iturbide et al. 2021). The brackets represent the 5 to 95 percentiles and the values outside the brackets represent the median value across the projections.

Time period	Scenario	Global mean, climate emulator (°C)	Global mean, CMIP6 (°C)	Northern Europe, CMIP6 (°C)	Ratio northern Europe to global mean, CMIP 6
2041–2060	SSP1-2.6	0.9 [0.5 to 1.3]	1.0 [0.6 to 1.6]	1.1 [0.1 to 2.1]	1.1
	SSP2-4.5	1.1 [0.8 to 1.6]	1.3 [0.8 to 1.9]	1.5 [0.5 to 2.6]	1.2
	SSP3-7.0	1.3 [0.9 to 1.7]	1.4 [0.9 to 2.3]	1.6 [0.5 to 3.0]	1.1
	SSP5-8.5	1.5 [1.1 to 2.1]	1.7 [1.2 to 2.5]	2.0 [0.9 to 3.2]	1.2
2081–2100	SSP1-2.6	0.9 [0.5 to 1.5]	1.2 [0.6 to 2.0]	1.3 [0.0 to 2.6]	1.1
	SSP2-4.5	1.8 [1.2 to 2.6]	2.0 [1.4 to 3.0]	2.4 [1.0 to 3.9]	1.2
	SSP3-7.0	2.8 [2.0 to 3.7]	3.1 [2.2 to 4.7]	3.5 [1.9 to 5.1]	1.2
	SSP5-8.5	3.5 [2.4 to 4.8]	4.0 [2.7 to 5.7]	4.4 [2.7 to 6.3]	1.1

The SAT change at Forsmark until 2100 AD is assessed using regional climate-change projections for the IPCC reference region "northern Europe" (the reference regions are outlined in Iturbide et al. 2020), which encompasses Fennoscandia and the UK (data are derived from IPCC Interactive Atlas; see Gutiérrez et al. 2021, Iturbide et al. 2021). Representing Forsmark climate change by the average regional conditions may introduce an error because intra-regional differences are not accounted for. Nevertheless, the IPCC reference regions were chosen partly based on the criterion of climate consistency. This implies that the spatial climate variability within a region is generally less pronounced than the differences observed between regions, resulting in relatively minor differences within the selected region (Iturbide et al. 2020).

On average, the projected annual-mean warming until 2100 AD in the northern European region is projected to be 10–20 % higher than the global mean across the emissions scenarios (Table 3-6). The projected warming in the region is, however, slightly smaller than that projected for other regions at comparable latitudes. For example, under the SSP3-7.0 scenario, the projected annual- and latitudinal-mean warming at 60ºN for the 2081–2100 period falls between 4 °C and 5 °C in the CMIP6 models (Figure 4.22 in Lee et al. 2021), which is slightly higher than the 3.5 °C projected for northern Europe by the same models (Table 3-6). The reduced warming in the region can also be demonstrated by examining the ratio of the warming at 60ºN to the global mean (1.1–1.2) which is in the lower end of the range projected for this latitude (Section 3.2.3). The reduced warming can be explained by the effect of a weakened AMOC, which contributes to a cooling over the North Atlantic and northern Europe due to a reduced heat transport in the ocean (Section 3.2.4).

Thus, whilst the projected global-mean warming signal over land areas in northern Europe is amplified due to Arctic amplification and the land-ocean-warming contrast (Sections 3.2.3 and 3.2.4), it is also mitigated by a postulated reduction of the AMOC strength.

The warming in the "northern Europe" reference region is projected to be significant during all seasons (Table 3-7). Although there is a minor tendency towards enhanced warming during the winter and autumn seasons, particularly for the high emission scenarios, the difference in the warming between the seasons is relatively small.

Table 3-7. Projected seasonal warming for 2081–2100 and the IPCC "northern Europe" reference region (relative to 1995–2014) based on the CMIP6 models. The brackets represent the 5 to 95 percentiles and the values outside the brackets represent the median projection across the CMIP6 simulations. Data are derived from IPCC Interactive Atlas (Gutiérrez et al. 2021, Iturbide et al. 2021)

Scenario	Winter (DJF) (°C)	Spring (MAM) (°C)	Summer (JJA) (°C)	Autumn (SON) (°C)
SSP1-2.6	1.3 [-0.3 to 2.8]	1.2 [-0.2 to 2.3]	1.3 [0.3 to 3.0]	1.5 [0.0 to 2.9]
SSP2-4.5	2.5 [1.1 to 4.2]	2.3 [0.8 to 3.6]	2.3 [1.0 to 4.0]	2.5 [1.0 to 4.2]
SSP3-7.0	3.8 [1.9 to 5.5]	3.3 [1.7 to 4.7]	3.4 [2.0 to 5.3]	3.5 [2.0 to 5.4]
SSP5-8.5	4.8 [2.8 to 6.5]	4.1 [2.4 to 5.7]	4.3 [2.2 to 6.9]	4.5 [2.6 to 7.0]

Precipitation

The average precipitation at Forsmark is projected to increase with a warmer climate. Based on the CMIP5 projections, it was found in PSAR SFR that the annual precipitation at Forsmark can be expected to increase almost linearly with the increased SAT (SKB TR-23-05, Appendix B). Large seasonal differences were also identified in PSAR SFR; the increase in precipitation was projected to be largest in winter (DJF), whereas the summer response (JJA) was ambiguous as CMIP5 models projected both an increase and decrease in the summer precipitation.

A similar precipitation response to a warmer climate is also projected in the CMIP6 projections for the northern Europe reference region (Figure Atlas.24 in Gutiérrez et al. 2021). In these models, the projected median increase in winter precipitation in this region is about 5 % $^{\circ}C^{-1}$, while the corresponding median summer precipitation is projected to be approximately the same as present-day precipitation (Table 3-8). The variability across the models is significant, implying that some models project a decrease of the summer precipitation in the region whereas others project an increase (Table 3-8).

Table 3-8. Sensitivity of winter (DJF), summer (JJA) and annual precipitation to the SAT change in the IPCC reference region "northern Europe" based on the CMIP6 projections for 2100 AD. The values are inferred from Figure Atlas.24 in Gutiérrez et al. (2021) and are thus approximate. They correspond to the median sensitivity (outside brackets) and to the 10th – 90th percentile sensitivity of the modelling projections (inside brackets)

	Winter (DJF)	Summer (JJA)	Annual
Precipitation sensitivity (% $^{\circ}C^{-1}$)	5 [3 to 7]	0 [-3 to 3]	2.5 [0 to 5]

PET and P–PET

In PSAR SFR, changes in potential evapotranspiration (PET) in response to a warmer climate was projected using the model of Pereira and Pruitt (2004) (SKB TR-23-05, Appendix D), hereafter referred to as the PP2004 model. In contrast to comprehensive PET models (e.g. the Penman or the Penman-Monteith models, see e.g. Gustafsson 2022), which require abundant meteorological data (e.g. relative humidity, cloudiness and wind speed) as input, the PP2004 model estimates PET only from changes in SAT based on the equations from Thornthwaite (1948) and Willmott et al. (1985). An important characteristic of these models is that PET only increases with SAT when daily-mean SAT > 0 °C. If daily-mean SAT < 0 °C, PET remains zero regardless of imposed SAT change. Details about the PP2004 model is provided in SKB (TR-23-05, Appendix D).

The advantage of using a simplified temperature-based model for estimating future PET changes is that projected SAT changes and the associated uncertainty ranges are relatively well-constrained when compared to changes in parameters that are required as input to more comprehensive PET models (e.g. wind speed or cloudiness). Despite its simplicity, the simplified temperature-based PP2004 model behaves similarly in response to warming as more comprehensive models (SKB TR-23-05, Figure D-1).

PET changes until 2100 AD are not critical for post-closure safety. However, in order to illustrate the sensitivity of PET to a certain SAT increase, and to enable comparison with the precipitation sensitivities in Table 3-8, the PP2004 model is here used to estimate the PET change for the 2081–2100 period based on the median SAT changes in Table 3-7. As a first step, the PP2004 model is calibrated to yield the annual PET of the Baseline Forsmark period (2014-2017) using the Baseline Forsmark SAT as input (Table 3-2). Thereafter, PET for the 2081–2100 period is calculated with the calibrated PP2004 model using the SAT increases in Table 3-7 combined with the SAT for the Baseline Forsmark period[7]. The resulting PET change for the 2081–2100 period, as compared to the PET of the Baseline Forsmark period, is shown in Table 3-9.

Table 3-9. Projected median winter (DJF), summer (JJA) and annual change in PET (mm) for the 2081–2100 period (relative to the Baseline Forsmark period) using the PP2004 model. The relative change in PET per degree of warming is also indicated

	Winter (DJF) (mm)	Summer (JJA) (mm)	Annual (mm)	Annual PET sensitivity (% ºC^{-1})
SSP1-2.6	+5	+12	+34	5
SSP2-4.5	+10	+22	+61	5
SSP3-7.0	+16	+35	+89	5
SSP5-8.5	+19	+46	+112	5

As can be seen in Table 3-9, the increase in PET is projected to be significantly greater in the summer season than in the winter season despite a smaller SAT increase in the summer (Table 3-7). This is explained by the threshold behaviour of the PET model when daily SAT drops below 0 °C; the coldest winter days at Forsmark remain below freezing also in a warmer climate and, thus, the PET remains zero during those days. In summer, on the other hand, the elevated SAT will contribute to an increased PET for all days.

The sensitivity of the PET to the projected SAT change in the PP2004 model is about 5 % ºC^{-1} across all emissions scenarios (Table 3-9). Thus, the relative increase in annual PET per degree of warming at Forsmark is projected to be higher than the corresponding median increase in annual precipitation (cf. Table 3-8) which results in a reduction of the annual P–PET in the region across all emissions scenarios (Table 3-10). However, despite this reduction, P-PET remains positive in Forsmark even under the most extreme scenario (SSP5-8.5). This result is consistent with other projections of P–PET changes in southern Sweden for a warmer climate (e.g. Abraham et al. 2018). These results indicate that significant changes in the average depth of the groundwater table in Forsmark are unlikely due to global warming, which is consistent with the findings in Vikberg et al. (2015).

Another notable result is that the seasonal cycle in P–PET is projected to be further amplified as a result of the anthropogenic warming (Table 3-10); a slight increase in winter PET, coupled with significant precipitation increases during the winter, is projected to lead to an overall increase in P–PET in Forsmark until 2100 AD. Meanwhile, the summer conditions are projected to experience a decrease in P–PET due to a notable increase in PET along with only a small precipitation change during that season. The drier average summer conditions increase the risks of droughts[8] in the region compared to present day.

---

[7] This approach introduces an inconsistency because the SAT anomalies in Table 3-6 are calculated with respect to the 1995–2014 period and not the normal year. However, given the similarity of the estimated Forsmark SAT between the 1995–2014 and the 2014–2017 reference periods (Table 3-2), the introduced error of using different periods is small.

[8] Droughts are defined as periods of time with substantially below-average moisture conditions (Seneviratne et al. 2021).

Specifically, the occurrence of 1-in-10-year soil-moisture droughts in the region is projected to be approximately twice as frequent under 2 °C warming, and 4–8 times more frequent under 4 °C warming (Figure 11.19 in Seneviratne et al. 2021).

Table 3-10. Projected median winter (DJF), summer (JJA) and annual change in P–PET (mm) for the 2081–2100 period (relative to the Baseline Forsmark period). The median seasonal and annual precipitation change is calculated by multiplying the factors (Table 3-8) with the projected seasonal and annual SAT changes for the "northern Europe" reference region (Tables 3-6 and 3-7). The median seasonal and annual PET change is shown in Table 3-9

	Winter (DJF) (mm)	Summer (JJA) (mm)	Annual (mm)
SSP1-2.6	+3	–12	–17
SSP2-4.5	+7	–22	–30
SSP3-7.0	+9	–35	–43
SSP5-8.5	+13	–46	–54

3.5.2 Beyond 2100 AD until the next glacial inception

In this section, the future climate evolution at Forsmark until the next glacial inception is described. As detailed in Section 3.5.3, the next glacial inception is expected to occur after at least 50 kyr AP. However, the timing of this event could be several hundred thousand years later, depending on the levels of anthropogenic GHGs present in the atmosphere. As the next glacial inception coincides with an overall cooling following the initial ice-sheet growth in the Northern Hemisphere, it is highly likely that this period will mark the first occurrence of periglacial conditions in Forsmark. In other words, the time leading up to the next glacial inception will be characterized by the continuation of the temperate climate domain in Forsmark (Section 1.2.3). Importantly, this conclusion also holds true when considering a potential collapse of the AMOC (Section 3.2.4), which is further explained in Appendix A1.

The main relevance for post-closure safety of the climate evolution within the temperate climate domain is associated with how *warm* the climate can become as this will result in longer vegetation periods and, on average, lower P–PET during the summer months. This, in turn, may increase the irrigation demand for crops and/or the groundwater uptake by crops (Section 3.1.2). Changes in the climate towards colder, but still temperate, conditions have not been identified as relevant for post-closure safety for any of SKBs repositories. Therefore, this section describes primarily warmer-than-present conditions at Forsmark until the next glacial inception.

The future climate evolution in Forsmark until the next glacial inception is expected to vary somewhat with the Milankovitch-driven insolation variations, which are predicted to be relatively modest over the next 50 kyr (Section 2.5.2). Beyond 50 kyr, insolation variability will increase, potentially influencing Forsmark SAT by several degrees, especially on a seasonal basis (cf. Section 3.3.1). However, the maximum SAT increase in Forsmark due to any peak insolation is expected to be considerably smaller than the potential warming caused by anthropogenic GHGs. Consequently, this section focuses primarily on the potential warming associated with anthropogenic GHG emissions, as described by the SSP scenarios (Section 2.5.1).

A few underlying assumptions are made in this analysis, outlined in the following. First, we assume that the urgency in mitigating climate change will increase for each degree of warming, such that net-zero emissions are reached within the next few centuries, regardless of emissions scenario. This assumption is accounted for in the SSP scenarios, all of which reach net-zero emissions before 2300 AD (Section 2.5.1 and Meinshausen et al. 2020). Second, as with the likelihood assessment of future GHG emissions (Section 2.6.1), we assume that net-zero anthropogenic emissions will prevail indefinitely in the future once they have been achieved. Third, all anthropogenic forcing agents besides CO_2 are omitted in the analysis. This is motivated by that CO_2 is the dominant radiative forcing contributor in the SSP scenarios, and this becomes even more evident after 2100 AD due to the long atmospheric residence time of CO_2 compared to other prominent GHGs (Section 2.2.2).

Whilst CO_2 amounts to about 80 % of the total anthropogenic radiative forcing in all SSP scenarios until 2100 AD, this ratio increases to about 90 % for SSP2-4.5 and SSP3-7.0 and nearly 100 % for SSP5-8.5 by 2300 AD.

To provide a broader context for anthropogenic warming in Forsmark, this section also introduces so-called *climate analogues* for each of the SSP scenarios. These analogues are identified regions with present-day conditions comparable to the future projected SAT and precipitation in Forsmark. Climate analogues can also facilitate obtaining relevant data for parameterising the effect of a warmer climate on the surface systems in the safety assessments. In addition, potential Köppen-Geiger climate classifications (Section 3.4.2) for a warmer Forsmark are presented.

The assessment of future projected changes in Forsmark precipitation and PET over millennial timescales can be assumed to be controlled by the SAT changes in a similar fashion as changes until 2100 AD (Section 3.5.1). Analyses of future changes of these quantities in this section use the Baseline Forsmark data (2014-2017) as present-day reference period (Section 3.4).

As anthropogenic emissions are confined to the initial centuries after present, the most significant warming effects are anticipated within the following millennia. The assessment of future SAT change on these timescales necessitates a departure from the comprehensive ESM projections used for 2100 AD, given that the CMIP6 models have not been integrated beyond 2300 AD. In PSAR SFR, SAT change assessments for the next millennia relied on a few climate projections utilising more simplified EMICs (SKB TR-23-05, Appendix B). In the present report, the assessment of future SAT change for the next millennia is further updated and, in many ways simplified, compared to the methodology used in PSAR SFR. This includes, for instance, a more consistent handling of global-mean SAT change with respect to the IPCC AR6 estimate of ECS (corresponding to the projections by the emulator in Table 3-6). The updates since PSAR SFR, related to the methodology of assessing the long-term SAT change, are documented in Appendix A2.

SAT

First, the SAT change in Forsmark over the next millennia is estimated by computing the global-mean SAT change according to Equation 3-3, using the best estimate and likely ranges of ECS provided by IPCC AR6 (Section 3.2.1). This equation implicitly assumes that the resulting SAT change caused by anthropogenic forcing will be in equilibrium. This assumption is considered to be reasonable on these timescales since the climate is expected to change more slowly once the GHG emissions have ceased.

Another underlying assumption of Equation 3-3 is that the land-ice cover on Earth will not change relative to the present, and so potential changes in the planetary albedo are not accounted for (Section 3.2.1). This is arguably a crude simplification given that the warming caused by anthropogenic emissions may result in significant melting of Earth's ice sheets (see further Chapter 5). Back-of-the-envelope calculations however indicate that the combined effect of the current Greenland and Antarctic ice sheets on the planetary albedo is relatively small, together contributing with an additional warming of less than 1 °C (Appendix A3). Thus, potential additional contributions to SAT of future ice losses are not accounted for in this analysis.

The maximum global-mean warming is expected to occur around the same time as the net-zero emissions are reached in the emissions scenarios (Section 2.2.2). To compute the maximum global-mean SAT increase from Equation 3-3, the radiative forcing, ΔF, is calculated from the peak CO_2 concentrations of each emission scenario (Table 2-5) using the same methodology as in IPCC AR6 (Smith et al. 2021). The calculations are only carried out for the emission scenarios that do not achieve net-zero emissions before 2100 AD (i.e. SSP2-4.5, SSP3-7.0 and SSP5-8.5). For SSP1-2.6, which achieve net-zero emissions within this century (Section 2.5.1), the maximum SAT increase is also expected to occur before 2100 AD and can therefore be derived directly from IPCC AR6 (Table 3-6).

The resulting maximum global-mean SAT increase for the SSP2-4.5, SSP3-7.0 and SSP5-8.5 scenarios are shown in Table 3-11. Significant SAT increases are projected relative to 2100 AD (Table 3-6) for the SSP3-7.0 and SSP5-8.5 scenarios, since most anthropogenic emissions under these scenarios is projected to occur after 2100 AD (Section 2.5.1). For SSP2-4.5, on the other hand, most emissions are projected to occur within this century and, hence, the maximum warming is only less than 1 °C higher than until 2100 AD.

After the anthropogenic emissions have ceased, the atmospheric CO_2 concentration will gradually begin to decline. It is estimated that some 15–30 % of the cumulative anthropogenic CO_2 emissions will remain in the atmosphere after 10 kyr (Section 2.5.2). Thus, the global-mean SAT change after 10 kyr is projected to be substantially lower than the maximum SAT change within the next few centuries for all emission scenarios (Table 3-11). For the SSP2-4.5 scenario, it is projected that the SAT will have returned to approximately present-day levels after 10 kyr. The projected SAT increase after 10 kyr under SSP3-7.0 and SSP5-8.5 scenarios is comparable to the maximum warming under the SSP2-4.5 scenario, illuminating the potential long-term consequences of the anthropogenic GHG emissions.

Table 3-11. Projected global-mean maximum future warming and warming after 10 kyr relative to 1995–2014 baseline period for the SSP scenarios that do not exhibit net-zero emissions within this century. For the SSP1-2.6 scenario, which describe net-zero emissions before 2100 AD, the maximum global warming is the same as in Table 3-6. The global warming estimates for the SSP2-4.5, SSP3-7.0 and SSP5-8.5 scenarios are calculated using Equation 3-3. For these scenarios, the values outside the brackets represent the warming based on best-estimate ECS (3 °C), whereas the uncertainty interval inside the brackets represent the warming based on the likely ECS range (2.5–4 °C), see further Section 3.2.1. In addition to the ECS, the uncertainty in the warming after 10 kyr also includes the uncertainty due to the prevailing CO_2 concentrations at that time (15–30 % of cumulative anthropogenic emissions, see Section 2.5.2)

Scenario	Maximum warming (ºC)	Warming after 10 kyr (ºC)
SSP1-2.6	0.9 [0.5 to 1.3]	~0
SSP2-4.5	2.5 [2.0 to 3.7]	0.1 [-0.3 to 0.8]
SSP3-7.0	6.8 [5.6 to 9.4]	2.0 [0.9 to 3.9]
SSP5-8.5	8.5 [7.0 to 11.7]	3.0 [1.6 to 5.6]

Next, the global-mean SAT changes are translated to Forsmark conditions. As illustrated in Table 3-6, the SAT increase in northern Europe is projected to be between 1.1 and 1.2 times higher than the associated global-mean increase by the end of this century. This difference arises as a result of projected contributions from the Arctic amplification and land-ocean warming contrast (Sections 3.2.2 and 3.2.3), both of which serve to enhance warming at Forsmark compared to the global mean, as well as an AMOC weakening, which serves to cool the climate in the region. In the analysis conducted here, it is for simplicity assumed that the regional-to-global warming ratio until 2100 AD will continue also after 2100 AD. Given that one of the underlying objectives of the analysis in this section is to estimate how warm the climate in Forsmark can become (see above), the upper value of 1.1–1.2 Forsmark-to-global mean warming range is chosen for this purpose. This is arguably a crude simplification, especially for high emission scenarios under which significant disintegrations of the Greenland ice sheet is expected (Fox-Kemper et al. 2021). Under those scenarios, a further weakening, or even collapse, of the AMOC are plausible outcomes due to the additional fresh water input into the North Atlantic (Section 3.2.4). However, in order not to underestimate the future warming at Forsmark, a potential collapse of the AMOC is not explicitly included in the present analysis. Instead, the possibility of an AMOC collapse and its potential impact on the Forsmark climate is discussed separately in Appendix A1.

The projected SAT change at Forsmark (relative to present-day) over the next millennia is shown in Figure 3-2a. As expected, there is a large difference in the maximum warming in Forsmark depending on emission scenario. Whilst the best-estimate maximum warming in Forsmark is projected to remain well below 5 °C for the SSP2-4.5 scenario, it reaches 8 °C above the present SAT under the SSP3-7.0 scenario, and above 10 °C under the SSP5-8.5 scenario.

It should be emphasised that such extreme warming, projected under the SSP3-7.0 and SSP5-8.5 scenarios, would have enormous consequences on a global scale. Such consequences, which also have a significant impact on post-closure safety, involve the extensive melting of ice sheets and glaciers, leading to a substantial rise in the global sea level by several tens of metres within the considered timescales (Section 5.5.2).

In such a scenario, the repository sites of both the spent fuel repository and SFR would be submerged beneath the Baltic Sea for several millennia (Sections 5.5.2 and 5.6). When the repository site is submerged, the surrounding landscape becomes inaccessible to humans and the magnitude of the groundwater flow in the bedrock is significantly reduced (Section 5.1.2). Thus, when Forsmark is covered by the sea, the direct impact of climate evolution on post-closure safety is considerably reduced compared to terrestrial conditions (see also e.g. SKB TR-23-01, Chapter 7).

Potential durations of sea-covered (submerged) conditions at Forsmark as a result of global warming are analysed in detail in Chapter 5. In summary, the analysis shows that a warming of 5 °C above pre-industrial temperatures (that is ~4 ºC above the present-day mean temperature), which corresponds approximately to a low-end peak warming under SSP3-7.0 (Table 3-11), is projected to result in submerged conditions at Forsmark for the first 5000–8000 years in the future (Figure 5-6). The only identified study accounting for even higher warming levels (about 8.5 °C above pre-industrial, i.e. ~7.5 °C above present-day; Clark et al. 2016), comparable to the best-estimate warming under SSP3-7.0 and a low-end warming under SSP5-8.5 (Table 3-11), suggests that a significant portion of the East Antarctic ice sheet would melt, resulting in the Forsmark region being submerged beneath the sea for about 15 kyr AP (Sections 5.5.2 and 5.6).

Based on these results, 10 000 and 15 000 years are considered to be reasonable durations for which the Forsmark region can be expected to be submerged beneath the sea under the SSP3-7.0 and SSP5-8.5 scenarios, respectively, starting shortly before or after the year 2100 (see further Section 5.5.1). However, to account for uncertainties in the projected warming and the projected sea-level rise for a certain warming, the minimum durations of submerged conditions under the SSP3-7.0 and SSP5-8.5 scenarios are selected to be 5000 and 10 000 years, respectively (arrows in Figure 3-2). Thus, terrestrial conditions can be expected to emerge in Forsmark earliest after 5000 years under the SSP3-7.0 scenario and after 10 000 years under the SSP5-8.5 scenario.

If only considering periods when terrestrial conditions can prevail at Forsmark, the maximum warming under the SSP3-7.0 and SSP5-8.5 scenarios is substantially reduced (Table 3-12) compared to the maximum warming during submerged conditions. Furthermore, the maximum warming becomes less sensitive to the employed emission scenario if only periods with terrestrial conditions are considered, thereby reducing the uncertainty in future climate evolution due to anthropogenic emissions. For example, the difference in maximum warming between the SSP2-4.5 and SSP5-8.5 scenarios is <1 °C for terrestrial conditions (Table 3-12), as opposed to approximately 6 °C if periods when Forsmark is covered by the sea are included (Table 3-11). The relatively small difference between the emission scenarios is also evident when considering suitable climate analogues for each scenario (Appendix A4). This analysis shows that the peak warming during terrestrial conditions for both the SSP2-4.5, SSP3-7.0 and SSP5-8.5 scenarios corresponds approximately to the present-day climate of France (albeit different regions, see Table 3-12 and Appendix A4). For the SSP1-2.6 scenario, which reach a maximum warming before 2100 AD, the corresponding climate-analogue region is the northwestern part of France och southeastern part of England.

The maximum possible future warming at Forsmark, if only considering periods of terrestrial conditions, is about 5 °C above the present-day SAT, and this occurs after 5000 years under the SSP3-7.0 scenario. Assuming that this warming is equally large for all the seasons (roughly in accordance with the projections until 2100 AD, see Table 3-7), the length of the vegetation period under this scenario is projected to be between March and December (using the Baseline Forsmark period as reference) and between March and November (using the IPCC reference period), i.e. three to four months longer than at present (Tables 3-5 and 3-12). For the SSP2-4.5 and SSP5-8.5 scenarios, the warming during terrestrial conditions is slightly smaller than for SSP3-7.0. Thus, the length of the vegetation period for these scenarios is shorter than for SSP3-7.0, albeit still longer the present-day conditions (Table 3-12). For the SSP1-2.6 scenario, the vegetation period is projected to be one month longer than for present day.

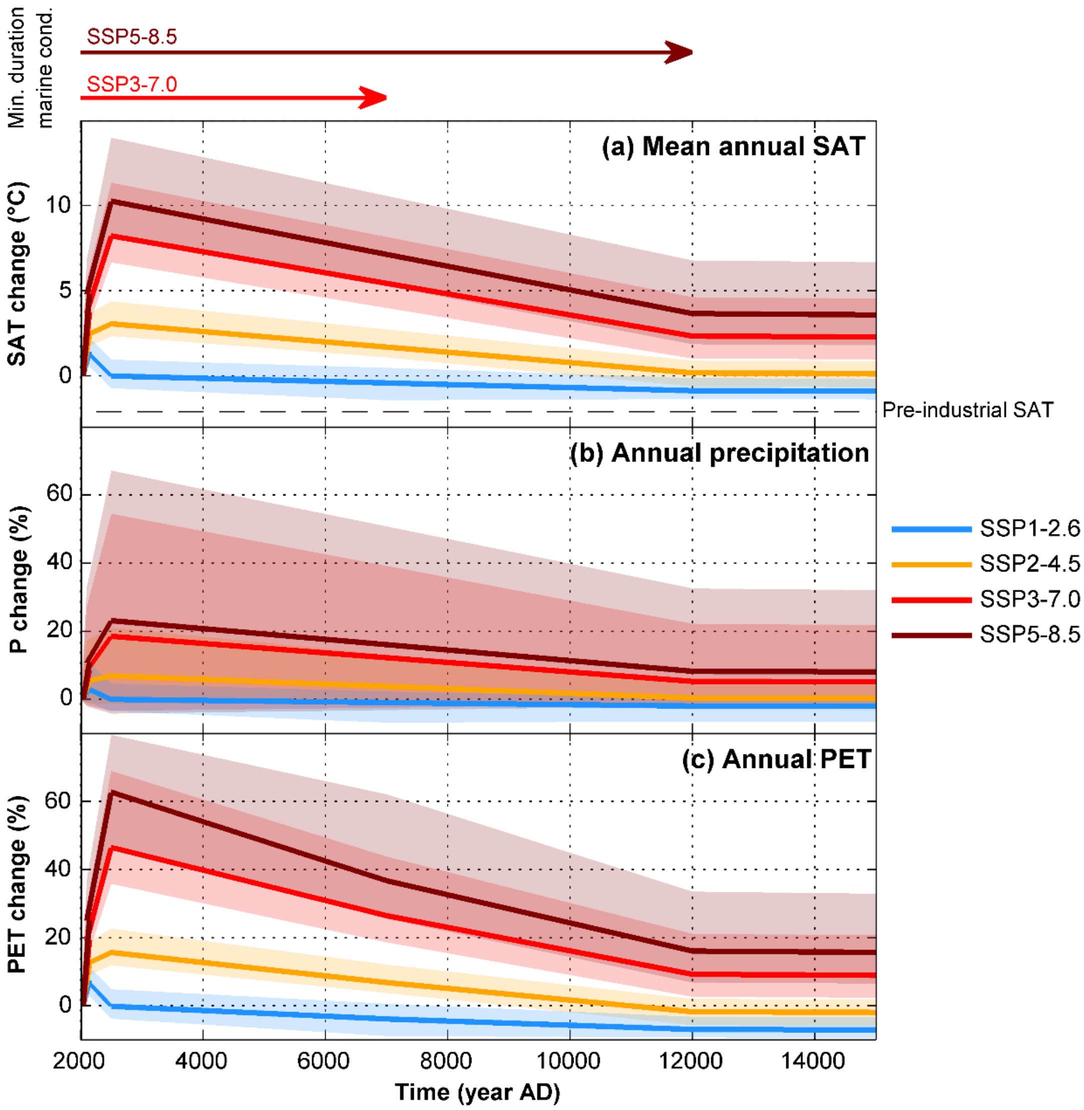

Figure 3-2. *Projected changes in mean annual (a) SAT (°C), (b) precipitation (%) and (c) PET (%) until 15 000 AD at Forsmark relative to Baseline Forsmark data (Section 3.4.1). The colours represent the SSP emissions scenarios given by the legend. The solid lines represent the best-estimate SAT, precipitation and PET for each emission scenario, and the transparent shading represents the uncertainty range, see text for details. The minimum durations during which Forsmark can be expected to be submerged beneath the sea under the SSP3-7.0 and SSP5-8.5 scenarios are also indicated (top arrows). The dashed line in panel (a) indicates the pre-industrial SAT at Forsmark.*

Table 3-12. Maximum change of mean annual SAT as well as annual precipitation and PET (relative to the Baseline Forsmark data, see Section 3.4.1) at Forsmark during terrestrial conditions at the site, i.e. after present-day for SSP1-2.6 and SSP2-4.5, after 5000 years for SSP3-7.0 and after 10 kyr for SSP5-8.5 (see the text). Values outside the brackets represent best estimates. For SAT and PET, the interval inside the brackets represent the uncertainty in ECS, whereas for precipitation, the interval inside the brackets represent the uncertainty in ECS combined with the uncertainty in the precipitation response to SAT (Table 3-8). Corresponding climate analogues, i.e. regions that exhibit a similar present-day mean summer SAT and precipitation to that projected for Forsmark, are also indicated for each emission scenario. The climate analogues are computed based on the median changes in the summer climate, see Appendix A4 for details. Finally, the length of the vegetation period is indicated. These are computed using the Baseline Forsmark period (2014-2017) as reference following the methodology described in Section 3.4.3

Scenario	Variable	Maximum annual change during terrestrial conditions	Climate analogue	Vegetation period	Potential Köppen-Geiger classification
SSP1-2.6	SAT (ºC)	1.4 [0.7 to 2.4]	France (Normandy), South East England	Apr–Oct	Dfb
	Precip (%)	3 [0 to 12]			
	PET (%)	7 [4 to 12]			
SSP2-4.5	SAT (ºC)	3.1 [2.3 to 4.4]	France, Paris region (Île-de-France)	Mar–Nov	Dfb, Cfb
	Precip (%)	7 [1 to 21]			
	PET (%)	16 [12 to 23]			
SSP3-7.0	SAT (ºC)	5.4 [4.0 to 8.2]	France, Toulouse region (Occitanie)	Mar–Dec	Cfb, Cfa
	Precip (%)	12 [–1 to 39]			
	PET (%)	26 [19 to 44]			
SSP5-8.5	SAT (ºC)	3.7 [1.9 to 6.8]	France, Paris region (Île-de-France)	Mar–Nov	Dfb, Cfb, Cfa
	Precip (%)	8 [–1 to 33]			
	PET (%)	16 [7 to 34]			

The projected Köppen-Geiger climate classifications for terrestrial conditions in Forsmark are shown in Table 3-12 for each emissions scenario. Using the classification described by Peel et al. (2007) (Table 3-3), Forsmark is expected to undergo a transition from a *Dfb* to a *Cfb* climate type (i.e. from cold to warm temperate climate with average winter SATs above freezing) once the annual-mean SAT rises by ~2.5 °C relative to present-day. If the warming exceeds 4.4 °C, a *Cfa*-type climate (warm temperate climate with warm summers) is expected. One can note that a Mediterranean-type climate (*Csa*), characterised by strong seasonal differences in precipitation, is not expected to occur in a future terrestrial Forsmark, despite the possibility of reduced summer precipitation as a result of global warming (Table 3-8). This is because summer is currently the season with the highest precipitation in Forsmark (Table 3-2). Even if precipitation were to be reduced during summer (and increased during winter) due to the warming, the seasonal contrast would remain smaller than that observed in the Mediterranean region.

P–PET

Both annual precipitation and PET are projected to increase with the annual-mean SAT over the next millennia (Figure 3-2b and c), in accordance with the precipitation sensitivity factors and the PP2004 model (Section 3.5.1 *PET and P–PET*), respectively. Annual PET is projected to increase faster than annual precipitation in Forsmark except for the most extreme case with high-end winter and summer precipitation increases; in this case, the annual precipitation increase is comparable to that of the annual PET (Figure 3-2b and c). Thus, because annual PET will likely increase faster with SAT than the annual precipitation, annual P–PET in Forsmark will, similar to until 2100 AD (Section 3.5.1), likely decrease over the next millennia as a result of anthropogenic warming. Similar to the SAT increase, the largest decrease in P–PET is projected for future periods when Forsmark is submerged beneath the sea under the SSP3-7.0 and SSP5-8.5 scenarios. However, as argued above and in Section 3.2, the climate evolution, including P–PET, is less relevant for post-closure safety during periods when the Forsmark area is submerged beneath the sea. If only considering periods when terrestrial conditions can be expected, changes in P–PET are more modest than if including also submerged periods.

The projected maximum annual and summer changes in P–PET at Forsmark during terrestrial conditions are summarised in Table 3-13. Overall, the largest change in P–PET, both annually and in the summer season, is obtained under the SSP3-7.0 scenario after 5000 years, when terrestrial conditions are first possible under that scenario. The best estimate (corresponding to ECS = 3 °C) for the annual P–PET decrease under this scenario is about 60 mm, resulting in a total P–PET at Forsmark close to zero. Similar to the response until 2100 AD (Section 3.5.1), the reduced annual P–PET is driven by a comparatively large decrease in the summer, which contributes to about 85 % of the annual decrease under the SSP3-7.0 scenario (Table 3-13).

The total uncertainty in future P–PET is the results of the combined uncertainty in (i) the ECS, (ii) the amount of atmospheric CO_2 remaining at the time of terrestrial conditions under the SSP3-7.0 and SSP5-8.5 scenarios, and (iii) the magnitude of the precipitation change in response to the SAT increase. These sources of uncertainty result in a large total P–PET uncertainty range, especially for the SSP3-7.0 and SSP5-8.5 scenarios (Table 3-13). For example, under the SSP3-7.0 scenario, the total uncertainty range of the maximum annual P–PET change is estimated to be between -234 mm and 14 mm. However, the extreme values in this range is considered to be less likely than the best estimates (ECS = 3 °C and median precipitation sensitivity). Importantly, except for the most extreme cases, the annual P–PET will remain positive during terrestrial conditions at Forsmark also in a warmer climate.

Table 3-13. Projected maximum change in annual and summer (JJA) P–PET during terrestrial conditions at Forsmark for different SSP scenarios and magnitudes of the ECS, corresponding to the likely range (2.5–4 °C) and the best estimate (3 °C) (Section 3.2.1). The values outside the brackets are calculated from the median projected precipitation change, and the range inside the brackets represent the uncertainty in projected precipitation change (Table 3-8). All changes are shown relative to the P–PET of the Baseline Forsmark period (+59 mm annually and –86 mm during JJA, see Section 3.4.1)

Annual		**Maximum P–PET change (mm)**		
Scenario	**Time (AD)**	**ECS=2.5 °C**	**ECS=3 °C**	**ECS=4 °C**
SSP1-2.6	2100	-10 [-20 to 1]	-19 [-40 to 2]	-32 [-66 to 3]
SSP2-4.5	2500	-30 [-64 to 3]	-40 [-84 to 4]	-58 [-121 to 4]
SSP3-7.0	7000	-43 [-100 to 14]	-64 [-142 to 14]	-117 [-234 to 0]
SSP5-8.5	12000	-11 [-37 to 16]	-34 [-87 to 18]	-83 [-180 to 15]
Summer (JJA)		**Maximum P–PET change (mm)**		
Scenario	**Time (AD)**	**ECS=2.5 °C**	**ECS=3 °C**	**ECS=4 °C**
SSP1-2.6	2100	-7 [-11 to -2]	-14 [-22 to -5]	-24 [-37 to -10]
SSP2-4.5	2500	-22 [-36 to -9]	-31 [-48 to -13]	-47 [-71 to -22]
SSP3-7.0	7000	-35 [-57 to -13]	-54 [-85 to -24]	-102 [-148 to -56]
SSP5-8.5	12000	-9 [-20 to 1]	-29 [-50 to -9]	-74 [-112 to -36]

3.5.3 Timing of the next glacial inception

Glacial inception marks the end of an interglacial period and the beginning of a glacial period, with ice sheets forming on Northern Hemisphere land masses currently without ice. Glacial inception includes both the initial accumulation of ice, often referred to as "glacial nucleation", and the initial growth phase of ice sheets. Once the ice sheets have grown in size they contribute to the planetary albedo, which results in a decreased SAT (e.g. Abe-Ouchi et al. 2007). As a result of the colder climate, the atmospheric CO_2 content is reduced (e.g. Petit et al. 1999, Lüthi et al. 2008; see also Section 2.3) which, in turn, leads to a further cooling and ice sheet growth.

At present, the annual-mean SAT at Forsmark amounts to about 6.5 °C (Section 3.4.1). Since permafrost begins to develop when the annual-mean SAT is slightly below zero (Section 6.2.1), Forsmark SAT must drop by at least ~7 °C relative to the present for a transition to the periglacial climate domain to occur[9]. Following the approach in PSAR SFR (TR-23-05, Section 4.3.1), it is judged that such a large drop of SAT can only occur at Forsmark if it is embedded in a planetary-scale cooling trend that would result in the initiation and growth of ice sheets elsewhere in the Northern Hemisphere. Therefore, the next global glacial-inception event also marks the first possible future transition from a temperate to periglacial climate domain at Forsmark. The possibility of ice-sheet growth, i.e. the formation of glacial conditions, at Forsmark in conjunction with the next glacial inception is considered to be unlikely; this is further motivated in Section 3.6.1. The next glacial inception also defines the end of the period during which the climate has been significantly altered by human activities[10]. This is because, in order for the next glacial inception to occur, the anthropogenic GHG forcing must be reduced to a level that allows substantial growth of the ice sheets and cooling at high latitudes. Thus, following the next glacial inception, it is expected that the climate over the next 1 Myr will vary similarly to that of the past 800 kyr (Section 3.5.4), when it was not influenced by anthropogenic activity (Sections 2.3 and 3.3)[11].

As mentioned in Section 2.5.2, glacial inception is controlled by the high-latitude summer insolation and the prevailing atmospheric CO_2 concentration. These two variables determine whether glacial inception is possible, such that, if CO_2 levels drop below a critical threshold for a certain summer insolation, glacial inception is expected to occur. Such a "critical insolation-CO_2" model was first developed by Archer and Ganopolski (2005), and was later refined in Ganopolski et al. (2016) based on insolation and CO_2 data of the past eight glacial inceptions (Section 2.3). Applying this model to future insolation conditions over the next 100 kyr indicates that CO_2 levels below 240 ppmv, i.e. well below typical interglacial concentrations of 260–300 ppmv (Section 2.3), are required for glacial inception to occur during the initial 50 kyr (Figure 3-3b). The low-amplitude variability of the summer insolation during this period (Figure 3-3a) is the reason why such low CO_2 levels are required for the next glacial inception to occur. In contrast, at around 54 kyr AP, when the first major insolation minimum occurs (Figure 3-3a), the threshold model projects that CO_2 concentrations higher than 260 ppmv are sufficient to enable glacial inception (Figure 3-3b).

The results from this simple threshold model can help to explain the projected timing of the next glacial inception from the most recent climate model simulations over the next 100 kyr or longer (Figure 3-4). For example, in agreement with the threshold model of Ganopolski et al. (2016), virtually all of the modelling exercises over these longer timescales projects that the next glacial inception will occur in response to the 54-kyr insolation minimum under no or low (< 800 Pg C) anthropogenic emissions. Under medium (800–2000 Pg C) or high (> 2000 Pg C) emissions, the model simulations project that significant anthropogenic emissions will remain in the atmosphere after 50 kyr such that atmospheric CO_2 levels will not drop below the critical threshold for glacial inception. Under these emission scenarios, the models project that the next glacial inception will not occur before 100 kyr AP, and possibly even after 500 kyr AP in cases of high anthropogenic emissions. These conclusions are consistent with the BIOCLIM project (Calvez et al. 2001), which demonstrated that elevated anthropogenic CO_2 could postpone the next glacial inception for several hundred thousand years.

---

[9] Transition directly from the temperate to the glacial climate domain is not considered realistic (see SKB TR-23-05, Section 1.4.3)

[10] this period, or era, is sometimes referred to as the *Anthropocene* (e.g. Ruddiman 2013).

[11] This assessment assumes that anthropogenic influence on the climate will remain small indefinitely after net-zero GHG emissions have been achieved.

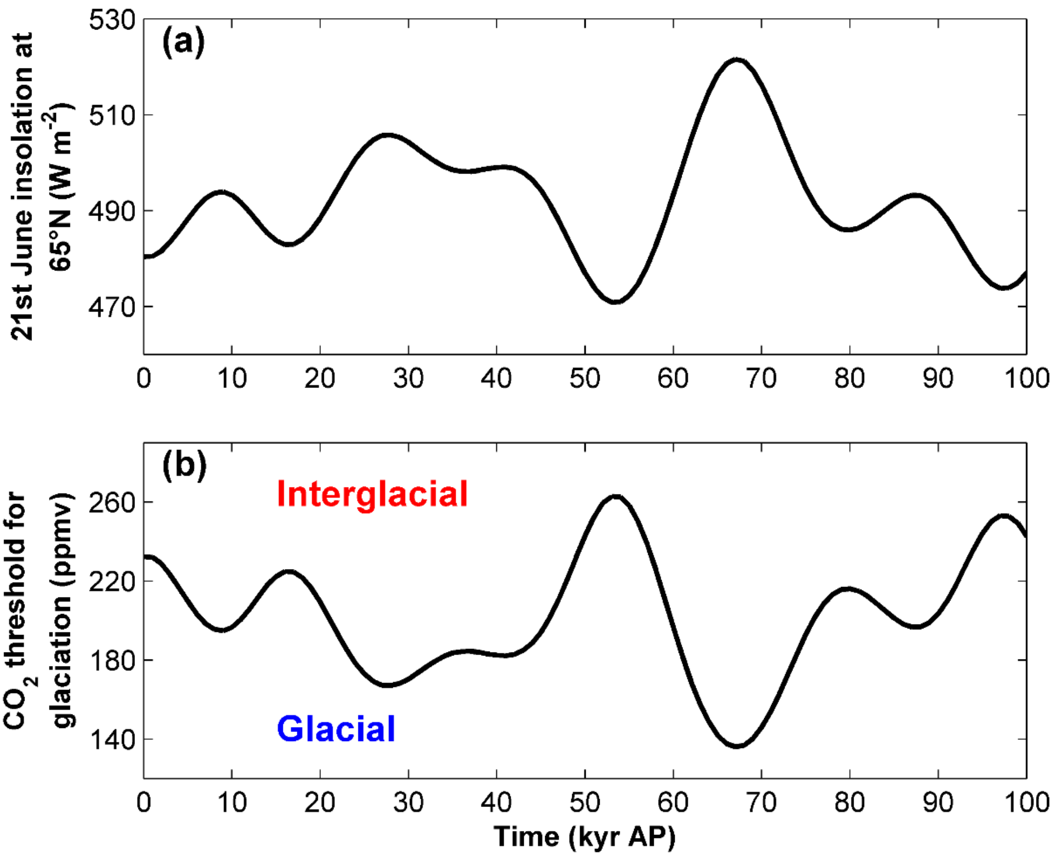

Figure 3-3. *(a) 21st June insolation at 65°N derived from the solution in Laskar et al. (2004). (b) Atmospheric CO_2 threshold for glacial inception during the next 100 kyr, adopted from Ganopolski et al. (2016). According to Ganopolski et al. (2016), the next glacial inception is projected to occur once the actual CO_2 drops below the CO_2 threshold. Note that an ice-sheet could reach the Forsmark area considerably later than the time of Northern Hemisphere glacial inception (see text).*

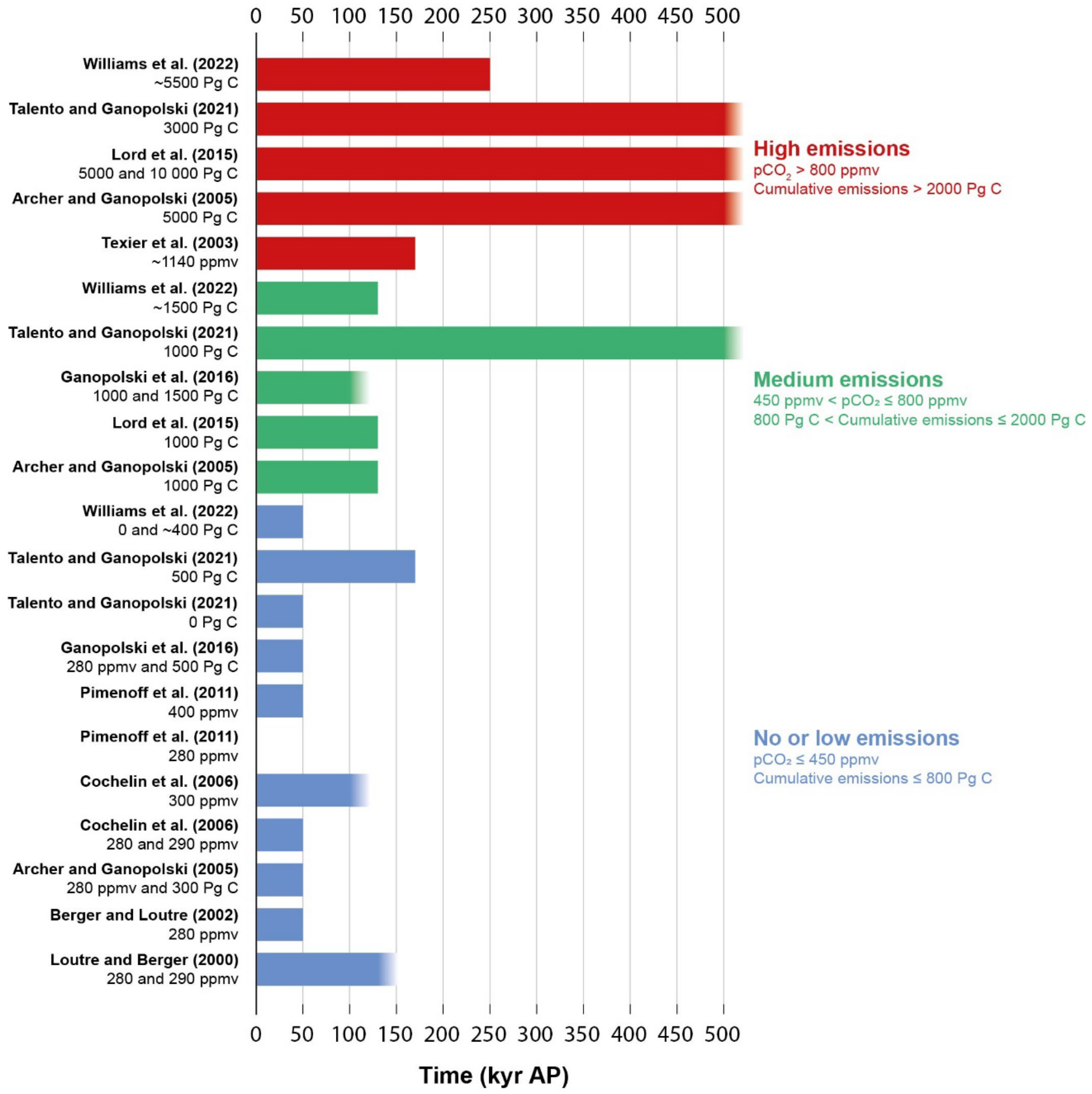

Figure 3-4. *Approximate timing of the next glacial inception from different modelling studies. The bars ending with a colour-to-white gradient represent simulations that were not integrated sufficiently far into the future to project the next glacial inception. For those simulations, the bars thus show how long the simulations were integrated without glacial inception to occur. The study of Pimenoff et al. (2011) projects that glacial inception would be immediate for pre-industrial atmospheric CO_2 concentrations (280 ppmv). For Talento and Ganopolski (2021), only the projected glacial inception in their "best estimate" model is shown, and for Williams et al. (2022) the timing of the next glacial inception as projected in the majority of the simulations is shown. Since the Industrial Revolution, humanity has emitted a total of approximately 700 Pg C to the atmosphere. While the timing of the next glacial inception under these cumulative emissions has not been explicitly studied, existing projections indicate that, if emissions stopped today, the next glacial inception would likely occur around 50 kyr AP. Based on Figure 11.3 in Liakka et al. (2021).*

Most of the individual studies in Figure 3-4 were discussed extensively in the PSAR SFR climate report (SKB TR-23-05, Section 3.4.5), so the discussion is not repeated here. Instead, only the studies that have been published since the PSAR SFR report was prepared are described in the following; this concerns the studies of Talento and Ganopolski (2021) and Williams et al. (2022).

Talento and Ganopolski (2021) developed a model describing a simplified representation of the physical mechanisms relevant for the evolution of the climate–ice sheet–carbon cycle system on timescales longer than thousand years. Model parameters were calibrated using paleoclimate reconstructions and results from more comprehensive models. Projections for the next 1 Myr were carried out for different emission scenarios, and the uncertainty in parameters and assumptions were accounted for in probabilistic simulations and sensitivity experiments.

The study of Williams et al. (2022) builds on previous work by Lord et al. (2019) and, consequently, uses a near-identical methodology to that study. The study of Lord et al. (2019) aimed to provide physically-based projections of the future climate on the 1 Myr timescale, both globally and in the Forsmark region. The projections were calibrated against available paleo-proxy records of the last 500 kyr. Rather than considering only one ensemble member, as in Lord et al. (2019), a total of 90 different ensemble members were considered in Williams et al. (2022) for a number of key climate variables, providing a range of possible climate evolutions over the coming 1 Myr both globally and in the Forsmark region. In both Lord et al. (2019) and Williams et al. (2022), the timing of the next glacial inception was estimated using a conceptual global model (CGM) based on an insolation-threshold model originally developed by Paillard (1998). The critical insolation required for glacial inception was also modified with regard to the prevailing atmospheric CO_2 concentration according to the methodology in Archer and Ganopolski (2005). The temporal evolution of atmospheric CO_2 under different scenarios was in turn provided from a carbon-cycle model.

In Figure 3-4, the projected timing of the next glacial inception in the “best estimate” simulation of Talento and Ganopolski (2021) and in the majority of the simulations of Williams et al. (2022) are shown, together with inception timings from other studies. The results of Williams et al. (2022) are similar to most other studies in that the next glacial inception is projected to occur around 50 kyr AP for low emissions, and after 100 kyr AP for medium and high emissions. The results of Talento and Ganopolski (2021), on the other hand, clearly exhibit a higher sensitivity to anthropogenic forcing than in Williams et al. (2022) and other studies. Specifically, Talento and Ganopolski (2021) projects that the next glacial inception will be delayed until after 100 kyr AP as a result of the CO_2 that has already been emitted by humans (~700 Pg C; see Table 2-2). Furthermore, the projections of Talento and Ganopolski (2021) suggest that future anthropogenic emissions corresponding to medium emissions will delay the timing of the next glacial inception by more than 500 kyr (Figure 3-4). This result stands in stark contrast to other studies, which suggest that the next glacial inception occur at some point between 100 kyr and 200 kyr AP under similar emission scenarios (Figure 3-4). Other studies suggest a ≥500 kyr glacial inception delay only under high emission scenarios.

It is important to note that the projected timing of the next glacial inception is associated with considerable uncertainties, mostly associated with the specific models that were used in the simulations. By design, simulations over timescales relevant for the next glacial inception typically need to use simplified climate models, such as energy balance models or EMICs. This is because coupled atmosphere-ocean circulation models, which are used e.g. by the IPCC to project climate change until 2100 AD (see further Section 3.5.1), are computationally too expensive to be integrated over several hundreds of thousands of years. A major drawback of these simpler models, however, is that they are generally more sensitive to changes in internal model parameters than more complex ones (e.g. Paillard 1998, Lord et al. 2019). Small changes in these parameters can therefore result in widely different projections of the future climate, even if the model has been calibrated “correctly”.

An example of how the uncertainty in internal model parameters may influence the timing of the next glacial inception is presented in Williams et al. (2022). The results are also summarised in Figure 3-5, which shows, for each emission scenario, the percentage of the 90 simulations in Williams et al. (2022) that have entered a glacial state over the next 1 Myr. The only difference between these 90 simulations is the representation of internal model parameters. The results of Williams et al. (2022) show that the sensitivity of the timing of the next glacial inception to the set of model parameters is clearly higher under high anthropogenic emissions than under low or no emissions (Figure 3-5). For instance, if assuming no anthropogenic emissions, the model projects that the next glacial inception will occur in response to the insolation minimum at 54 kyr AP for virtually all examined combinations of model parameters. On the other hand, under high emissions the next glacial inception occurs after more than 500 kyr in approximately half of the simulations, while it occurs between 200 and 300 kyr AP for the remaining half. Thus, the sensitivity analysis of Williams et al. (2022) indicates that the uncertainty in the timing of the next glacial inception increases with the amount of anthropogenic emissions, and thus explains why most studies project similar timings of the next glacial inception for low, or no, emissions, while they increasingly diverge for higher emissions (Figure 3-4).

(a) No anthropogenic emissions (0 Pg C)

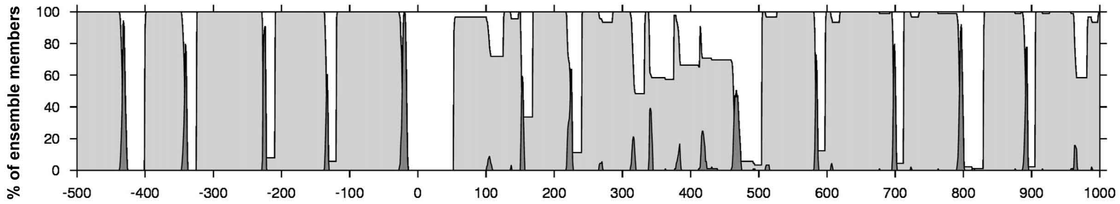

(b) 400 Pg C

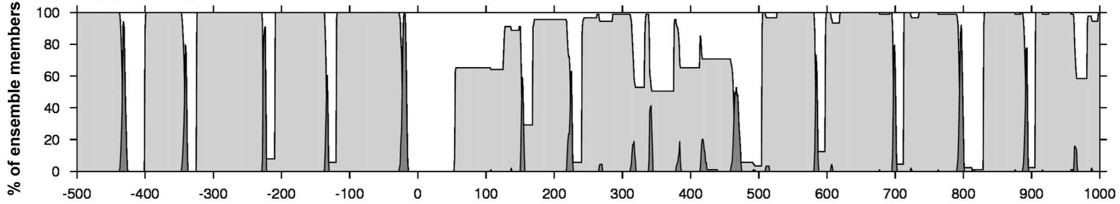

(c) 1500 Pg C

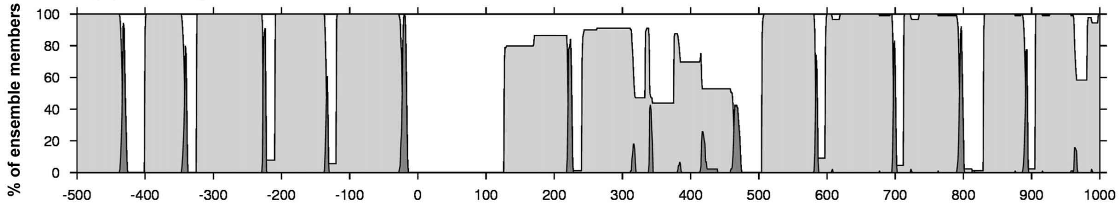

(d) 5500 Pg C

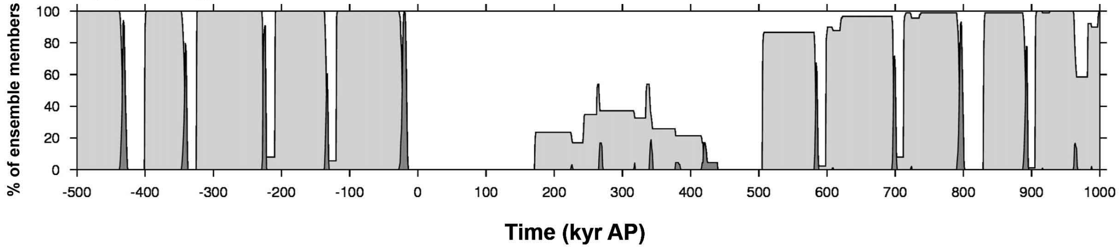

***Figure 3-5.** Percentage of ensemble members going into a climate state (either interglacial (white), partially glacial (light grey) or full glacial (dark grey)) in the CGM simulations of Williams et al. (2022) assuming (a) no, (b) low, (c) medium and (d) high anthropogenic emissions. All anthropogenic emissions are assumed to occur between 0 and 1 kyr AP. Glacial inception is in the model defined as transitions from an interglacial state (white) to a partially glacial state (light grey). Each ensemble member uses a different set of internal model parameters. The total number of ensemble members is 90 for each emission scenario. Figure modified from Williams et al. (2022).*

3.5.4 Beyond the next glacial inception until 1 Myr AP

In general, the climate evolution beyond the next glacial inception until 1 Myr AP is expected to be similar to that of the last 800 kyr, characterised by recurrent glacial-interglacial cycles on timescales of approximately 100 kyr. Moreover, similar patterns of ice-sheet growth can be expected, with relatively long periods of stepwise ice growth, followed by shorter warm phases with interglacial conditions.

This notion is supported by climate modelling projections over the next 1 Myr by Williams et al. (2022). In that study, 90 model simulations were carried out to account for uncertainties in internal model parameters (Section 3.5.3). The evolution of the Forsmark SAT in each of these simulations are shown in Figure 3-6 for all investigated emission scenarios. The figure shows a significant variation of the Forsmark SAT over the next 1 Myr, ranging from approximately –20 °C during the coldest periods to almost 5–10 ºC during the warmest periods.

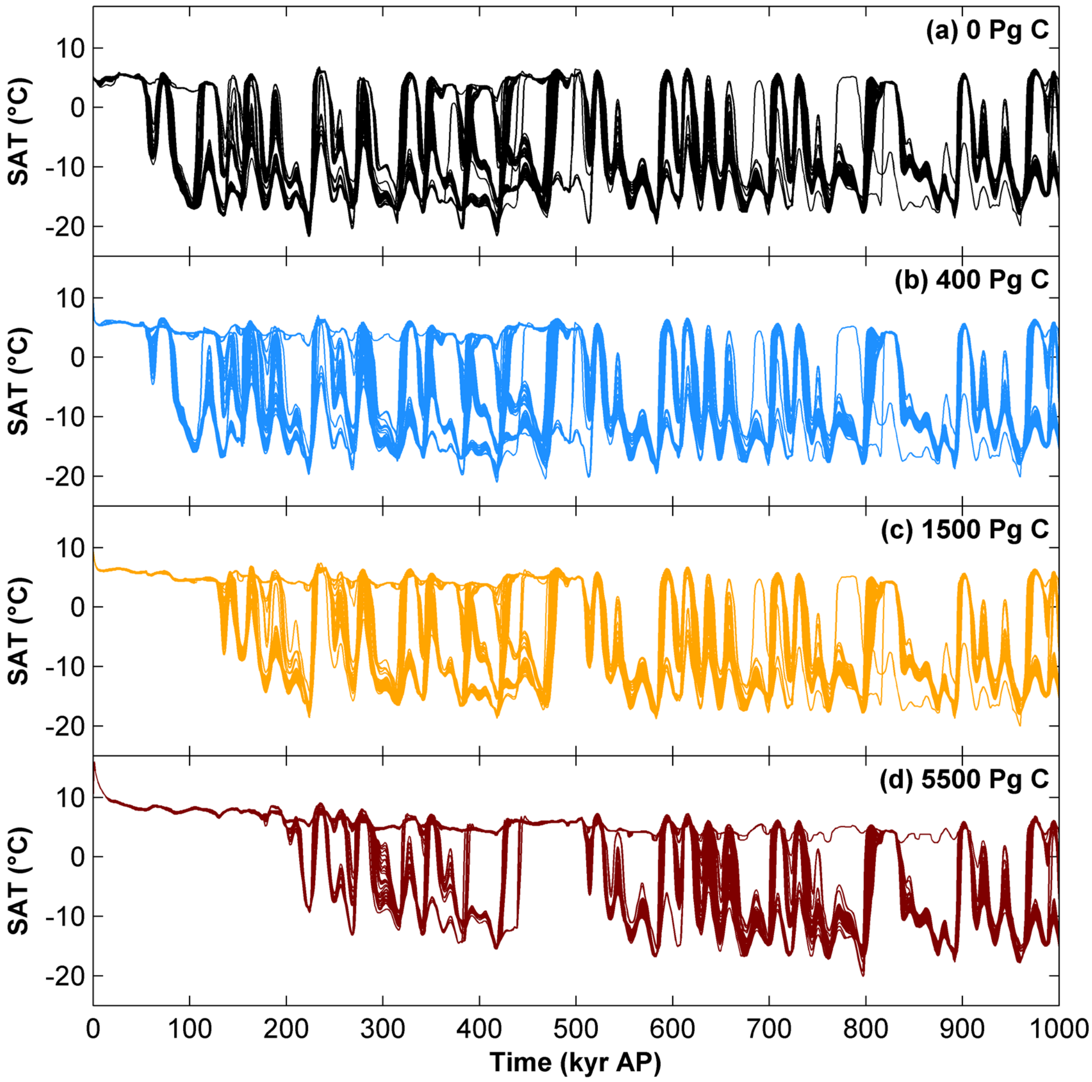

Figure 3-6. *Projected evolution of Forsmark SAT over the next 1 Myr in the 90 simulations of Williams et al. (2022) for (a) 0 Pg C, (b) 400 Pg C, (c) 1500 Pg C and (d) 5500 Pg C anthropogenic emissions.*

To further illustrate the glacial-interglacial variability in the simulations, Forsmark SAT = –1 °C is crudely defined as a limit for when transitions between interglacial and glacial states can be expected. This threshold approximately corresponds to the limit when transitions from temperate to periglacial conditions occur in Forsmark (Section 6.5.1), although this limit also depends on the surface conditions and may, therefore, in reality be a couple of degree lower than this (Hartikainen et al. 2010, Brandefelt et al. 2013).

After the Forsmark SAT has first dropped below –1 °C in the simulations of Williams et al. (2022) (Table 3-14), which approximately correspond to the projected timing of the next glacial inception in that study (Figure 3-5), the climate is on average projected to be considerably colder than at present. Specifically, it is projected that Forsmark SAT will be below –1 °C for about 65–80 % of the time from the next glacial inception until 1 Myr AP for all emission scenarios (Table 3-14). These periods are likely to be characterised by periglacial or glacial conditions at Forsmark and abundant ice-sheet coverage elsewhere on Earth. The result that the climate is mostly cold over timescales extending to 1 Myr is also consistent with paleo-proxy data from historical records (Sections 2.3 and 3.3).

Table 3-14. Median (outside brackets) and min/max values (inside brackets) of different statistics related to the Forsmark SAT declining below zero across the 90 simulations over the next 1 Myr in Williams et al. (2022). The results are shown for four scenarios with different levels of anthropogenic emissions (see further Williams et al. 2022)

Cumulative anthropogenic emissions (Pg C)	First occurrence of Forsmark SAT<–1 °C (kyr AP)	% time with SAT<–1 °C after the first future glacial inception
0	58 [56–133]	76 [68–83]
400	85 [59–513]	76 [60–84]
1500	147 [132–531]	74 [58–87]
5500	306 [215–915]	64 [53–88]

The simulations also illustrate that whilst the anthropogenic emissions play an important role in determining the timing of the next glacial inception (Sections 2.5.2 and 3.5.3), the dynamics of the climate *after* this event is largely insensitive to the anthropogenic emissions. Even if considering the warmest simulation under the highest anthropogenic forcing, the conditions after the next glacial inception are predominantly cold (SAT < –1 °C) rather than warm (SAT >–1 °C) in the simulations (Table 3-14).

Another interesting result from the simulations is that the Forsmark climate during any interglacial subsequent to the next glacial inception will not be significantly warmer than present-day climate. Beyond the next glacial inception, annual average SAT in Forsmark reaches a maximum value greater than 7 °C in 20 % of simulations, and 8 °C in only 4 % of simulations (across all emission scenarios). The interglacial featuring the highest temperatures in the simulations occurs around 230 kyr AP, especially for the scenarios accounting for anthropogenic CO_2 emissions (Figure 3-6b-d). As for the early Eemian (Section 3.3.1), this period is characterised by a higher obliquity than at present. Thus, the annual insolation at high latitudes, including Forsmark, is projected to be higher than at present (Section 2.2.1). In sum, however, the annual warming caused by these insolation changes will not be larger than the potential warming caused by anthropogenic GHGs, described in Section 3.5.2.

The Williams et al. (2022) simulations over the next 1 Myr are analysed further in conjunction with the assessment of future periglacial variability in Section 6.5.1.

3.6 Safety-assessment specific information

3.6.1 Likelihood assessment of periglacial and glacial conditions at Forsmark within the next 100 kyr

In this section, the likelihood of periglacial and glacial conditions at Forsmark within the next 100 kyr is assessed. This question is mostly relevant for the selection of safety assessment scenarios for SFR (Section 3.1.2). The question is of less importance for the spent fuel repository, having an assessment period covering 1 Myr. A likelihood assessment of future periglacial and glacial conditions was first introduced in the climate report for PSAR SFR (SKB TR-23-05, Chapter 4), where the likelihoods were assessed separately for the first 50 kyr AP and for the period between 50 and 100 kyr AP. The likelihoods assessed in PSAR SFR are used as starting point in the present work, and the approach of separating the assessment between two distinct periods is also adopted in this report. The likelihoods of periglacial and glacial conditions within the next 100 kyr are measured according to the qualitative likelihood scale presented in Table 2-3.

Assessment in PSAR SFR (SKB TR-23-05, Section 4.3)

In the assessment of future periglacial conditions, it was noted that a substantial cooling required for periglacial conditions in the Forsmark area can only occur if embodied in a planetary-scale cooling trend, which would inevitably result in the initiation and growth of ice sheets elsewhere in the Northern Hemisphere. Therefore, it was judged that the first occurrence of periglacial conditions at Forsmark can only occur in conjunction with, or subsequent to, the next glacial inception in the Northern Hemisphere. It was further noted that cumulative emissions consistent with RCP2.6 or lower were required for glacial inception to occur in response to the insolation minimum at 54 kyr AP. Therefore, since the likelihood of RCP2.6 was set to *moderate* in PSAR SFR, the likelihood of periglacial conditions at Forsmark following the insolation minimum at 54 kyr AP was also set to *moderate* (definitions of the likelihoods are shown in Table 2-3).

The likelihood of achieving periglacial conditions before 50 kyr AP was assessed to be *very low* based on the fact that the summer insolation will be higher than at present for the next 50 kyr (see e.g. Figure 3-3). In order to achieve the large cooling required for periglacial conditions at Forsmark under similar-to-present insolation conditions (e.g. at 17 kyr AP, see Figure 3-3), very pessimistic assumptions must be made about the ground surface conditions and the future evolution of atmospheric CO_2 and climate (Brandefelt et al. 2013).

The likelihood of glacial conditions at Forsmark was in PSAR SFR only assessed for the first major future summer insolation minimum at 54 kyr AP. Because potential radiological consequences of a glaciation primarily are of interest after *deglaciation* of the area, when humans are again present for exposure, the potential development of glacial conditions at Forsmark in response to later insolation minima (particularly at 97 kyr AP; see e.g. Figure 3-3) were assessed to be of minor relevance for post-closure safety for SFR. The likelihood of glacial conditions at Forsmark in response to the 54-kyr insolation minimum was assessed to be *low*. This assessment was motivated by that; (i) glacial inception in response to the 54-kyr minimum likely requires low anthropogenic emissions (RCP2.6 or lower), and; (ii) both paleo-proxy data and modelling have shown that ice sheets following a glacial inception tend to grow slowly and in a stepwise pattern, with ice-sheet advances during relatively cold phases and ice-sheet retreat during warmer phases (see also Section 3.3.1). During the Weichselian glaciation, for instance, this slow and stepwise pattern of ice-sheet growth meant that it took about 50 kyr for the ice sheet to reach the Forsmark site after the initial glaciation in the Scandinavian mountain range.

The likelihood of glacial conditions at Forsmark prior to 50 kyr AP was judged as exceptionally low, and was therefore not assessed according to the qualitative likelihood scale. It was noted that the only situation that could possibly result in a glaciation at Forsmark before 50 kyr AP is an imminent glacial inception. However, given the current elevated concentrations of greenhouse gases in the atmosphere, such situation was considered unrealistic.

Assessment in the present report

The conclusion in PSAR SFR that low cumulative future anthropogenic emissions (corresponding to SSP1-2.6 or lower) are necessary to enable glacial inception in response to the 54-kyr insolation minimum holds true also in the present assessment (Section 3.5.3). Furthermore, similar to PSAR SFR, the likelihood of achieving these low cumulative emissions is assessed to be *moderate* also in this report (Table 2-5). Thus, the likelihood of periglacial conditions between 50 and 100 kyr AP is assessed to be *moderate* (Table 3-15), i.e. the same as in PSAR SFR.

The assessment in PSAR SFR that the likelihood of periglacial conditions before 50 kyr AP is *very low* is also still valid (Table 3-15), despite increasing concerns of a future AMOC collapse that could potentially cool the Forsmark climate by several degrees (Section 3.2.4 and Appendix A1). The possibility of a complete AMOC collapse is still uncertain. However, recent studies agree that the probability of such an event increases with each degree of warming because a warmer climate will increase the freshwater input to the North Atlantic (Section 3.2.4). The probability of an AMOC collapse is therefore considered to be highest within the next few centuries, when the warming is expected to reach its peak value for most emission scenarios (Section 3.5.2). The climate cooling induced by an AMOC collapse would likely be masked by the anthropogenic warming (i.e. the underlying cause of the collapse), such that the SAT would remain well above the threshold for periglacial conditions in the Forsmark region (Appendix A1).

In fact, even in the highly unlikely case of an imminent AMOC collapse resulting in the largest cooling over northern Europe found in the literature, the conditions would remain above freezing in the Forsmark region (Appendix A1). Furthermore, since the AMOC is expected to recover following a collapse (at least partially, see Appendix A1), the climate impact of a complete collapse is expected to decline as the anthropogenic warming tapers off. Thus, by the time of the next future insolation minimum at 17 kyr AP, the impact on the Forsmark climate of an anthropogenically-induced AMOC collapse should be negligible or significantly diminished.

As in PSAR SFR, the possibility of glacial conditions at Forsmark before 50 kyr AP is considered to be exceptionally low; therefore, a likelihood assessment of such event is also not considered here. The likelihood of glacial conditions at Forsmark in response to the 54-kyr insolation minimum is assessed to be *low* also in the present report (Table 3-15). This assessment has been strengthened by climate modelling results published after the preparation of PSAR SFR. For example, the study of Talento and Ganopolski (2021) found that the time lag between the initial glacial inception and the development of more extensive glacial conditions may be substantial. In the majority of simulations with low anthropogenic emissions (500 Pg C), Talento and Ganopolski (2021) found that the first development of "full glacial" conditions (defined by the authors as more than 50 % of the LGM ice volume) is projected to occur several hundreds of thousands of years after the glacial inception.

Further, in this report (Section 4.5.2) and in Liakka et al. (2024), the potential for ice-sheet coverage over Forsmark is examined using conceptual global climate-model simulations by Lord et al. (2019). The analysis indicates that without anthropogenic emissions, Forsmark is projected to experience its first ice coverage around 95–100 kyr AP. When anthropogenic emissions are included, all simulations project that the next period of ice coverage will occur after 100 kyr AP. This supports the conclusion that a glacial period in Forsmark followed by a temperate period is unlikely to occur within the next 100 kyr.

Table 3-15. Assessed likelihoods of periglacial and glacial conditions at Forsmark within the next 100 kyr AP. The likelihoods are assessed according to the qualitative likelihood scale of Table 2-3

Climate domain	Timing of first transition to the climate domain	Likelihood of occurrence
Periglacial	<50 kyr AP	Very low
	50–100 kyr AP	Moderate
Glacial	<50 kyr AP	-
	50–100 kyr AP	Low

4 Ice-sheet development

4.1 Introduction

4.1.1 Definitions

Glaciers and ice sheets form in regions where the winter snow precipitation does not completely melt during summer. A *glacier* is an ice mass that has been formed by successive local accumulation of snow, with ice movement due to ice deforming under its own weight. An *ice-sheet* is defined as a glacier that spreads out in all directions from a central dome, i.e. a large glacier (> 50 000 km^2 in area) that is not confined by the underlying topography (e.g. National Snow and Ice Data Center, 2024).

The margin of an ice sheet may be situated either on land or in water. If the ice margin is positioned in the sea or in a lake, it is common that the outer part of the ice-sheet is floating on the water, constituting an *ice shelf*. The boundary between the floating and grounded ice is the ice-sheet *grounding line*.

Of specific interest for the post-closure safety assessments are the conditions beneath the ice sheet, especially the basal thermal, and associated hydrological, conditions. An ice sheet can either be *cold-based* or *warm-based*. A cold-based ice sheet has basal ice with a temperature below the pressure melting point temperature, and is therefore frozen to its bed. There is no free water at the bed, and virtually no sliding of basal ice over the substrate is taking place. A warm-based ice sheet has basal ice with the temperature at the pressure melting point, i.e. thawed basal conditions prevail. In this case, free water is present at the ice/bed interface, and the ice may slide over the substrate.

Ice sheets may develop in Forsmark in the future following glacial inception in the Scandinavian Mountains (Section 3.5.3). While the development of an ice sheet over SKB's repositories is unlikely within the next 100 kyr, it is expected over the next 1 Myr (Section 3.6.1).

4.1.2 Importance for post-closure safety

The development of ice sheets in Forsmark is considered in post-closure safety assessments for both SFR and the spent fuel repository; the presence of ice sheets over the repositories is in the climate cases described by the glacial climate domain (Section 1.2.3). Furthermore, ice sheets significantly impact the other three climate-related issues described in this report, i.e. relative sea-level change, permafrost and denudation (Chapter 5–7).

First, as an ice sheet melts, the resulting mass unloading causes a glacial rebound, a vertical uplift of the crust that continues for tens of thousands of years after the ice disappears. The post-glacial rebound is a crucial factor when assessing future relative sea-level changes in the Forsmark area, both in the coming millennia and after potential future glaciations (Chapter 5).

Second, if the ice sheet is cold-based, low basal ice temperatures will lead to the formation of, or in cases preservation of pre-existing, permafrost. Conversely, during periods of warm-based ice coverage, basal ice temperatures at the pressure melting point will cause a complete or partial degradation of sub-glacial permafrost (Chapter 6).

Third, ice-sheet development influences the extent of glacial erosion under warm-based conditions. Glacial erosion contributes to the total bedrock denudation in the Forsmark area, resulting in the repository to become closer to the surface over time, potentially facilitating freezing of the bedrock and the engineered barriers (Chapter 7). Glacial erosion may also affect local topographical gradients and, thereby, the patterns of groundwater flow in the area. Since an ice sheet is unlikely to cover the Forsmark area within the next 100 kyr (Section 3.6.1), glacial erosion is primarily a concern for the spent fuel repository (safety assessment covering 1 Myr) rather than for the SFR (safety assessment covering 100 kyr) (see Chapter 7 for more details).

In addition to the climate-related issues mentioned above, ice sheets can also influence the conditions in the geosphere variables. These changes may in turn impact the integrity of the engineered barriers in the repositories as well as the transport of radionuclides released from the repositories. Table 4-1 summarises how the hydrological, chemical and mechanical conditions in the geosphere may be directly affected by ice-sheet development in Forsmark.

Potential impacts of these altered geosphere conditions on post-closure safety for the spent fuel repository and SFR are described in relevant safety assessment documents. For the latest safety assessment PSAR, these are primarily SKB (TR-21-04; see Tables 1-4 and 1-5 in that report for an overview), SKB (TR-21-01, Sections 8.3.4, 10.4.5 and 12.7) for the spent fuel repository and in SKB (TR-23-01, Sections 8.3 and 8.7.2) for SFR.

Table 4-1. Summary of influence of ice-sheet variables on the conditions in the geosphere

Geosphere variable	Ice-sheet variable	Summary of influence
Groundwater pressure	Basal thermal condition Ice-sheet thickness Meltwater supply Sub-glacial hydrological system	If the ice-sheet is warm-based, abundant melt water supply and the flow properties of sub-glacial hydrological systems may result in water pressure at the ice/bed interface reaching ice-sheet overburden pressure, and in certain cases even higher pressures. The groundwater pressure is also affected by the ice-load compression of the bedrock pores and fractures.
Groundwater flow	Basal thermal condition Slope of ice-sheet surface Rate of migration of ice-sheet margin	If the ice-sheet is cold-based at a certain location, virtually no free water is available and there will be no groundwater recharge from basal melt water at that location. If the ice-sheet is warm-based, basal melting occurs at the ice/bed interface and groundwater recharge takes place, both from basal melting and in places from surface melt. The type and extent of permafrost in front of the ice-sheet will determine how efficient the groundwater-surface water coupling is. In general, hydraulic gradients in the bedrock will be greatest in the vicinity of the ice-sheet margin, as they are sensitive to the slope of the ice-sheet surface, with steeper slopes resulting in higher hydraulic gradients and higher groundwater flow. The duration of periods with enhanced groundwater flow is determined by the rate of ice-sheet margin retreat. Groundwater flow during glacial conditions in Forsmark was analysed by Vidstrand et al. (2010).
Groundwater composition	Basal thermal condition Glacial melt water composition Duration of ice coverage	If a warm-based ice sheet is located above the repository, groundwater recharge is by glacial melt water, which typically has a lower salinity and a higher concentration of dissolved oxygen than groundwater formed by meteoric water. This will reduce the salinity and increase the oxygen content of the groundwater during such glacial periods. The combination of abundant melt water supply and high water pressures may cause injection of glacial melt water to larger depths than groundwater recharge during non-glacial conditions. Also, the consumption of oxygen close to the surface may be limited due to the lack of organic matter and microbiological activity.
Bedrock stresses	Basal thermal conditions Ice-sheet thickness Ice-sheet extent Rate of migration of ice-sheet margin Duration of ice coverage	Bedrock stresses will be influenced by the ice load and the groundwater pressure (Lund et al. 2009). Upon glacial advance, the earth's crust in front of the ice margin is bent upwards forming a so called "forebulge", where horizontal bedrock stresses perpendicular to the ice margin are decreased. The resulting differential stresses promote instability along primarily steeply dipping faults and fractures. Beneath the ice-sheet, the vertical and horizontal bedrock stresses increase, reaching additional loads corresponding to the ice thickness, generally stabilising existing fractures. Upon retreat of the ice-sheet, the stresses are restored to the background value, with horizontal stresses decaying at a slower rate than the vertical stresses, promoting instability on gently dipping faults and fractures. The bedrock stress response to glacial loading is not immediate but depends on the composition of the Earth's crust and mantle and the inherent mechanical properties. The induced glacial stresses in one point depend also on the duration of ice load, its spatial variation, the rate of change and the extent of the ice sheet.

Previous documentation

Ice-sheet development in Forsmark has previously been described in the climate reports produced for SKB's safety assessments for the spent fuel repository and SFR (e.g. SKB TR-10-49, SKB TR-13-05, SKB TR-20-12 and SKB TR-23-05). The latest climate reports (PSAR) for the spent fuel repository and SFR both included a dedicated section on the most important processes controlling the potential ice-sheet overriding in the Forsmark area as well as a reconstruction of the ice-sheet development during the Weichselian glacial cycle using numerical modelling (SKB TR-20-12, Section 3.1 and SKB TR-23-05, Section 2.3). Simulations of the penultimate glacial cycle, including its maximum extent, have been conducted in Colleoni et al. (2014), Quiquet et al. (2016) and Colleoni and Liakka (2020). The penultimate glacial maximum (during MIS 6; see Table 3-1) is the most extensive glaciation in Eurasia as inferred from geological records. Therefore, a dedicated section assessing the maximum ice-sheet thickness during this glacial maximum, based on the results of Colleoni et al. (2014) and Quiquet et al. (2016), was included in the PSAR for the spent fuel repository (SKB TR-20-12, Section 5.4). Finally, the possibility for temporary halts of the ice-sheet margin over the repository area (so-called *ice-marginal stillstands*) was analysed in SR-Site and PSAR for the spent fuel repository (e.g. SKB TR-20-12, Sections 4.2.2 and 4.5.1).

Most of the information about ice-sheet development compiled in previous SKB documents is only briefly summarised in this chapter. Instead of repeating previously published information, this chapter focuses on new results since the preparation of the PSAR climate reports. Specifically, this concerns an assessment of ice-sheet variability in Forsmark over the next 1 Myr based on future insolation changes and various scenarios of anthropogenic GHG emissions (Section 4.5.2). Additionally, this report includes a complementary analysis of the possibility and extent of ice-marginal stillstands over Forsmark during periods of maximum ice-sheet extent (Section 4.6.2).

The PSAR climate report for the spent fuel repository includes a section on glacial hydrology, providing detailed descriptions of key processes and recent observations from contemporary ice sheets (SKB TR-20-12, Section 3.2). The information on glacial hydrology presented in the PSAR climate report for the spent fuel repository remains scientifically robust and sufficient for post-closure safety assessments. As such, no updates to this information are considered necessary in this report.

4.2 Controlling variables and conditions

In this section, the most important variables and conditions for ice-sheet development are described. The discussion is complemented by Figure 4-1, which provides visual aid.

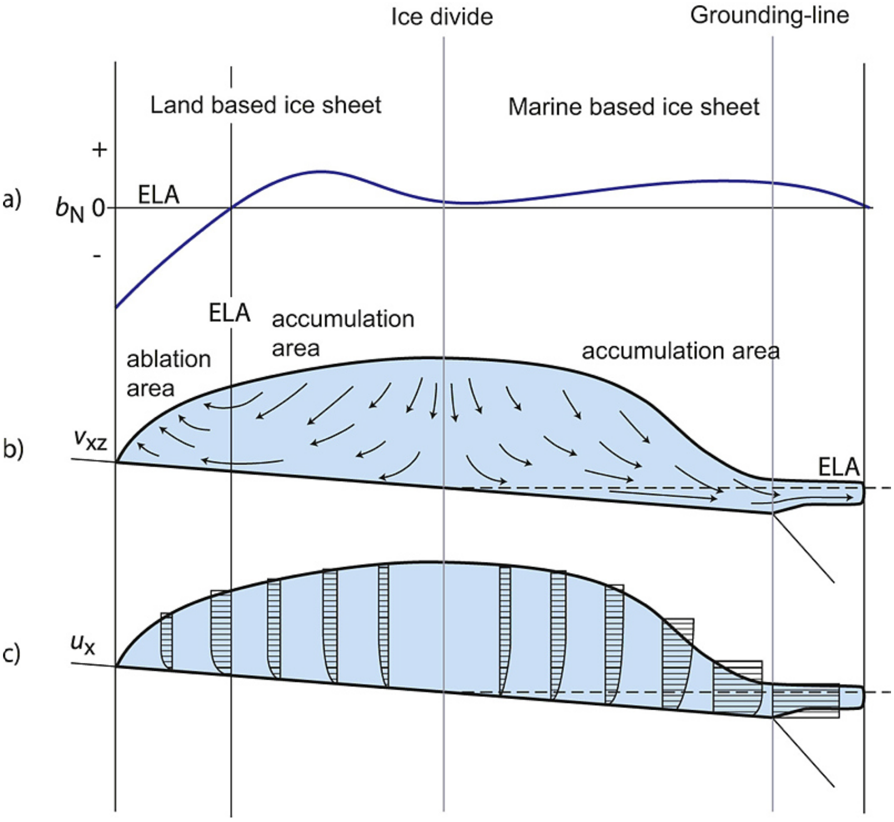

Figure 4-1. Schematic ice sheet-ice shelf cross section. Panel a) shows the surface mass balance distribution (b_N), with positive values representing accumulation of ice and negative values ice-sheet ablation. Panel b) shows ice velocity trajectories (v_{xz}) as well as distribution of accumulation- and ablation areas, and panel c) shows the horizontal velocity component (u_x). ELA denotes equilibrium line altitude and represents the boundary between the accumulation and ablation areas. Modified from Holmlund and Jansson (2003),

4.2.1 Mass balance and climate

The growth and decay of an ice-sheet is determined by its mass balance, which is the sum of the mass gain (accumulation) and the mass loss (ablation) over one year. The mass gain of an ice sheet is completely dominated by the process of snow accumulation. Most of the snow falls and accumulates during winter seasons, but snow may also accumulate during summer. For ice-sheet ablation, on the other hand, several processes may be involved, the two most significant being surface melting of snow and ice and calving of icebergs from ice shelves (in the case of a marine ice-sheet margin). Mass may also be lost through melting of basal ice and through sublimation of ice and snow. If the total ice-sheet accumulation over an ice sheet is greater than the total ablation over a year, the mass balance is defined to be positive, whereas the opposite situation is associated with a negative mass balance. A positive mass balance over several successive years leads to ice-sheet growth, whereas a negative mass balance reduces its size.

The mass balance is strongly controlled by the prevailing climate, with snow accumulation being determined by the precipitation and surface melting taking place if the local SAT is greater than 0 °C. In climates cold enough to sustain ice sheets, the SAT typically only becomes this high during summer.

Snow accumulation and surface ablation are not distributed evenly over the ice-sheet surface. Precipitation over an ice sheet is largely controlled by the ice-surface elevation and degree of continentality, often yielding a pattern of high accumulation rates close to the ice-sheet margin with diminishing values towards the interior. However, most of the ice sheet typically experiences some precipitation over a year. Also, significant amounts of snow redistribution may occur by wind. This may influence the local mass balance for parts of an ice sheet, but not the mass balance of an entire ice sheet.

The SAT over an ice sheet depends on the prevailing background climate which is mainly controlled by insolation and CO_2 on the timescales relevant for post-closure safety (Section 2.2). In addition to this background climate, there is a mutual interaction between ice sheets and the local climate through various feedback mechanisms. Two of the most important feedbacks for sustaining and growing ice sheets are the so-called *temperature-albedo* and *height-mass balance* feedbacks.

The temperature-albedo feedback occurs because ice and snow reflect more sunlight than the surrounding landscape, leading to lower SAT over ice sheets (e.g., Källén et al. 1979). This feedback mechanism is particularly important during the initial growth phase of an ice sheet, before the height-mass balance feedback becomes significant (Kageyama et al. 2004). One factor that could potentially reduce the albedo effect is dust deposited on the snow surface of the ice sheet (e.g. Colleoni et al. 2009; Willeit and Ganopolski 2018). Ice core analyses have shown that atmospheric dust concentrations were higher during glacial periods than they are today due to an expansion of unvegetated areas (Mahowald et al. 1999).

The height-mass balance feedback mechanism operates because SAT typically decreases with elevation according to the atmospheric lapse rate. As a result, mass balance tends to be higher in the interior compared to the margins (e.g. Figure 4-1). An important implication of this feedback is that once the ice sheet becomes thick enough, it can sustain itself (e.g., Weertman 1976; Oerlemans 1980). Calculations with simple ice-sheet models show that this feedback can lead to two stable steady-state solutions under a range of climate conditions: one with zero ice thickness and one with a large ice sheet. This is currently the case for the Greenland ice sheet. If the ice on Greenland were suddenly removed, it would not re-grow under present climate conditions (e.g. Oerlemans and van der Veen 1984).

Another implication of the height-mass balance feedback is that surface ablation often occurs only in narrow zones near the margins of the ice sheet, with virtually no effect elsewhere. When a part of an ice sheet experiences more accumulation than ablation over a year, it is considered to be in the *accumulation area*. This stands in contrast to the *ablation area*, which experiences a net loss of mass over a year. Central parts of ice sheets generally constitute accumulation areas, while lower parts, where surface melting occurs, form ablation areas (Figure 4-1). The boundary between the accumulation and ablation areas is known as the *equilibrium line* or *equilibrium line altitude* (ELA) (Figure 4-1).

4.2.2 Ice deformation and ice flow

The typical distribution of surface mass balance over an ice sheet, with accumulation areas at high elevations and ablation areas at lower elevations, suggests that without any ice movement, the slopes of the ice sheet would gradually steepen over time. However, since ice is a deformable material, gravity-induced stresses within the ice sheet give rise to deformation (strain) that counteract the uneven mass balance distribution by causing ice to flow from higher elevations (ice-sheet interior) towards lower elevations at the margins. The magnitude of these stresses is proportional to the ice sheet's thickness and the steepness of the slopes, implying that the highest stresses occur near the base and beneath the slopes. The shear stress, σ, at the base of an ice-sheet can be estimated using the following equation (see e.g. van der Veen 2013):

$$\sigma = \rho g H \sin \alpha \qquad \text{Equation 4-1}$$

where ρ is the density of ice, g the acceleration of gravity, H the ice thickness and α the ice-sheet surface slope. The most commonly used flow law for describing the strain rate of ice under pressure is Glen's flow law (Glen 1955):

$$\dot{\varepsilon} = \left(\frac{\sigma}{B}\right)^{n} \qquad \text{Equation 4-2}$$

where $\dot{\varepsilon}$ is the strain rate and B a viscosity parameter that increases as the ice gets more difficult to deform. B depends primarily on the ice temperature and crystal and/or micro-structure. The parameter n is an empirically determined constant (typically set to around 3, see e.g. van der Veen 2013), which depends on the specific creep process in operation. The main effect of Glen's flow law is that moderate increases in stress (i.e. the ice thickness or slope, see Equation 4-1) result in a substantial increase in strain rate. For example, a doubling of the amount of stress results in 8 times higher deformation rate (Figure 4-2).

At the highest points of the ice sheet, known as *ice divides* (Figure 4-1), the slope steepness is virtually zero meaning that the resulting stresses and ice deformation are also zero. However, at the margins where the surface slope is steeper, driving stresses increase, leading to higher rates of ice deformation and, thus, greater horizontal ice flow. For an ice sheet terminating on land with an ablation area, the maximum horizontal velocity is found at the ELA. In contrast, for a marine ice-sheet margin, the peak velocity occurs at the grounding line of the ice sheet (Figure 4-1).

In general, ice flow velocities are moderate to slow within an ice sheet, with ice moving only a few tens of metres per year. However, certain well-defined parts of an ice sheet known as *ice streams* can exhibit much faster flow. Ice streams often have specific basal thermal and hydrological conditions compared to that of the surrounding ice sheet. They are typically some tens of kilometres wide and several hundreds of kilometres long. Ice velocities within present-day ice streams are several hundred metres per year, in some cases exceeding 1000 m a^{-1} (e.g. Bennett 2003, Joughin et al. 2004). Since the surrounding ice moves much more slowly, the high velocity gradients at the margins of ice streams create distinct shear zones with significant crevassing. Due to their high ice flux, ice streams can drain substantial portions of an ice sheet.

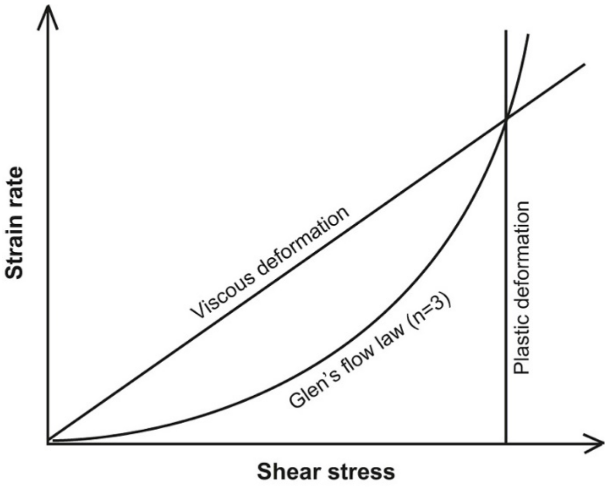

Figure 4-2. Deformation rate versus shear stress for various types of deformation, including Glen's flow law for ice. Modified from Holmlund and Jansson (2003).

4.2.3 Ice temperature

The temperature of the ice is important for the behaviour and characteristics of glaciers and ice sheets, significantly affecting their movement, dynamics and hydrology. For example, ice temperature influences ice deformation through the parameter B in Equation 4-2 (e.g. Jansen et al. 2005). Glacier ice can be classified into two types based on temperature: (i) temperate ice (or warm ice), which is at the prevailing pressure melting point, and (ii) polar ice (or cold ice), which temperature is below the pressure melting point. Cold ice is harder than warm ice, and therefore does not deform as easy. Cold ice is also impermeable to water unless crevasses or other cavities are present.

While a temperate ice sheet is inherently warm-based, a polar ice sheet may be either cold-based or warm-based. In warm-based polar ice sheets, only the lowermost portion is typically at the pressure melting point temperature, whereas the majority of the ice remains cold. Consequently, different parts of a polar ice sheet can have varying temperature characteristics. This is the case for the present-day Greenland and Antarctic ice sheets.

The pressure melting point temperature decreases with depth. At 3 km depth beneath the ice, for example, it decreases by approximately 2 °C compared to the surface (e.g., van der Veen, 2013). This is important, since the basal conditions change drastically if the bed of an ice-sheet becomes melted or frozen. This affects ice-sheet flow by turning on and off basal sliding, governs if glacial erosion can take place or not, and has a profound impact on basal hydrology.

4.2.4 The ice-sheet bed

The lower boundary condition of an ice-sheet system is its bed, which typically consists of either bedrock (normally crystalline rocks in Fennoscandia) or bedrock covered by till. The ice-sheet bed affects the basal thermal conditions of the ice sheet, primarily through the topography of the landscape and the spatially varying geothermal heat flow.

The topography of the bed influences basal thermal conditions because a bed with significant relief creates stronger lateral temperature gradients compared to a bed with smooth topography. A stronger relief also leads to more pronounced spatial variations in basal meltwater production.

Geothermal heat flux impacts basal ice temperatures, hydrology, ice dynamics and the erosional capacity of the ice. For instance, in a steady-state 3 km thick ice sheet, a 20 % change in geothermal heat flux can alter the basal ice temperature by up to 6 °C (Näslund et al. 2005).

4.3 Historical evolution

To estimate how ice sheets might evolve in the future, it is useful to study their historical changes. Marine sediment records provide valuable insights into past ice sheet dynamics. By examining the ratio of heavy to light oxygen in these sediments, changes in global ice volume over time can be inferred (see, e.g., Figure 2-1a). Such analysis reveals important patterns about past glacial and climate dynamics, such as the cyclical nature of glaciations, which occurred approximately every 100 kyr over the past 800 kyr. These glacial cycles are characterized by relatively slow (order 100 kyr) and gradual ice accumulation followed by rapid (order 10 kyr) ice-sheet decay (Figure 2-1a). Marine sediment records are useful for understanding global changes in continental ice sheets, but they do not reveal the specific geographic distribution of past ice sheets. To gain this information, it is necessary to examine physical traces left in the landscape or conduct numerical ice-sheet modelling.

Typical geological features indicating past glaciations include (i) materials transported and deposited by ice sheets, such as moraines, and (ii) scratches and erosional marks in the bedrock surface (e.g. (glacial striations) and in sediments (till lineations) caused by glacial abrasion. The abundance of these features has provided an understanding of the maximum extents of past ice sheets (e.g. Svendsen et al. 2004, Kleman et al. 2013). The most recent maximum extent of Northern Hemisphere ice sheets occurred at the LGM around 20 kyr ago. Figure 4-3 shows the maximum extents of the Northern Hemisphere ice sheets during this period. As illustrated in the figure, the Eurasian ice sheet covered all of Fennoscandia, the British Isles, and the northernmost parts of Germany and Poland. In contrast, the North American ice sheet was significantly larger than the Eurasian counterpart, extending across most of Canada and the northernmost parts of the USA during the LGM.

Assessing ice-sheet extents before the LGM is more challenging than for the LGM itself. This difficulty mainly arises because many traces of pre-LGM ice sheets were obliterated by the ice sheets that expanded to their LGM extents. Consequently, data outlining pre-LGM ice-sheet configurations are scarce. The existing evidence mainly consists of glacial striations and till lineations. In particular, crosscutting striations and lineations are valuable because they help determine relative-age relationships (e.g., Kleman et al. 2010). These features provide information about the ice flow direction at the time they were formed.

Pre-LGM extents of the Eurasian ice sheet have been reconstructed for the MIS 4 (74–59 kyr BP) and the MIS 6 periods (~192–135 kyr BP) (e.g. Svendsen et al. 2004). MIS 4 represents the first cold period with substantial ice growth during the Weichselian (Section 3.3.2). MIS 6, also often referred to as the "Late Saalian glaciation" or the "penultimate glaciation", includes the maximum ice-sheet extent that occurred during the penultimate, Saalian, glacial cycle. Figure 4-4 shows reconstructions of the maximum Eurasian ice-sheet extents for MIS 4 and MIS 6, as documented by Svendsen et al. (2004). According to these reconstructions, the MIS 4 Eurasian ice sheet was roughly comparable in size to the LGM ice sheet, whereas the MIS 6 ice sheet was significantly larger than the LGM counterpart, with a larger extent eastward and southward. Although some details, such as the exact timing of these maximum extents, remain uncertain, the general characteristics of the Eurasian ice-sheet configuration during the MIS 4 and MIS 6 periods, as outlined by Svendsen et al. (2004), are well established and supported by later studies (e.g. Batchelor et al. 2019).

Geological evidence also shows that LGM, MIS 4 and MIS 6 represent the last three periods of ice coverage in Forsmark (Svendsen et al. 2004). Recent climate reconstructions support this view as they indicate that the intermediate periods, MIS 3 and MIS 5, were relatively warm and ice free in northern Fennoscandia (see further Section 3.3.2).

Section 4.3.1 presents an ice-sheet modelling reconstruction of the Weichselian glacial cycle which includes the LGM and MIS 4. This reconstruction has featured in several previous safety assessments and is therefore only briefly summarised here; for a more detailed description, please refer to SKB (TR-20-12, Section 3.1). Section 4.3.2 provides a brief overview of transient simulations for the Saalian glacial cycle, which were originally presented by Colleoni and Liakka (2020).

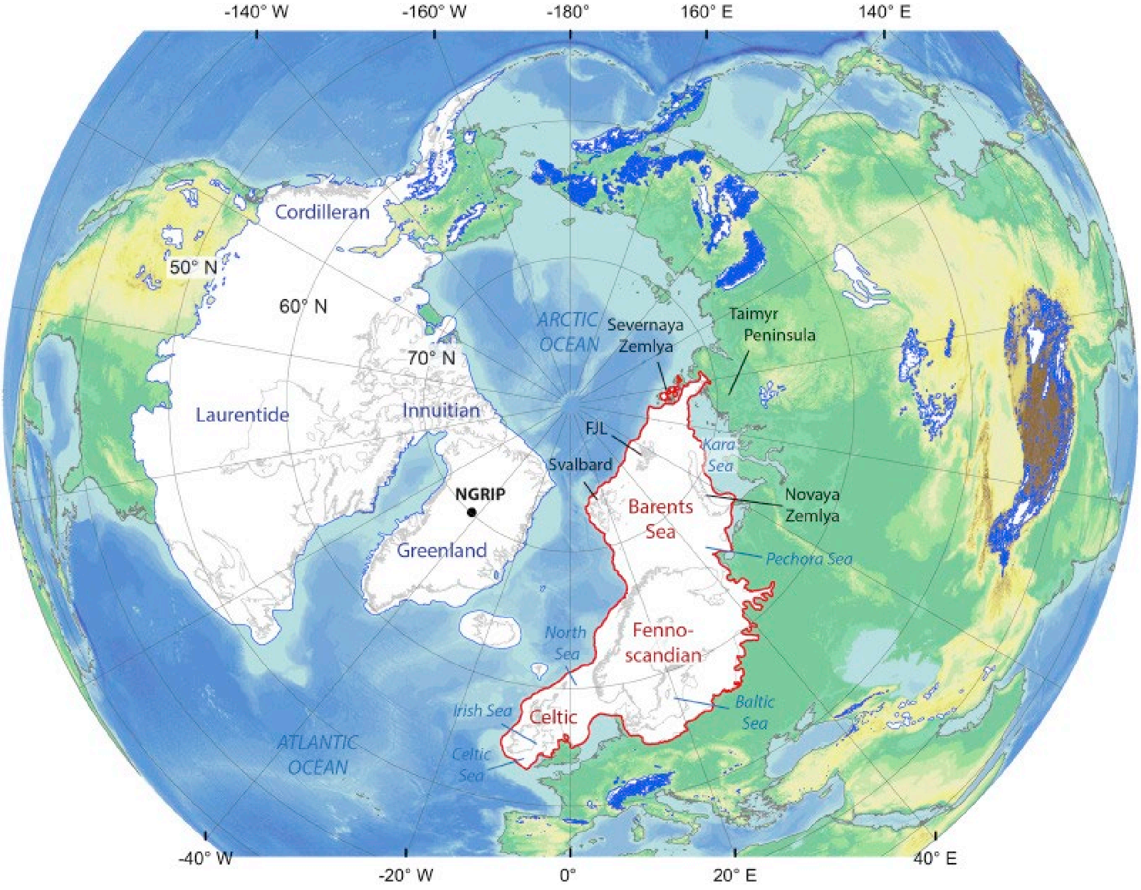

Figure 4-3. LGM Northern Hemisphere ice-sheet extent (white). From Patton et al. (2016).

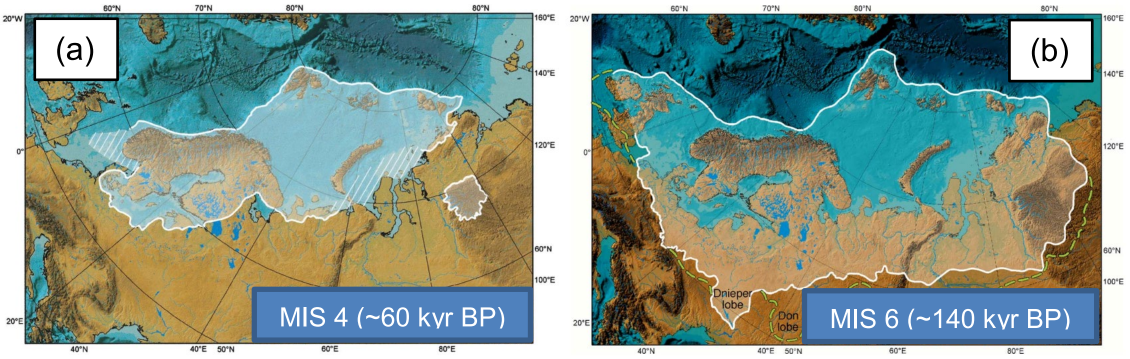

Figure 4-4. Reconstructed Eurasian ice-sheet extents at the (a) MIS 4 (~60 kyr BP) and (b) MIS 6 (~140 kyr BP) glacial maxima. Modified from Svendsen et al. (2004).

4.3.1 Weichselian glacial cycle

Numerical model and experimental design

The evolution of past ice sheets is typically reconstructed using two main types of numerical models. The first type includes thermo-mechanical ice-sheet models, which are based on principles of ice physics and thermo-mechanical interactions (e.g. Fastook 1994, Greve 1997, Ritz et al. 2001). The second type consists of isostatic rebound models, which interpret observations of crustal rebound and shoreline positions to estimate paleo-ice thicknesses (e.g. Lambeck et al. 1998, Peltier 2004, Peltier et al. 2015). In SKB's safety assessments, the Weichselian ice-sheet reconstruction uses simulations performed with the thermo-mechanical ice-sheet model UMISM (University of Maine Ice-sheet Model) (cf. Fastook and Chapman 1989, Fastook 1994). It is important to note that since the primary aim of these simulations is to represent the general historical extent of the ice sheet, calibrated by geological information, the specific choice of model is not critical for the conclusions drawn.

UMISM solves the coupled mass, momentum, and energy conservation equations (Fastook and Chapman 1989, Fastook 1994) using a time-dependent finite-element method. The model has been utilised in a broad range of applications (e.g. Holmlund and Fastook 1995, Johnson and Fastook 2002, Kleman et al. 2010, Kleman et al. 2013). In SKB's Weichselian reconstruction, the model was run from 120 kyr BP until present-day using a five-year time step.

The model version used here employs the shallow ice approximation (SIA) (Hutter 1983), which assumes that basal shear stress of the grounded ice is completely balanced by the gravitational driving stress. The resulting strain rates are calculated from the stresses using Glen's flow law (Section 4.2.2). The primary input to the model is the bedrock topography, the mean annual SAT, the geothermal heat flux and the net mass balance at the ice sheet surface. The model output consists of ice thickness, ice-surface elevation, ice velocities, the temperature field within the ice sheet, the amount and distribution of water at the bed resulting from basal melting, and the amount of bed depression resulting from the ice load.

The bedrock topography is represented by a 50 km resolution Digital Elevation Model (DEM). This resolution is sufficient to capture the general large-scale dynamics of the ice-sheet but is too coarse in regions with large and highly variable topography. However, this is not the case for south-central Sweden, including Forsmark, which in general is characterised by a flat topography. DEM data were derived from the ETOPO2 data base[12], depicting both continental topography and bathymetry. These data were then combined with reconstructions of the prevailing sea level for each timestep to obtain changes in the background topography over time. The geothermal heat flux was taken from Näslund et al. (2005).

The top boundary condition is represented by the prevailing climate conditions, represented by mean annual SAT and precipitation. The spatial and temporal distribution of the precipitation is calculated from the air temperature field, based on an empirical relationship (Fastook and Prentice 1994). A SAT proxy record from the Greenland ice core project (GRIP; Dansgaard et al. 1993) was employed as time-dependent forcing of the ice-sheet model (see also Section 3.3.2).

Model calibration and results

In SKB's reconstruction of the Weichselian ice-sheet, the UMISM model was calibrated by adjusting the GRIP proxy SAT curve. In this process, the entire SAT curve was shifted and the amplitude of the SAT variations was modified (Figure 4-5) to obtain calibrated ice-sheet configurations that fitted well with geological observations on dated marginal positions. All other input data was kept constant in the calibration process. Model calibration was made for ice margins as described in Lokrantz and Sohlenius (2006) for MIS 5d (~ 110 kyr BP), MIS 5b (~ 85 kyr BP), MIS 4 (~ 60 kyr BP), LGM (~ 20 kyr BP), and for the Younger Dryas (~ 12 kyr BP).

---

[12] ETOPO2, 2001. Global Digital Elevation Model (ETOPO2) representing gridded (2 minute by 2 minute) elevation and bathymetry for the world. Data were derived from the National Geophysical Data Center (NGDC) ETOPO2 Global 2' Elevations data set from September 2001.

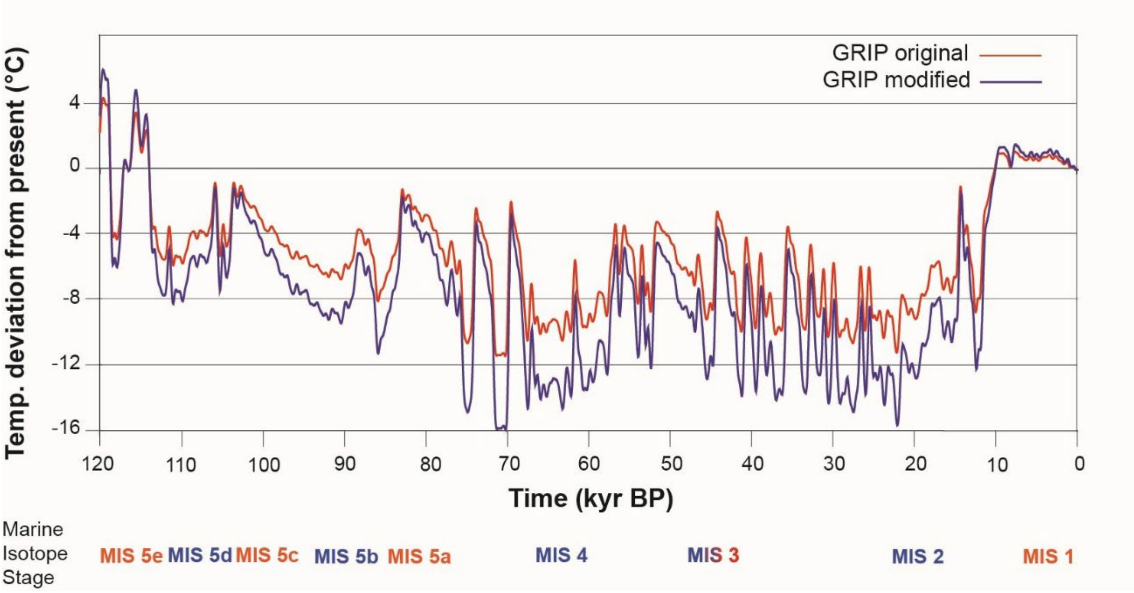

Figure 4-5. *Paleo-proxy SAT curves from the calibration process of the UMISM ice-sheet model. The final calibrated curve that was used (blue) has a larger amplitude and a lower average SAT compared to the original data (red). The temperature curve is discussed in detail in SKB (TR-20-12, Appendix A).*

The calibrated reconstruction of the Weichselian ice sheet is illustrated in Figures 4-6 and 4-7. These figures depict periods of ice expansion during cold stadials, such as MIS 5d, 5b, 4, and 2 as well as during younger dryas, in contrast to more limited ice cover during warmer interstadials like MIS 3. This dynamic behaviour of the reconstructed ice sheet is consistent with the Fennoscandian climate reconstruction for this period (Section 3.3.2), which reveal a highly variable climate during the Weichselian. For instance, the climate reconstructions indicate cold, ice-covered conditions during MIS 4 and LGM, in agreement with the ice-sheet reconstruction, while MIS 3 experienced relatively warm and temperate conditions.

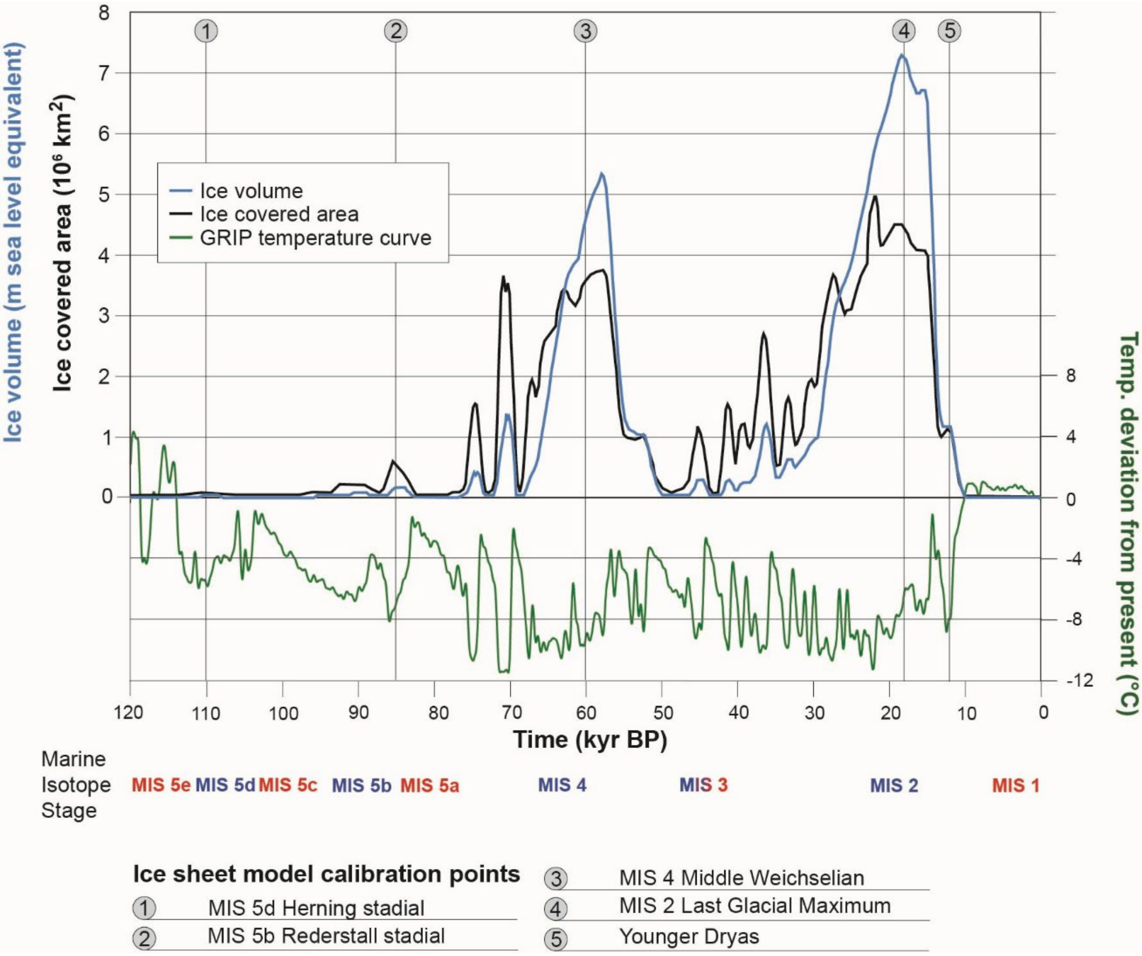

Figure 4-6. *Ice-covered area and ice volume for the reconstruction of the Weichselian ice sheet in Eurasia. Times of model calibration are also shown, as well as the Marine Isotope Stages (MIS) (warm stages in red and cold stages in blue) and the calibrated GRIP SAT curve (green) (see also Figure 4-5).*

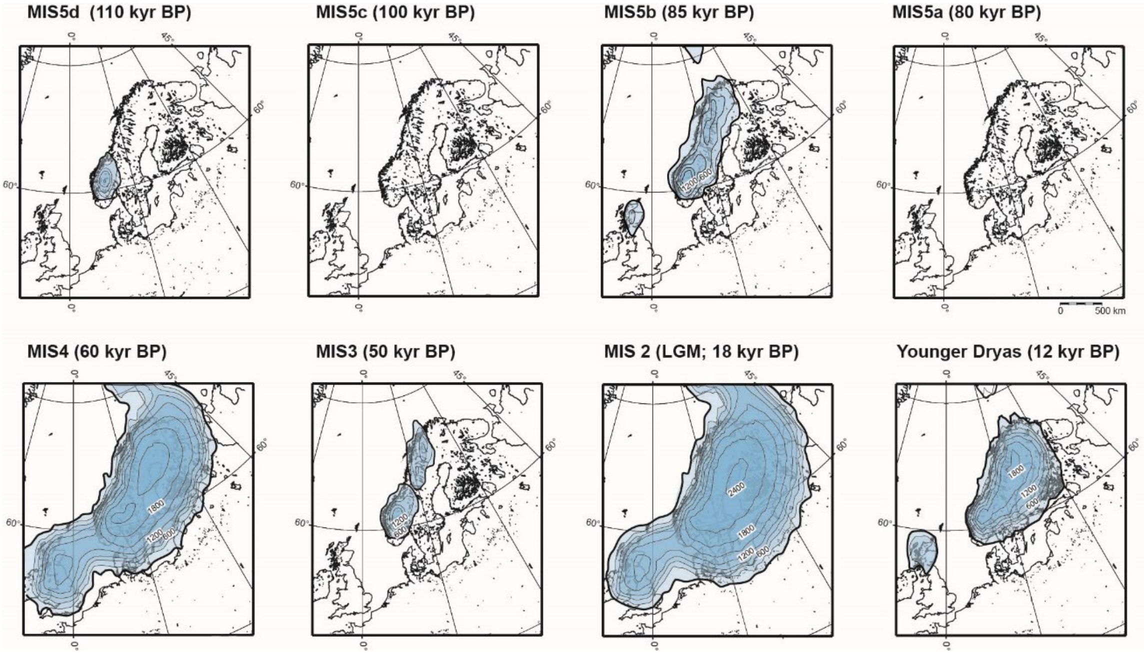

Figure 4-7. *Selected snap-shots of ice-sheet surface topography for the reconstructed Weichselian ice sheet. The ice sheet grows to its full LGM configuration in progressive phases of increasing maximum extent during stadials, with intervening periods of more restricted ice coverage during intestadials. Contour lines show ice-surface elevation with a 300 m contour interval. All maps show present day shoreline position.*

In summary, the Weichselian ice-sheet reconstruction indicates that the Forsmark region was subject to two phases of ice coverage, during MIS 4 and LGM (Figure 4-8). This result is consistent with other Weichselian reconstructions (Section 3.3.2). According to the modelling, the first glaciation lasted approximately 9 kyr and reached a maximum ice thickness of around 2000 m. In contrast, the second glaciation was more extensive, lasting about 19 kyr and achieving a maximum thickness of approximately 2900 m (Figure 4-8). Overall, the reconstruction suggests that the Forsmark area was covered by ice for nearly 30 kyr during the Weichselian, which is roughly 25 % of the total duration of the glacial cycle. Additionally, the modelling indicates that the Forsmark area was covered by warm-based ice for ~23 kyr, corresponding to about 80 % of the ice-covered time (Figure 4-8). This means that during most of the time when the reconstructed ice sheet covered the site, water from basal melting was present at the ice-sheet bed, typically produced at rates of a few mm yr^{-1}, up to ~10 mm a^{-1}, leading to groundwater recharge by glacial meltwater. In addition, surface meltwater also penetrates to parts of the bed during the melt season, adding large amounts of water to the basal hydrological system.

The shorter periods characterised by cold-based conditions, when no basal water production occurs, immediately follow the ice sheet's initial coverage of the site (Figure 4-8). During these cold intervals, as well as during deglaciation phases when the site is approaching ice-free conditions, surface melting water may still reach the bed. However, when and if the ice-sheet margin is situated over ground with permafrost, this meltwater is unlikely to significantly contribute to groundwater recharge. This situation can only arise under cold climate conditions, and is therefore more prevalent during phases of ice-sheet advance than during retreat.

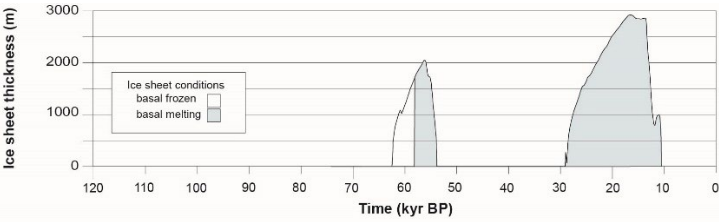

Figure 4-8. *Reconstructed ice-sheet thickness over Forsmark for the Weichselian glacial cycle. Periods of frozen (cold-based) and melted (warm-based) conditions beneath the ice sheet are also indicated. Note that a period of cold-based conditions is reconstructed also for the beginning of second glaciation in Forsmark although this period is too short to be visible in the figure.*

4.3.2 Saalian glacial cycle

The Saalian glacial cycle includes the MIS 6 glacial maximum, which constitutes the largest Eurasian ice sheet as interpreted from Quaternary geological records (approximately the last 2.6 Myr) (Figure 4-4). While the maximum extent of the Eurasian ice sheet during this period is relatively well-documented, there is limited geological information about the ice-sheet extents throughout the entire Saalian glacial cycle. Moreover, emerging evidence suggests that different regions of the MIS 6 Eurasian ice sheet reached their maximum extents at different times (see further Section 4.5.1). This indicates that using the observed extents of the MIS 6 maximum ice-sheet extent as a benchmark for model-based reconstructions may also pose challenges.

Furthermore, the scarcity of observational evidence for the Saalian ice-sheet extents, apart from its maximum extent, makes it challenging to spatially constrain ice-sheet simulations for this period. Consequently, the simulated extents during the Saalian glacial cycle become highly sensitive to the climate forcing applied and to other internal parameters in the ice-sheet model. As a result, previous attempts to reconstruct this glacial cycle has revealed a high sensitivity to unconstrained parameters, especially those related to the climate evolution through the glacial cycle (Colleoni and Liakka 2020).

4.4 Present-day conditions and trends

Following the LGM, when ice sheets covered vast areas of North America and Eurasia, Earth entered a period of climate warming and associated rapid deglaciation. Global temperatures gradually increased, leading to the melting of ice sheets and glaciers. This resulted in rising sea levels and the exposure of many regions that had previously been covered by ice. This deglaciation period marked the transition to the current interglacial epoch, the Holocene, which began approximately 11.7 kyr ago (Section 3.3). By the end of the deglaciation, only two major ice sheets remained on Earth: the Antarctic ice sheet (~14 million km²) and the Greenland ice sheet (~1.7 million km²). Both of these ice sheets have substantial thicknesses: the Greenland ice sheet exceeds 3 km at its thickest point, while the Antarctic ice sheet reaches nearly 4.9 km at its maximum thickness. Currently, anthropogenic global warming is causing both the Greenland and Antarctic ice sheets to lose mass at an accelerating rate, contributing to global sea level rise (see Section 5.2.1 and Fox-Kemper et al. 2021 for further details).

4.5 Future evolution

In this section, future ice-sheet evolution is described. The present interglacial conditions at Forsmark are expected to persist for at least 50 kyr into the future, potentially extending to several hundred thousand years depending on the amount of anthropogenic carbon emissions (Sections 3.5.3 and 3.6.1). Accounting for the time it takes for an ice sheet to reach Forsmark following the initial inception in northern Fennoscandia, the overall conclusions is that the presence of ice sheets in Forsmark is unlikely over the next 100 kyr (Section 3.6.1). However, the presence of an ice sheet in Forsmark can be expected within the next 1 Myr.

The analysis of the two preceding glacial cycles in Fennoscandia (Weichselian and Saalian) shows that the spatial and temporal distributions of the North American and Eurasian ice sheets may vary widely within as well as between glacial cycles (Section 4.3). Since the underlying causes of these differences remain elusive, predicting the future spatiotemporal evolution of ice sheets is inherently uncertain. Therefore, rather than presenting deterministic trajectories of potential future ice-sheet developments, this section focuses on delineating reasonable uncertainty ranges in key variables associated with ice-sheet development over the next million years, of relevance for post-closure safety. These variables constitute (i) the maximum ice-sheet thickness in Forsmark over the next 1 Myr (Section 4.5.1) and (ii) the frequency and duration of ice coverage in Forsmark over the same timeframe (Section 4.5.2). Both variables are relevant for post-closure safety of the spent fuel repository (Section 4.1.2).

4.5.1 Maximum ice-sheet thickness

A comprehensive evaluation of this potential maximum ice-sheet thickness in Forsmark was carried out in the PSAR (SKB TR-20-12, Section 5.4). The assessment conducted for the PSAR remains up-to-date, so this section mainly summarizes the most significant findings from that assessment.

In the PSAR, the assessment of maximum ice-sheet thickness relied primarily on modelling studies conducted by Colleoni et al. (2014) and Quiquet et al. (2016). These studies utilised the GRISLI ice-sheet model (GRenoble Ice Shelf and Land Ice model; Ritz et al., 2001), forced by climate conditions derived from two atmosphere-ocean general circulation model (AOGCM) experiments conducted with the NCAR CESM1.0.5 model (Gent et al. 2011). The target period for simulations in both studies was the MIS 6 glacial maximum (Figure 4-4), which represents the most extensive glaciation in Eurasia over the past 2 Myr, as documented in geological records (Section 4.3.2).

Simulations design

Both AOGCM experiments employed by Colleoni et al. (2014) and Quiquet et al. (2016) were identical except for the representation of the North American ice sheet. The first experiment, named *topo1*, utilised an LGM representation of the North American ice sheet (derived from Peltier 2004). However, insights from marine proxy records of past ice-volume changes suggest that the North American ice sheet was likely smaller during the MIS 6 glacial maximum than during the LGM. This interpretation arises from the similarity in estimated ice-volume changes between the MIS 6 maximum and the LGM (e.g. Figure 2-1), despite the presence of a substantially larger Eurasian ice sheet during MIS 6. Consequently, the second AOGCM experiment, named *topo2*, adopted a smaller configuration of the North American ice sheet (derived from Colleoni 2009), in better agreement with the global sea-level records of the MIS 6 glacial maximum.

The SAT and precipitation fields generated from the *topo1* and *topo2* AOGCM experiments served as climate forcing in the GRISLI ice-sheet model experiments. GRISLI incorporates three types of ice flow regimes: grounded ice, ice streams and ice shelves. The horizontal resolution was set to 20 km in both studies, and all ice-sheet experiments were carried out with constant-in-time forcing and boundary conditions and integrated until steady state (~200 kyr). Hence, no transient simulations were performed.

Together, Colleoni et al. (2014) and Quiquet et al. (2016) conducted multiple sensitivity experiments aimed at assessing the impact of diverse sources of uncertainty on the steady-state ice-sheet thickness during MIS 6 glacial maximum over Forsmark. These sources of uncertainty encompassed potential errors linked to the initialization of the ice-sheet model, climate forcings and model selection. Moreover, both studies extensively examined the sensitivity of ice-sheet thickness to poorly constrained parameters within the ice-sheet model. These ice-sheet parameter sensitivity simulations resulted in the thickest and thinnest ice sheets in both studies.

In Colleoni et al. (2014), the ice-sheet thickness sensitivity to parameters within the ice-sheet model was primarily evaluated by means of uni-variate sensitivity experiments, i.e. the effect of altering individual parameters on the ice-sheet thickness was evaluated. In contrast, Quiquet et al. (2016) employed the Latin Hypercube Sampling (LHS) sampling technique to systematically explore the parameter space. LHS facilitated a multi-variate parameter analysis, allowing the authors to investigate how changing combinations of two or more parameters impacted ice-sheet thickness. Additionally, Quiquet et al. (2016) explored a broader range of the potential parameter values compared to Colleoni et al. (2014), encompassing the full range of the values found in the literature. In total, they conducted 100 experiments for each climate forcing field (*topo1* and *topo2*) with different combinations of 10 parameters, shown in Table 4-2.

Table 4-2. Evaluated parameters in multi-variate ice-sheet model sensitivity simulations (Quiquet et al. 2016)

Parameter		Units
Ice ablation coefficient	C_{ice}	mm °C^{-1} day^{-1}
Snow ablation coefficient	C_{snow}	mm °C^{-1} day^{-1}
Topographic lapse rate	λ	°C km^{-1}
Daily temperature variability	σ	°C
Solid precipitation threshold	p_{solid}	°C
Accumulation ratio	γ	°C^{-1}
Thermoactive layer thickness	d	m
SIA enhancement factor	E_{sia}	-
GHF modificatory	γ_{GHF}	-
Basal drag coefficient	C_f	-

Main results

The uni-variate parameter sensitivity analysis conducted in Colleoni et al. (2014) helped to identify critical parameters that are important for determining the ice-sheet thickness. However, their simulated ice-sheet thicknesses were, as expected, generally lower compared to the multi-variate sensitivity experiments carried out by Quiquet et al. (2016). Specifically, the maximum ice thickness over Forsmark in Colleoni et al. (2014) was approximately 3500 m (3200 m) using the *topo1* (*topo2*) climate forcing data. In contrast, the corresponding maximum thicknesses in Quiquet et al. (2016) reached approximately 4200 m (4000 m) for the *topo1* (*topo2*) climate forcing data.

Figure 4-9 displays the simulated MIS 6 ice-sheet thickness over Forsmark from the multi-variate sensitivity experiments using the *topo2* climate forcing, which is deemed to be more realistic than the *topo1* forcing (as discussed above). Due to the broad range of parameter values evaluated in Quiquet et al. (2016), approximately half of the sensitivity experiments failed to simulate an ice sheet over Forsmark (red stars in Figure 4-9). Among the experiments that successfully managed to reproduce an ice sheet over Forsmark, the simulated ice-sheet thickness predominantly fell within the range of 3000 to 4000 m (black stars in Figure 4-9).

The sensitivity of simulated ice thickness to each evaluated parameter can be identified from the slope of the black stars in Figure 4-9. In most cases, the black stars are distributed horizontally along the x-axis, indicating minimal correlation between simulated ice thickness and these parameters. However, two exceptions stand out: there is a small negative correlation observed for the flow enhancement factor (E_{sia}), indicating thicker ice for lower E_{sia} values, while a slightly stronger (positive) correlation is evident for the basal drag coefficient (C_f), implying generally thicker ice for higher C_f values.

The thicker simulated ice sheets observed in the multi-variate compared to the uni-variate sensitivity experiments can be partly attributed to the basal drag coefficient being permitted to vary by a factor of 10 in Quiquet et al. (2016), as opposed to a factor of 3 in Colleoni et al. (2014). Quiquet et al. (2016) justified this broad range by the absence of reliable direct observations of this parameter. Moreover, they noted that indirect estimates beneath present-day ice sheets and glaciers suggest significant spatial variability in this parameter, rendering these estimates inadequate for constraining it (e.g., Schäfer et al. 2012, Morlighem et al. 2013). This large spatial variability of basal drag beneath present-day ice sheets has been corroborated in studies published subsequent to the PSAR (e.g. Ranganathan et al. 2021, Hudson et al. 2023). Consequently, even if considering more recent research, it remains inconclusive whether lower values of the basal drag coefficient are more probable than higher ones, or vice versa.

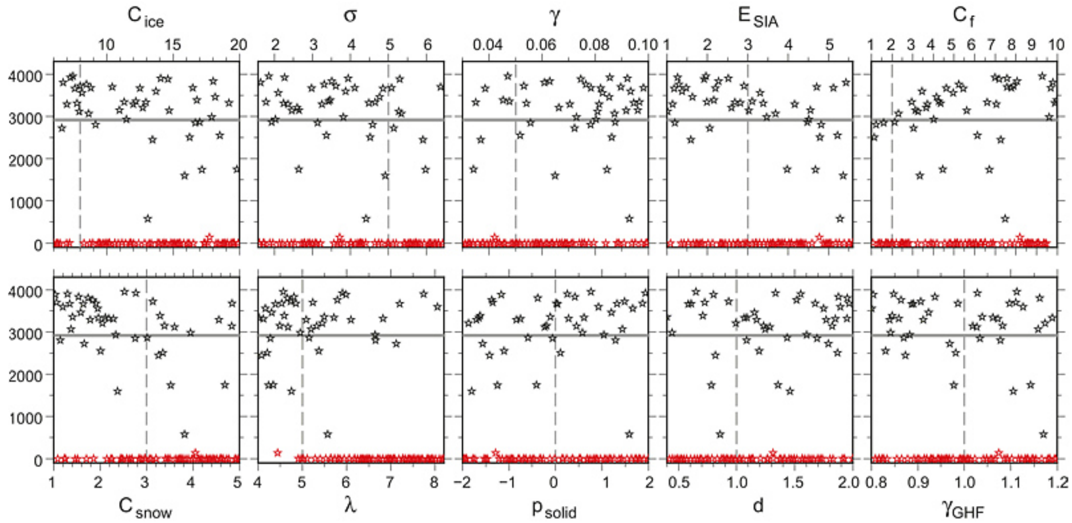

Figure 4-9. *Ice thickness over Forsmark using the topo2 climate forcing for each member of the multi-variate sensitivity analysis as a function of parameter values (Quiquet et al. 2016). Horizontal lines correspond to the ice thickness simulated in the reference simulation in Colleoni et al. (2014). The vertical dashed lines either correspond to the parameter value used in the reference simulation (if this parameter was used), or to a standard value from literature. The red stars are the simulations that are discarded since they do not preserve ice (thickness less than 500 m) at the Forsmark site (i.e. an unrealistically large ice-sheet retreat). A description of each parameter is provided in Table 4-2. From Quiquet et al. (2016).*

Conclusion and discussion

The assessment of maximum ice-sheet thickness in Forsmark over the next 1 Myr is set to 4000 m. This assessment is the same as in the PSAR for the spent fuel repository (SKB TR-20-12, Section 5.4.5), and is based on the modelling of Colleoni et al. (2014) and Quiquet et al. (2016), together with considerations of their experimental design and assumptions made in relation to knowledge on the behaviour of the natural ice sheet/climate system.

One important consideration in relation to their experimental design is the fact that a smaller-than-LGM-sized North American ice sheet is considered to be more realistic for the MIS 6 glacial maximum (see above), whereby the ice-sheet model experiments using the *topo2* climate forcing has been given a larger weight in the maximum thickness assessment than the *topo1* experiments.

Another issue is to that all ice-sheet model simulations in Colleoni et al. (2014) and Quiquet et al. (2016) were integrated to steady state using a constant-in-time climate forcing, which is not realistic in nature. Since Colleoni et al. (2014) and Quiquet et al. (2016) used a climate forcing representative for MIS 6 glacial maximum, which is known to be a cold stadial, the steady-state assumption most likely resulted in an overestimation of the "true" peak ice-sheet thickness over Forsmark.

Finally, the maximum extent of the MIS 6 ice sheets, as employed by Colleoni et al. (2014) and Quiquet et al. (2016), was likely overestimated. Geological findings suggest a significant retreat of the MIS 6 ice sheet around ~150 kyr BP (Astakhov 2004, Svendsen et al. 2004). Given that the MIS 6 extent utilised in both studies corresponds to the MIS 6 glacial maximum at ~140 kyr BP, the Eurasian ice sheet must have regrown to its extensive size within only 10 kyr. This rapid rate of regrowth is not plausible, indicating that the maximum extent might have occurred at different stages of the cycle rather than precisely at 140 kyr BP. Moreover, a synthesis of geological evidence by Rohling et al. (2017) suggests that the actual extent of the MIS 6 glacial maximum was likely smaller than depicted in the simulations. Thus, it is likely that the maximum extents of the MIS 6 ice sheet were attained at various points in time, potentially rendering the maximum extent used in the simulations as overstated.

It should also be emphasised that the estimated maximum ice-sheet thickness presented here serves as an upper limit rather than a probable outcome during future glaciations. The mean ice-sheet thickness range resulting from the simulations in Quiquet et al. (2016) (approximately 3200–3600 m) is considered the most plausible range for the maximum ice thickness over Forsmark under conditions resembling a MIS 6-sized Eurasian ice sheet. This range aligns closely with maximum ice thickness estimates found in both Colleoni et al. (2014) and in SR-Site, based on Lambeck et al. (2006) (estimated at 3400 m).

4.5.2 Frequency and duration of ice coverage

In this section, the frequency and duration of ice coverage in Forsmark over the next 1 Myr is assessed. This is relevant mainly for the analysis of containment for the spent fuel repository because the variability of future glaciations may affect conditions relevant for the integrity of the buffer and canisters, such as the hydrological and chemical conditions in the geosphere (Section 4.1.2).

The variability of future glaciations is primarily controlled by the latitudinal and seasonal insolation distribution (Sections 2.2.1 and 2.3) as well as by complex interactions among Earth system components, such as ice sheets, atmosphere and ocean circulations, the lithosphere and the carbon cycle. The role of these interactions in the overall dynamics of glacial cycles (cf. Figure 2-1a) has been relatively well studied (e.g. Oerlemans 1980, Pollard 1982, Ganopolski and Calov 2011, Abe-Ouchi et al. 2013, Ganopolski and Brovkin 2017, Watanabe et al. 2023). However, their impact on regional ice-sheet evolution remains elusive, complicating efforts to assess future ice-sheet variability over a certain site. Assessing future ice-sheet variability is further complicated by anthropogenic impacts on the climate system, affecting the timing of the next glacial inception (see further Section 3.5.3).

One approach for projecting ice-sheet variability involves simulations using comprehensive ice-sheet and climate models. This approach has been used for the last glacial cycle (Abe-Ouchi et al., 2013). These comprehensive models typically exhibit high complexity, aiming to resolve most of the known processes and interactions within the climate system. However, despite their complexity, they are limited by our incomplete understanding of glacial dynamics, resulting in that several parameters are poorly constrained. Furthermore, computational demands of such models are substantial, making it time-consuming to perform numerous simulations to address these uncertainties.

In the present work, future ice-sheet variability in Forsmark is instead assessed using a simplified methodology based on conceptual modelling and geological data. The methodology is outlined in detail in Liakka et al. (2024) and builds upon previous work in Lord et al. (2019). Despite its simplicity, the methodology is designed to effectively capture identified uncertainties in anthropogenic emissions and future climate evolution.

Methodology

The conceptual global model (CGM; see Section 3.5.3 and Lord et al. 2019) is used for this exercise. The primary forcing for the model is the northern hemisphere high-latitude summer insolation, here defined as the average between June 21 and July 20 at 65°N (Laskar et al. 2004). The model calculates the normalised global ice volume, v, based on changes in insolation, with $v=0$ representing the global ice volume at present day, and $v=1$ the global ice volume at LGM. The model contains eight tunable parameters (Table 3-1 in Lord et al. 2019). One of these parameters, the critical insolation threshold (i_0), determines transitions from an interglacial to a glacial state and is set to depend on anthropogenic CO_2 perturbations in the atmosphere, according to the methodology described by Archer and Ganopolski (2005). The CGM yields projected changes in the *global-mean* climate. Periods of *local* ice coverage at Forsmark based on these projections are estimated using a multistep approach summarised below. For a more detailed description, please refer to Lord et al. (2019) and Liakka et al. (2024).

First, the CGM is calibrated against historical observational data of global climate change, here represented by deep-ocean $\delta^{18}O$ data (Figure 2-1a). To this end, 1000 simulations are performed with the CGM using different parameter combinations, and only those that exhibit a good agreement with the past 500 kyr of the $\delta^{18}O$ data are retained. This resulted in 90 of the 1000 simulations being retained, shown in Figure 4-10. To enable straightforward comparison between the simulated and observed global climate, both datasets are converted to global- and annual-mean SAT change (ΔT) using linear scaling.

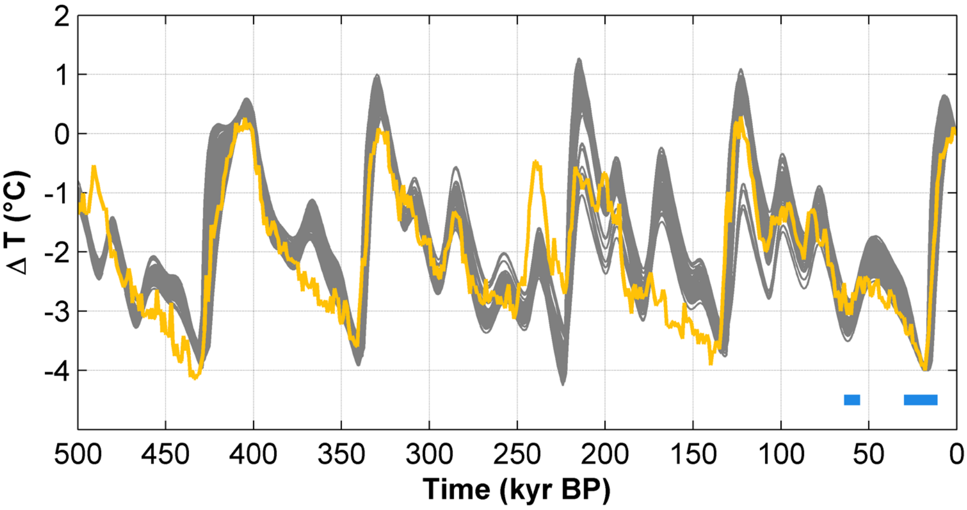

__Figure 4-10.__ Time series of the global-mean surface air temperature change (ΔT). Grey lines depict ΔT from 90 calibrated simulations using the CGM, and the orange line shows reconstructed ΔT from δ18O data (Lisiecki and Raymo 2005; see also Figure 2-1). Blue horizontal lines indicate reconstructed periods of ice coverage in Forsmark during the last glacial cycle (Figure 4-8).

The 90 calibrated model configurations are thereafter integrated 1 Myr into the future using predicted changes in summer insolation and anthropogenic CO_2 as input (Figure 2-4). Four scenarios of carbon emissions are considered, encompassing a natural scenario with zero anthropogenic emissions as well as three scenarios corresponding to low (400 Pg C), medium (1500 Pg C) and high (5500 Pg C) cumulative anthropogenic emissions (relative to pre-industrial). The resulting atmospheric CO_2 concentrations over the next 1 Myr from these emissions scenarios are depicted in Figure 2-4c. The projected global mean SAT change for each emissions scenario over the next 1 Myr is shown in Figure 4-11.

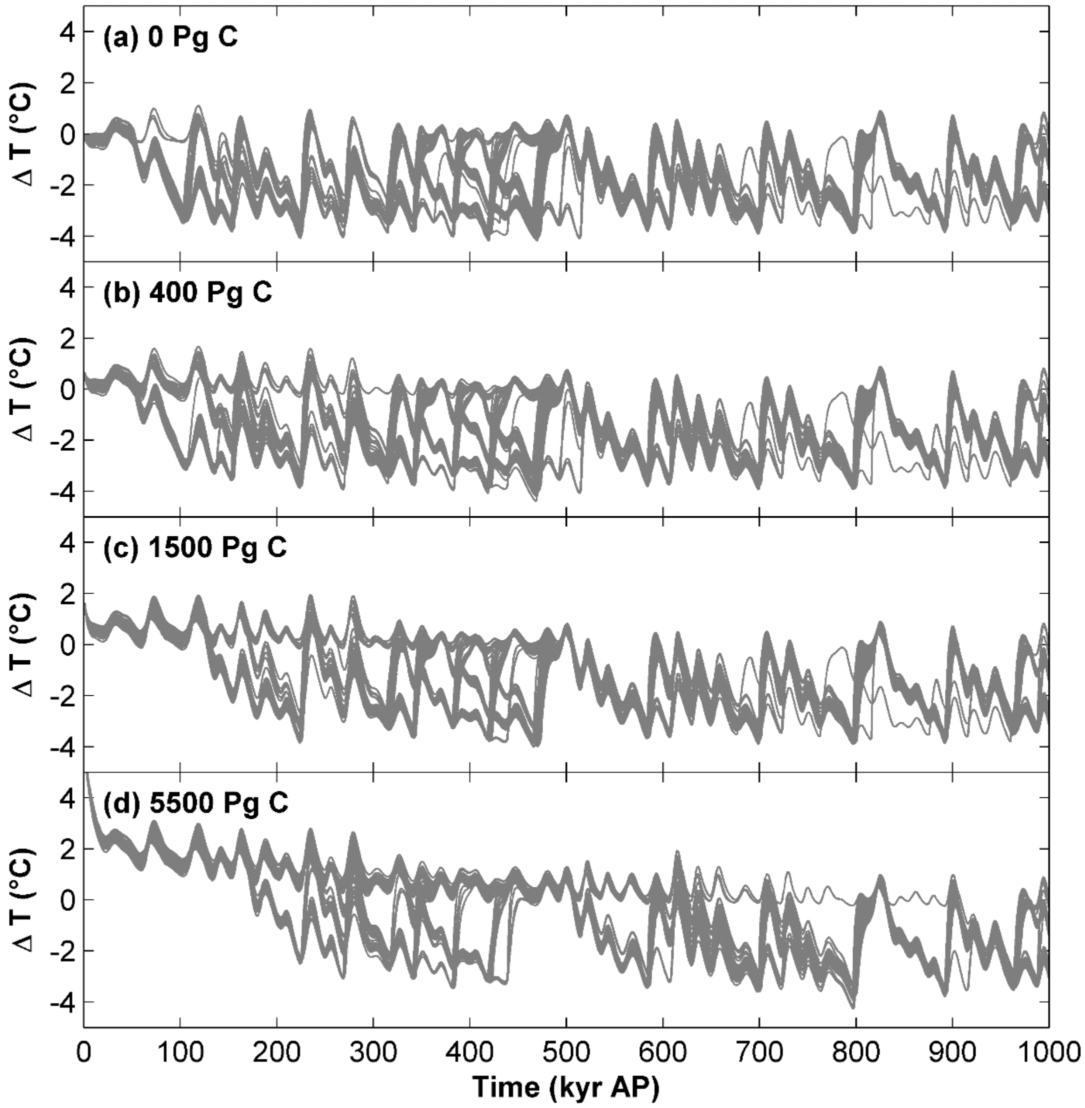

Figure 4-11. *Projected ΔT over the next 1 Myr for (a) 0 Pg C, (b) 400 Pg C, (c) 1500 Pg C and (d) 5500 Pg C emissions scenarios for each of the 90 calibrated configurations of the CGM.*

Next, potential periods of ice coverage in Forsmark are estimated from the simulated global-mean ΔT in Figure 4-11. The underlying assumption is that the lower the ΔT, the more extensive were the glaciations, and the higher was the probability that also Forsmark was covered by an ice sheet. Thus, if the climate becomes gradually colder, ΔT will at some point cross a threshold, $\Delta T_{threshold}$, at which point a glaciation can be considered to be extensive enough such that the ice sheet also covers the Forsmark site. To determine potential values of $\Delta T_{threshold}$, for Forsmark, reconstructed timings of ice coverage during the Weichselian glaciation are used. This reconstruction shows that Forsmark experienced two periods of ice coverage during the last 120 kyr. These periods coincide closely with minima in ΔT (Figure 4-10), indicating that there is a high correlation between the global-mean ΔT and Eurasian ice-sheet extent.

To constrain $\Delta T_{threshold}$, we first examine how many of the 90 simulations successfully project two periods of ice coverage in Forsmark over last 120 kyr, consistent with the Weichselian reconstruction, for different values of this threshold. In this exercise, glaciation is assumed to occur when ΔT drops below $\Delta T_{threshold}$. The results show that for only one of the investigated thresholds, namely $\Delta T_{threshold} = -2.8$ °C, are both periods of glaciation successfully projected in all 90 simulations (Figure 4-12). This value is therefore chosen as a *best-estimate* $\Delta T_{threshold}$ for Forsmark glaciation.

Since the method for calculating the best-estimate $\Delta T_{\text{threshold}}$ is based on the reconstructed Weichselian ice coverage, the projected future regional ice-sheet extents using this threshold will similarly resemble that of the Weichselian. However, geological records indicate that this is not necessarily the case. For instance, the Eurasian ice sheet during the Saalian glacial cycle was likely significantly larger than during the Weichselian, despite exhibiting similar changes in global ice volume (Section 4.3). To address this uncertainty, a wider range of $\Delta T_{\text{threshold}}$ is adopted here in addition to the best estimate. This range is defined to be roughly compatible with the conditions of the Weichselian, while also allowing for a wide variety of alternative ice-sheet developments. Specifically, the range encompasses all values of $\Delta T_{\text{threshold}}$ that meet the following two criteria; (i) at least one of the 90 simulations must project two periods of glaciation during the Weichselian, and (ii) the projected glacial periods must, at least marginally, overlap with the corresponding periods in the Forsmark Weichselian ice-sheet reconstruction. The latter criterium is evaluated by measuring the average root mean square error (RMSE) of the projected timings of glacial periods across the 90 simulations with respect to those of the reconstruction. An overlap between projected and reconstructed glacial periods is only deemed possible if the RMSE is lower than the maximum duration of ice coverage in the reconstruction (19 kyr). Using these two criteria, the *lowest* potential $\Delta T_{\text{threshold}}$ is –3.5 °C, as no simulations yield two glaciations in Forsmark for lower values, and the *highest* potential $\Delta T_{\text{threshold}}$ is –2.1 °C, as the RMSE exceeds 19 kyr for higher values of $\Delta T_{\text{threshold}}$ (Figure 4-12).

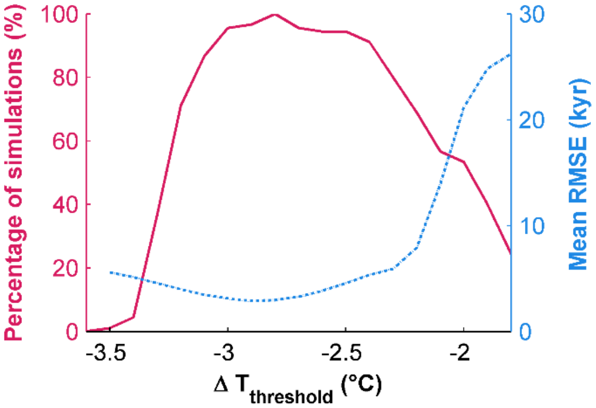

Figure 4-12. *Percentage of simulations across the 90 calibrated model configurations that project two periods of glaciation in Forsmark during the last 120 kyr (red solid line), along with the average RMSE of projected glaciation/deglaciation timings compared to the ice-sheet reconstruction (blue dashed line).*

Results

Future ice-sheet variability in Forsmark is here represented by the following four quantities, all of which are relevant for post-closure safety (Sections 3.1.2 and 4.1.2);

1. Timing of the next glaciation (t_{glac}): defined as the first future occurrence when projected ΔT drops below $\Delta T_{\text{threshold}}$.
2. Number of glaciations (n_{glac}): defined as the number of times projected ΔT drops below $\Delta T_{\text{threshold}}$.
3. Maximum duration of an individual glaciation ($d_{\text{glac,ind}}$): defined as the longest uninterrupted period during which ΔT remains below $\Delta T_{\text{threshold}}$.
4. Total duration of glaciations ($d_{glac,\text{tot}}$): defined as the total time during which ΔT is below $\Delta T_{\text{threshold}}$.

Best-estimate $\Delta T_{threshold}$

Projections of ice-sheet variability over the next 1 Myr in Forsmark, using the best-estimate $\Delta T_{threshold}$ (–2.8 °C, see above) are presented in Table 4-3 for each considered emissions scenario. The values outside the brackets represent the median, while those inside the brackets show the 5th to 95th percentile ranges of t_{glac}, n_{glac}, $d_{glac,ind}$, and $d_{glac,tot}$ across the 90 simulations. The table also features a reference scenario which assumes that all future glaciations are identical to those of the reconstructed Weichselian. In this scenario, it is thus assumed that the conditions of the last 120 kyr, including the two periods of glaciation, are repeated from the present day until 1 Myr into the future. A repetition of the conditions reconstructed for the last glacial cycle over the coming 1 Myr is also an assumption used in previous safety assessments for the spent fuel repository (e.g. SKB TR-23-01, Chapter 2).

Table 4-3. Projected t_{glac}, n_{glac}, $d_{glac,ind}$ and $d_{glac,tot}$ in Forsmark over the next 1 Myr, calculated using the best-estimate threshold for glaciation ($\Delta T_{threshold}$ = –2.8 °C). The values outside the brackets show the median projection across the 90 simulations, whereas the values inside the brackets represent the 5th–95th percentile range of the simulations. For reference, corresponding projections for a reference scenario where the Weichselian glacial cycle (last 120 kyr) is repeated 1 Myr into the future are also shown

	Emissions scenario (Pg C)	t_{glac} (kyr)	n_{glac} (-)	$d_{glac,ind}$ (kyr)	$d_{glac,tot}$ (kyr)
Repetition of last glacial cycle until 1 Myr AP	n.a.	56	16	28	224
Projections with $\Delta T_{threshold}$ = –2.8 °C	0	99 [95–101]	17 [14–19]	29 [13–53]	222 [150–289]
	400	103 [101–223]	16 [12–19]	27 [13–52]	191 [124–264]
	1500	216 [178–558]	14 [9–17]	22 [12–33]	154 [92–220]
	5500	486 [266–699]	8 [6–10]	15 [9–24]	84 [53–116]

For the 0 Pg C scenario, the median projections for n_{glac}, $d_{glac,ind}$, and $d_{glac,tot}$ are very similar to the scenario of repeating the Weichselian over the next 1 Myr (Table 4-3). This similarity is anticipated, given that the best-estimate $\Delta T_{threshold}$ has been derived from the reconstructed conditions of the Weichselian. However, for the timing of the onset of the next glaciation at the site (t_{glac}), projections indicate a delay of approximately 45 kyr when compared to the onset of the first glaciation when repeating the Weichselian glacial cycle. This delay of the onset of the next glacial cycle is a consistent feature found across several modelling projections (Section 3.5.3), and is attributed to the next 50 kyr being characterised by relatively low summer-insolation variability (Figure 2-4b).

Consistent with other modelling studies (Section 3.5.3), anthropogenic emissions are found to further delay the onset of the next glacial inception, and consequently, the timing of the next glaciation in Forsmark. This is evident from the significant increase in the projected t_{glac} values with higher emissions (Table 4-3). The delay is most pronounced under the 1500 and 5500 Pg C emissions scenarios, where the next glaciation in Forsmark is projected to occur after 200 kyr and 400 kyr, respectively, in most simulations. Under the 400 Pg C scenario, anthropogenic emissions are relatively small – even lower than the total emitted to date (~700 Pg C, see Section 2.5.1) – so ΔT remains similar to that in the 0 Pg C scenarios. Consequently, in most simulations, the timing of the next glaciation under the 400 Pg C scenario is the same as in the 0 Pg C scenario. However, even under the 400 Pg C scenario, a few simulations project that an ice sheet will not return to Forsmark for at least 200 kyr (Table 4-3). This suggests that carbon emissions released by humans to date may have already contributed to a delay of the next glaciation in Forsmark.

The delayed onset of the next glaciation due to anthropogenic emissions leads to an anticipated reduction of n_{glac} and $d_{glac,tot}$ (Table 4-3). Perhaps more surprisingly, this trend is also observed for $d_{glac,ind}$, which is notably reduced under the 1500 and 5500 Pg C scenarios (Table 4-3). This decline occurs because the longest individual glaciations typically take place between 300 and 500 kyr AP, when insolation variations are relatively small (Figure 2-4b). Thus, during this period, the duration of individual glaciations becomes more sensitive to the prevailing atmospheric CO_2.

Sensitivity to $\Delta T_{threshold}$

Next, the effect of the uncertainty in $\Delta T_{threshold}$ on the future glacial variability is examined. Figure 4-13 shows the projected t_{glac}, n_{glac}, $d_{glac,ind}$, and $d_{glac,tot}$ as a function of potential $\Delta T_{threshold}$ values, which range from –3.5 °C to –2.1 °C (see above). The results are presented for both extreme emission scenarios, 0 and 5500 Pg C, to identify the most extreme potential cases of future glaciations, or lack thereof, at the Forsmark site.

For the 0 Pg C scenario, we found that t_{glac} is not sensitive to the value of $\Delta T_{threshold}$. Except for very low values of $\Delta T_{threshold}$, n_{glac} also shows little change. This suggests that variations in the regional ice-sheet distribution during future glacial cycles, in absence of anthropogenic emissions, are not of critical importance for the timing of the first glaciation or the frequency of glaciations in Forsmark. However, unlike t_{glac} and n_{glac}, the projected durations ($d_{glac,ind}$, and $d_{glac,tot}$) increase notably with $\Delta T_{threshold}$ in the 0 Pg C scenario. In the most extreme case, with the highest identified values of $\Delta T_{threshold}$, projections of $d_{glac,ind}$, and $d_{glac,tot}$ reach almost 70 kyr and 500 kyr, respectively (Figure 4-13).

In stark contrast to the largely glaciation dominated futures featured in the 0 Pg C scenario, the results under the 5500 Pg C scenario suggest that anthropogenic emissions could lead to mostly ice-free conditions in Forsmark over the next 1 Myr. This possibility persists regardless of $\Delta T_{threshold}$, as shown by the 95th percentile projection of t_{glac}, which remains around 700–800 kyr for all investigated values of $\Delta T_{threshold}$ (Figure 4-13).

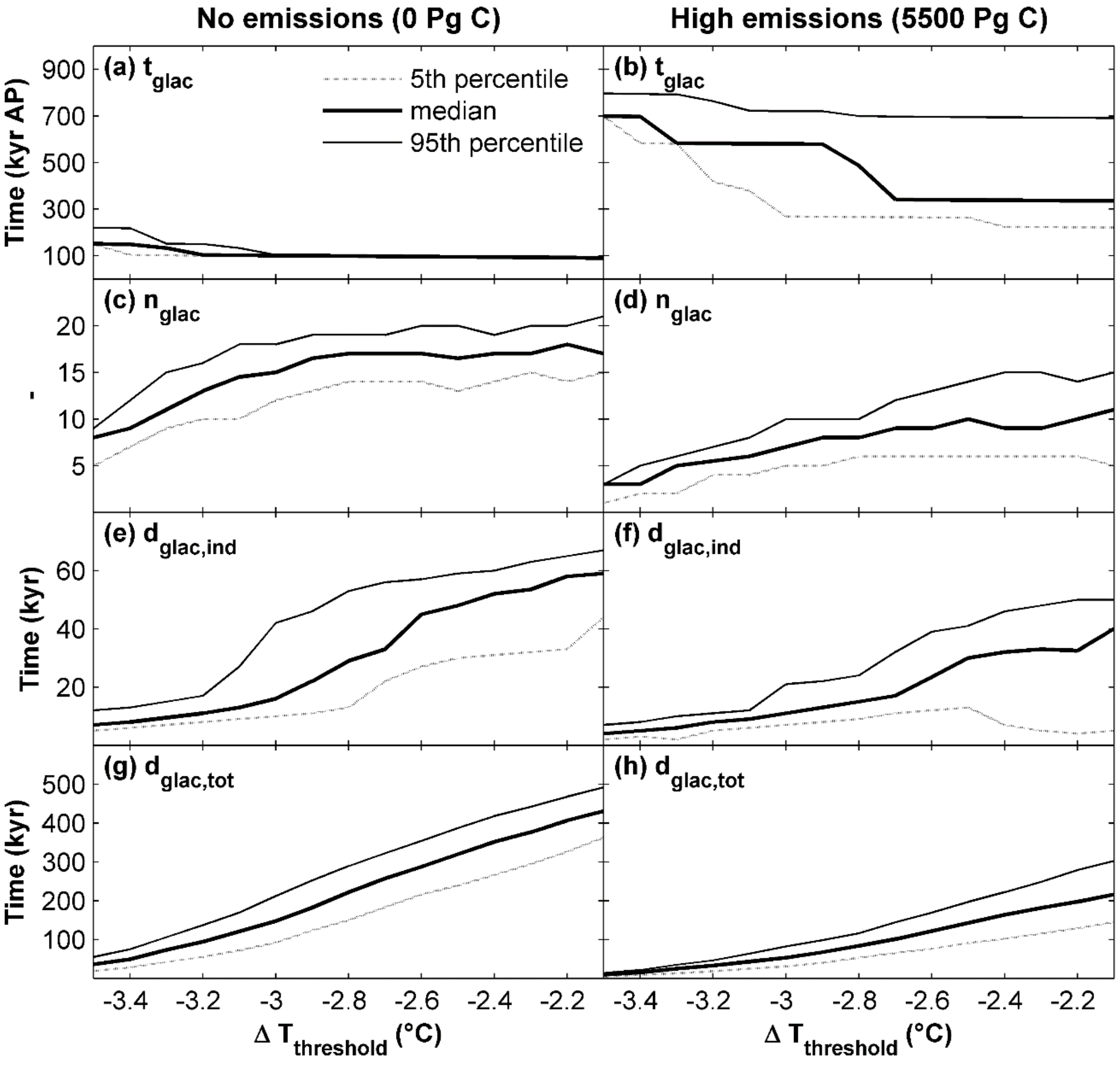

Figure 4-13. *Projected t_{glac} (a,b), n_{glac} (c,d), $d_{glac,ind}$ (e,f) and $d_{glac,tot}$ (g,h) for Forsmark over the next 1 Myr as a function of $\Delta T_{threshold}$. The results are shown for the 0 (left panels) and 5500 Pg C scenarios (right panels), with median projections (thick solid line) and 5th (dashed thin line) and 95th (thin solid line) percentiles across the 90 simulations.*

Conclusions

Following the methodology outlined in Lord et al. (2019) and Liakka et al. (2024), the frequency and duration of ice coverage in Forsmark has been projected for the next 1 Myr. A major advantage of the methodology is that it accounts for uncertainties in both future climate evolution and anthropogenic emissions without requiring time- and resource-intensive modelling, such as simulations with coupled ice sheet-climate models. Conversely, a major limitation with our results is they mirror glacial cycles used for calibration. In our case, the model was calibrated with data covering the last 500 kyr, a period dominated by glacial-interglacial cycles with a characteristic timescale of 100 kyr. Though unlikely, the possibility that future glaciations may exhibit different variability compared to the last few glacial cycles cannot be excluded. For a comprehensive discussion about the limitations, see Liakka et al. (2024).

The analysis provided here leads to the following conclusions regarding future glacial variability in Forsmark, which are relevant for post-closure safety of the spent fuel repository.

- Even if considering all identified climate-system uncertainties, none of the simulations under the scenario with similar-to-present cumulative CO_2 emissions (400 Pg C) yield glaciation in Forsmark before 100 kyr AP. This supports the notion that glaciation in Forsmark within the next 100 kyr is an unlikely event, as argued in Section 3.6.1. Some simulations under this scenario also project that an ice sheet will not return to Forsmark for at least 200 kyr. Thus, it cannot be excluded that carbon emissions released by humans to date may have already considerably delayed the next glaciation in Forsmark.
- Under the 1500 Pg C scenario, which can be considered a likely scenario given current climate policies (Section 2.6.1), the results indicate that the next glaciation in Forsmark will not occur for at least 200 kyr, and possibly even several hundred thousand years longer than this depending on the extent by which remaining anthropogenic CO_2 inhibits the next glacial inception. Thus, the frequency and duration of glaciations in Forsmark over the next 1 Myr will likely be lower compared to the case of repeating the conditions of the Weichselian glacial cycle for 1 Myr into the future.
- Considering the full range of uncertainties in anthropogenic emissions and future climate evolution reveals a wide spectrum of possible outcomes, some of which diverge significantly from the likely scenario depicted above. At the extremes of this uncertainty range, the Forsmark site could experience ice coverage for nearly half of the next 1 Myr or remain almost completely ice-free throughout this entire period. Both of these extremes are judged to have a low likelihood of occurrence. This is particularly true for the case with glaciations for nearly 500 kyr, as it assumes that *all* future glaciations will be associated with a considerably more extensive ice-sheet development in Eurasia compared to that of the Weichselian glacial cycle.
- In Chapter 8, examples of likely evolutions ($\Delta T_{threshold} = -2.8$ °C combined with 400 Pg C and 1500 Pg C) of glacial conditions in Forsmark over the next 1 Myr are illustrated as evolutions of climate domains (Section 1.2.3). The same chapter also presents examples of extreme developments of glacial conditions over the next 1 Myr ($\Delta T_{threshold} = -2.1$ °C combined with 0 Pg C).

4.6 Safety assessment-specific information

4.6.1 Ice-sheet profiles

Ice-sheet profiles, together with gradients in bedrock topography, are important for understanding how groundwater flow and the bedrock stress field are affected during glaciations. In Forsmark, bedrock-topography gradients are generally low, meaning that the overall topographic gradients during glaciations are mainly controlled by the profile of the overlying ice sheet.

The surface steepness of an ice sheet is determined by the interplay of several factors, including basal shear stresses, ice temperatures, temperatures at the ice-sheet bed, basal hydrological conditions, and the presence or absence of deformable sediments at the bed. In general, warm basal conditions, which include the presence of basal water and deformable bed sediments, lead to a gentler ice-sheet profile compared to cold-based conditions.

In the present work, the minimum and maximum ice-sheet slopes are the same as used in the PSAR for the spent fuel repository (SKB TR-20-12, Appendix B) and SFR (SKB TR-23-05, Appendix E). In these PSAR reports, various ice-sheet profiles were examined using both theoretical considerations and numerical ice-sheet modelling. Based on these investigations, two extreme profiles were selected for the safety assessments, summarised below. For information on the intermediate profiles, please refer to SKB (TR-20-12, Appendix B) or SFR (SKB TR-23-05, Appendix E).

Theoretical profiles, which omit processes that would otherwise reduce the steepness of the ice surface, are considered to represent the maximum possible steepness for a given ice-sheet size. The profile used for that purpose is described by the following equation:

$$(h(x)/H)^{2+2/n} + (x/L)^{1+1/n} = 1, \qquad \text{Equation 4-3}$$

where h is the ice thickness at distance x from the centre, H the ice-sheet thickness at the centre, and n is the flow parameter (the strain-rate exponent) in Glen's flow law (Section 4.2.2). Following the PSAR reports, using $L = 400$ km, $H = 3000$ m and $n = 3$, this profile is considered to represent the maximum ice-sheet steepness also in the present work (Figure 4-14).

A minimum steepness estimate was in the PSAR derived from the retreating phase of the Weichselian ice sheet numerical reconstruction (see SKB TR-20-12, Appendix B for details). This approach is reasonable because, according to theory, ice sheet slopes are generally less steep during the retreating phase of a glacial cycle compared to the advancing phase. The steepness of the slope of the retreating Weichselian ice sheet, i.e. the resulting steepness of this profile, is considerably smaller than the theoretical counterpart (Figure 4-14).

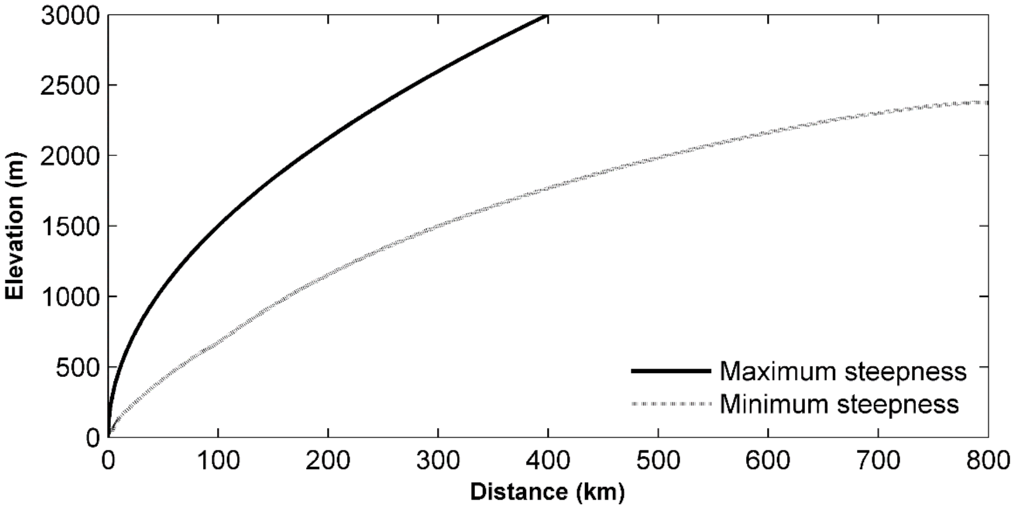

Figure 4-14. *Ice-sheet slopes representing minimum and maximum ice-sheet profile steepness selected for the present assessment.*

4.6.2 Characteristic timescales of ice sheet growth and retreat

This section describes the characteristic timescales for transitioning to and from glacial conditions at the Forsmark site. When considering only a repository footprint area, the timescales for ice-sheet growth and retreat can be described as nearly instantaneous. However, on a site-scale, encompassing several hundred square km, the transition to and from glacial conditions occurs gradually, both spatially and temporally.

Examples of the typical timescales of ice-sheet growth and retreat can be deduced from the Weichselian reconstruction (Section 4.3.1). In this reconstruction, ice-sheet advance in the Forsmark area occurs in a landscape dominated by permafrost (see Section 6.3 for more details), and ice-sheet retreat is followed by an extended period during which the area is submerged beneath the sea (Section 5.3). These overall landscape changes are likely to recur with future glaciations of the area, although variations in ice-sheet development patterns are likely. This includes the potential for temporary halts, or stillstands, of the ice-sheet margin over the repository area discussed further below. Additionally, the extent of permafrost before glaciation and the submerged conditions after glaciation are uncertain. Nonetheless, the last glacial cycle may be considered a typical glaciation for the area, so the characteristic timescales of ice-sheet advance and retreat inferred from this reconstruction are considered to represent typical values.

The transition to glacial conditions at the site is generally marked by a slow southward migration of the ice-sheet margin. In the Weichselian reconstruction, the ice-sheet margin advances over the site at a rate of approximately 50 m yr^{-1}. The duration of this transition, i.e. the time it takes for the ice sheet to advance over the Forsmark site, is around 250 years.

The transition from glacial to temperate (and most likely submerged) conditions constitutes the deglaciation phase, which is typically faster than the corresponding rate of ice-sheet advance (Section 4.3). In the Weichselian reconstruction, the retreat rate of the ice sheet margin during deglaciation of the Forsmark site is ~ 300 m a^{-1}. The duration of this transition, i.e. the time during which a deglaciation occurs over the Forsmark site in the reconstruction of the last glacial cycle, is around 50 years.

In summary, characteristic timescales of ice-sheet advance and retreat over the Forsmark site is estimated to be approximately 250 and 50 years, respectively. Future glaciations in Forsmark are likely to be characterised by similar advance and retreat durations as these estimates. Only in the unlikely situation of temporary halts of the ice-sheet margin may the durations be significantly longer. The probability of achieving such stillstands over the Forsmark site, and the duration of these, is discussed in the following.

Ice-marginal stillstands

Ice-marginal stillstands are of importance because groundwater flow becomes notably elevated beneath the ice-sheet margin if thawed conditions prevail in that section of bedrock (Section 4.1.2). According to the modelling of Vidstrand et al. (2010), there is an approximately one-kilometer-wide zone of high groundwater fluxes in front of the ice-sheet margin and a similarly wide zone of increased flux behind the margin. This results in an approximately two-kilometer-wide influence area with significantly increased groundwater flow when there is no permafrost at the Forsmark site. If continuous permafrost is present, which is likely during advancing phases of future glaciations in Forsmark, the zone of increased groundwater flow is significantly less pronounced, or non-existent (Vidstrand et al. 2010).

Assessment in the PSAR

In the PSAR, estimates of the longest potential stillstands were based on Quaternary geological information (SKB TR-20-12, Sections 4.2.2 and 4.5.1), particularly from several studies that inferred stillstands from geological observations during the deglaciation phase of the Weichselian ice sheet (e.g., Lundqvist and Wohlfarth 2000, Fredén 2002, Houmark-Nielsen and Kjær 2003, Lunkka et al. 2004). Focusing on deglaciation is reasonable, as no moraines indicative of temporary halts have been discovered from the growth phases of the Eurasian ice sheet. While stillstands might have occurred during growth phases, any resulting moraines would likely have been erased by the subsequent ice coverage. Moreover, stillstands during the growth phase of an ice sheet are more likely to be associated with frozen bedrock conditions, as climate conditions during this phase are typically much colder than during deglaciation. Consequently, a potential stillstand under such frozen conditions would have less impact on groundwater flow in the bedrock compared to the typically thawed bedrock conditions prevailing during deglaciation.

According to the studies mentioned above and other studies, the most significant halt during the Weichselian deglaciation occurred during the cold Younger Dryas stadial (between 12.9 and 11.7 kyr BP), when ice-marginal stillstands in Sweden and elsewhere in Fennoscandia lasted up to approximately 900 years (Fredén 2002). However, the ice-sheet margin was not necessarily stable during this period. For instance, the zone of ice-marginal deposits from the Younger Dryas is typically around 20–25 km wide in central and eastern Sweden (Fredén 2002). Despite this, the maximum possible duration of a stillstand within a 2-km wide zone affected by enhanced groundwater flows was pessimistically set to 1000 years in the PSAR. Pessimistically assuming that one such major stillstand occurs per deglaciation of the future ice sheet in the area, the probability of a 1000-year long stillstand in Forsmark was estimated to be 0.0008 (2 km / 2500 km), based on the assumption that a stillstand is equally likely to occur anywhere along a 2500-km transect between northern Germany/Poland and the Scandinavian mountain range (SKB TR-20-12, Section 4.5.1).

Assessment in the present work

Since the preparation of the PSAR climate report (SKB TR-20-12), new studies have emerged regarding the presence of ice-marginal stillstands during the last deglaciation, both in Eurasia (Patton et al. 2017, Tylmann et al. 2022) and North America (Darvill et al. 2018, Young et al. 2020). The overall conclusions from these studies support the findings in the PSAR, indicating that the longest potential stillstand during deglaciation is approximately 1000 years.

Another possibility, not examined in the studies mentioned above, is the potential for a stillstand over Forsmark when the ice-sheet margin reaches its maximum southward position during a glaciation. During the Weichselian and Saalian glaciations, the southernmost position of the ice-sheet margin was located well south of Forsmark (Figures 4-3 and 4-4). However, during a future glaciation, it cannot be excluded that the ice-sheet margin could reach its maximum extent directly over the repository area. To estimate the maximum possible duration of such an unlikely stillstand, we use a conceptual model that incorporates the lag effect of an ice sheet through a linear response equation (Appendix B1).

Figure 4-15 shows the temporal evolution of a sinusoidal forcing (Equation A-3) of the conceptual model using a period, T = 40 kyr and an amplitude of E_A = 500 km, along with the resulting changes in the ice-sheet extent. T = 40 kyr corresponds approximately to the period of the obliquity Milankovitch component (Section 2.2.1). This is considered to be a pessimistic choice, because potential migrations of the ice-sheet margin due to variations of the shorter precession component (~20 kyr, see Section 2.2.1), which would arguably lead to shorter stillstands, are omitted. In addition to T, however, the maximum stillstand duration also depends on the climate forcing amplitude, E_A, as a higher forcing amplitude leads to higher ice-sheet migration rates. This is demonstrated in Figure 4-16, which shows the maximum stillstand duration as a function of the maximum ice-sheet extent, calculated using different values of E_A. The figure indicates that only for very low maximum extents (corresponding to E_A around 100 km) are the stillstands considerably longer than 1000 years. Apart from this, the maximum stillstands projected by the conceptual model are about 1000 years or less. For a realistic ice sheet reaching the Forsmark site from northern Fennoscandia, the ice-sheet extent would be about 800 km, resulting in stillstands just slightly exceeding 1000 years (Figure 4-16).

It is important to emphasise that the simplicity of this model more likely leads to an overestimation rather than an underestimation of stillstand durations. For instance, besides disregarding higher-frequency Milankovitch cycles (~20 kyr), the model does not consider internal climate variability or interactions between the ice sheets and the lithosphere. These factors would naturally lead to higher frequency fluctuations of the ice margin compared to that of the conceptual model. Therefore, the actual stillstand duration for an ice sheet reaching its maximum extent at the Forsmark site would likely be considerably shorter than the 1000 years predicted by the model. Nonetheless, similar to the stillstands during the deglaciation phase, 1000 years can be regarded as an upper limit for potential stillstand duration of a future ice sheet reaching its maximum extent over Forsmark.

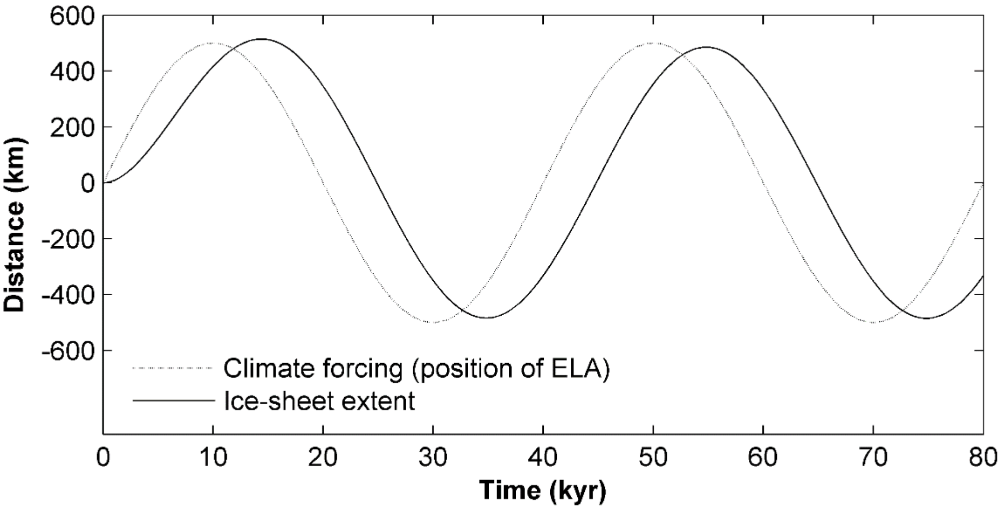

Figure 4-15. *Position of ELA (Equation 4-6) and resulting ice-sheet extent as calculated with the linear response equation (Equation 4-4) using* T *= 40 kyr,* $E_A = 500$ *km and* τ*= 6000 years.*

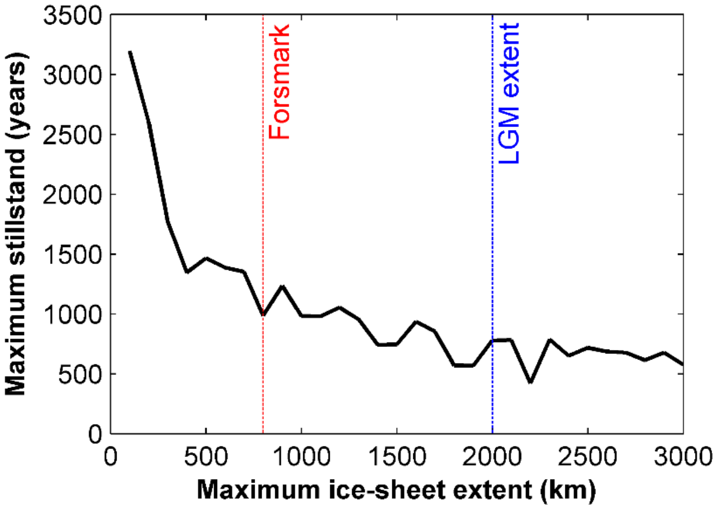

Figure 4-16. *Projected maximum stillstand duration using the linear response model (Equation A-1) as a function of the maximum ice-sheet extent (distance from northern to southern margin), calculated using climate-forcing amplitudes ranging from* E_A*=50 to 1500 km.*

5 Relative sea-level change

5.1 Introduction

5.1.1 Definitions

Relative sea level (RSL) is defined as the vertical position of the sea surface relative to the seafloor or to a land reference point along the shoreline. It is controlled by changes in the absolute sea level[13] (ASL) and vertical movement of the land surface. In the Forsmark region, the vertical movement of the land surface is presently manifested by an isostatic uplift following the last glaciation. Changes in RSL result in horizontal shoreline displacement; a rise in RSL leads to an inland migration of the shoreline (transgression), while a fall in RSL leads to a migration of the shoreline towards the sea (regression).

Forsmark is located along the coast of the southernmost part of the Gulf of Bothnia which constitutes an integral part of the Baltic Sea. In this chapter, the sea outside of Forsmark is consistently referred to as the Baltic Sea unless there are specific reasons to highlight Gulf of Bothnia in relation to other parts of the Baltic Sea.

Changes in RSL determine future timings and lengths of periods when areas above SKB's repositories will be covered by land or sea, respectively, in the future. The situation when the area above the repositories is covered by the sea is referred to as *submerged* conditions (Section 1.2.3). The situation when the area above the repositories is land is referred to as *terrestrial* conditions.

5.1.2 Importance for post-closure and operational safety for SKB's repositories

Future RSL changes at Forsmark are important for post-closure and operational safety for SKB's repositories at Forsmark. The main effects of future RSL changes on post-closure safety are associated with groundwater flow. Due to smaller hydraulic gradients, the magnitude of the groundwater flow in the bedrock surrounding the repositories is typically much lower during periods of submerged conditions than during periods of terrestrial conditions. Further, changes in the groundwater chemical composition may occur as a result of transitions between submerged and terrestrial conditions. These changes may influence processes that effect barrier properties, such as leaching of concrete barriers and mineral transformations in bentonite barriers in SFR (e.g. SKB TR-23-01, Section 6.2.9), as well as buffer erosion and canister corrosion in the spent fuel repository (e.g. SKB TR-21-01). Submerged conditions also result in less effective transport of repository-derived radionuclides to the surface (e.g. SKB TR-23-01, Section 7.4.5). Furthermore, shoreline migration and landscape development associated with the RSL changes, affect transport pathways from the repository to the surface systems and thus, which areas in the landscape that can receive discharge of repository radionuclides. Results from previous safety assessments have shown that the highest exposure to radionuclides originating from the repositories results from cultivation and well-water usage (e.g. SKB TR-23-06, Section 9.3). Under submerged conditions, discharge areas for radionuclides from the repositories are covered by the sea. The productivity of sea ecosystems is low compared to agricultural ecosystems, and the dilution due to exchange of water between sea basins is relatively large. Thus, doses to humans are typically several orders of magnitude lower during submerged than terrestrial conditions.

SFR is located below the sea today, and the majority of the radioactivity in SFR decays within the millennia after repository closure. Thus, future RSL evolution, and associated transition from submerged to terrestrial conditions above SFR, constitutes a key question. In the latest safety assessment for SFR (PSAR), it was demonstrated that the resulting dose to humans gradually decreases with the duration of submerged conditions above SFR, such that the total dose for a duration of 10 000 years is half that for a duration of 1000 years (SKB TR-23-09, Section 5.8.1).

---

[13] In previous SKB reports (e.g. SKB TR-20-12 and SKB TR-23-05), "absolute sea level" is often referred to as "eustasy" – a term commonly used in geology, but less frequent in contemporary studies about historical, present and future sea-level change cited in this chapter. Thus, for consistency with those studies, absolute sea level is used throughout this chapter instead of eustasy.

Another key question, for both SFR and spent fuel repository, concerns the duration of submerged conditions following future glaciations. In previous safety assessments, historical RSL changes in response to past glaciations have been used as basis when estimating the duration of submerged conditions following future glaciations at Forsmark (see e.g. SKB TR-23-09, Section 7.2).

In addition to the longer timescales relevant for post-closure safety, possible changes in RSL within this century are relevant for the operational periods of SKB's planned and existing facilities at Forsmark. In this context, estimates of the maximum ASL during storms (i.e. *sea-level extremes*), on top of the potential future rise of mean ASL, are particularly interesting as these define an upper bound of adaptation measures needed to protect the facilities until repository closure. Previous analyses for the spent fuel repository[14] and SFR[15] concluded that the most critical parts of the repositories need to be protected against future sea-level extremes about 4 m higher than the present-day mean ASL.

Within century variations in RSL are also considered in post-closure safety assessments in order to determine when drilling a drinking-water well is feasible (SKB TR-23-06, Section 5.5). A prerequisite for drilling or digging a well is not only that the area is terrestrial, but also that the capture zone of the well is not affected by frequent episodes of salt water intrusions from surface water. In previous safety assessments, the threshold for extracting drinking water from a well (1 m above the mean sea level) was determined from the highest daily average RSL recorded in the Forsmark tide-gauge data (Grolander 2013, Werner et al. 2014).

5.1.3 Previous documentation

SKB has provided several compilations of the current state of knowledge with regard to historical, present and possible future RSL changes at Forsmark, the most recent of which are summarised in the climate reports in support of the PSAR safety assessments for the spent fuel repository (SKB TR-20-12, Sections 3.3, 5.1.3 and 5.2.3) and SFR (SKB TR-23-05, Sections 2.2 and 3.5). Abundant information in those reports, especially that concerning the historical RSL, was adopted from previous safety assessment climate reports (e.g. SKB TR-10-49, Section 3.3 and SKB-13-05, Section 2.2), which in turn were based on results from supporting SKB reports (e.g. Påsse 2001, Brydsten 2009, Whitehouse 2009 and Pellikka et al. 2020) and numerous scientific publications.

In this chapter, new data and literature that has been published since the last RSL compilation (SKB TR-20-12 and SKB TR-23-05) are evaluated. In particular, this concerns information and ASL projections given in the IPCC AR6 (Fox-Kemper et al. 2021). Furthermore, this chapter includes a thorough review of processes that may affect the RSL in the Baltic Sea and in the Forsmark area; such complete review was not included in previous climate reports. Other information about RSL that was compiled in previous SKB documents will only be briefly summarised in this chapter.

5.2 Controlling variables and conditions

The Baltic Sea is a semi-enclosed basin with a narrow connection to the North Sea through the Danish straits. With an area of about 420 000 km^2 (Jakobsson et al. 2019), the Baltic Sea is among the largest brackish surface water bodies in the world. The brackish nature of the Baltic Sea is maintained by the combination of freshwater inflow from rivers in primarily the northern parts of the basin and an inflow of saline water from the adjacent North Sea. This results in a relatively large spatial salinity gradient across the basin with surface salinities ranging from 1–2 psu (practical salinity units, equal to parts per thousand) in the northern parts to 32 psu in the adjacent Kattegat (Gräwe et al. 2019).

The RSL in the Baltic Sea is controlled by several processes, summarised in Figure 5-1. These processes act on widely different spatial and temporal scales. While some of the processes are constrained to the Baltic Sea and operate on characteristic timescales of seconds to minutes, others are of global character and operate over centennial to millennial timescales.

---

[14] SKBdoc 1716621 ver 1.0. (Internal document, in Swedish.)

[15] SKBdoc 1860136 ver 1.0. (Internal document, in Swedish.)

Owing to a limited transport capacity across the Danish straits, the mean sea level in the Baltic Sea is typically governed by processes acting on timescales longer than a couple of weeks, whereas processes operating over shorter timescales primarily serve to redistribute water within the Baltic Sea (Weisse et al. 2021 and references therein). In the following, processes affecting the RSL in the Baltic Sea and along the Baltic Sea coast are described.

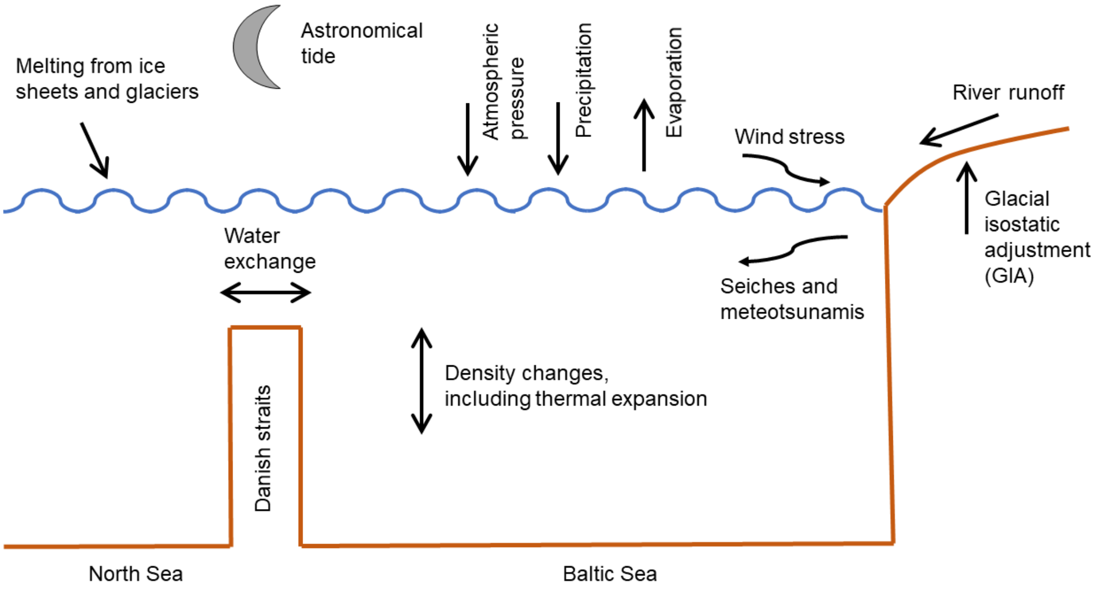

Figure 5-1. Schematic illustration of processes contributing to RSL variability on shorter and longer timescales in the Baltic Sea. Based on Figure 3 in Weisse et al. (2021).

5.2.1 Global mean ASL change

Global mean ASL change is defined as the sum of changes related to variations in ocean density due to temperature and/or salinity variations (*steric sea level change*) and changes related to variations in the ocean volume as a result of variations in the amounts of land ice and/or land-water storage. Owing to these effects, global mean ASL is currently rising, and it is expected to continue to rise over the coming centuries to millennia, as a result of the current and future projected global warming (see further Section 5.5).

Steric sea level change can be separated into thermosteric changes (often referred to as *thermal expansion*), defined as changes in ocean density caused by changes of the ocean temperature, and halosteric changes, which account for the contribution to the ocean density from salinity changes. Of these processes, only thermal expansion contributes to the current global mean ASL rise, whereas the global mean halosteric change is negligible (Fox-Kemper et al. 2021). According to the IPCC, there is high confidence in the understanding of processes causing thermal expansion and uncertainties are low (Fox-Kemper et al. 2021).

Changes in the amount of land ice on Earth is controlled by changes in the mass balance of the ice sheets in Greenland and Antarctica as well as that of the glaciers. As described in Section 4.2.1, ice sheets and glaciers gain mass through snowfall, whereas the mass loss may be controlled by several processes, including melting, calving and sublimation. A decrease in the combined mass of all land ice would contribute to a global ASL rise, whereas a mass increase would contribute to a global ASL fall. Furthermore, when the mass of a specific ice sheet or glacier changes, almost immediate changes in Earth's gravitational field and rotation as well as crustal deformation are induced (see also Section 5.2.2). These changes in turn give rise to distinct geographical patterns of ASL change, known as sea-level change *fingerprints* (e.g. Kopp et al. 2010, Kopp et al. 2014, Grinsted et al. 2015). For example, if melting of an ice sheet occurs, the ensuing local reduction in ice mass gives rise to a weakening of the gravitational pull on the nearby sea water, resulting in an ASL fall in the vicinity of the ice sheet and to an ASL rise elsewhere (Mitrovica et al. 2018). The impact of such fingerprints in the Baltic Sea is significant due to its proximity to the Greenland ice sheet.

As a result of a reduced gravitational pull, melting of the Greenland ice sheet leads to an ASL fall in most of the North Atlantic region and close-to zero ASL change in most of the Baltic Sea (e.g. Whitehouse 2009, Kopp et al. 2014). Specifically, it is estimated that the ASL rise in the Forsmark region, caused by melting of the Greenland ice sheet, is only 5 % of its contribution to the global-mean ASL rise (Pellikka et al. 2020). With regard to melting of glaciers, the corresponding fingerprint at Forsmark is also well below the global average (~20 % of the global mean), whereas the situation is reversed for the Antarctic ice sheet with generally higher than global-mean ASL changes in the Baltic Sea. At Forsmark, corresponding fingerprints from Antarctica is estimated to be in the range 105–110 % of the global mean (Pellikka et al. 2020). Thus, the impact of land ice changes on the Forsmark ASL is dominated by changes in the Antarctic ice sheet, and so the following discussion focuses on processes affecting the mass of this ice sheet.

Processes affecting the Antarctic ice sheet

At present, the Antarctic ice sheet is the largest ice sheet on Earth. It covers virtually the entire Antarctic continent and holds more than 60 % of Earth's freshwater reservoir. If all this water were to be released to the oceans, the global mean ASL would increase by 58 m above the present level (Fretwell et al. 2013). Most of the ice is located in East Antarctica where the majority of the ice sheet constitutes a terrestrial ice sheet that rests on a bed situated above the present-day sea level. In contrast, in West Antarctica most of the ice-sheet bed is located below sea level, so it can be considered a marine ice sheet. The West Antarctic ice sheet is currently kept at a stable position by buttressing ice shelves and confined regions of the bathymetry, preventing warm ocean water to penetrate beneath the ice sheet (e.g. van de Wal et al. 2022).

The Antarctic ice sheet gains mass through snowfall, and – since the current climate in Antarctica is too cold to generate any significant ice melt – mass loss is mainly achieved through glacier dynamics. Ice is then transported under the influence of gravity from the interior towards the coast, at which point it forms ice shelves that ultimately melts or calves into the ocean.

In recent decades, an overall negative mass balance has been observed over Antarctica, i.e. the mass loss has on average exceeded the mass gained (The IMBIE team 2021). The general conclusion from recent studies is that the observed excess mass loss is caused by an increased melting from below the ice shelves due to changes in the ocean circulation outside West Antarctica, which in turn has resulted in an acceleration of the ice flow toward the sea (Fox-Kemper et al. 2021 and references therein). Antarctic snowfall is projected to increase in a future warmer climate (Fox-Kemper et al. 2021). While also likely to increase, sub-shelf melting remains one of the most poorly constrained processes, both from observations and in present ice sheet models (Levermann et al. 2020, Edwards et al. 2021). As a result, it has not yet been established whether the recent increased net mass losses of the ice sheet are attributed to anthropogenic climate change, natural variability, or both (Jenkins et al. 2018, Holland et al. 2019). Furthermore, owing to the challenges in accurately describing sub-shelf processes in the models, they largely fail to simulate the historical evolution of the ice sheet to its present state and, consequently, yield widely different future projections of the ice sheet (Aschwanden et al. 2021). Consequently, current models do not even agree on whether the ice sheet will grow or shrink in the coming decades (e.g. Bamber et al. 2022).

Another major uncertainty in the fate of the Antarctic ice sheet is associated with the possibility of a rapid ice loss caused by instabilities in the marine parts of the ice sheet. Specifically, two such instabilities have been proposed in the literature (e.g. Fox-Kemper et al. 2021): Marine Ice Sheet Instability (MISI) and Marine Ice Cliff Instability (MICI). A pre-requisite for MISI is that the ice sheet rests on a so-called reverse bed, i.e. a bed that slopes downwards toward the interior of the ice sheet (which is the case for most of West Antarctica) as this enables relatively warm ocean water to penetrate beneath the ice sheet without any additional external forcing when the ice starts to retreat. As mentioned above, floating ice shelves currently exert back stress on the inland ice, resulting in an overall stable ice sheet configuration. However, as the climate becomes warmer, ice shelves will become thinner and increasingly fractured (e.g. Lai et al. 2020), resulting in weaker buttressing, which in turn may trigger the onset of MISI. This notion has received some support from paleo-proxy records which suggest that MISI may have driven rapid ice loss in the past (Liu et al. 2016, Wise et al. 2017). The level of warming needed to trigger MISI is highly uncertain, as is the magnitude of the ice loss that would pursue if it was triggered (e.g. Fox-Kemper et al. 2021, van de Wal et al. 2022).

This is also complicated by a low mantle viscosity in the region, which results in a relatively rapid land uplift in response to the retreating ice sheet; this effect may postpone, or even prevent, MISI to be triggered all together (Kachuck et al. 2020, Pan et al. 2021). According to IPCC AR6, MISI is not expected to contribute to the sea level rise during this century regardless of warming scenario but is increasingly likely to occur after 2100 AD (Fox-Kemper et al. 2021).

The MICI hypothesis describes a rapid calving triggered by ice-shelf collapse. According to IPCC AR6, there is low agreement on the exact MICI mechanism and limited evidence of its occurrence in the present or the past (Fox-Kemper et al. 2021). They also note that MICI is represented in only one ice-sheet model (DeConto and Pollard, 2016, DeConto et al., 2021) and that it has not been found to be essential for reproducing ASL evolution inferred from paleo-proxy records (Edwards et al. 2019, Gilford et al. 2020). Like MISI, MICI is triggered by the loss of buttressing ice shelves. However, a major difference is that MICI is hypothesized to trigger a faster ice-sheet retreat than MISI due to a rapid calving of ice cliffs at the front of the ice sheet. MICI is therefore accounted for in the 2100 AD ASL rise projections in IPCC AR6, though they are tagged as "low confidence".

Owing to the great challenges in accurately simulating the Antarctic mass balance and the large uncertainty related to the potential onset of ice-sheet instabilities, the fate of the Antarctic ice sheet constitutes the greatest source of uncertainty regarding future global ALS change, and hence also for the RSL projections at Forsmark over the coming centuries and millennia. The large uncertainty has in recent years also prompted a development where model projections to a greater extent have been replaced with structured expert judgements (SEJ, see e.g. Bamber et al. 2022). These are formal quantitative expert assessments that aim to account for all processes that could potentially contribute to the ASL rise in combination with ASL records inferred from paleo-proxy data. However, since individual experts participating in the SEJ studies may incorporate processes that are poorly understood, and the experts' reasoning in these studies cannot be examined in detail, SEJ estimates are also, similar to MICI, marked with "low confidence" in IPCC AR6 (Fox-Kemper et al. 2021).

5.2.2 Glacial isostatic adjustment (GIA)

The redistribution of mass associated with the growth and decay of continental ice sheets gives rise to major glacial loading and unloading effects over timescales of several tens of thousands of years. For instance, during the decay of a major ice sheet, the unloading of mass results in a post-glacial rebound (i.e. a vertical uplift) of the crust that continues for tens of thousands of years after the disappearance of the ice. This process is well known from previously glaciated regions such as Canada and the United States, Fennoscandia, the British Isles and Siberia (e.g. Ekman 1991), i.e. areas where the rebound process is still active today, some 10–15 kyr after the last deglaciation. The response of Earth's crust, mantle and gravitational field is referred to as Glacial Isostatic Adjustment (GIA).

During the Last Glacial Maximum, around 20 kyr ago, the Laurentide ice sheet of North America, and the Fennoscandian ice sheet had maximum thicknesses of around 2.5–3 km, corresponding to a total of c. 120–130 m of global ASL lowering (Lambeck et al. 2014). When these large ice masses slowly formed, their weight resulted in a slow downwarping of Earth's crust. One important factor that governed both this process and the following glacial unloading is the physical properties of Earth's crust and mantle. In the downwarping process, ductile mantle material was displaced and flowed laterally in order to make room for the flexing crust. At times of ice-sheet decay, mantle flow is reversed and the crust rebounds. The magnitude of mantle depression, and hence the present-day uplift rates, approximately scale with the thickness of the most recent ice sheet in the region. In Sweden, the fastest uplift rates (~10 mm yr^{-1}) are observed in the County of Västernorrland (e.g. Vestøl et al. 2019), approximately where the last ice sheet was at its thickest.

The glacial isostatic adjustment process manifests itself not only in the rebound of regions of past ice sheets. Current melting of present glaciers produces additional GIA effects. As an example, Iceland is undergoing rapid glacial rebound due to a mass loss of Vatnajökull and other smaller ice caps (e.g. Árnadóttir et al. 2009). Since the viscosity of the mantle is inferred to be three orders of magnitude lower beneath Iceland (Árnadóttir et al. 2009) than, for example, Fennoscandia, uplift rates on Iceland are on the order of 20 mm yr^{-1}, in spite of the much smaller volume of ice loss. Further, the low mantle viscosity found in Antarctica results in a relatively rapid regional uplift in response to the recent ice loss.

Outside the ice-sheet margin, an uplifted forebulge, or peripheral bulge, is formed (e.g. Fjeldskaar 1994, Lambeck 1995). The forebulge is caused by flexure and a lateral displacement of mantle material extending outside the ice margin, and it may stretch for several hundreds of kilometres beyond a major ice sheet. The uplift of the forebulge is considerably smaller, on the order of tens of metres, than the downwarping of the crust beneath the central parts of the ice sheet which is on the order of hundreds of metres. During and after deglaciation, the area of the forebulge experiences land subsidence, exemplified by the ongoing lowering of the Netherlands, southern England and the east coast of the United States. It is worth noting that land subsidence in these regions is also a result of ongoing marine sediment loading, graben tectonics and gas extraction. The location of maximum forebulge uplift migrates toward the formerly glaciated region as the ice sheet withdraws.

The processes involved in GIA, and their effect upon RSL change, are well understood. The main uncertainty in future RSL changes due to GIA stem from the ice loading (Section 5.5.3); it is thus primarily associated with future climate evolution and ice-sheet dynamics. For more information about the controlling factors of GIA as well as its sensitivity to ice loading and other processes, see SKB (TR-10-49, Section 3.3.4).

5.2.3 Freshwater input

The brackish nature of the Baltic Sea is maintained by more than 500 km^3 of freshwater that enters the basin each year (Meier and Kauker 2003). About 90 % of this freshwater input comes from river runoff, whereas the remaining 10 % comes from excess precipitation (i.e. precipitation minus evaporation) (Meier and Kauker 2003, Gräwe et al. 2019). If the freshwater input were to be altered, ASL may change directly due to a change in the water volume, or it may change indirectly due to a shift in the salinity and, thus, the density of the sea water (e.g. Kniebusch et al. 2019). The conceptual uncertainty about the effect of freshwater input on RSL is low.

5.2.4 Water exchange with the North Sea

Water exchange between the Baltic Sea and North Sea only occurs if the local RSL in the Danish straits is sufficiently high. Specifically, if the local RSL falls 18 m or more below the present-day level (e.g. SKB TR-20-12, Section 4.5.2), the Baltic Sea is transformed into a lake, and the exchange with the North Sea ceases.

The water exchange through the Danish straits can be conceptualised to occur in two vertical layers, where the brackish water from the Baltic Sea flows into the North Sea in an upper layer close to the sea surface, and more saline (and thereby denser) water from the North Sea flows into the Baltic Sea in the bottom layer close to the seabed (Weisse et al. 2021). To compensate for the net freshwater input to the Baltic Sea, the outflow to the North Sea is on average greater than the corresponding inflow. However, the water exchange is highly variable in time. While the long-term average outflow amounts to ~7 km^3 day^{-1} (Winsor et al. 2001), transport can, under some circumstances, exceed 40 km^3 day^{-1} in both directions, corresponding to an ASL change of more than 10 cm day^{-1} across the entire basin (Mohrholz 2018). Major inflow events typically have volumes in the order of 100 km^3, corresponding to a mean Baltic ASL increase of about 24 cm (Matthäus and Franck 1992). Typically, such variations occur over timeframes of 10 days or longer.

Several studies have found that the ASL variability in the Baltic Sea on monthly to annual timescales also depend on the water exchange with the North Sea. Variability on these timescales can be linked to the atmospheric circulation (Samuelsson and Stigebrandt 1996, Gräwe et al. 2019, Passaro et al. 2021). In particular, a positive correlation has been found between the Baltic ASL variability and the North Atlantic Oscillation (NAO)[16]; this is explained by the fact that stronger westerly winds during periods of positive NAO phases induce a larger transport of water from the North Sea, which in turn increases the mean ASL in the Baltic Sea. During periods of negative NAO, on the other hand, reduced westerly winds, or even easterly winds, lead to an enhanced outflow and a lower mean ASL in the basin (e.g. Weisse et al. 2021).

Owing to generally stronger westerly winds in winter than in summer, inflow rates from the North Sea and, consequently, the mean ASL in the Baltic Sea, are also typically higher in winter than in summer. Passaro et al. (2021) found that the correlation between NAO and winter ASL anomalies exceed 0.7 in most of the Baltic Sea.

---

[16] NAO is an index based on the difference in atmospheric pressure at sea level between the Azores High and Icelandic Low. In Scandinavia, positive values of NOA are typically associated with higher-than-average westerly winds and relatively mild conditions whereas the opposite is true for negative NAO values.

The dependency of Baltic Sea inflow rates on the prevailing atmospheric conditions opens up the question whether global warming may lead to persistent changes in the large-scale atmospheric circulation, that would have significant effects on the ASL in the Baltic Sea. However, evidence of any persistent change in the mean wind fields under a warmer climate is weak, manifested by a large spread in the projected wind speed for 2100 AD among different atmospheric models (Christiansen et al. 2022). In conclusion, there is a good conceptual understanding about the processes controlling the net inflow rates to the Baltic Sea, while the uncertainty in the projected future changes of these processes, in particular the wind forcing, is high.

5.2.5 Meteorological conditions

As described in Section 5.2.4, the prevailing winds are important for controlling the water exchange between the Baltic Sea and the North Sea. However, while this exchange is primarily controlled by the average atmospheric conditions over at least a couple of weeks (e.g. Weisse et al. 2021), shorter atmospheric variability is important for redistributing water within the Baltic Sea. Wind and air pressure constitute key meteorological parameters in this context. Winds exert stress on the sea surface and, thereby, momentum is transferred from the lower atmosphere to the sea. As a result, the body of water begins to move which causes spatial variations in ASL. Extreme winds are of particular interest on shorter timescales as they may give rise to the highest storm surges (timescales of hours to days) and wind waves (timescale of seconds to minutes), both of which are important to consider for adaptation to protect infrastructures against high sea levels (see further Sections 5.4.2 and 5.5.1).

The effect of air pressure on the ASL is linked to the variability of low and high-pressure systems affecting the region. ASL is influenced by the air pressure through the inverse barometer effect, by which a lowering of the air pressure induces high ASL anomalies and vice versa. It is estimated that the ASL changes approximately 1 cm per hPa due to the inverse barometer effect (SMHI 2014). Given that variations in air pressure, due to the short-term variability of the weather patterns in the region, can be up to 20 – 30 hPa, the inverse barometer effect is highly relevant for the ASL variability in the basin. Furthermore, a persistent northward displacement of the storm tracks in the region, which can be expected in a warmer world (Section 3.2.4), may also alter the spatial ASL variability in the Baltic Sea (Gräwe et al. 2019). In summary, the conceptual uncertainty about the effect of meteorological conditions on the sea-level variability is low.

Less common phenomena that may arise from certain meteorological conditions are so-called meteotsunamis and seiches. Meteotsunamis are sudden sea level changes of short duration, caused by a small air pressure disturbance moving above the sea. When the velocity of the disturbance matches the velocity of a long, shallow water wave, the initially small wave is amplified through Proudman resonance (Proudman 1929). Amplitudes of meteotsunamis may be in the order of 1 m (Pellikka et al. 2014). The physics behind meteotsunamis are not well understood and thus conceptual uncertainties are relatively high. However, as the occurrence of these waves is linked to thunderstorms and therefore predominantly occur during the summer months, when the Baltic ASL is generally lower due to weaker westerly winds and hence a reduced inflow of water from the North Sea (Section 5.2.4), they are often omitted from extreme sea-level calculations in the Baltic Sea.

A seiche is a standing wave occurring in a body of water. Seiches typically arise when strong winds and rapid changes in atmospheric pressure push water from one end of a basin to the other. When the wind rapidly ceases, the water rebounds to the other side of the basin, and may continue to oscillate from coast to coast for hours, or even days. While basin-wide seiches in the Baltic Sea with periods of up to 31 h have been proposed by means of numerical modelling (Wübber and Krauss 1979), other authors have argued that the existence of such basin-wide oscillations is not supported by data. In summary, the underlying physics of seiches is well understood. However, the existence of basin-wide seiches in the Baltic Sea, which could in turn influence the ASL variability at Forsmark, is still debated.

5.2.6 Astronomical conditions

Astronomical conditions may also influence the ASL through their effect on tides. However, the effect of tides on the ASL is relatively minor in the Baltic Sea because the connection with the open sea is limited. Tides contribute only to 2 – 5 cm sea-level variability in the basin (Leppäranta and Myrberg 2009) and, at Forsmark, they contribute by less than 4 cm (Pellikka et al. 2020). The conceptual uncertainty related to tides is low.

5.3 Historical evolution

This section presents RSL reconstructions of Fennoscandia and Forsmark during past climates, focussing on the Weichselian glacial cycle and the Holocene.

5.3.1 The Quaternary period including the Weichselian glacial cycle

The evolution of RSL in Fennoscandia during the Quaternary, including the Weichselian glacial cycle, was primarily controlled by the alternating patterns of advancing and retreating of ice sheets during this time (Section 4.3.1). Specifically, the Quaternary ice sheets had a twofold effect on RSL. First, they modulated the global mean ASL by storing sea water on land in the form of ice; for the greatest land-ice volumes inferred from geological records of the Quaternary, sea water equivalent to more than 100 metres ASL change were stored in the ice sheets (Section 5.2.2). Second, owing to the presence of large ice sheets in the region, GIA was also an important factor for the RSL evolution in Fennoscandia; due to GIA, the maximum vertical isostatic uplift in Sweden since the last deglaciation until present day, has been more than 800 m (e.g. Fredén 2002). Thus, for most of Fennoscandia, GIA has likely contributed more to the total RSL variability during the Quaternary than the ASL change.

The RSL evolution of the Weichselian glacial cycle at Forsmark has been reconstructed by SKB using a GIA model (SKB TR-10-49, Section 3.3.4). The model was originally developed by Milne (1998), Milne and Mitrovica (1998) and Milne et al. (1999), and it solves the sea-level equation, which describes the gravitationally-consistent redistribution of water between ice-sheets and ocean basins, and thus the evolution of the distribution of water between oceans and land-based ice-sheets. Once an ice load is applied to the model, the resulting deformation of the solid Earth and the perturbation to the geoid was calculated. The new shape of the geoid[17] determines the redistribution of water in the oceans and the new extent of the oceans. However, this redistribution of water in turn affects the shape of the geoid and the deformation of the solid Earth in oceanic regions, therefore an iterative procedure was used to ensure the correct treatment of perturbations to the solid and geoid surfaces.

The GIA model was driven by ice-load data derived from SKB's ice-sheet reconstruction of the Weichselian glacial cycle (Section 4.3.1). The resulting evolution from that modelling suggests that RSL at Forsmark has varied by several hundreds of metres over the last glacial cycle (Figure 5-2), with the highest RSL values occurring a couple of thousand years after the ice sheet reached its maximum thickness in the region (at around 60 and 20 kyr BP). Conversely, the lowest RSL values in the simulation are obtained after long periods with uninterrupted isostatic uplift, i.e. after several tens of thousands of years of ice-free conditions.

There are considerable uncertainties associated with the reconstructed RSL evolution due to uncertainties in the input data and model representations of the governing processes. For instance, the GIA model was found to yield an overprediction of present-day uplift rates in Fennoscandia by several mm yr^{-1} when driven by the reconstructed Weichselian ice-sheet evolution (SKB TR-10-49, Section 3.3.4 and Whitehouse 2009). The sensitivity of modelled Forsmark RSL to different ice load histories as well as representations of Earth's rheology, isostatic memory and the presence of ice sheets in other regions than Fennoscandia was evaluated with additional simulations with the GIA model (documented in detail in SKB TR-10-49, Section 3.3.4). The sensitivity simulations revealed a closer agreement with the observed present-day GIA rates when using 80 % of the full simulated Weichselian ice-sheet thickness as input rather than with the original ice-sheet reconstruction. Thus, it is likely that the amplitude of the RSL variability in Figure 5-2 is somewhat overestimated. However, the duration of periods of submerged conditions at Forsmark in conjunction with ice-sheet retreat, which is more relevant for post-closure safety (Section 5.1.2), is not as strongly affected by a potentially exaggerated ice-load sensitivity as the amplitude (see e.g. Figure 3-31 in SKB TR-10-49). Furthermore, to reduce the bias in the reconstructed RSL during the last deglaciation phase of the Weichselian glacial cycle and the following Holocene interglacial, the results from GIA modelling were interpolated with an empirical reconstruction of the Holocene RSL (Section 5.3.2). Details on the interpolation are documented in SKB (TR-10-49, Section 4.5.2).

---

[17] Geoid is defined as the shape of ocean surface under the influence of the gravity of Earth, including gravitational attraction and Earth's rotation, if other effect such as winds and tides are absent.

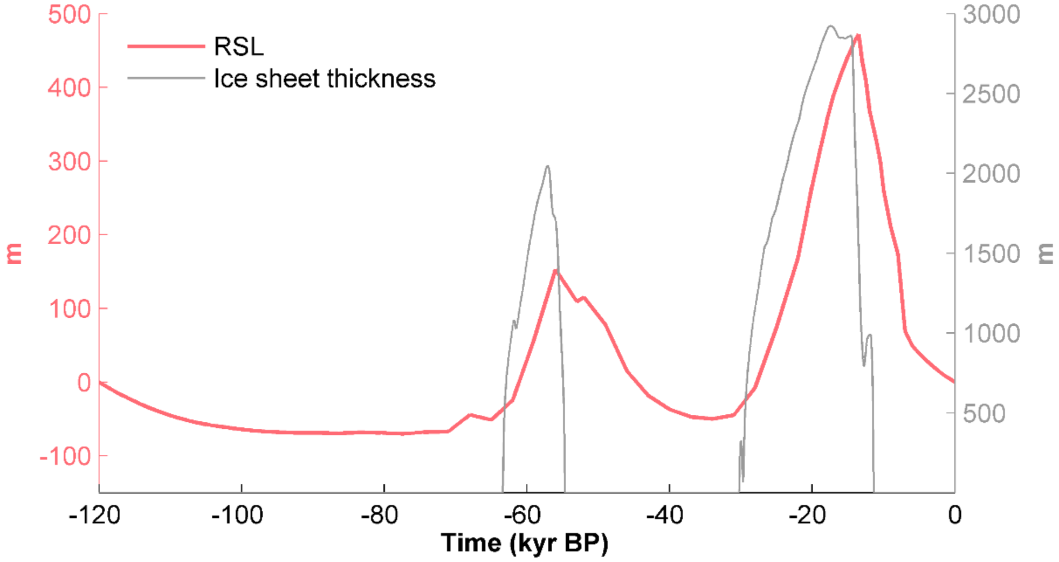

Figure 5-2. *Reconstructions of RSL relative to present-day (red) and ice sheet thickness (grey) at Forsmark over the last 120 kyr, i.e. the Weichselian glacial cycle. RSL was reconstructed based on GIA modelling and empirical reconstruction of the Holocene RSL (Section 5.3.2).*

5.3.2 The Holocene interglacial

The evolution of RSL at Forsmark during the Holocene has been reconstructed independently from the GIA modelling using an empirical model constrained by geological data consisting of mainly organic C-14 and lake-tilting information (Påsse 2001). The model parameters were subsequently derived specifically for Forsmark in Brydsten (2009). The resulting reconstruction, from the time of deglaciation in the area (~10.8 kyr BP, see Section 3.3.2) up until present day, demonstrates that RSL at Forsmark has decreased by well over 100 m since the deglaciation in the area (Figure 5-3). This decrease is mostly attributed to the effect of GIA since the last deglaciation.

The empirical model of Påsse (2001) was later updated with new observational data in the study of Påsse and Daniels (2015). The effect of this update on the RSL evolution at Forsmark was found to be small, especially for the middle and late Holocene, whereas for the early Holocene, the difference between the original and updated model becomes more significant, reaching ~20 m (Figure 5-3). However, during the early Holocene, the entire landscape in the Forsmark area is covered by the sea in both reconstructions, and the difference in water depth between the reconstruction is not considered to affect the subsequent landscape development to a large extent. Owing to these results, no new landscape modelling was carried out in preparation for the PSAR assessments (e.g. SKB TR-23-06, Chapter 4); in other words, the RSL development originally introduced by Brydsten (2009) was also used to describe the landscape development in those assessments.

Uncertainty ranges of the Forsmark RSL evolution was also estimated in SKB (TR-23-05, Appendix G) for the middle and late Holocene based on uncertainties in radiocarbon-dating (Hedenström and Risberg 2003). These are included as 95 % confidence intervals in Figure 5-3. Based on this analysis, the uncertainty in Forsmark RSL amounts to ~3 m during the late Holocene and ~10 m during the middle Holocene.

The Baltic Sea was subject to two lake phases during the Holocene: the Baltic Ice Lake (~ 15–11.5 kyr BP) and the Ancylus Lake (~ 10.5–9 kyr BP) (Påsse and Daniels 2015). During those lake stages, the Baltic Sea was isolated from the Atlantic and hence not influenced by global ASL changes. Because Forsmark became deglaciated ~ 10.8 kyr BP, it was still covered by the ice-sheet during the phase of the Baltic Ice Lake, whereas it was mostly ice-free during the Ancylus Lake stage. The effect on the RSL of the Ancylus Lake was estimated to be 15 m or less (Påsse and Daniels 2015; see also SKB TR-23-05, Appendix G for further details). Thus, the RSL changes during lake phases were overall relatively small compared to the total ASL and GIA changes during the Holocene.

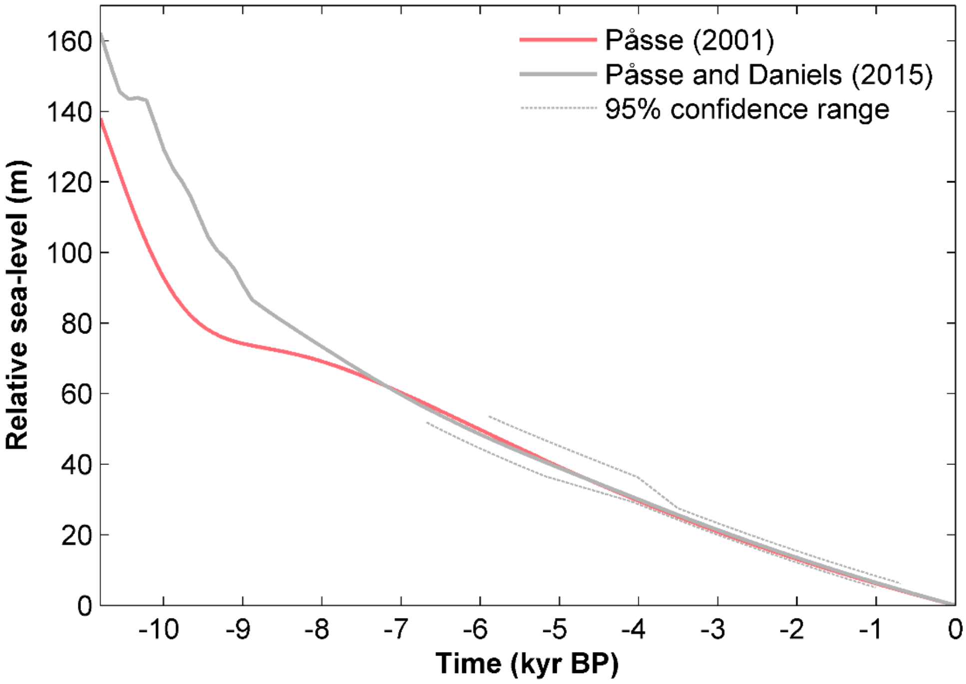

Figure 5-3. *Holocene RSL change at Forsmark relative to present-day based on Påsse (2001) (parameters were derived in Brydsten 2009; red line) and Påsse and Daniels (2015) (grey solid line). The dotted grey lines show the lower and upper confidence intervals (at 95 % level) based on uncertainties in the radiocarbon dating as reported by Hedenström and Risberg (2003).*

5.4 Present-day conditions and trends

Present-day RSL at coastal locations are most adequately measured by tide gauges (also referred to as "mareographs"), which record the height of the water level with respect to a local height reference. A tide-gauge station has been in operation at Forsmark since 1975, which measures RSL data every 10 min as well as the maximum and minimum RSL for every hour. Monthly and annual mean data from the measurements are freely available through the Permanent Service for Mean Sea Level (PSMSL) database (Holgate et al. 2013, PSMSL 2022).

Figure 5-4a shows the monthly-mean RSL measurements from the Forsmark tide gauge. The relatively large RSL changes from month to month in the figure reflect a high variability in driving processes (Section 5.2) over monthly, or shorter, timescales. Over these timescales, sea level extremes characterised by storm surges and wind waves are also relevant. Potential trends in processes acting over these short timescales and their impact on sea-level extremes are further discussed in Section 5.4.2. Embedded in the higher frequency monthly variability is also a long-term trend of the mean RSL that extends over several decades. This multi-decadal trend is more clearly visible if considering annual averages (red line in Figure 5-4b), and is discussed in detail in Section 5.4.1.

5.4.1 Mean RSL variability on annual to multi-decadal timescales

Two important results can be identified from Figure 5-4a,b with regard to multi-decadal trends. First, RSL at Forsmark has generally decreased since the start of the tide-gauge measurements, albeit slowly in relation to the monthly variations. This result is consistent with the overall trend of decreasing RSL caused by the ongoing isostatic uplift since the last glaciation (Section 5.3.2). Second, while RSL has generally decreased over the entire measurement period, the rate of the decrease has slowed down towards to the end of the period. This can be confirmed if applying linear regression (using the least square approach) of the monthly data until 2021, starting from different years. This exercise reveals that the rate of RSL decline at Forsmark between the period 1993–2021 is about 35 % slower than during the period 1975–2021, and that the RSL has been virtually constant over the last 10 years (Figure 5-4a). However, owing to the short timeseries length, the calculated trend over the last 10 years is sensitive to the start and end points used in the linear interpolation; this is illustrated by a remarkably high standard error of the regression slope over this period (see bottom panel in Figure 5-4a). Therefore, the calculated RSL trend over the last 10 years should be interpreted with caution.

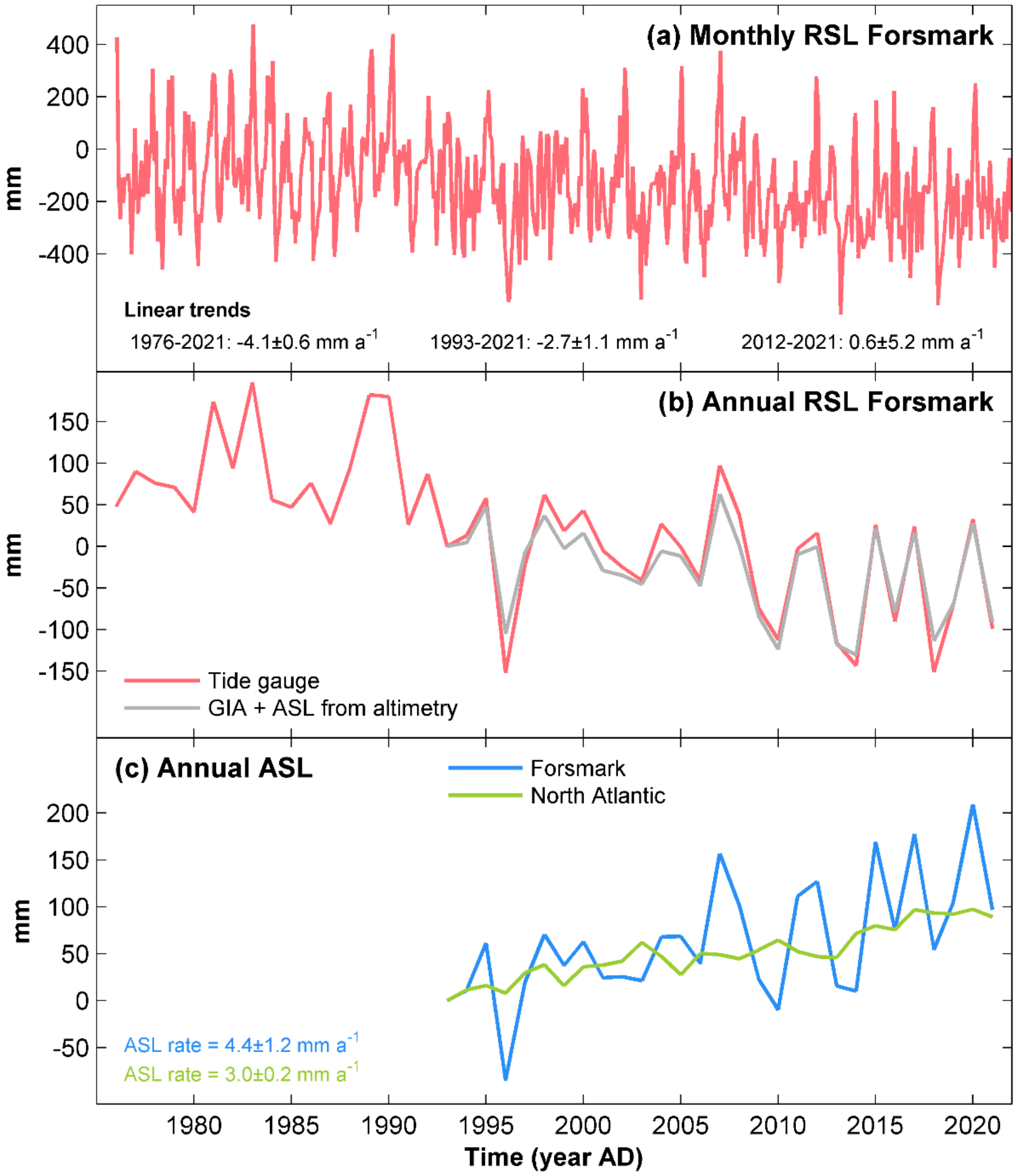

Figure 5-4. *Changes in Forsmark RSL and ASL since 1976 AD. (a) Monthly RSL variations at Forsmark as inferred from tide-gauge measurements. Linear trends for different periods and the standard error of those trends are given by the panel legend. (b) Annual RSL variations at Forsmark as inferred from tide-gauge measurements (red) compared with the sum of ASL inferred from satellite altimetry and present-day estimates of GIA (based on Vestøl et al. 2019) (grey). (c) Annual ASL variations since 1993 AD as inferred from satellite altimetry at Forsmark (blue) and at a location in the North Atlantic (green-yellow) with the same latitude as Forsmark. Calculated rates of sea-level rise (SLR) and the associated standard errors are given by the legend.*

As summarised in Section 5.2, RSL at Forsmark is controlled by several processes. The ones acting on multi-decadal timescales or longer are mainly GIA and processes influencing the ASL, such as melting of Earth's ice sheets and glaciers, thermal expansion of sea water and the large-scale atmospheric circulation. To obtain further insight into the individual processes contributing to the measured multi-decadal RSL changes in Figure 5-4, additional datasets of GIA and ASL rise are used. Both datasets have been produced independently of the tide-gauge measurements, and are thus suitable for assessing the relative contributions of GIA and ASL to the total RSL change.

Present-day rates of GIA are inferred from the semi-empirical NKG2016LU model (Vestøl et al. 2019), which combines an empirical model based on GPS measurements with a physical GIA model. In this model, the resulting vertical component of GIA at Forsmark amounts to 6.7 ±0.2 mm yr^{-1}.

This value was also used in both PSAR assessments (SKB TR-20-12, Section 3.3.3 and SKB TR-23-05, Section 2.2.3); it was revised from a significantly higher value (8.4 mm yr^{-1}), deduced from Lidberg et al. (2010), that was used in SR-PSU (SKB TR-23-05, Section 2.2.3). As GIA is a relatively slow process acting on multi-millennial timescales (Section 5.3.1), the estimated GIA of 6.7 ± 0.2 mm yr^{-1} is applicable for the entire 40-year period covered by the tide gauges.

In addition to GIA, altimetry satellite sea-level data from the Copernicus Marine Environment Monitoring Service (CMEMS) are used for the period 1993–2021 (Copernicus 2022). In contrast to tide gauges, which measure RSL, altimetry measures the sea-surface height relative to a geocentric reference characterised by a reference ellipsoid. As the effect of an elevated seafloor caused by GIA primarily is to redistribute water masses across the oceans rather than increasing the local height of the sea surface, altimetry is, at most, only very weakly influenced by GIA (see further below). Thus, altimetry essentially measures only the ASL.

Several studies have used altimetry data to analyse trends and variability of the Baltic ASL (e.g. Karabil et al. 2018, Agha Karimi et al. 2021, Passaro et al. 2021). One potential drawback of altimetry, as reported in those studies, is that it performs better over large areas of open water and therefore cannot resolve ASL trends in areas that are close to the coastline (e.g. Weisse et al. 2021). This may be particularly challenging for the Baltic Sea, because it constitutes a relatively small sea (compared to the global oceans) with approximately 200 000 islands that have the potential to disturb the signal received by the satellite. Further, about half of the Baltic Sea area is covered by sea ice for one or several months each year which may also inhibit accurate altimetry measurements. In the present analysis, daily altimetry data representative for Forsmark are deduced from a grid cell centred at approximately 60.4ºN and 18.4ºE (Forsmark coordinates are 60.4ºN and 18.1ºE). However, in order to evaluate the potential influence of these uncertainties, the analysis is also conducted for several additional grid cells adjacent to this one (Appendix C1). This comparison demonstrates that the calculated ASL trends are largely insensitive to the selected grid cell in the altimetry data. This suggests that the reported difficulties with unbiased altimetry measurements in the vicinity of coastal regions and in the presence of sea ice is not a significant issue in the sea outside Forsmark.

Combining altimetry and GIA data with the semi-empirical NKG2016LU model results in a similar RSL evolution to that inferred from tide gauges (cf. grey and red lines in Figure 5-4b). Accounting for the reported standard uncertainty in the GIA measurements (0.2 mm yr^{-1}), the RSL linear trend between 1993 and 2021 in tide gauge data is within the range estimated by the combination of altimetry and GIA. This result indicates that the three datasets are internally consistent and supports the reliability of present-day GIA measurements at Forsmark used in the PSAR.

Considering only altimetry data, it is possible to estimate to what extent the recent ASL rise has contributed to the overall RSL trend at Forsmark. According to these data, the average ASL rise at Forsmark between 1993 and 2021 was 4.4 ± 1.2 mm yr^{-1} (Figure 5-4c), which is more than 1 mm yr^{-1} faster than the global mean ASL rise between 1993 and 2018 as reported in IPCC AR6 (Fox-Kamper et al. 2021). The elevated ASL rise at Forsmark is linked to an enhanced acceleration of the ASL rise in the area. Specifically, the ASL acceleration at Forsmark is estimated to be approximately 0.03 mm a^{-2} for the period 1993–2021[18], which is about three times that of the global mean (Fox-Kemper et al. 2021). Furthermore, the ASL rise at Forsmark between 1993 and 2021 is nearly 50 % faster than the corresponding rise at locations of comparable latitude in the North Atlantic (Figure 5-4c). This indicates that the high rates of ASL rise at Forsmark are regionally confined to the Baltic Sea.

A significantly faster sea-level rise in the Baltic Sea compared to the global mean was also highlighted in Białas and Sośnica K (2024), who found that the water level of the Baltic Sea rose by 5.8 mm yr^{-1} on average between 2001 and 2021. Moreover, some studies have documented the existence of an ASL rise gradient across the Baltic Sea (Gräwe et al. 2019, Passaro et al. 2021). Specifically, the rates of mean ASL rise vary from about 2–3 mm yr^{-1} in the southwest to about 5–6 mm yr^{-1} in the northeastern parts of the basin (Passaro et al. 2021).

---

[18] The ASL acceleration is estimated by applying a second-order regression to the Forsmark ASL evolution in Figure 5-4c.

These spatial differences are likely linked to stronger southerly and westerly winds during positive NAO phases, which serve to push the water further north and east of the basin (Passaro et al. 2021), as well as a poleward migration of the low-pressure systems in recent decades (Gräwe et al. 2019), which has shifted the spatial ASL rise gradient through the inverse barometer effect (Section 5.2.5). As the spatial gradient of the observed ASL rise in the Baltic Sea correlates relatively well with the corresponding gradient of GIA, it has also been proposed that the enhanced ASL acceleration in the Baltic Sea is a consequence of the current deceleration of GIA (Spada et al. 2014). However, more recent studies have noted that the estimated ASL acceleration due to this effect is only about one order of magnitude lower than the observed acceleration in the basin (Weisse et al. 2021) and, thus, this effect cannot explain the observed spatial ASL rise differences in the basin.

As the estimated temporal trend in ASL at Forsmark (4.4 mm yr^{-1}, cf. Figure 5-4c) approximately corresponds to the average between the highest and lowest trends across the Baltic Sea (2–6 mm yr^{-1}), it is reasonable to assume that the processes that primarily redistribute water within the basin are less relevant to explain the recent Forsmark ASL rise compared to those that affect the mean ASL of the basin. Therefore, the following discussion focuses on processes affecting the mean ASL in the Baltic Sea compared to the adjacent North Sea (and the global mean) rather than those that redistribute water within the basin. Potential processes that could cause differences in ASL rise in the Baltic Sea as compared to the North Sea on annual-to-decadal timescales are those that result in (i) regional differences in ASL rise due to melting of ice sheets and glaciers (fingerprints), (ii) changes in the freshwater input, and (iii) changes in the net water exchange between the Baltic Sea and the North Sea (Section 5.2).

Modelling of fingerprints has found that melting of the Greenland ice sheet has only a negligible influence on the ASL rise across most of the Baltic Sea, whereas the basin-average ASL rise due to melting of the Antarctic ice sheet is higher than the global mean (Section 5.2.1). However, since the Antarctic ice sheets contributed by less than 10 % to the global mean ASL rise between 1993 and 2018 (Fox-Kemper et al. 2021), this effect cannot explain the observed elevated ASL rise at Forsmark. In fact, the Greenland ice sheet has contributed more to the global mean ASL rise than the Antarctic counterpart during this period. Thus, if regional differences in ASL rise would be determined by fingerprints alone, the resulting ASL rise at Forsmark in recent years would have been slower than that of the global mean.

Regarding trends in the freshwater balance, which is controlled by the excess precipitation and river discharge to the Baltic Sea (Section 5.2.3), studies have found that there are no major trends in these features that could explain the multi-annual trends in the Baltic ASL rise (Rutgersson et al. 2014, Johansson 2016). However, these studies arguably have not presented data that cover the most recent years, during which the ASL rise in the Baltic Sea have been the fastest (Figure 5-4c). Thus, the impact of the freshwater balance on the most recent ASL acceleration at Forsmark remains an open question.

Another plausible explanation is that the elevated mean ASL rise in the Baltic Sea is caused by an increased inflow of water to the Baltic Sea through the Danish straits. Along these lines, several studies have found a positive correlation between the ASL variability in the Baltic Sea and the large-scale atmospheric circulation, in particular the NAO (Section 5.2.4). For example, based on results from regional ocean modelling, the study of Gräwe et al. (2019) argue that the elevated ASL rise in the Baltic Sea compared to the North Sea between 1950 and 2015 is caused by an increase in the number of days with prevailing westerly winds, which has resulted in an elevated inflow of seawater to the Baltic Sea during this period. The study of Passaro et al. (2021) further noted that the mean ASL rise between 1995 and 2019 in the Baltic Sea is faster in winter than in summer, and that the winter ASL rise exhibits a strong positive correlation with NOA in virtually the entire basin. The results of Passaro et al. (2021) thus strengthen the conclusion of Gräwe et al. (2019) that the elevated basin-average ASL rise is induced by changes in the large-scale atmospheric circulation. Using both tide-gauge and altimetry data, the study of Agha Karimi et al. (2021) demonstrates the importance of timescales when analysing the potential influence of the large-scale atmospheric circulation on the Baltic ASL rise. While confirming that NAO has a strong influence on ASL variations on seasonal to decadal timescales, they also conclude that the impact of NAO is much smaller on multi-decadal timescales.

Agha Karimi et al. (2021) further notes that there are multi-decadal variations in the tide gauge and altimetry data, which make it difficult to estimate RSL and ASL trends accurately and, especially, to extract global warming-induced changes from the data. These variations also entail that estimated trends are sensitive to the period chosen for implementation in the regression model. This issue can be demonstrated by Baltic Sea ASL rise estimates reported in recent studies. For example, studies that only applied the regression model until mid-2010s report rates that are similar to, or only slightly higher, than the global average ASL rise (e.g. Gräwe et al. 2019, Madsen et al. 2019). On the contrary studies that included data covering the majority of the decade until 2020 report significantly higher basin-average rates of ASL rise (e.g. Agha Karimi et al. 2021, Passaro et al. 2021), similar to the estimated rates for Forsmark in Figure 5-4c. The high sensitivity to the selected regression period can also be noted for Forsmark; if the linear regression model of the Forsmark ASL trend is applied for the periods 1993–2014 and 1993–2015, the resulting ASL rise is 2.8 mm yr^{-1} and 3.8 mm yr^{-1}, respectively, thus substantially lower than the calculated trend between 1993 and 2021 (Figure 5-4c). Furthermore, applying the regression model to 2014 or 2015, there is no apparent ASL acceleration at Forsmark, which is in stark contrast to the estimated three times the global-mean acceleration obtained when applying the same model to 2021.

In summary, data from both satellite altimetry and tide gauges suggest that the ASL rise at Forsmark is currently about 50 % faster than corresponding rates in the North Atlantic and global mean. Most of this difference is explained by an elevated ASL rise since mid-2010s. ASL trends on annual to decadal timescales can, at least partially, be explained by variations in the large-scale atmospheric circulation, which regulates the inflow to the Baltic Sea from the adjacent North Sea (Gräwe et al. 2019, Passaro et al. 2021). However, a significantly smaller impact of the atmospheric circulation on Baltic Sea ASL trends has been noted over multi-decadal timescales (Agha Karimi et al. 2021), suggesting that the current elevated ASL rise trends at Forsmark may not persist over the coming decades. Continued monitoring of tide gauge and altimetry measurements is arguably essential in order to confirm, or refute, this notion.

5.4.2 Sea level extremes

The phenomena primarily contributing to sea level extremes in the Baltic Sea are storm surges and wind waves (Section 5.2.5). These processes may in turn be modulated by a changed inflow of water through the Danish straits (Section 5.4.1). Longer periods with prevailing westerly winds serve to increase the flow through the straits, which, in turn, results in elevated mean ASL across the entire Baltic Sea. Variations in the inflow rate to the Baltic Sea contributes to the high monthly variability of up to 80 cm that can be seen in Figure 5-4a.

Storm surges refer to changes in the ASL in coastal waters that are primarily caused by the prevailing meteorological conditions (Weisse et al. 2021). Storm surges in the Baltic Sea typically last from several hours to almost a day (Wolski and Wisniewski 2020). As storm-surge levels generally increase with wind speed and decrease with atmospheric pressure, they are higher and more frequent during fall and winter than during spring and summer. This also means that the highest storm-surge levels are recorded during extreme weather events, such as during storms or hurricanes.

To describe the characteristics of maximum storm-surge levels for a certain site, they are often mapped against so-called *return periods*. The maximum storm-surge level is then typically defined as the maximum daily mean ASL that can be expected to occur during this period. For example, a maximum storm-surge level with a return period of 100 years will be higher than the corresponding level with a return period of 10 years because more extreme storms can be expected to occur over a period of 100 years than over 10 years. Thus, the maximum storm-surge level with a long return period is associated with a lower statistical probability than a maximum level with a shorter return period. The concept of return periods is often adopted in risk-consequence assessments of coastal infrastructures; for infrastructure of critical importance (and high consequence costs in case of flooding) it is motivated and advisable to opt for a longer return period, whereas shorter return periods might be sufficient for less critical infrastructure.

Maximum storm-surge levels for different return periods are most typically estimated by forming a probability density function (PDF) based on a timeseries of the maximum daily mean RSL. A common limitation in this procedure is that the length of the timeseries does not extend beyond or are even shorter than the length of return periods that one wishes to estimate.

For example, only a handful of tide-gauge measurements extend over periods longer than 100 years, and thus estimating storm-surge levels for return periods for longer than 100 years typically requires extrapolation of the data for most stations. For such stations, the resulting storm-surge levels for return periods of 100 years or longer will be sensitive to the characteristics of the PDF selected to fit the data. In other words, even if the existing data to a large extent is captured by a certain PDF, a significant uncertainty remains related to the most extreme storm-surge levels that are associated with low annual probability (i.e. the tail of the applied PDF). This uncertainty is manifested by the fact that these extreme levels vary considerably among the possible PDFs, even if they exhibit a seemingly good fit with available data. To overcome this problem, studies often apply several PDFs when analysing storm-surge levels (e.g. Pellikka et al. 2020). For the Swedish Baltic coast, a typical uncertainty in the maximum storm-surge level depending on the selected PDF amounts to the order of 10 cm for 100-year return periods (Södling and Nerheim 2017).

Numerical sea-level modelling offers an alternative solution to the limitation of too short timeseries. After such models have been calibrated to existing data, they can be used to produce longer timeseries than those only inferred from the measurements; this can in turn reduce the uncertainty related to the PDF described above. A major disadvantage with this methodology is that it introduces additional uncertainties with regard to the formulation and parameterisation of the numerical model. Sea-level model simulations were used in the latest estimate of storm-surge levels at Forsmark (Pellikka et al. 2020). Pellikka et al. (2020) carried out a simulation covering 850 years using a multi-component sea level model that was forced by atmospheric data. The tail of the resulting PDF was thereafter extrapolated to include even longer return periods. The resulting maximum Forsmark storm-surge levels in the study range from about 1 m above the present mean sea level (10-year return period) to just above 2 m (100 000-year return period) (Table 5-1).

Table 5-1. Maximum daily storm-surge levels above the average water level at Forsmark. From Pellikka et al. (2020)

Return period (years)	Storm-surge levels Forsmark
10	114 cm
100	139 cm
1000	164 cm
10 000	189 cm
100 000	215 cm

Importantly, Pellikka et al. (2020) also showed that the resulting PDF from this simulation agrees well with existing tide-gauge observations at Forsmark. A similar result was also obtained in the study of Hieronymus and Kalén (2020). Using data from tide-gauge measurements, they estimated storm-surge levels at Forsmark of approximately 110 cm and 130 cm from the tide-gauge measurements corresponding to return periods of 10 and 100 years, respectively (see their Figure 5). The results of Pellikka et al. (2020) and Hieronymus and Kalén (2020) suggest that the threshold for drilling used in the safety assessments (1 m; see Section 5.1.2) corresponds to approximately storm-surge levels with a return period of 10 years.

Flood levels along a coastline are also affected by wind waves. These are local phenomena acting on timescales in the range of seconds. As with storm surges, wind waves in the Baltic Sea exhibit higher values in winter and lower values in summer due to the seasonal cycle in wind speeds (Björkqvist et al. 2018). Wind waves are typically significantly lower in coastal areas than in open waters, but can still contribute substantially to short-term sea level extremes at coastal locations. In addition, they may also affect sea-bottom and shore erosion (e.g. Brydsten 2009). However, their contribution to extreme sea levels depends strongly on the local conditions, such as the shape of the shoreline and the bathymetry. Thus, the impact of wind waves on the coastal landscape is often spatially confined to a restricted area.

These local effects are also seen in the sea around SKB's current and planned facilities at Forsmark. The effect of wind waves on the Forsmark repository area was modelled by Brydsten et al. (2009) using the STWAVE model, which simulates wave refraction and shoaling, wave breaking, diffraction, wind-induced wave growth, wave-wave interactions and white capping (McKee Smith et al. 2001). The winds that yield the highest waves at Forsmark are generated from northerly and north-easterly winds; westerly winds tend to push water towards the eastern coasts of the Baltic and waves originating from easterly or southerly winds are sheltered by the archipelago outside Forsmark (Brydsten et al. 2009). Assuming a northerly wind speed of 25 m s^{-1}, the resulting wave height (defined as the distance between the wave crest and trough) in the northern part of Öregrundsgrepen reaches more than 7 metres in the model, but declines rapidly towards the Forsmark area (Figure 5-5). The pier built adjacent to SFR shelters the shores to the south, so the simulated wave heights here are moderate (< 0.4 m). The southern shores of SFR are well sheltered from northerly winds and thus have negligible wave heights (Figure 5-5). The highest waves occur just north of the SFR repository with 1–2 m high waves. Since the wave height in STWAVE is defined as the distance between the wave crest and trough, the contribution from those waves to the extreme short-term sea level would be about 50 %, i.e. ~0.5–1 m. For comparison, the highest waves at the location of the planned spent fuel repository reach ~0.3–0.5 m.

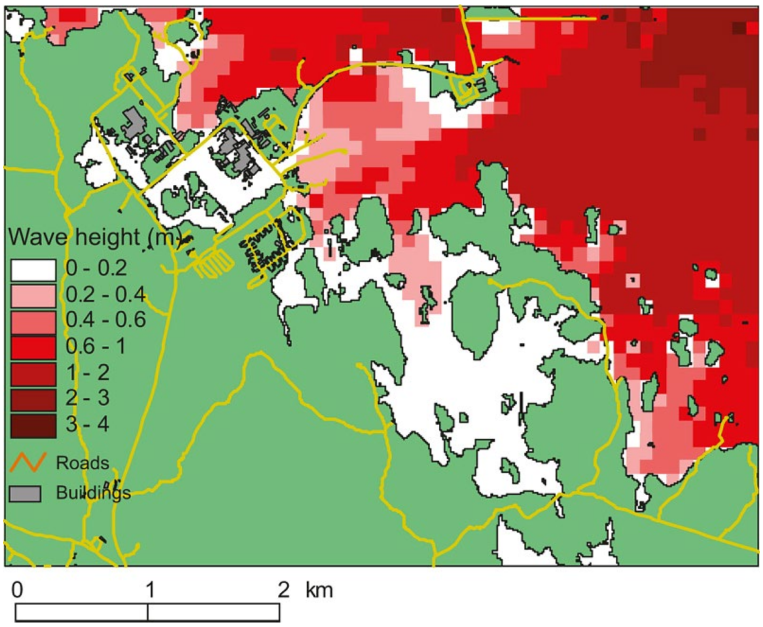

Figure 5-5. *Calculated height of wind waves induced by northerly winds of 25 m s^{-1} using the STWAVE model (Brydsten et al. 2009). Wave height is defined as the distance between the wave crest and trough. The contribution from wave height to the short-term extreme sea level would thus be 50 % of the values shown in the figure. Near the SFR repository this means that the maximum simulated wave height contribution is ~0.5–1 m, whereas it is ~0.3–0.5 m at the location of the planned spent fuel repository.*

5.5 Future evolution

5.5.1 Until 2100 AD

Global mean ASL rise

The current global-mean ASL rise is expected to continue until the end of the century irrespective of the amount of greenhouse-gas emissions during the century (Fox-Kemper et al. 2021). There is a high agreement among contemporary projections that the current global mean ASL-rise acceleration will remain relatively constant until 2050 AD, and that this acceleration will be largely insensitive to the amount of emissions (Fox-Kemper et al. 2021). After 2050 AD, the current acceleration is projected to continue at a similar rate for the remainder of the century under the highest emission scenarios (SSP3-7.0 and SSP5-8.5, see Section 2.5.1), while ASL rise is projected to begin to decelerate towards the end of the century under emission scenarios compatible with the Paris climate agreement (SSP1-1.9 and SSP1-2.6).

According to the IPCC, the global-mean ASL rise in the projections for 2050 AD is within the range 0.1–0.4 m (5th-95th percentiles) relative to the reference period 1995–2014 AD across all emission scenarios (Fox-Kemper et al. 2021). In contrast to the projections for 2050 AD, there is a low agreement across the global-mean ASL rise projections for 2100 AD. Omitting low confidence projections based on MICI or SEJ (Section 5.2.1), the projections for 2100 AD range from 0.2–1.0 m under the SSP1-2.6 and SSP2-4.5 emission scenarios to 0.3–1.6 m under the SSP5-8.5 scenario (Table 5-2). Including also MICI and SEJ, the upper-end of the IPCC projections increase significantly, particularly for the high emission scenario SSP5-8.5, whose 95th percentile estimate reaches 2.4 m (Table 5-2). The large variation in global-mean ASL rise projections for 2100 AD under SSP5-8.5 is attributed to a deep uncertainty with regard to the fate of the Antarctic ice sheet under such high anthropogenic greenhouse-gas emissions (Section 5.2.1).

Since IPCC AR6, two new studies based on SEJ have been published. However, these do not present significantly revised ASL rise projections compared to the IPCC. Importantly, this is also the case for the high-end (high percentile) projections of importance for the assessment of the maximum ASL rise during the operational phases of SKB's facilities. For example, considering only contributions to the ASL rise from the Greenland and Antarctic ice sheets, Bamber et al. (2022) hypothesized that the 95th percentile global-mean ASL rise for 2100 AD amounts to about 70 cm and 170 cm under a 2 °C (comparable to SSP1-2.6) and 5 °C (comparable to SSP5-8.5) climate stabilisation scenario, respectively. Adding contributions from thermal expansion of the oceans and melting of glaciers, these values are roughly consistent with the 95th percentiles of the global-mean ASL rise reported by the IPCC (Fox-Kemper et al. 2021).

The SEJ in Bamber et al. (2022) was conducted without the constraint that the processes resulting in the ASL rise need to be fully, or even partially, understood. For example, information on rapid ASL rise from paleo-proxy records was used in the judgement even if the process that caused this rapid change is not understood. An alternative approach was presented by van de Wal et al. (2022), who conducted a SEJ that focused on current process-understanding rather than on past records. While the global mean ASL will likely rise by several metres under high emissions during the centuries after 2100 AD, they argued that that there are several lines of evidence that a major disintegration of Antarctic ice shelves (which may cause MICI and MISI) is unlikely to occur during this century; this reduces the high-end ASL rise estimates for 2100 AD under high emission scenarios. In their study, a high-end global-mean ASL rise of 1.6 m was suggested for 2100 AD under 5 °C of warming comparable to the 83rd percentile estimate in IPCC AR6.

All in all, the studies published since IPCC AR6 largely confirm the conclusion drawn by the IPCC with regard to the global-mean ASL rise. However, owing to the deep uncertainty associated with, especially, the stability of the ice shelves around Antarctica, and hence also the stability of the grounded parts of the ice sheet, it cannot be excluded that the IPCC estimates will be significantly revised in the future. Thus, it is important that the latest developments in this and associated research fields are closely monitored.

Table 5-2. Projected global mean ASL rise by 2100 AD (5th- 95th percentiles) as reported in IPCC AR6 (Fox-Kemper 2021) and Pellikka et al. (2020), the latter of which was used in the evaluation of extreme sea levels until 2100 AD at Forsmark

	IPCC high confidence	IPCC low confidence	Pellikka et al. (2020) Global	Pellikka et al. (2020) Forsmark
SSP1-2.6 (RCP2.6)	0.2 – 1.0 m	0.2 – 1.0 m	0.3 – 0.7 m	0.2 – 0.6 m
SSP2-4.5 (RCP4.5)	0.2 – 1.0 m	0.2 – 1.6 m	0.3 – 1.2 m	0.2 – 1.1 m
SSP5-8.5 (RCP8.5)	0.3 – 1.6 m	0.4 – 2.4 m	0.4 – 2.1 m	0.4 – 1.8 m

Mean RSL change at Forsmark

Projections of the mean RSL change at Forsmark until 2100 AD is used in the assessment of flooding during extreme sea levels up until the closure of SKB's existing and planned repositories at Forsmark. The assessment of the mean RSL at Forsmark was conducted in three steps (Pellikka et al. 2020); (i) first, numerous scientific publications were used to compile estimates of global mean ASL rise under different emission scenarios (RCP2.6, RCP4.5 and RCP8.5; see Section 2.5.1 for a description about emission scenarios); (ii) these global-mean estimates were then regionalised to Forsmark using fingerprints from the respective ice sheets (Section 5.2.1) and regional thermal expansion derived from climate modelling; (iii) finally, the Forsmark ASL rise estimates were converted to RSL changes by adding the effect of GIA (Section 5.2.2). The resulting mean RSL change was presented for years 2050 AD, 2080 AD and 2100 AD for the three emission scenarios.

Although Pellikka et al. (2020) was published prior to IPCC AR6, estimates of global-mean ASL rise derived from this study[19] compares reasonably well with the IPCC projections (Table 5-2). The high-end (95th percentile) global-mean ASL rise until 2100 AD, as estimated from Pellikka et al. (2020), is located between the corresponding low- and high-confidence estimates by the IPCC (Table 5-2). This is reasonable as ASL rise estimates based on MICI were included in the compilation by Pellikka et al. (2020), albeit with a lower weight than other studies that did not account for low-confidence processes. Thus, in summary, the studies of global-mean ASL rise that were used to estimate the Forsmark mean RSL change agree reasonably well with the recent projections by the IPCC.

According to Pellikka et al. (2020), the effect on the ASL rise of sea-water density changes is projected to be slightly larger at Forsmark compared to the global mean. These changes are primarily driven by regional differences in thermal expansion as a result of the projected enhanced warming in the northern high latitudes (Section 3.5.1). In contrast, the effect on the density of salinity changes is projected to be relatively small because increased total river runoff to the Baltic Sea will be approximately compensated for by an increased inflow of saltwater through the Danish straits due to higher sea levels (Meier et al. 2022). Within this century, the contribution to the global-mean ASL rise from the Greenland ice sheet is projected to be larger than that from the Antarctic ice sheet (e.g. Fox-Kemper et al. 2021). As a result of these projections, and because melting of the Greenland ice sheet has only a negligible or small impact on the ASL in the Baltic Sea (Section 5.2.1), Pellikka et al. (2020) projected that the mean ASL rise at Forsmark until 2100 AD will be ~13 % lower than the global mean (Table 5-2).

This result arguably stands in stark contrast to present-day trends of altimetry data, which demonstrates that the current ASL rise at Forsmark is about 50 % faster than the global mean (Section 5.4.1). However, as discussed in Section 5.4.1, these elevated trends are mainly a result of an increased sea-level acceleration over the last 5–10 years, and there are several processes contributing to the natural variability over these timescales. However, further monitoring is needed in order to establish whether the trends of the last 5–10 years conform to natural variability or if they are embedded in regional ASL rise changes caused by global warming.

It is also important to note that the maximum extreme RSL increase of 4 m (with an approximate equal contribution from a mean rise in ASL and storm-surge level), used by SKB for construction and adaptation (Section 5.1.2), was estimated based on several (purposely chosen) cautious assumptions regarding the mean ASL rise. For example, it is based on the mean ASL rise projections under the high-end emission scenario (RCP8.5/SSP5-8.5), despite an increasing body of research in recent years arguing that this emission scenario is unlikely until 2100 AD (Section 2.6.1). For emission scenarios more consistent with current developments (e.g. SSP2-4.5), high-end ASL rise projections at Forsmark are 70–90 cm lower than under SSP5-8.5 (Pellikka et al. 2020, Table 2-4). Another example concerns the future extent of the projections; the estimated extreme RSL increase of +4 m is based on mean ASL rise projections for the year 2100 AD, despite the currently planned closure of SKB repositories being between 2080 AD and 2090 AD. The extended period of 10–20 years accounts for a significant contribution to the total mean RSL change under high emission scenarios, which exhibit a relatively constant acceleration during the entire century.

---

[19] Pellikka et al. (2020) only presented percentiles of RSL change at Forsmark. The corresponding global mean ASL rise were estimated from these RSL changes in combination with GIA and the estimated ratio of the Forsmark to the global ASL rise by 2100 AD. The latter is estimated to be 87 %, see Figure 2-1 in Pellikka et al. (2020).

Owing to this acceleration, the mean ASL rise under SSP5-8.5 between 2080 AD and 2100 AD is approximately equal to that between 2000 AD and 2080 AD (SKB TR-23-05, Figure 3-41). As a result, mean ASL rise projections under this emission scenario are about 50–60 cm lower for 2080 AD than for 2100 AD (Pellikka et al. 2020, Table 2-5). The inclusion of these cautious assumptions ultimately entails that the mean RSL used in the assessment of extreme sea levels at Forsmark is likely overestimated (even for the chosen low probability level). Moreover, the inclusion of these assumptions means that any gained knowledge that may emerge until closure of SKB's repositories – and that would revise the current mean ASL rise estimates to even higher values – would not necessarily result in a revised estimate of the high extreme RSL at the site. This may also include a potential continuation of the current higher-than-average ASL rise trends at Forsmark.

Extreme sea levels and total combined RSL change

Changes in sea-level extremes due to storm surges and wind waves in a future warmer climate will primarily depend on the prevailing meteorological conditions, in particular future changes in storminess. However, future changes in high-end wind velocities as well as their probability distributions are highly uncertain, since the models do not agree on the sign of future wind speed changes over the Baltic Sea (e.g. Christensen et al. 2022). Consequently, maximum storm-surge levels estimated for the present-day climate in Pellikka et al. (2020) (Table 5-1) was for simplicity assumed to prevail for the entire future period until 2100 AD. The same approach has also been used in other studies (e.g. Hieronymus and Kalén 2020).

For each of the investigated emission scenarios, the probability distributions for the mean RSL change and the storm-surge levels in Pellikka et al. (2020) were summed into new distributions for the years 2050 AD, 2080 AD and 2100 AD. The maximum extreme RSL of 4 m (Section 5.1.2) coincides with a probability of 10^{-5} derived from the resulting distribution for RCP8.5 in the year 2100 AD.

The summation of distributions of the mean RSL rise and storm-surge levels was carried out under the assumption that the individual distributions are independent (convolution) (Pellikka et al. 2020). This assumption is arguably not completely realistic because wind velocities control both storm surges and inflow rates to the Baltic Sea (albeit at different timescales, see Section 5.2). However, as the highest inflow to the Baltic Sea occurs during prevailing westerly winds, the maximum contribution of such interactions between storm surges and the mean RSL will mainly influence the eastern coast of the Baltic Sea (Weisse et al. 2021). Thus, wind conditions resulting in the highest storm surges over the western parts of the Baltic Sea, including Forsmark, typically do not coincide with the highest mean RSL values across the basin.

5.5.2 Until 12 000 AD

The projected RSL evolution over multi-millennial timescales is associated with an even greater uncertainty than the projected RSL change during this century. Over these longer timescales, primarily changes in mean RSL are of interest for SKB as these are used to determine the duration of submerged conditions in the area above SFR and the possibility of transgression that may result in submerged conditions in the area above the spent fuel repository after closure. Sea-level extremes (including storm-surge levels) are not relevant for SKB after 2100 AD when repositories are planned to be closed.

The processes of interest for the RSL evolution on multi-millennial timescales are mainly the global-mean ASL change and GIA, both of which have the potential to contribute to the RSL by several tens of metres during the coming 10 000 years (e.g. SKB TR-23-05, Section 3.5.3). Details on how processes that affect the regional ASL in the Baltic Sea, e.g. fresh water input or changes in the large-scale atmospheric circulation, may contribute to the mean RSL over these long timescales are inherently uncertain. However, as the maximum impact on the RSL of these processes are orders of magnitude lower than the potential tens-of-metres changes induced by global-mean ASL rise and GIA, they are omitted from the analysis.

Over the next 10 000 years, RSL evolution due to GIA will be determined by the remaining adjustment following the last glacial maximum, since no new ice-sheet build-up is expected during this time (Section 2.5.2). This situation is analogous to the situation about 120 kyr ago, after the previous interglacial period. Therefore, the reconstructed RSL evolution from the combined GIA/empirical model (Section 5.3, Figure 5-2) is used as an analogue for the coming 10 000 years at Forsmark. According to the reconstruction, the ongoing GIA will continue over the coming 10 000 years, albeit at an increasingly slower rate than at present. Specifically, for this period the rate of GIA is projected to decrease at a near exponential rate such that GIA is about 50 % lower than at present after 10 000 years. However, the present-day GIA in the reconstructed evolution amounts to ~6.0 mm yr^{-1}, which is slightly slower than the GPS-based estimate of 6.7 mm yr^{-1} (Section 5.4.1). Therefore, for consistency with the current knowledge of the present-day rate of GIA, the future evolution at Forsmark is here approximated using an exponential function constrained by the condition that the present-day GIA rate is 6.7 mm yr^{-1} (Appendix C2). This approximation yields a similar GIA contribution over the next 10 000 years as the reconstruction obtained from GIA/empirical modelling (Appendix C2, Figure C-1). The exact representation of GIA over the next 10 000 years is arguably subject to great uncertainty as it is essentially based on simulations from only one model. The effect of this uncertainty for the safety assessments for SFR and spent fuel repository is further discussed in Section 5.6.

Owing to the slow uptake of heat in the oceans and slow equilibration of the ice sheets to the prevailing climate conditions, ASL is expected to continue to rise for several thousands of years after the atmospheric warming has stopped. It has been estimated that even if the total anthropogenic warming would be limited to 1.5–2 °C, the multi-millennial ASL rise commitment, could potentially reach several metres above the pre-industrial level due to irreversible ice loss from Greenland and Antarctica (e.g. Levermann et al. 2013, Pattyn et al. 2018). In general, due to the long lifetime of atmospheric CO_2 (Section 2.2.2), some percentage of historical and future anthropogenic emissions will remain in the atmosphere for the next 10 000 years regardless of the amount of future emissions (unless the excess CO_2 is removed from the atmosphere by technical measures). Thus, the next 10 000 years will likely, on average, be characterised by warmer-than-present climate conditions at Forsmark (Section 3.5.2), and this warming will gradually increase the ASL-rise commitment over this time period.

The number of ASL rise projections for the next 10 000 years is much more limited than corresponding projections for the next century. Low- and high-end RSL projections for 12 000 AD at Forsmark were therefore only based on two modelling studies in the PSAR assessments for the spent fuel repository and SFR (Table 5-3). The two studies (Levermann et al. 2013, Clark et al. 2016) present widely different sensitivities of the Antarctic ice-sheet disintegration to global warming, conforming to the large conceptual uncertainty related to ASL contributions from processes governing the stability of the Antarctic ice sheets. Whilst a major disintegration of the West Antarctic ice sheet occurs in both studies, the projections in Levermann et al. (2013) suggest that the East Antarctic ice sheet remains relatively stable even for a forcing corresponding to 4 °C temperature increase. In contrast, the modelling of Clark et al. (2016) projects that also the East Antarctic ice sheet will experience major ice losses for relatively modest emissions (Table 5-3) that limit the warming to < 3 °C (Tables 2-2 and 3-8). As a result of the different Antarctic ice-sheet responses in the studies, the uncertainty in global-mean ASL rise for the next 10 000 years was very large in the PSAR assessments, ranging from 11 to 38 m for moderate global warming (approximately corresponding to RCP4.5) and from 14 to 52 m for strong global warming (approximately corresponding to RCP8.5). Owing to the widely different Antarctic ice-sheet responses in the studies, it was assessed not to be meaningful to account for differences in the regional ASL rise due to fingerprints from different ice sheets. Hence, in the PSAR, it was reasonable to assume that the global mean ASL rise projections for the next 10 000 years were representative also for Forsmark.

Subsequent to the preparation of the PSAR climate reports, another modelling study on multi-millennial ASL changes has been published (Van Breedam et al. 2020; see Table 5-2). The projections in that study show minor disintegrations of the East Antarctica ice sheet under the highest emission scenarios. This arguably stands in contrast to the projections in the study of Clark et al. (2016), which feature continental-scale disintegrations of the East Antarctic ice sheet under similar emission scenarios.

The discrepancy between these studies can primarily be explained by differences in the modelled climate sensitivity, i.e. the projected global-mean warming under high emissions in Van Breedam et al. (2020) is lower than under comparable emissions in Clark et al. (2016)[20]. In consequence, when mapping the ASL rise to the maximum global-mean SAT increase (relative to pre-industrial over the simulation time of 10 000 years) instead of emission scenarios, differences in the ASL rise commitment between the studies are noticeably reduced. For example, both studies project an ASL rise in the range of 35–40 m for SAT increases of about 5 °C (Table 5-3). Remaining differences in ASL rise projections between the studies can primarily be explained by differences in the sensitivity of specific ice sheets to a certain level of warming, with melting of the Greenland ice sheet being more sensitive in Van Breedam et al. (2020) and disintegrations of the Antarctic ice sheets occur at lower warming levels in Clark et al. (2016). However, both studies generally project higher ASL rise over the next 10 000 years than Levermann et al. (2013); this is particularly evident for warming levels of 3 °C or higher (Table 5-3).

Table 5-3. Projections of published global-mean ASL rise for 12 000 AD under different warming/emission scenarios. Approximate values of the projected maximum warming (relative to pre-industrial SAT) from the publications that used scenarios based on carbon emissions are also indicated. Note that the timing of this warming varies between the studies. The grey shading in the two rightmost columns indicates that the study was included in the RSL-compilations in the PSAR (SKB TR-20-12 and SKB TR-23-05) and in IPCC AR6 (Fox-Kemper et al. 2021). Note that only median/best-estimate projections are given in the table; associated uncertainty estimates are provided in the original publications

Study	Global-mean ASL rise at 12 000 AD	Emission scenario	Maximum global-mean warming	PSAR	IPCC AR6
Levermann et al. (2013)	2.5 m	*No emissions underlying the warming levels were assumed.*	1 °C	▨	
	10.9 m		2 °C		
	12.5 m		3 °C		
	13.9 m		4 °C		
Clark et al. (2016)	3.7 m	320 Pg C total emissions	1.5 °C	▨	▨
	12.7 m	640 Pg C total emissions	2.0 °C		
	17.2 m	960 Pg C total emissions	2.5 °C		
	25.2 m	1280 Pg C total emissions	3 °C		
	37.5 m	2560 Pg C total emissions	5.5 °C		
	45.7 m	3840 Pg C total emissions	7 °C		
	52 m	5120 Pg C total emissions	8.5 °C		
Van Breedam et al. (2020)	9.2 m	461 Pg C total emissions	1.5 °C		▨
	10.1 m	1361 Pg C total emissions	2.5 °C		
	15.4 m	2234 Pg C total emissions	3 °C		
	21.9 m	3393 Pg C total emissions	4 °C		
	30.1 m	5288 Pg C total emissions	4.5 °C		
	37.4 m	5888 Pg C total emissions	5 °C		

---

[20] In general, the equilibrium climate sensitivity (ECS) derived from the Clark et al. (2016) projections is more consistent with the central estimate by the IPCC (2.0 – 4.5ºC per doubling of atmospheric CO_2 concentration; see Section 3.2.1), while the sensitivity derived from Van Breedam et al. (2020) is lower than that reported by the IPCC.

In IPCC AR6, the committed ASL rise over the next 10 000 years was compiled for global warming up to 5 °C above pre-industrial SAT based on the results of Clark et al. (2016) and Van Breedam et al. (2020) (Table 5-4); these were also compared with evidence from paleo-proxy records[21]. The IPCC emphasises that the estimated ranges of global-mean ASL rise over these longer timescales are based on only a few studies; thus, there is limited evidence on the magnitude of the multi-millennial ASL rise.

In this report, the global-mean ASL rise over the next 10 000 years compiled in IPCC AR6 is used together with results of the GIA simulations mentioned above to estimate the Forsmark RSL evolution over the next 10 000 years for a global warming of between 1.5 °C and 5 °C. The resulting low- and high-end ASL rise estimates (blue lines in Figure 5-6) are estimated by fitting an arctan function to the highest and lowest IPCC-based ASL rise projections in Table 5-4 (see Appendix C2 for details). The resulting RSL evolution (red lines in Figure 5-6) is obtained by adding the ASL rise projections to the GIA contribution (green lines in Figure 5-6). The results show that RSL at Forsmark is projected to continue to decrease (i.e. a continued marine regression) over the next 10 000 years for warming levels ≤ 3 °C above the pre-industrial SAT, while an initial RSL increase (a marine transgression) is projected for warming levels of 4 °C or higher. However, even under these higher warming levels, the effect of GIA will eventually exceed that of the ASL and, thus, the RSL will be lower than at present after 10 000 years in all considered warming scenarios.

In their latest compilation of the multi-millennial ASL rise, the IPCC omitted projected multi-millennial warming levels corresponding to unlikely high emission scenarios, such as SSP5-8.5. While the global-mean warming under this scenario is projected to be limited below 5 °C until 2100 AD, it is projected to continue to increase for several centuries after 2100 AD, potentially reaching double-digit warming levels after a few centuries (Table 3-10). Therefore, the compilation by the IPCC is here complemented by an upper-bound estimate, corresponding to a scenario resulting in 8.5 °C warming (see Table 5-3) in Clark et al. (2016). Under this extreme scenario, almost all land ice is projected to melt resulting in an ASL rise commitment of 52 m (this can be compared with the ASL rise from melting of *all* land ice, which amounts to approximately 58 m). The same upper-bound estimate of the multi-millennial ASL rise was used in the PSAR, and results in approximately 15 000 years of higher-than-present RSL at Forsmark (SKB TR-20-12, Section 5.3 and SKB TR-23-05, Section 3.5).

Table 5-4. Global mean ASL rise commitments under different warming levels as estimated in IPCC AR6 (Fox-Kemper et al. 2021) based on Clark et al. (2016) and Van Breedam et al. (2020). Values are reproduced from Table 9.10 in Fox-Kemper et al. (2021)

Temperature increase above pre-industrial	2000-year commitment	10 000-year commitment
1.5 ºC	2 – 3 m	6 – 7 m
2 ºC	2 – 6 m	8 – 13 m
3 ºC	4 – 10 m	10 – 24 m
4 ºC	12 – 16 m	19 – 33 m
5 ºC	19 – 22 m	28 – 37 m

---

[21] Notably, the IPCC concludes that processes such as MICI, which contributes to the deep uncertainty on centennial timescales, do not have a substantial effect on the multi-millennial ASL rise.

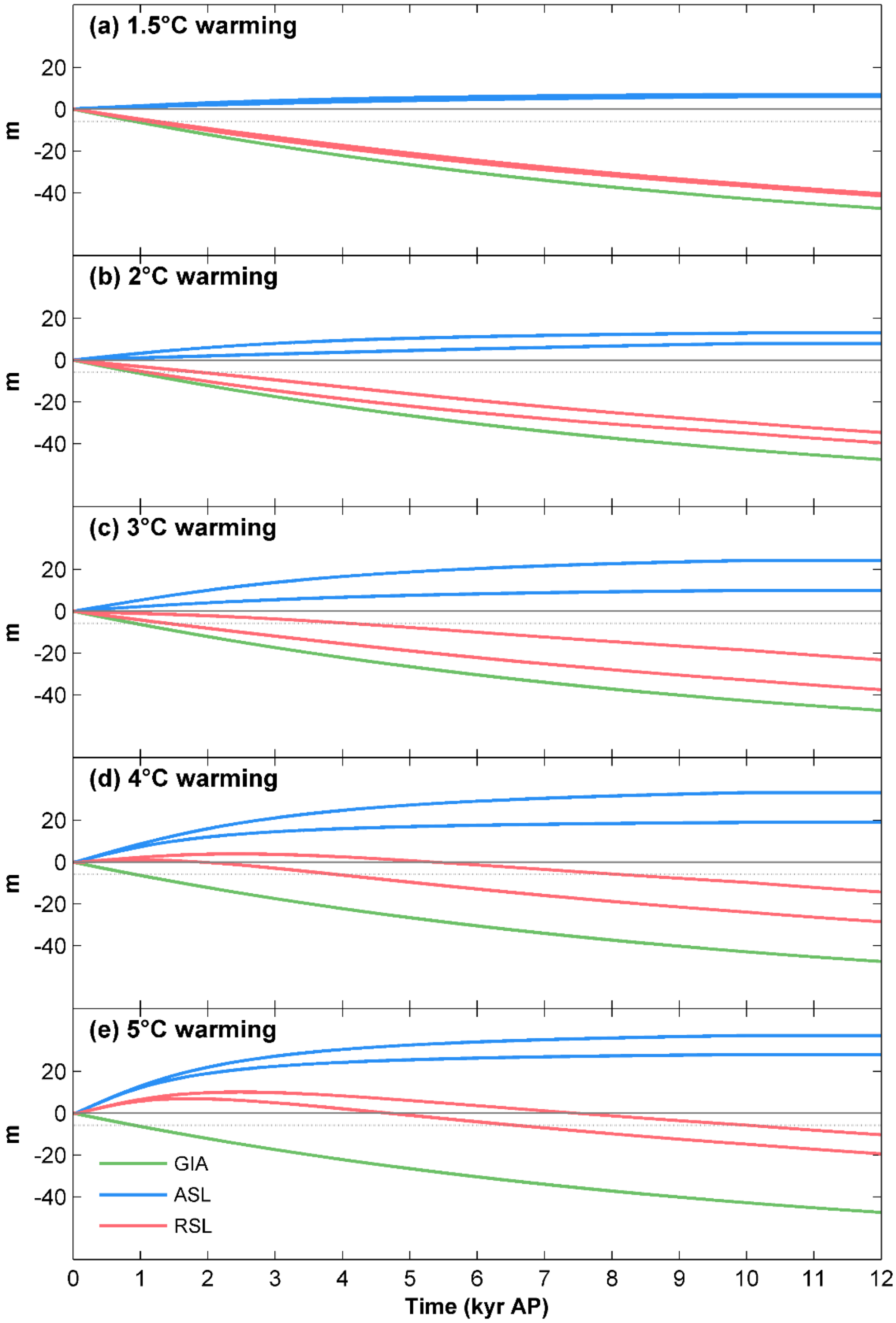

Figure 5-6. *Projected changes of GIA (green), ASL (blue) and RSL (red) at Forsmark over the next 12 kyr (relative to present-day) under global warming scenarios corresponding to 1.5 °C (a), 2 °C (b), 3 °C (c), 4 °C (d) and 5 °C (e) above the pre-industrial SAT. The two ASL evolutions correspond to low- and high-end estimates provided in IPCC AR6 (Fox-Kemper et al. 2021). The corresponding RSL evolutions are calculated by adding GIA to the two ASL evolutions. The grey dotted line indicates the threshold (-5.8 m below the present annual average water level at the site) by which transitions between submerged and terrestrial conditions are defined for SFR (see further Section 5.6.1). The grey solid line indicates zero RSL, which is used as a threshold by which transitions between submerged and terrestrial conditions are defined for the spent fuel repository (see further Section 5.6.2).*

5.5.3 Beyond 12 000 AD and future glacial cycles

Regardless of the degree of anthropogenic warming during the next few centuries, the rate of ASL rise is projected to gradually decline towards zero over the next 10 000 years (Figure 5-6), resulting in that RSL at Forsmark will be dominated by GIA uplift beyond 12 000 AD. Modelling simulations indicate that the GIA uplift will contribute to a lowering of RSL by more than 60 m over the next 30 000 years (see e.g. Appendix C2, Figure C-1), despite a declining rate of GIA during this period. This value is subject to great uncertainty due to uncertainties in the input data and representations of the governing processes in the GIA model (Appendix C2). Accounting for the GIA uncertainty, it cannot be excluded that the effect of GIA uplift will result in the isolation of the Gulf of Bothnia from the rest of the Baltic Sea towards the end of this 30 000 year-period if the ASL rise is low (SKB TR-10-09). Such development would result in reduced salinity in the Gulf of Bothnia, since the Gulf at this stage would constitute a large lake fed by freshwater from surrounding terrestrial regions. Note however that Forsmark, if this scenario were to occur, would be situated far from the shoreline of the Gulf of Bothnia due to the GIA uplift.

After 30 000 years, RSL at Forsmark is expected to remain relatively constant, or slightly decline, until the onset of the next glaciation in the Northern Hemisphere (this ranges from ~50 kyr to >500 kyr AP depending on the amount of future GHG emissions, see Section 2.5.2). The possibility of RSL decline during this period is motivated by that the anthropogenic warming will gradually decrease, resulting in potential regrowth of previously disintegrated land ice.

After the first glaciation in the Forsmark region, the RSL response will be primarily determined by the spatiotemporal evolution and thickness of the overriding ice sheets. For example, if most of the land ice associated with future glaciations would be located in North America, with no, or only very limited, ice-sheet expansion in Fennoscandia, RSL at Forsmark would decrease due to a fall of the global-mean ASL along with a small or negligible effect of GIA. In contrast, if the future ice sheets are sufficiently large to cover Fennoscandia, including the Forsmark area, it is likely that the magnitude of the resulting isostatic depression exerted by the load of the ice sheet exceeds the magnitude of the ASL decrease. Under such development, submerged conditions would prevail in Forsmark for some time after the ice sheet has left the area, i.e. similar to the development reconstructed for the Weichselian glacial cycle (Section 5.3.1).

To estimate potential future durations of post-glacial submerged conditions in Forsmark, we assume that RSL following a glaciation will be controlled by GIA, similar to during the Weichselian glacial cycle. To this end, we use the so-called Local Lithosphere and Relaxing Asthenosphere (LLRA), which is a simple model of glacial isostasy (see further Appendix C3). The model assumes that the steady-state vertical displacement of the lithosphere is proportional to the local overburden ice thickness. However, owing to the viscous properties of the asthenosphere, the actual displacement will not be in steady-state immediately. Instead, the response is lagged and the model parameterises this lag by a time constant, τ_a (Appendix C3). Forcing the LLRA model with the reconstructed ice loads of the Weichselian (Section 4.3.1) shows that τ_a= 5000 years yields a good agreement of post-glacial submerged periods with the results of the comprehensive GIA model for the Wechselian (Section 5.3.1).

It is important to note that the duration of the post-glacial submerged period during the Weichselian was determined by both ASL and GIA changes, of which only GIA is explicitly represented in the LLRA model. Consequently, when the model is calibrated against full Weichselian RSL data, ASL changes are implicitly accounted for in the estimation of the time-lag constant τ_a. A limitation of the model is therefore that any prediction of future submerged durations assumes a similar ASL-to-GIA ratio as in the calibration data. In those data, the GIA component at Forsmark exceeds the ASL component by roughly a factor of six during periods of ice coverage[22].

The calibration of the simple LLRA model enables exploring the duration of post-glacial submerged conditions for a wide range of ice-coverage durations and ice thicknesses. The shortest investigated duration for an ice sheet covering the Forsmark region is set to 1000 years.

---

[22] For example, during the LGM the reconstructed RSL in Forsmark was about +500 m relative to the present day (Figure 5-2). Since the observed ASL change at that time was around –100 m (Section 5.2.2), the GIA component must have been approximately +600 m – about six times larger in magnitude than the ASL change.

The corresponding longest duration is set to 50 kyr, which is comparable with the longest durations found in the analysis of future ice-sheet variability in Forsmark (Section 4.5.2). Ice thicknesses range from 100 to 4000 m, the latter corresponding to the estimated maximum ice thickness in the region over the next 1 Myr (Section 4.5.1). For all investigated ice configurations, we assume that the advance and retreat of the ice sheet, from zero to the maximum ice thickness and vice versa, occurs over a period of 500 years[23]. During these time intervals, interpolation to and from the maximum ice thickness follows a square-root function. Compared to a traditional linear interpolation, this function yields a faster ice build-up during the initial part of the advance and a faster disintegration during the latter part of the retreat, in line with Weichselian ice-sheet reconstruction of Forsmark (Figure 4-8).

The simulated time of post-glacial submerged conditions in Forsmark in response to the considered ice durations and thicknesses are shown in Figure 5-7. Submerged conditions in Forsmark occur when the vertical down-warping exceeds 70 m; this approximately corresponds to the remaining land uplift in the area due to the Weichselian ice sheet (see further Appendix C3). The main results are summarised in the following.

- For ice thicknesses lower than ~500 m, the down-warping of the lithosphere is less than 70 m. The same is true for thicknesses lower than ~2000 m if Forsmark is ice-covered for only 2000 years or less. Thus, for these cases, terrestrial conditions will prevail at Forsmark following a glaciation. Although such cases cannot be excluded on a 1-Myr timescale, they are considered to have a low likelihood of occurrence. This conclusion is based on the ice-sheet projections (Section 4.5). For example, in the analysis of future ice-sheet variability (Section 4.5.2), only about 5 % of the projected ice durations in Forsmark have a duration of 2000 years or shorter across all scenarios and simulations. Furthermore, the parameter sensitivity simulations of the MIS 6 ice sheet in Eurasia suggest either a considerable thickness (>2000 m) over Forsmark or that the ice sheet fails to reach Forsmark; none of the sensitivity simulations projected an ice sheet of a thickness of 500 m or lower (Section 4.5.1).
- The duration of the submerged period increases substantially for ice cover durations up to approximately 10 kyr. However, for an ice coverage of 10 kyr or longer, the sensitivity of the submerged period to the ice cover duration is dramatically reduced. For example, for a 3000 m thick ice sheet, the duration of the submerged period increases from 2 to 11 kyr between ice durations of 1 and 10 kyr, while the corresponding increase of the submerged period is only 1 kyr between ice durations of 10 and 50 kyr. The reason for this is that for long ice-cover durations, the lithosphere displacement in the LLRA model reaches near steady-state with the underlying viscous asthenosphere and the overburden ice load.
- For longer periods of ice coverage (>10 kyr), the duration of the post-glacial submerged period is primarily determined by the ice thickness. However, for typical ice thicknesses simulated over Forsmark (2000–3500 m, see Sections 4.3.1 and 4.5.1), differences in the duration of the ensuing submerged period, which ranges from ~8 to ~12 kyr, are relatively small compared to the projected differences in ice duration (Section 4.5.2). Consequently, assuming 10 kyr as a typical duration of a post-glacial submerged period would be reasonable simplification for ice-cover durations exceeding 10 kyr.

Examples of likely and bounding case evolutions of climate domains in Forsmark, including periods of post-glacial submerged conditions calculated with the LLRA model, are shown in Chapter 8.

---

[23] This is a crude simplification. For instance, in the Weichselian reconstruction the characteristic timescales of ice-sheet advance (250 years) and retreat (50 years) were both shorter than 500 years (Section 4.6.2). The simplification is nevertheless justified because the submerged durations produced by the LLRA model are not sensitive to the exact rates of ice-sheet advance or retreat (not shown).

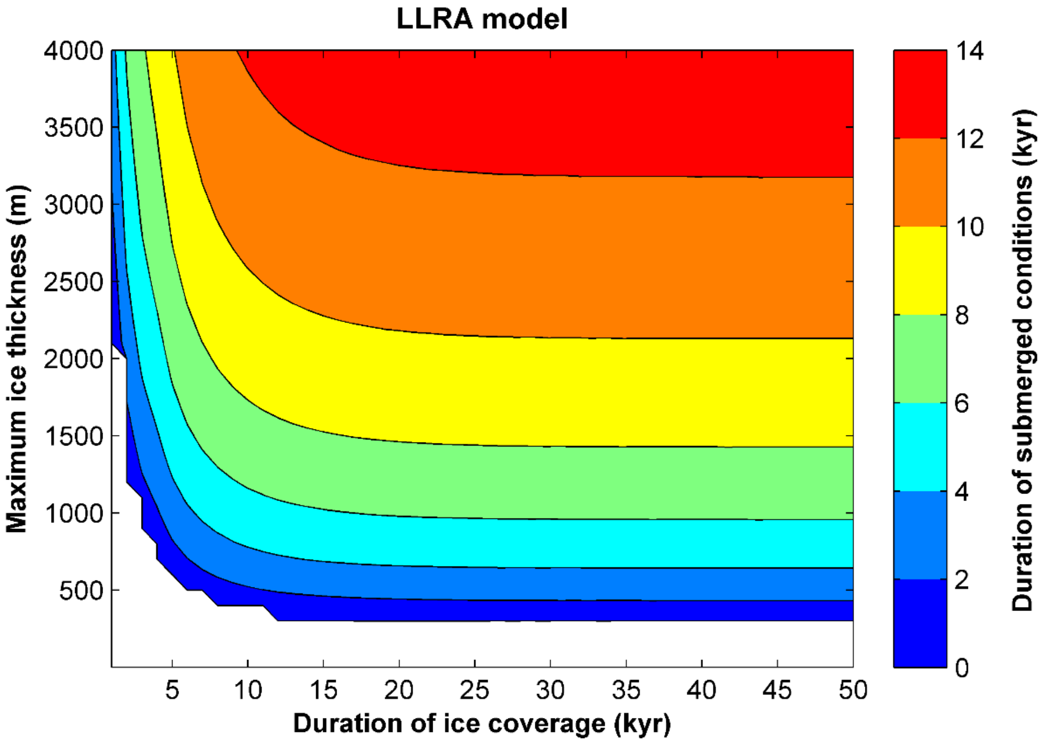

Figure 5-7. *Simulated time of post-glacial submerged conditions using the LLRA model forced by hypothetical ice loads with different ice thicknesses and ice-cover durations. The LLRA model has been calibrated using Weichselian conditions (see Appendix C3).*

5.6 Safety assessment-specific questions

5.6.1 Duration of initial submerged conditions above SFR

As discussed in Section 5.1.2, one key question for the post-closure safety of SFR is how long the area above the repository will remain located beneath the sea after closure. At present, the maximum water depth above SFR is defined to be 5.8 m (SKB TR-23-05, Section 1.4.3). If the RSL decreases below this level, the area is considered to be terrestrial even if limited areas above the repository are still covered by the sea, or can be temporarily submerged in connection with storm surges. Terrestrial conditions imply a higher groundwater flow through the bedrock and repository as well as the emergence of potential discharge areas for radionuclides above sea level (Section 5.1.2). Based on this threshold, a wide range of durations of submerged conditions, ranging from approximately 1000 to 18 000 years, were considered possible outcomes in the PSAR (SKB TR-23-05, Section 3.5.3). This range emanated from the uncertainty in the climate warming and how the ice sheets will respond to that warming.

The assessment of the highest possible RSL over the next 10 000 years is based on the same simulations as in the PSAR (8.5 °C warming scenario in Clark et al. 2016) (Table 5-3). Thus, the maximum possible duration of the initial submerged period in the area above SFR is assessed to be the same as in the PSAR, i.e. approximately 18 kyr (Table 5-5). The most recent estimates of the shortest durations of the submerged period also agree reasonably well with the assessment in the PSAR: 1000 years of submerged conditions correspond approximately to the projected duration under the lowest (1.5 °C) warming scenario as well as to lower-end projections under 2–3 °C warming (Table 5-5). Table 5-5 also shows that the initial duration of the submerged period will be 10 000 years or shorter if global warming is limited to 5 °C above the pre-industrial SAT. A maximum warming lower than 5 °C above the pre-industrial (~4 ºC above present-day SAT) is projected for all emission scenarios except for SSP3-7.0 and SSP5-8.5 (Table 3-10).

The evaluation of Forsmark RSL in Section 5.5.2, as well as the resulting duration of the submerged conditions in the area above SFR, has only accounted for the uncertainty in the ASL rise for each degree of warming. However, also the future GIA evolution is subject to great uncertainty; this mainly concerns the magnitude of the remaining post-glacial GIA uplift which likely amounts to several tens of metres (SKB TR-10-49, Section 3.3). Given that it has been demonstrated that submerged conditions above SFR serve to mitigate potential post-closure consequences (Section 5.1.2), it is important to evaluate how this GIA uncertainty may affect the future durations of submerged conditions estimated here. This is particularly important for the shortest estimated durations as these have been demonstrated to yield the highest radiological consequences (e.g. SKB TR-23-09, Section 5.8.2). To account for this uncertainty, it is pessimistically assumed that the observed present-day GIA will continue at the same rate (6.7 mm yr^{-1}) for the next 10 kyr. This is considered to be a bounding case, because the rate of GIA uplift will decline at least to some degree during this period. The analysis shows that the effect of a constant GIA uplift on the low-end durations of the submerged period is limited; under 1.5 °C and 2 °C warming, the duration of the initial submerged period with this GIA approximation is shortened by only 100 years compared to using an exponential GIA uplift rate.

The uncertainty in GIA may also affect the maximum duration of submerged conditions estimated here. In the most extreme case if taking these uncertainties into account, projected RSL changes due to GIA could even be smaller than the maximum ASL contribution under the assumption that virtually all land ice on Earth were to disintegrate into the oceans. However, it is considered highly unlikely that the maximum period of submerged conditions will be significantly longer than the 18 kyr estimated here. The reason is that the anthropogenically-induced warming is expected to gradually decrease over multi-millennial timescales (Section 3.5.2), and this would likely result in a regrowth of some of the previously disintegrated land ice and, thus, in a lowering of the ASL. For reference, it is estimated that ice-sheet inception at Antarctica began once the atmospheric CO_2 concentrations declined to levels within the range 600–900 ppmv (Gasson et al. 2014, Galleotti et al. 2016). This corresponds approximately to the projected range of CO_2 concentrations after 10 kyr under the most extreme SSP5-8.5 scenarios (assuming that 15–30 % of anthropogenic emissions are remaining, see further Section 2.5.2).

Table 5-5. Estimated durations of submerged conditions above SFR based on projected future changes due to GIA (Figure 5-6, Appendix C2) and the ASL rise. ASL-rise projections of IPCC AR6 (Fox-Kemper et al. 2021) are used for global SAT increases up to 5 °C above the pre-industrial value. The projection based on Clark et al. (2016), corresponding to a global SAT increase of 8.5 °C, represents an upper-end estimate of the possible duration of submerged conditions above SFR

Global SAT increase	Duration of submerged conditions above SFR (years AP)	Source (ASL rise)
1	1100 – 1200	Fox-Kemper et al. (2021)
2	1100 – 1900	Fox-Kemper et al. (2021)
3	1400 – 4100	Fox-Kemper et al. (2021)
4	3900 – 8100	Fox-Kemper et al. (2021)
5	6600 – 10 000	Fox-Kemper et al. (2021)
8.5	18 300	Clark et al. (2016)

5.6.2 Duration of initial submerged conditions above the spent fuel repository

In contrast to SFR (Section 5.6.1), a specific threshold representing transitions between submerged and terrestrial conditions has not been defined for the spent fuel repository. Most of the area above the planned repository is presently above sea level, implying that such threshold would be at the same elevation as the present sea level or higher. In order not to underestimate possible durations of submerged conditions above the spent fuel repository, the present sea level was cautiously chosen as threshold for submerged conditions in the PSAR (SKB TR-20-12, Section 5.1.3). The same threshold is for simplicity chosen also for the present analysis.

If the global-mean warming is limited to 3 °C, or less, compared to the pre-industrial value (corresponding to the SSP2-4.5 scenario or lower, see Section 3.5.2), the area above the spent fuel repository will likely remain terrestrial for the next millennia and beyond (Table 5-6). In fact, under these scenarios, the area above the repository will likely remain terrestrial until after the next phase of ice sheet coverage in the region, which is likely to be more than 100 kyr into the future (Section 2.5.2).

Submerged conditions over the coming millennia is only expected if global-mean warming reaches 4 °C or higher (Table 5-6). However, because of the higher elevation of the surface above the spent fuel repository compared to that above SFR, the estimated durations of submerged conditions above the repository are consistently shorter than for SFR. Specifically, possible durations of initial submerged conditions above the spent fuel repository remains well below 10 000 years for a warming up to 5 °C, whereas the maximum duration is estimated to be almost 14 000 years (Table 5-6).

Table 5-6. Estimated durations of initial submerged conditions above the spent fuel repository based on projected future changes due to GIA (Figure 5-6, Appendix C2) and the ASL rise. ASL-rise projections of IPCC AR6 (Fox-Kemper et al. 2021) are used for global SAT increases up to 5 °C above the pre-industrial value. The projection based on Clark et al. (2016), corresponding to a global SAT increase of 8.5 °C, represents an upper-end estimate of the possible duration of submerged conditions above the spent fuel repository

Global SAT increase compared to the pre-industrial value	Duration of submerged conditions above spent fuel repository (years AP)	Source (ASL rise)
1	0	Fox-Kemper et al. (2021)
2	0	Fox-Kemper et al. (2021)
3	0	Fox-Kemper et al. (2021)
4	1900 – 5400	Fox-Kemper et al. (2021)
5	4700 – 7400	Fox-Kemper et al. (2021)
8.5	13 700	Clark et al. (2016)

6 Permafrost

6.1 Introduction

6.1.1 Definitions

Permafrost is defined as ground that remains at or below the 0 °C isotherm for at least two consecutive years (French 2007). This definition is based exclusively on temperature, and disregards the texture, degree of compaction, water content, and lithologic character of the material. As a result, the term permafrost does not always equate to perennially frozen ground, since, depending on the ambient pressure and chemical composition of groundwater and on adsorptive and capillary properties of the soil, water in the ground may freeze at temperatures below 0 °C. Therefore, permafrost typically encompasses the perennially frozen ground and a surrounding so-called *cryopeg*, i.e. a ground layer in which water remains unfrozen at sub-zero temperatures.

Permafrost distribution is characterised into: i) continuous (more than 90 % spatial permafrost coverage of an area), ii) discontinuous (between 90 and 50 % coverage), and iii) sporadic (less than 50 % coverage).

6.1.2 Importance for post-closure safety

At repository depth, sufficiently low temperatures could cause pore water in engineered barriers (bentonite in buffer and tunnel backfill as well as concrete barriers) to freeze. In the most recent safety assessment for the spent fuel repository (PSAR), a threshold of –6 °C was established for detrimental freezing of the buffer clay and back-fill material (SKB TR-21-01, Section 8.3.2). The assessment concluded that such low temperatures cannot be reached at repository depth, even under the most extreme future climate conditions (SKB TR-21-01, Section 12.3). For SFR, the first potential freezing of pore water in the concrete barriers is estimated to occur following the first major insolation minimum at 54 kyr AP (SKB TR-23-01, Section 6.5.3). At this point in time, it is however expected that the physical structure of the concrete has been considerably altered compared to the original material with abundant cracks and a high porosity. Therefore, any additional degradation caused by freezing of the concrete pore water is considered to have a limited impact on the structure and properties of the concrete barriers in SFR (SKB TR-23-01, Section 6.5.9).

Freezing of water within permafrost affects thermal, hydraulic, mechanical and chemical properties in the bedrock and ground surface. Thermal properties change from those of unfrozen ground to those of frozen ground, affecting the heat transfer process. Ice formation in fractures in the bedrock and pores in the overlying soil confines groundwater flow through the presence of almost impermeable frozen ground, therefore altering the overall groundwater circulation. Ice formation can also cause deformation of the ground and changes in the mechanical stress state. Frost weathering and degradation of the ground surface and patterned ground are additional consequences of cyclic freezing and thawing processes. Moreover, exclusion of salts in the freezing of saline groundwater can lead to increased salinity concentrations in the unfrozen cryopeg. The effect of permafrost on geosphere variables is summarised in Table 6-1.

Permafrost and frozen conditions also influence the pathways of radionuclide transport from the repositories to the surface. During periglacial conditions, radionuclide transport primarily occurs in sections of the bedrock that remain unfrozen. These unfrozen layers, or *taliks*, often occur beneath a body of water, such as a lake or a river.

Table 6-1. Influence of permafrost development on geosphere variables

Geosphere variable	Climate issue variable	Summary of influence
Temperature	Permafrost depth	Permafrost is by definition a thermal condition hence having no influence on temperature.
Groundwater flow	Frozen/unfrozen fraction of groundwater	Freezing occurs at temperatures below the freezing point of bulk water. Groundwater transformed from liquid to solid phase can be regarded as immobile. Ice in fractures and pores also affects groundwater flow through permeability, which decreases with the fraction of frozen water.
Groundwater pressure	Frozen/unfrozen fraction of groundwater	The volume increase in the phase change of water from liquid to solid state causes an increase in the pressure of water which remains liquid. Moreover, freezing of water in porous soil can lead to cryosuction and a decrease of groundwater pressure in the unfrozen ground.
Groundwater composition	Frozen/unfrozen fraction of groundwater	When saline water is transformed from liquid to solid phase, the solutes are not incorporated in the crystal lattice of ice but transferred in the liquid phase. Therefore, the salinity in the unfrozen fraction increases.
Rock stresses	Frozen fraction of groundwater	Deformations due to ice formation will lead to changes in rock stresses. The effect of the changes is strongest nearest to the surface where in situ stresses are lowest.
Fracture geometry	Frozen fraction of groundwater	Freezing can have some influence on the fracture geometry at shallow depths due to frost cracking.

6.1.3 Previous documentation

Development of permafrost and frozen ground in Forsmark has been described in previous climate reports produced for SKB's safety assessments of the spent fuel repository and SFR (e.g. SKB TR-10-49, SKB TR-13-05, SKB TR-20-12 and SKB TR-23-05). The latest climate reports (PSAR) for both the spent fuel repository and SFR include dedicated sections on the key processes controlling permafrost and frozen ground development in the Forsmark area (SKB TR-20-12, Section 3.4, SKB TR-23-05, Section 2.1). The PSAR climate report for the spent fuel repository featured a reconstruction of the development of permafrost and perennially frozen ground during the Weichselian glacial cycle based on numerical modelling (SKB TR-20-12, Section 3.4.4). That report also includes an assessment of maximum permafrost depth, incorporating both the Weichselian reconstruction and a severe permafrost case with ~70 kyr of uninterrupted permafrost conditions in Forsmark (SKB TR-20-12, Sections 4.4.3 and 5.5.3). For SFR, the PSAR climate report includes an assessment of the timing of the first future occurrence of permafrost and frozen ground based on numerical modelling by Brandefelt et al. (2013) (see also SKB TR-23-05, Section 2.1).

Most of the information about the development of permafrost and perennially frozen ground compiled in previous SKB documents are only briefly summarised in this chapter. Instead of repeating previously published information, this chapter focuses on new results since the preparation of the PSAR climate reports. Specifically, this includes an assessment of permafrost variability in Forsmark over the next 1 Myr, based on climate simulations driven by future insolation changes and various anthropogenic GHG emission scenarios (Section 6.5.1), as well as an evaluation of permafrost depth based on these projections (Section 6.5.2).

6.2 Controlling variables and conditions

6.2.1 Climate and surface conditions

The principal factors controlling the heat exchange between the atmosphere and the Earth's surface are climate, topography, vegetation and snow cover, soil characteristics and water bodies. These factors are mutually dependent and can vary considerably in time and space. The main climate quantities of importance for permafrost formation are insolation, SAT, wind and precipitation. Insolation is a driving force governing the heat exchange between the atmosphere and the Earth's surface and affecting the other climatic parameters. SAT, which is commonly applied to map permafrost distribution, controls the longwave atmospheric radiation, turbulent heat exchange, and evaporation and condensation. Wind, in turn, mainly influences the sensible heat exchange, but also latent heat production and loss. Precipitation together with evaporation and condensation determine groundwater recharge, affecting the groundwater composition and flow, and hence the terrestrial heat flux.

Topography has a significant impact on climate conditions. Generally, SAT decreases as altitude increases being affected by radiation, convection and condensation. The average SAT decrease is approximately 0.65 °C for every 100 metres increase in height. In addition, inversions are common in hilly terrain causing low-slope low-lying areas to experience significantly lower temperatures than higher lying and steeper-slope areas. Furthermore, the slope angle and azimuth affect the flux of shortwave radiation, and where topographical differences are large, a patchier distribution of permafrost is expected.

Vegetation and snow cover are sensitive to climatic conditions and topography. The characteristic parameters of the surface cover are surface albedo, emissivity, and roughness controlling the incoming shortwave radiation, the longwave terrestrial radiation and turbulent heat exchange, respectively, as well as the thermal properties and the thickness of the surface cover affecting terrestrial heat transfer.

In general, vegetation and snow cover mitigate the reduction of ground temperature, and thus the aggradation of permafrost. Vegetation is an insulating cover limiting cooling in winter and warming in summer, hence reducing the annual fluctuation of ground temperature. Vegetation is also important for the creation of snow cover, which protects the ground from heat loss in winter. However, the high albedo of snow can lead to a snow surface temperature almost 2 °C lower than the mean winter SAT (Yershov 1998). In general, for most surface covers, permafrost can build downward from the ground surface if the annual mean SAT is lower than a value ranging between −9 and −1 °C (Washburn 1979, Williams and Smith 1989, Yershov 1998, French 2007). An exception occurs with peat layers, which can insulate the ground from warming in summer more effectively than from cooling in winter, with the resulting effect that permafrost can establish where the mean annual SAT is above 0 °C (Williams and Smith 1989).

Properties and thickness of the soil cover affect the terrestrial heat flow. Of importance are the porosity and water content of the soil, influencing the annual fluctuation of ground temperature and the thickness of the *active layer*, i.e. the seasonally thawing ground layer. The soil cover also acts as an insulating cover, since the thermal conductivity of the soil cover is lower than that of the underlying bedrock.

Water bodies, i.e. sea, lakes, and watercourses, influence permafrost creation and distribution considerably since they have high specific heat content. A talik can exist beneath water bodies that do not freeze to their bottom in winter. Depending on the climate, the critical depth of a water body to remain unfrozen in winter is approximately 0.2 to 1.6 m (Yershov 1998).

Sea water extensively inhibits permafrost development. On the other hand, when the relative sea-level of a highly saline sea is rising, submerged permafrost and perennially frozen deposits can survive for a long time beneath a cold seabed (Washburn 1979, Yershov 1998).

The hydrological conditions on the ground surface affect the freezing of groundwater. Especially under glaciated conditions, a warm-based overlying ice-sheet increases the subglacial groundwater pressure, in which case the freezing point may decrease to such a degree that the subglacial ground is kept unfrozen. A similar, but minor, effect may occur when cold ground becomes submerged and submarine freezing is reduced by the pressure of the sea water. Furthermore, groundwater flow, whether carrying fresh glacial meltwater or saline seawater, can influence the freezing process by altering groundwater salinity.

6.2.2 Bedrock and heat generation from spent fuel

The ground temperature that defines the presence of permafrost and primarily governs the freezing of water in the ground is principally controlled by the ground thermal energy balance in terms of heat transfer, geothermal heat production, the specific heat content and the amount of heat generated by phase change processes of water. Heat transfer within the ground can occur through conduction, convection and radiation (Sundberg 1988). In general, only conduction is regarded as important to permafrost development, since radiation is of importance only in unsaturated high-porosity ground at high temperatures, and convection is of importance only when groundwater and gas fluxes are large.

Heat conduction depends on the ground temperature gradient, ambient temperature conditions, and the thermal properties of the ground matter. Thermal conductivity, describing the ability of material to transport thermal energy, and heat capacity characterising the capability of material to store heat, depend on several variables such as mineralogy, porosity and groundwater content. Having typically three to four times higher conductivity than other common rock-forming minerals, quartz is the most important mineral for determining thermal characteristics in native rock materials.

Also, the spent fuel will generate heat, warming the surrounding bedrock (SKB TR-21-04). The heat production will peak at the time of repository closure and then decrease exponentially over time (e.g. Hartikainen et al. 2010).

6.3 Historical evolution

This section presents reconstructions of permafrost development in Forsmark during the last glacial cycle (Weichselian; past 120 kyr). These reconstructions were carried out using two types of numerical models: (i) a 1D permafrost model and (ii) a 2D permafrost model, which was further developed from the 1D model.

The 1D modelling was performed for the SR-Can safety assessment SKB (TR-06-23, Section 3.4). The 1D simulations were conducted specifically for the spent fuel repository location. The 2D modelling (Hartikainen et al. 2010, Hartikainen 2018) was conducted for the SR-Site and PSAR assessments and covers a 15 km long and 10 km deep vertical cross-section crossing most of the Forsmark site, including the spent fuel repository and SFR. Both simulations used site-specific input data from the Forsmark site investigation programme. Details on the input data used for the 1D permafrost simulations are found in SKB (TR-06-23, Section 3.4), and for the 2D simulations in Hartikainen et al. (2010).

The permafrost models include mathematical expressions for freezing and thawing of saline groundwater-saturated bedrock. The bedrock is considered as an elastic porous medium and the groundwater as an ideal solution of water and ionic solvents. The models are based on the principles of continuum mechanics, macroscopic thermodynamics and the theory of mixtures being capable of describing heat transfer, freezing of saline water, groundwater flow and deformations of bedrock. In the 2D version of the model, the freeze-out and transport of solutes is included (Hartikainen et al. 2010). The models are described further in Hartikainen (2004), SKB (TR-06-23), Hartikainen et al. (2010) and Hartikainen (2018).

The reconstruction of Weichselian permafrost evolution in Forsmark is based on information from both the Weichselian ice-sheet reconstruction (Section 4.3.1) and associated relative sea-level changes (Section 5.3.1), the latter of which helps to identify periods of submerged conditions. A key difference between the permafrost reconstructions presented here and the ice-sheet reconstruction in Section 4.3.1 is the availability of observational evidence. While the ice-sheet reconstruction is constrained by well-dated traces of past ice-marginal positions in the landscape, no evidence useful in this context exists for past permafrost extent. As a result, the simulated ice-sheet extents could be calibrated against observational evidence, making the boundary conditions (e.g. climate forcing) for the ice sheet simulation less critical for the accuracy of the reconstruction. In contrast, due to the lack of useful observational constraints for permafrost, greater emphasis has been placed on evaluating model performance and input data in the permafrost reconstructions. To address these uncertainties, several sensitivity simulations have been conducted – particularly with the 2D permafrost model – accounting for variations in input data. Additionally, a comprehensive validation study has been performed to compare the permafrost model output with real-world permafrost and bedrock temperature observations (Hartikainen et al. 2022).

In previous safety assessments for the spent fuel repository, the reconstructed permafrost evolution of the Weichselian was repeated 120 kyr into the future, as part of a reference glacial cycle climate case (see also Section 6.5). Because of this, both the 1D and 2D permafrost reconstructions included heat production from the spent fuel repository, with peak heat generation occurring in the beginning of the modelled glacial cycle (can be clearly seen in e.g. the top panel of Figure 6-5), followed by an exponential decline. This heat production had a minor impact on permafrost development during the first 10 kyr but was insignificant thereafter. Importantly, the inclusion of repository heat did not affect the maximum depth of permafrost and frozen ground in the simulations, as these conditions developed after several tens of thousands of years. Therefore, it is not discussed further in this report.

The following section provides a brief summary of the key results from the 1D and 2D modelling reconstructions of the development of permafrost and frozen ground in Forsmark during the Weichselian glacial cycle, including the main findings from the sensitivity simulations conducted with the 2D model. For more detailed information on these sensitivity simulations, refer to SKB (TR-20-12, Section 3.4.4) and the references therein. In both models, a reference simulation was conducted using a similar SAT forcing as for the ice-sheet reconstructions (described in Section 6.3.1) along with reference data on surface and subsurface conditions at the Forsmark site (described in detail in TR-20-12, Section 3.4.4). The section ends with a discussion of remaining uncertainties that were not covered by sensitivity simulations (Section 6.3.4), focusing on the validity of the permafrost model and the SAT forcing applied.

6.3.1 SAT forcing

The temperature in the ground is primarily controlled by the prevailing climate conditions, especially the SAT. In both the 1D and 2D permafrost simulations, the same SAT forcing was applied for Forsmark. This forcing is similar to that used in the Weichselian ice-sheet reconstruction and was initially derived from Greenland ice-core data (Section 4.3.1). To ensure that the modelled ice-sheet configurations aligned well with observed, dated ice-marginal positions in Fennoscandia, the model was calibrated by adjusting the original Greenland SAT curve (see Section 4.3.1 for details). The calibrated SAT curve was further modified (Figure 6-1) to account for periods when Forsmark was covered by ice (Section 4.3.1) or submerged beneath the sea (Section 5.3.1). Specifically, during periods of ice coverage, the SAT forcing was adjusted to reflect basal ice temperatures from the ice-sheet reconstructions, while during periods of submerged conditions, it was set to +4 °C. The final SAT forcing used in the reference permafrost simulations is represented by the blue curve in Figure 6-1.

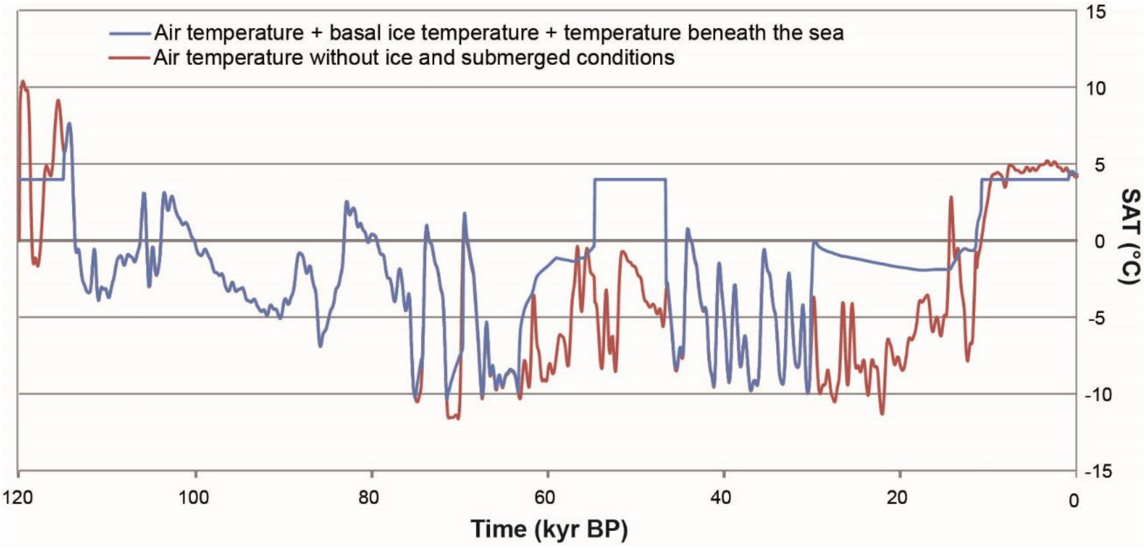

Figure 6-1. *Reconstructed SAT and basal ice temperature during glacial conditions for the Forsmark region over the past 120 kyr derived from the Greenland ice core project (see also Section 4.3.1) and used as input to the 1D and 2D permafrost simulations. The red line shows reconstructed last glacial cycle SAT curve without the presence of an ice sheet and submerged periods. The blue line includes periods of ice-sheet coverage and submerged periods, i.e. it shows simulated basal ice temperatures for periods with ice coverage over the Forsmark (Section 4.3.1) and for periods when Forsmark is submerged beneath the sea (Section 5.3.1). The SAT forcing is set to +4 °C during submerged periods.*

6.3.2 1D permafrost modelling

The 1D permafrost model was used to reconstruct permafrost conditions at the spent fuel repository location during the last glacial cycle. The results, showing the development of permafrost, perennially frozen ground and cryopeg under reference surface and subsurface conditions (SKB TR-20-12, Table 3-6), are presented in Figure 6-2. The corresponding rates of permafrost aggradation and degradation are shown in Figure 6-3.

In summary, the 1D permafrost simulations shows that SAT is the primary driver of permafrost development at Forsmark. This is evident from the correlation between the simulated permafrost depth (Figure 6-2) and the applied SAT forcing (Figure 6-1), where colder climate conditions lead to deeper permafrost and warmer conditions result in shallower depths. While subsurface conditions, e.g. bedrock thermal conductivity and ground water salinity, are less critical for determining permafrost depth, they can either enhance or reduce the depth depending on their characteristics.

The maximum permafrost depth during the last glacial cycle reconstruction occurs at around 70 kyr BP, just before the first major ice-sheet advance over the site (Section 4.3.1). At this point, the simulated permafrost depth reaches approximately 250 m at the repository location, with the frozen ground extending to about 230 m (Figure 6-2). However, the effects of uncertainties in surface and subsurface conditions on permafrost and frozen ground depths were not considered in this simulation. These uncertainties are addressed in the 2D permafrost simulations presented in Section 6.3.3.

Finally, the 1D modelling shows that permafrost can aggregate from some centimetres to some decimetres in a year whereas its degradation can occur several times faster, especially when the surface temperature rises above 0 °C and permafrost degrades simultaneously from the bottom upwards and from the top downwards (Figure 6-3).

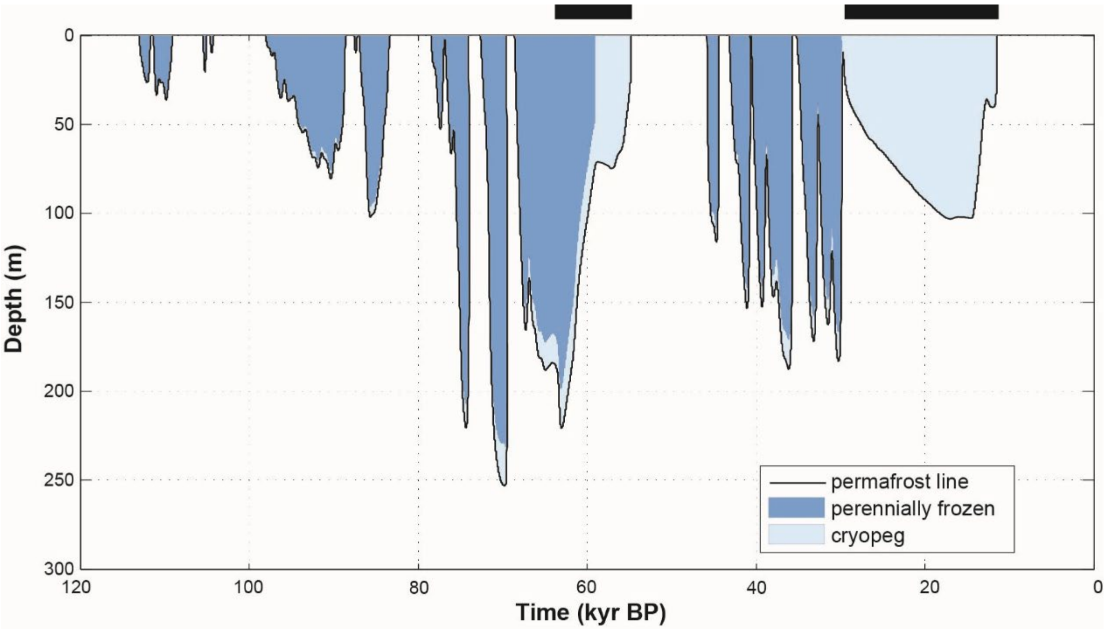

***Figure 6-2.** Reconstructed evolution of permafrost, perennially frozen ground and cryopeg at the spent fuel repository location in Forsmark using the 1D permafrost model with reference surface and subsurface conditions (see SKB TR-20-12, Section 3.4.4 for details), including the SAT forcing shown in Figure 6-1. The thick black lines above the figure mark periods of ice coverage in the simulations (as in Figure 4–8).*

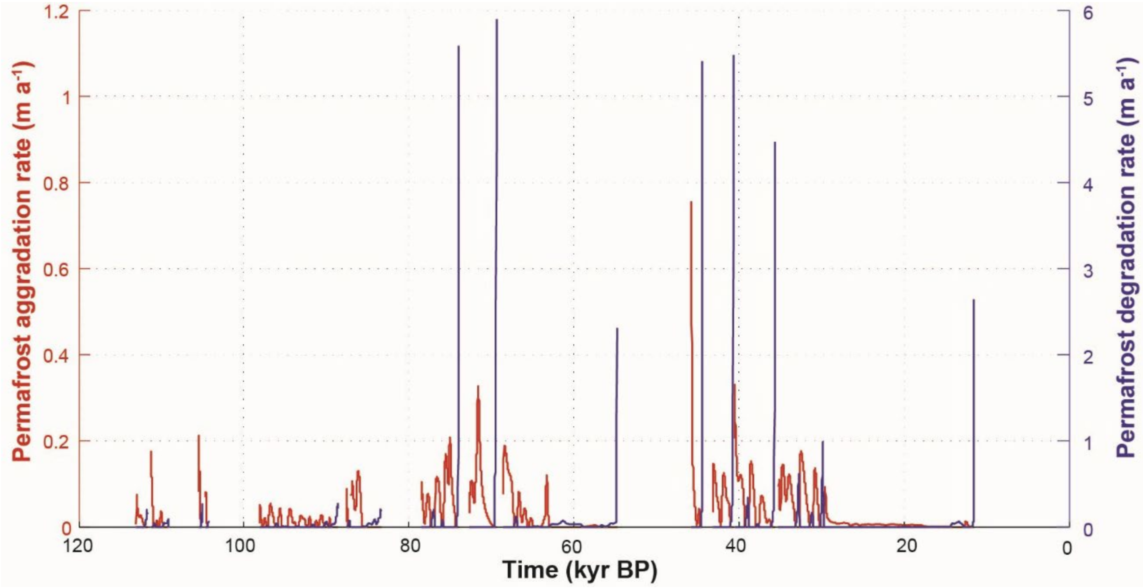

***Figure 6-3.** Reconstructed permafrost aggradation and degradation rates at the spent fuel repository location in Forsmark using the 1D permafrost model with reference surface and subsurface conditions (see SKB TR-20-12, Section 3.4.4 for details), including the SAT forcing shown in Figure 6-1.*

6.3.3 2D permafrost simulations

The 2D permafrost study was a continuation of and complement to the 1D study described above. The overall aim was to exemplify how permafrost and frozen ground develops over the Forsmark site (and not only at the repository location) during cold but ice-free periglacial phases of glacial cycles, and to further demonstrate the effects of uncertainties associated with processes and phenomena of importance for permafrost development. To this end, the 2D study provides a numerical estimation of the development of permafrost and perennially frozen ground along a ~15 km long profile covering a major portion of the Forsmark site and crossing the repository location (Figure 6-4), using site-specific time-transient surface and subsurface conditions. The vertical section of the profile is 10 km, consisting of six soil layers, 23 rock domains and 31 deformation zones. For a more detailed discussion about the profile and input data, see SKB (TR-20-12, Section 3.4.4) and references therein.

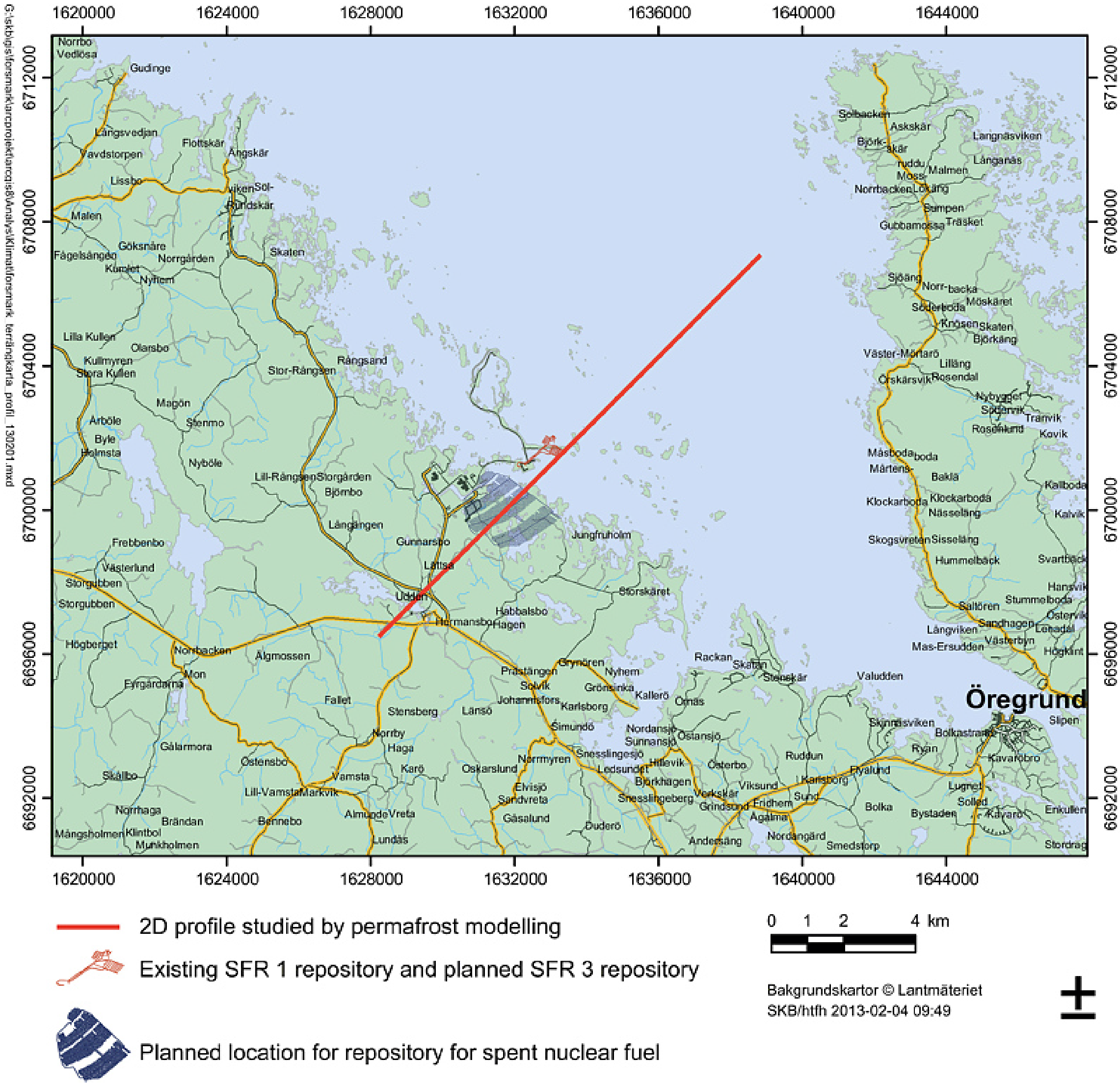

Figure 6-4. The ~15 km long profile analysed in the 2D permafrost modelling simulations (red line). The planned location of the spent fuel repository is indicated by the grey colour and the SFR repository is indicated by the orange colour.

Unlike the 1D simulations, the 2D Weichselian permafrost reconstruction for Forsmark did not cover the entire last glacial cycle. Instead, it focused on the ice-free period from 115 to 70 kyr BP, which corresponds to the time before the first phase of ice coverage in the associated ice-sheet reconstruction (Section 4.3.1). This period was selected because it includes the deepest permafrost of the last glacial cycle, as reconstructed by the 1D permafrost model (Section 6.3.2). The initial conditions for the 2D simulations were based on present-day conditions, including bedrock temperature, groundwater, salinity and pressure. Over time, the shoreline location in the simulations were adjusted according the historical relative sea-level reconstruction (Section 5.3), resulting in terrestrial conditions across the entire profile. In addition, the 2D model accounted for groundwater flow and salt transport processes; these processes were neglected in the 1D study. Arguably, also the 2D model only contains a simplified representation of the actual 3D groundwater flow network in Forsmark. However, this uncertainty is considered to be small because the topography of the Forsmark site is flat and therefore does not generate significant hydraulic gradients.

The correlation between SAT and ground surface temperature in the simulations was derived from an empirical approach based on so-called n-factors (Lunardini 1978). These factors also depend on the ground surface conditions, with low n-factors representing humid conditions with thick vegetation and winter snow cover while high n-factors are related to dry conditions with thin vegetation and snow cover.

Simulations

For the Weichselian permafrost reconstruction in Forsmark, two main simulations were conducted using the 2D model: a *dry* climate variant and a *humid* climate variant of the last glacial cycle. The difference between these two variants lies in the surface conditions. The dry variant was assigned the highest n-factors derived for the Forsmark site, representing a climate with reduced winter snow and thin vegetation, whereas the humid variant obtained the lowest n-factors, representing thick vegetation and winter snow (see further Section 2.4 in Hartikainen et al. 2010).

In addition to these two main simulations, several sensitivity simulations were also conducted with the 2D model to examine the uncertainty in the following parameters (and their combinations): SAT, geothermal heat flow, bedrock thermal properties (and diffusivity, conductivity), surface conditions (vegetation cover, soil water content and snow thickness), and (convective) heat transfer by groundwater flow.

Main results and concluding remarks

Across the main simulations conducted with the 2D model (see above), the dry variant consistently resulted in a greater depth of permafrost and frozen ground compared to the humid variant. Therefore, only the ground temperatures and extent of permafrost and perennially frozen ground for the dry variant are shown here, at four specific time slices between 115 and 70 kyr BP (Figure 6-5).

As shown in Figure 6-5, similar to the 1D model, frozen ground reaches its maximum depth around 70 kyr BP. At this time, the depth of permafrost and frozen ground is relatively uniform throughout the profile, varying by only a few tens of meters. The depth of permafrost and frozen ground reaches ~250 meters at the location of the spent fuel repository, which is consistent with the results from the 1D model (Figure 6-3). In contrast, for the humid variant, the maximum depth of permafrost and perennially frozen ground at the repository location is less than 200 meters (see SKB TR-20-12, Figure 3-57).

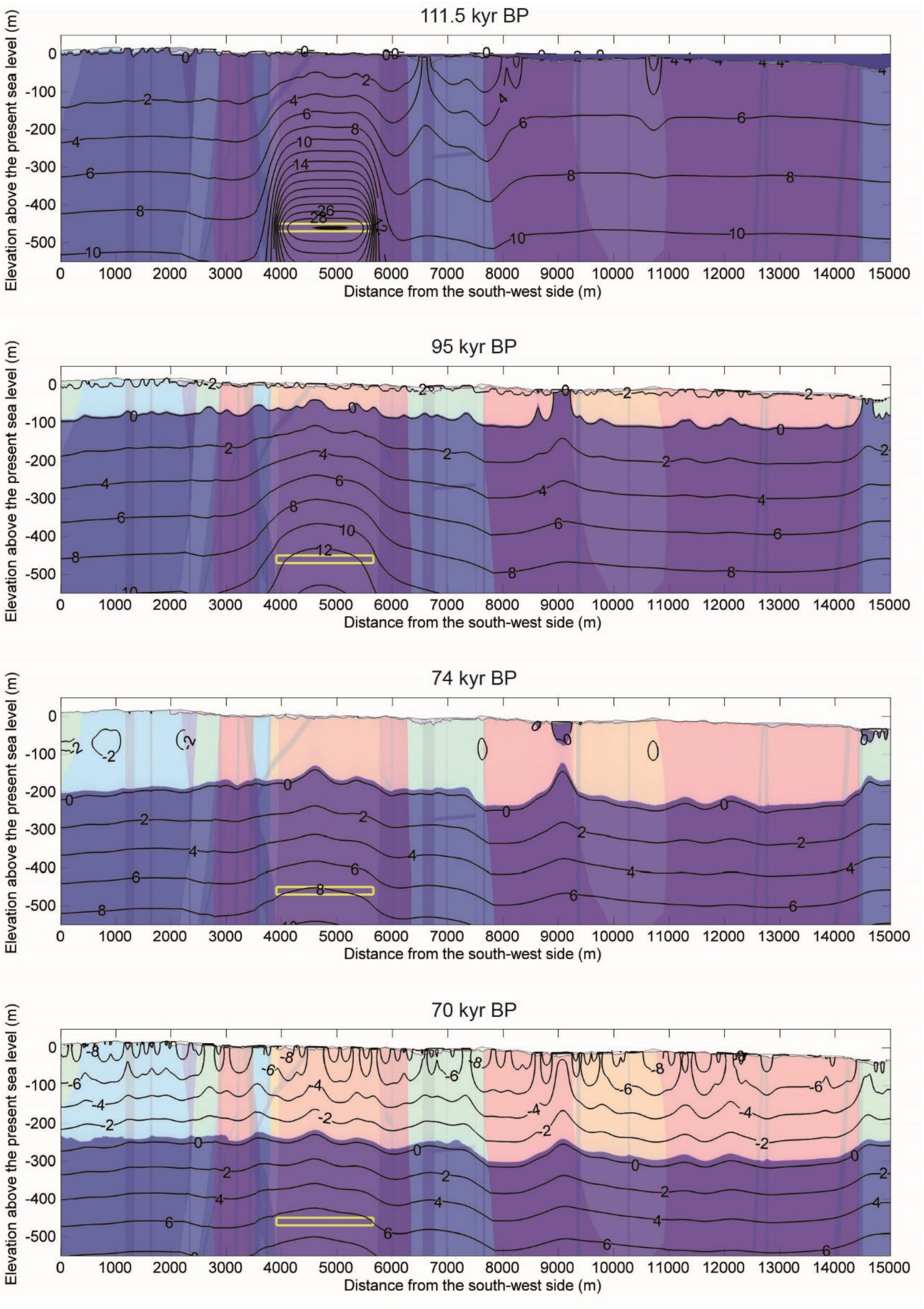

Figure 6-5. Temperature contours (in °C) and the extent of perennially frozen ground (light colour) and permafrost (0 °C isotherm) at times 111.5, 95, 74, 70 kyr BP for the dry variant of the reconstruction of last glacial cycle conditions. Blue colour on the top of the profile at 111.5 kyr BP shows the Baltic Sea. The yellow rectangle indicates the location of the spent fuel repository.

Based on the results from all sensitivity simulations conducted with the 2D model, which explored the identified uncertainties listed above, the following conclusions can be drawn (for more detailed discussion on each sensitivity simulation, see SKB TR-20-12, Section 3.4.4).

- The results of the 2D model shows that the prevailing surface conditions, such as the SAT forcing and surface moisture conditions, are the main factors governing the spatial and temporal development of permafrost and perennially frozen ground at the Forsmark site.
- Subsurface conditions, such as bedrock thermal properties, geothermal heat flow and groundwater salinity, affects the spatial and temporal development of permafrost and perennially frozen ground, but are of secondary importance for modelled permafrost depths compared with surface conditions.
- For the reconstruction of last glacial cycle conditions, the simulated maximum permafrost (0 °C isotherm) depth over the repository is between 180 and 260 m depending on the surface conditions. The corresponding range for the entire investigated profile is from 220 to 300 m.
- The simulated maximum depth of perennially frozen ground over the repository is between 180 and 250 m depending on the surface conditions. The corresponding range for the entire investigated profile is from 210 to 300 m. For comparison, a similar study in the Netherlands reported a maximum depth of perennially frozen ground of 140–170 m during the Weichselian (Govaerts et al. 2016). The shallower depths compared to Forsmark are reasonable given the higher SATs assumed for the Netherlands.
- The variation in thermal properties along the profile as well as 2D groundwater flow only has a small influence on permafrost development. Therefore, the uncertainties introduced by excluding lateral variations in thermal properties, boundary conditions and convective heat transfer in the 1D model study (Section 6.3.2) are considered insignificant.
- If pessimistically setting all known uncertainties (in SAT, surface conditions, bedrock thermal conductivity and heat capacity and geothermal heat flow) as favourably for permafrost growth as possible, permafrost may extend to 450 m depth in the reconstruction. However, it should be noted that such combination of assumptions is not realistic.
- Under continuous permafrost conditions (>90 % permafrost coverage), the unfrozen groundwater content in the perennially frozen ground under lakes can exceed 10 % down to a ~50 m depth. This indicates that taliks are able to form under lakes through perennially frozen ground if favourable groundwater flow conditions with open flow paths prevail. When the unfrozen groundwater content decreases below 10 %, groundwater flow is reduced considerably, and taliks are no longer able to form or survive.
- Freezing can induce salt exclusion and salt transport when perennially frozen ground develops deeper than ~200 m. At shallower depths the impacts of freezing are difficult to see since the salinity of groundwater has been diluted prior to the development of perennially frozen ground. When salt transport occurs more slowly than the freezing zone advances, the salinity concentration is increased within the perennially frozen ground.

6.3.4 Uncertainties not covered by the sensitivity simulations

In the following, uncertainties that were not covered by the sensitivity simulations are discussed. This includes the uncertainty related to the numerical model used. This uncertainty has already been evaluated and discussed in a previous report (Hartikainen et al. 2022) and is therefore only summarised here. Another source of uncertainty, related to the temporal variability of the SAT forcing used for the simulations (Figure 6-1), has not been discussed in previous documents and is therefore discussed more comprehensively in this section.

Numerical model

A major uncertainty concerns the choice of numerical model used for the permafrost simulations, especially the 2D simulations which explored relevant uncertainties in input data through various sensitivity simulations. To evaluate the importance of the uncertainty related to the numerical model itself, a comprehensive study was carried out evaluating the model performance to real-world permafrost conditions (Hartikainen et al. 2022).

In this study, the 2D permafrost model was evaluated against measured bedrock temperature data from a 650 m deep bedrock borehole situated at the ice-sheet margin in western Greenland. A large number of different input data were used in the simulations, originating from different types of measurements made within the study area, other model simulations, interpretations of aerial photographs and compilations of data from the literature. Several sensitivity simulations were carried out to study the effects of these uncertainties. Taking all identified uncertainties in input data into account, the permafrost model predicted the present-day bedrock temperature (91–491 m below the ground surface) to be within −2.2 and +1.6 °C of the observed bedrock temperature. This uncertainty range encompass both input data uncertainties and intrinsic model errors. However, the fact that the uncertainty range in the simulated temperature was nearly centred around the measured temperature indicates that any systematic intrinsic model error is small.

Temporal variability of the SAT forcing

Uncertainty in the SAT forcing was considered in the 2D permafrost sensitivity simulations by uniformly increasing or decreasing the SAT over a range of 22 °C throughout the entire simulation period (see e.g. SKB TR-20-12, Section 3.4.4). However, the uncertainty associated with temporal variability in the SAT curve was not explored in these simulations. A notable feature of this variability is the occurrence of sudden warming fluctuations on millennial timescales, as exemplified by MIS 3 between approximately 50 and 30 kyr BP (Figure 6-1). These fluctuations, known as Dansgaard-Oeschger events (DO-events) (e.g. Li and Born 2019), do not follow any external forcing signal, such as changes in solar insolation. Although the exact mechanism behind the DO-events remains unclear, studies generally agree that they are driven by coupled interactions within the atmosphere-ice-ocean system under glacial conditions, which affect poleward heat transport (see e.g. Li and Born 2019 for a summary). The key interactions are believed to have taken place in the Nordic Seas, just south of Greenland.

There is also evidence suggesting that the occurrence of DO-events during the last glacial cycle may be linked to the specific development of the Laurentide ice sheets in North America at that time. This is because average wind velocities over the Atlantic Ocean, which influence ocean circulation and the presence of sea ice, have been found to be sensitive to the extent and height of the Laurentide ice sheet. For example, a modelling study (Armstrong et al. 2023), which managed to reproduce DO-events in a comprehensive atmospheric-ocean circulation model, found that even slight changes in the extent of the Laurentide ice sheet led to a complete cessation of the DO-events. Thus, these results indicate DO-events can only occur under certain environmental conditions and that, although these conditions occurred during the last glacial cycle, it is far from certain that they occurred during previous cycles or that they will occur in the future.

DO-events are known to have had a global-scale impact on climate. For example, during these events, climate conditions in western and central Europe are thought to have been warmer and wetter, while the tropical rain belt is believed to have migrated northward (Izumi et al. 2023). In Fennoscandia, including the Forsmark area, SAT changes during a DO-event correlated with those recorded in Greenland, suggesting that a warming event in Greenland likely corresponded to warmer conditions also in Fennoscandia and Forsmark. However, despite the global influence of DO-events, the magnitude of these changes was likely smaller outside of Greenland. For instance, Izumi et al. (2023) found that the largest SAT response during a DO-event occurred in the North Atlantic region, just south of Greenland, and on Greenland itself. The SAT signal from the DO-events then diminished with distance from these areas. A similar response is also seen in projections of a potential AMOC collapse due to current anthropogenic warming (Appendix A1). Thus, while millennial-scale SAT fluctuations likely occurred to some extent in the Forsmark area during MIS 3, their amplitude was probably much smaller than what was recorded in Greenland. As a result, the temporal variability in the SAT forcing for Forsmark has likely been slightly overestimated in the permafrost simulations, leading to an overestimation of the permafrost variability. The potential effect of the temporal SAT variability on future permafrost depth and variability is discussed in Section 6.5.

6.4 Present-day conditions and trends

Permafrost currently underlies about 15 % of the exposed land surface in the Northern Hemisphere and more than 50 % of the unglaciated land north of 60°N (Fox-Kemper et al. 2021). It also occurs in high-altitude mountain regions in both hemispheres. In addition, permafrost is present in most unglaciated parts of Antarctica (Fox-Kemper et al. 2021).

The deepest known permafrost occurs in the central part of Siberia in Russia, where thicknesses of up to 1500 m have been reported (e.g. Fotiev 1997). The extensive region of continuous permafrost in central Siberia corresponds to areas that are believed not to have been covered by ice sheets during the last glacial cycle (see e.g. Section 4.3).

Over the past three to four decades, permafrost temperatures have increased across permafrost regions (Fox-Kemper et al. 2021), and continued global warming is expected to cause further loss of near-surface permafrost. In recent decades, substantial thawing has been observed in areas with discontinuous and sporadic permafrost (Fox-Kemper et al. 2021). The volume of perennially frozen ground within the upper 3 m is projected to decrease by approximately 25 % for every 1 °C rise in global SAT (Fox-Kemper et al. 2021).

6.5 Future evolution

This section presents the projected future evolution of permafrost and frozen ground. Similar to the analysis of future ice-sheet development (Section 4.5), the focus here is on identifying uncertainty ranges in permafrost development in Forsmark over the next 1 Myr, rather than outlining deterministic developments. The analysis includes an assessment of the frequency and duration of periglacial conditions in Forsmark (Section 6.5.1), including the timing of the first potential permafrost period. Additionally, this section evaluates the maximum depth of permafrost and frozen ground in Forsmark (Section 6.5.2), and whether these conditions could extend to the depths of the SFR and the spent fuel repository within the next 100 kyr and 1 Myr, respectively. The latter analysis is based on both reconstructions of past permafrost development in Forsmark (Section 6.3) – which were primarily used to estimate maximum permafrost depth in previous safety assessments (e.g. SKB TR-20-12, Sections 4.5.3 and 5.5.3) – and future climate projections combined with idealised permafrost simulations. The assessment of permafrost depth based on future climate projections is a new feature introduced in this report.

It is important to note that residual heat from the spent fuel will not have an impact on the future permafrost formation and extent in the Forsmark area. The earliest occurrence of permafrost in the Forsmark area is projected to be after 50 kyr (Section 3.6.1). However, already after 1000 years, more than 90 % of the initial heat production will have dissipated, and after 10 kyr, it will be reduced by nearly 99 % (Hartikainen et al. 2010, Figure 2-8).

6.5.1 Frequency and duration of periglacial conditions

This section analyses the frequency and duration of periglacial conditions in Forsmark over the next 1 Myr. Periglacial conditions are defined as terrestrial environments with permafrost but without the presence of an ice sheet (Section 1.2.3). The permafrost coverage is not critical for this definition, meaning that even sporadic permafrost within a region is classified as periglacial. The assessment is based on the same 90 global climate projections used to analyse ice-sheet frequency and duration (Section 4.5.2). However, because permafrost is more strongly influenced by local climate conditions, the global SAT projections from the ice-sheet analysis must be adjusted to reflect representative SAT values for Forsmark. Additionally, since periglacial conditions only occur when the Forsmark area is above sea level, estimating the frequency and duration of these conditions must also account for periods of submerged conditions following ice-sheet retreat.

A key limitation of this analysis is that it provides no information about the vertical extent of permafrost and frozen conditions, and the temperature at depth; this is instead analysed in Section 6.5.2. Additionally, it does not address the surface distribution of permafrost, meaning the analysis cannot distinguish between sporadic, discontinuous, or continuous permafrost coverage.

Methodology

To estimate the frequency and duration of periglacial conditions in Forsmark over the next 1 Myr, we use climate model projections from Williams et al. (2022) (see also Sections 3.5.3 and 3.5.4). This study projects local mean annual SAT in Forsmark for the next 1 Myr using a statistical emulator (Lord et al. 2019) based on the same emissions scenarios (0, 400, 1500, and 5500 Pg C) and 90 global climate projections from the conceptual global model (CGM), which was also used in the assessment of future ice-sheet variability (Section 4.5.2).

In this analysis, periglacial conditions in Forsmark are assumed to occur when the projected local mean annual SAT, T_{Forsmark}, falls within a defined range suitable for permafrost formation: $T_{\text{per,lower}} < T_{\text{Forsmark}} < T_{\text{per,upper}}$. The upper SAT threshold, $T_{\text{per,upper}}$, has been estimated to range between –0.5 °C and –2 °C in Forsmark, depending on surface and bedrock conditions (Hartikainen et al. 2010, Brandefelt et al. 2013). In this analysis, we use $T_{\text{per,upper}} = -1$ °C as an upper SAT threshold for permafrost development in Forsmark. The introduction of a lower SAT threshold, $T_{\text{per,lower}}$, is motivated by the analysis of future ice-sheet variability (Section 4.5.2). This analysis indicate that ice sheets will advance over Forsmark when the SATs are sufficiently low, and thus Forsmark would be dominated by glacial rather than periglacial conditions. Specifically, ice-sheet coverage in Forsmark is projected to occur when the global mean SAT falls below a defined threshold, $\Delta T_{\text{threshold}}$ (Section 4.5.2). Thus, $T_{\text{per,lower}}$ corresponds the local Forsmark SAT when the global-mean SAT has decreased by $\Delta T_{\text{threshold}}$.

The SAT threshold for glaciation, $\Delta T_{\text{threshold}}$, was estimated based on the reconstructed periods of ice coverage in Forsmark during the Weichselian (Figure 4-8), resulting in a best-estimate value of –2.8 °C. To account for potential differences in regional ice-sheet development during future glacial cycles compared to the Weichselian, a broader uncertainty range of –2.1 °C to –3.5 °C was also considered (Section 4.5.2). Since the Forsmark climate projections by Williams et al. (2022) are based on the same global climate simulations used for the ice-sheet variability projections, we use these simulations to estimate the corresponding threshold for Forsmark's local SAT, $T_{\text{per,lower}}$.

The relationship between global and local SATs is shown in Figure 6-6, which displays the projected SAT in Forsmark for each timestep across all 90 simulations under the 0 Pg C scenario[24] (Williams et al. 2022), against corresponding changes in global-mean SAT from the CGM. As expected, there is a strong correlation between Forsmark SAT and global SAT changes, with colder global conditions generally associated with colder conditions also in Forsmark. However, Figure 6-6 also reveals variability in this relationship, as the same change in global mean SAT can correspond to different SAT values in Forsmark depending on the timestep and simulation. For example, a global SAT change of –3 °C is associated with Forsmark SATs ranging from –18 °C to –13 °C. To simplify the transfer between global and local SATs, we assume that each global SAT change corresponds to the average of the Forsmark SAT range (indicated by the red line in Figure 6-6). Based on this average, we estimate that the best-estimate global threshold for glaciation, $\Delta T_{\text{threshold}} = -2.8$ °C, corresponds to a local SAT of approximately $T_{\text{per,lower}} = -14$ °C. Similarly, the uncertainty range of $\Delta T_{\text{threshold}}$ (–3.5 °C to –2.1 °C) corresponds to a local SAT range of approximately $T_{\text{per,lower}} = -16$ °C to $T_{\text{per,lower}} = -11$ °C.

Thus, if future ice-sheet development over Forsmark were to follow a similar pattern to that of the Weichselian ($\Delta T_{\text{threshold}} = -2.8$ °C), this analysis suggests that periglacial conditions may prevail in Forsmark when the local SAT is between –1 °C and –14 °C (Figure 6-6). However, periglacial conditions may occur in Forsmark when the local SAT is between –1 °C and –11 °C if the expansion of the Fennoscandian ice sheet is more sensitive compared to that of the Weichselian, and between 1 °C and –16 °C if it is less sensitive.

---

[24] Using another emissions scenario to derive the Forsmark SAT from the global SAT change would only marginally change the outcome (not shown).

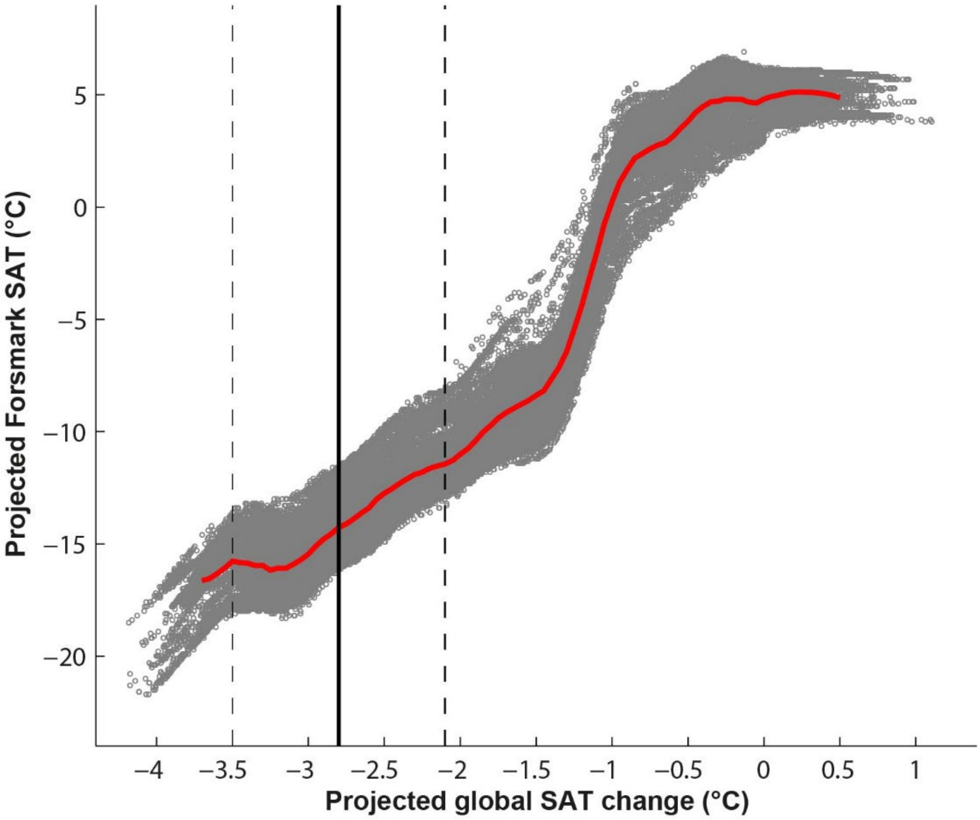

Figure 6-6. *Relationship between the projected Forsmark SAT and global-mean SAT. The grey markers represent projected Forsmark SAT for each timestep (each 1 kyr up to 1 Myr AP) across all 90 simulations in the 0 Pg C scenario (Williams et al. 2022), plotted against the corresponding changes in global-mean SAT change from the conceptual global model (CGM; Lord et al. 2019). The CGM was also used in the ice-sheet variability projections in the present report (Section 4.5.2). The red line shows the average projected Forsmark SAT for each change in global SAT. The solid vertical line indicates the best-estimate threshold in global-mean temperature change ($\Delta T_{threshold}$), below which ice coverage in Forsmark can be expected. The uncertainty in this threshold (Section 4.5.2) is indicated by the dashed vertical lines.*

It is important to note that not all periods within these SAT limits will correspond to terrestrial conditions in Forsmark. Therefore, as a final step, we must also account for post-glacial periods when the area is submerged beneath the sea. The analysis in Section 5.5.3 indicates that submergence will generally occur following ice-sheet retreat, except in specific cases where the retreat involves very thin ice sheets (less than 500 m thick) or intermediate-thickness ice sheets (~2000 m) that persist for only a short duration (typically less than 2000 years). Section 5.5.3 also describes the application of the LLRA model, a simple isostasy model calibrated against reconstructed Weichselian conditions. This model was used to assess how variations in ice-sheet thickness and duration influence the extent of post-glacial submerged conditions in Forsmark.

The LLRA model is also used to estimate the duration of submerged conditions over the next 1 Myr as part of the analysis of future periglacial variability. While the duration of future ice sheets is directly derived from the ice-sheet variability analysis (Section 4.5.2), the thickness of these ice sheets remains unknown. However, for simplicity, we assume a maximum ice sheet thickness of 2500 m, based on the average maximum thickness reconstructed for Forsmark during the Weichselian (Figure 4-8). It is important to emphasise that the duration of the post-glacial submerged period is relatively insensitive to specific ice thickness, especially when compared to the variability in ice-sheet duration (Section 4.5.2). For instance, increasing ice thickness from 2500 m to 3500 m during a typical ice-sheet duration of 20 kyr only increases the submerged period by about 2000 years (from ~11 kyr to ~13 kyr). Thus, while varying ice thickness in the LLRA model may affect the details of the results, it does not alter the main conclusions regarding future periglacial variability presented in this section.

Using (i) the 90 Forsmark SAT projections from Williams et al. (2022) for each emission scenario, (ii) the calculated Forsmark SAT thresholds for periglacial conditions ($T_{\mathrm{per,lower}}$ and $T_{\mathrm{per,upper}}$; see above), and (iii) the duration of submerged conditions following ice-sheet retreat as calculated with the LLRA model, we estimate the following quantities representing future periglacial variability in Forsmark over the next 1 Myr:

- Timing of the next occurrence of periglacial conditions, t_{per}
- Number of periglacial periods, n_{per}
- Total duration of periglacial conditions, $d_{\mathrm{per,tot}}$
- Maximum duration of an individual periglacial period, $d_{\mathrm{per,ind}}$
- Average duration of a periglacial period, $d_{\mathrm{per,ave}}$

As with the assessment of future ice-sheet variability, the projected values of these quantities are compared to SKB's Weichselian reconstruction[25] (from the 1D permafrost modelling study; see Section 6.3). For this comparison, we assume that the reconstructed permafrost development of the past 120 kyr is repeated up to 1 Myr into the future.

Results

The frequency and duration of periglacial conditions in Forsmark over the next 1 Myr, based on the best-estimate ice coverage projections ($\Delta T_{\mathrm{threshold}} = -2.8$ °C), are presented in Table 6-2 for each emission scenario. The corresponding results for the low-end ($\Delta T_{\mathrm{threshold}} = -3.5$ °C) and high-end ($\Delta T_{\mathrm{threshold}} = -2.1$ °C) ice coverage projections are shown in Table 6-3. The main results are summarised in the following.

- The total duration of periglacial conditions ($d_{\mathrm{per,tot}}$) in the best-estimate projections (Table 6-2) aligns well with the hypothetical case of repeating Weichselian conditions into the future. However, the number of periglacial periods (n_{per}) is significantly lower in the projections, and the duration of these periods ($d_{\mathrm{per,ind}}$ and $d_{\mathrm{per,ave}}$) are considerably longer compared to the Weichselian reconstruction. These differences can be attributed to the much higher temporal variability – particularly on millennial timescales – in the SAT curve used for the Weichselian reconstruction (Figure 6-1) compared to projected SAT evolution from the simulations. As discussed in Section 6.3.4, this high variability can only occur under certain environmental conditions, and it is far from certain that these conditions will occur during future glaciations. Even during the last glacial period, the SAT variability was likely lower in regions outside of Greenland compared to that depicted in Figure 6-1. On the other hand, it is plausible that ice-ocean-atmosphere interactions could introduce a variability on sub-Milankovitch timescales also during future glaciations, although such potential variability is not captured by the climate simulations[26]. Thus, while the temporal permafrost variability is likely overestimated in the Weichselian reconstruction, it may be underestimated in 90 climate simulations.
- The first emergence of periglacial conditions in Forsmark (t_{per}) is projected to occur after 50 kyr into the future, significantly later than in the future development based on repetitions of the Weichselian reconstruction (Table 6-2). This difference is attributed to the relatively low variability in summer insolation over the next 50 kyr (Section 2.5), compared to the much higher insolation variability (and thus lower minima) at the onset of the Weichselian (Section 2.3).
- The number of periglacial periods (n_{per}) in Forsmark over the next 1 Myr is projected to be around 20 for both 0 and 400 Pg C anthropogenic emissions (Table 6-2). These estimates are similar to the number of periods with ice coverage over Forsmark during the same time frame, based on the best-estimate glaciation threshold ($\Delta T_{\mathrm{threshold}} = -2.8$ °C).

---

[25] In this reconstruction, periglacial conditions is defined as any period when permafrost occurs in the 1D model

[26] This is partly because the simulations use a relatively long timestep of 1000 years (Williams et al. 2022).

- As expected, the first occurrence of permafrost in Forsmark is delayed with higher levels of anthropogenic emissions (Table 6-2). In the highest emission scenario (5500 Pg C), both the number of periglacial periods (n_{per}) and the total duration of periglacial conditions over the next 1 Myr ($d_{\mathrm{per,tot}}$) decrease notably compared to the 0 Pg C scenario. However, this trend is not observed for the 400 Pg C and 1500 Pg C scenarios (Table 6-2). For these intermediate scenarios, n_{per} and $d_{\mathrm{per,tot}}$ remain largely similar to the 0 Pg C scenario, despite a later onset of the first periglacial period and overall higher average SATs. The similarity arises from two compensating effects. On one hand, the higher SAT in the 400 Pg C and 1500 Pg C scenarios reduces the total time during which the Forsmark SAT falls below –1 °C, leading to shorter periods with permafrost. On the other hand, it also shortens the time during which Forsmark SAT drops below the ice-coverage threshold (–14 °C) by a comparable amount. Consequently, increased emissions, at least up to 1500 Pg C, primarily impact ice coverage in the region (as shown in Table 4-3) rather than significantly altering the extent of permafrost.
- If Forsmark is more susceptible to future glaciations than suggested by the reconstructed Weichselian glaciation ($\Delta T_{\mathrm{threshold}} = -2.1$ °C), the total duration of periglacial conditions in Forsmark over the next 1 Myr is significantly reduced. In such a scenario, ice sheets occupy the region during many of the cold episodes that would have been dominated by permafrost under the $\Delta T_{\mathrm{threshold}} = -2.8$ °C scenario. Depending on the emissions scenario, the total duration of periglacial conditions with $\Delta T_{\mathrm{threshold}} = -2.1$ °C is about 100–200 kyr shorter compared to the case with $\Delta T_{\mathrm{threshold}} = -2.8$ °C (cf. Tables 6-2 and 6-3). Conversely, if future ice-sheet development over Forsmark is inhibited compared to the Weichselian ($\Delta T_{\mathrm{threshold}} = -3.5$ °C), these cold periods become increasingly dominated by permafrost. In the most extreme cases – especially under the 0 Pg C and 400 Pg C scenarios – more than half of the next 1 Myr could be characterized by periglacial conditions in Forsmark. This increase in the total duration of periglacial conditions is not caused by an increased number of periglacial periods over the next 1 Myr, but rather by a significantly longer average duration of each permafrost period, at the expense of ice-sheet development (Table 6-3).

In Chapter 8, examples of likely evolutions ($\Delta T_{\mathrm{threshold}} = -2.8$ °C combined with 400 Pg C and 1500 Pg C) of periglacial conditions in Forsmark over the next 1 Myr are illustrated as evolutions of climate domains. The same chapter also presents examples of extreme developments of periglacial conditions over the next 1 Myr ($\Delta T_{\mathrm{threshold}} = -3.5$ °C combined with 0 Pg C).

Table 6-2. Projected next occurrence of periglacial conditions (t_{per}) as well as projected number of periglacial periods (n_{per}), maximum duration of an individual periglacial period ($d_{per,ind}$), average duration of a periglacial period ($d_{per,ave}$) and total duration of periglacial conditions ($d_{per,tot}$) in Forsmark over the next 1 Myr, calculated based on the best-estimate threshold for glaciation ($\Delta T_{threshold}$ = –2.8 °C, see further Section 4.5.2). The values outside the brackets show the median projection across the 90 climate simulations (Williams et al. 2022), whereas the values inside the brackets represent the 5th–95th percentile range of the simulations. For reference, corresponding projections for a reference scenario where the reconstructed periods of periglacial conditions of the Weichselian (last 120 kyr) is repeated 1 Myr into the future are also shown

Best-estimate permafrost coverage ($\Delta T_{threshold}$=–2.8 °C)					
	t_{per} (kyr)	n_{per} (-)	$d_{per,ind}$ (kyr)	$d_{per,ave}$ (kyr)	$d_{per,tot}$ (kyr)
Repetition of Weichselian reconstruction (Section 6.3)	7	119	9	3	386
0 Pg C	58 [57–60]	22 [18–25]	42 [35–48]	17 [14–21]	348 [291–393]
400 Pg C	85 [61–199]	22 [15–29]	37 [34–49]	16 [12–19]	351 [269–393]
1500 Pg C	147 [133–513]	21 [12–26]	46 [33–54]	17 [14–20]	354 [206–399]
5500 Pg C	306 [216–648]	13 [8–18]	47 [31–56]	20 [16–26]	269 [140–336]

Table 6-3. Same as Table 6-2, but for high-end ($\Delta T_{threshold}$=–2.1 °C) and low-end ($\Delta T_{threshold}$=–3.5 °C) thresholds for Forsmark glaciation

High-end ice coverage ($\Delta T_{threshold}$=–2.1 °C)					
	t_{per} (kyr)	n_{per} (-)	$d_{per,ind}$ (kyr)	$d_{per,ave}$ (kyr)	$d_{per,tot}$ (kyr)
0 Pg C	58 [57–60]	18 [15–22]	30 [19–40]	8 [7–10]	145 [131–198]
400 Pg C	85 [61–199]	18 [13–23]	28 [17–40]	8 [6–10]	142 [104–189]
1500 Pg C	147 [133–513]	19 [11–25]	17 [14–37]	7 [6–9]	133 [79–177]
5500 Pg C	306 [216–648]	13 [6–19]	21 [16–46]	9 [6–11]	131 [64–177]
Low-end ice coverage ($\Delta T_{threshold}$=–3.5 °C)					
	t_{per} (kyr)	n_{per} (-)	$d_{per,ind}$ (kyr)	$d_{per,ave}$ (kyr)	$d_{per,tot}$ (kyr)
0 Pg C	58 [57–60]	22 [18–26]	60 [46–87]	23 [19–28]	520 [440–578]
400 Pg C	85 [61–199]	21 [16–25]	61 [48–90]	24 [20–29]	534 [399–579]
1500 Pg C	147 [133–513]	21 [12–23]	59 [48–83]	24 [20–28]	491 [302–546]
5500 Pg C	306 [216–648]	12 [7–16]	58 [50–69]	28 [21–34]	346 [217–434]

6.5.2 Depth of permafrost and perennially frozen ground over the next 100 kyr and 1 Myr

In SKB's safety assessments for the spent fuel repository, including the PSAR, the evaluation of the maximum depth of permafrost and perennially frozen ground in Forsmark over the next 1 Myr has been primarily based on the reconstruction of the last glacial cycle (Section 6.3), supplemented by sensitivity simulations exploring various modifications of that reconstruction. This assessment was also further refined through sensitivity simulations that explored various modifications of the reconstruction. One such modification introduced a severe permafrost case, where the last glacial cycle was adjusted to include an extended period of periglacial conditions at Forsmark, lasting approximately 70 kyr (SKB TR-20-12, Section 5.5.3; SKB TR-21-01, Section 12.3).

Estimating permafrost depth based on reconstructed last glacial conditions is relevant only for the spent fuel repository, but not for SFR. This is because the next 100 kyr – the post-closure assessment period for SFR – are expected to be relatively warm, differing significantly from the past 120 kyr (Sections 3.5.4 and 3.6.1). Instead, for SFR, the potential for permafrost was previously investigated using permafrost modelling combined with climate modelling, which incorporated predicted future changes in insolation (Brandefelt et al. 2013). Their findings indicate that permafrost and frozen conditions at SFR depth could first occur in response to the next major summer insolation minimum at 54 kyr AP, under reasonable climate scenarios and boundary conditions. However, using highly pessimistic assumptions regarding ground surface conditions, future atmospheric CO_2 levels and climate evolution, they were also able to simulate permafrost at SFR depth – though not frozen conditions – during a weaker insolation minimum at 17 kyr AP. These assumptions, however, are considered to be unrealistic (see also Section 3.6.1).

This section introduces a new alternative method to complement previous approaches for estimating maximum permafrost depth. This new method integrates existing idealised permafrost simulations (SKB TR-06-23, Section 3.4.4) – driven by constant surface temperature forcing – with the 90 future climate projections (Williams et al. 2022) used in the analysis of permafrost variability (Section 6.5.1). By combining these simulations and projections, the likelihood of permafrost and frozen conditions at both SFR and the spent fuel repository can be assessed over the next 100 kyr and 1 Myr, respectively.

Approach 1 – Repetition of the last glacial cycle, including a severe permafrost case

Repetition of the last glacial cycle

Assuming that the Weichselian glaciation represents a typical glacial cycle, and that similar conditions to those reconstructed for the past 120 kyr will likely recur over the next 1 Myr, the historical permafrost reconstruction (Section 6.3) can serve as a proxy for future conditions. Permafrost simulations of the last glacial cycle using the 1D model indicate a maximum permafrost depth (the 0 °C isotherm) of approximately 250 m at the location of the spent fuel repository, with a maximum frozen ground depth of around 230 m (Section 6.3.2). When accounting for surface and subsurface uncertainties (Section 6.3.3), the 2D model projects a permafrost depth between 180 and 260 m, while the depth of perennially frozen ground is estimated to range from 180 to 250 m (Section 6.3.3).

These results are consistent with projections of future permafrost depth for the Finnish nuclear waste disposal site at Olkiluoto, where permafrost was estimated to extend to a maximum depth of approximately 270 m over the next 120 kyr (Cohen-Corticchiato and Zwinger 2021). They also align with reconstructions of maximum permafrost depth at Olkiluoto during the last glacial cycle (Hartikainen 2013). This similarity arises despite Cohen-Corticchiato and Zwinger (2021) using a climate forcing based on insolation changes over the next 120 kyr[27], which differ significantly from those of the past 120 kyr. Their results suggest that a maximum permafrost depth of approximately 250–300 m is reasonable in this region for a typical glacial cycle. However, this interpretation is somewhat limited by the fact that their simulations did not extend beyond 120 kyr into the future – particularly since the next 100 kyr are expected to be relatively warm compared to the following hundreds of thousands of years.

The reconstruction of permafrost conditions from the last glacial cycle suggests that significantly colder temperatures than those used in the permafrost simulations would be required for permafrost to reach the depth of the spent fuel repository (450 m). Specifically, analyses indicate that the reconstructed SAT curve for the last glacial cycle (Figure 6-1) would need to be lowered by 8 °C for permafrost to reach this depth (e.g. SKB TR-21-01, Section 12.3).

---

[27] The climate forcing also included anthropogenic emissions based on the RCP4.5 scenario. However, these emissions did not affect the maximum permafrost depths projected by their model. In their study, maximum permafrost depths occurred after 50 kyr, whereas atmospheric CO_2 concentrations returned to near pre-industrial levels already after about 10 kyr (Thölix et al. 2019).

A severe permafrost case

In this sensitivity experiment, the same initial and boundary conditions were used in the 2D permafrost model as for the last glacial cycle simulations, except for the following additional assumptions:

- The climate is so dry that no ice-sheet forms that is large enough to reach the Forsmark site at any time during the glacial cycle, i.e. ice-free conditions prevail during the entire glacial cycle.
- In line with the above assumption, it is assumed that the repository location is not isostatically depressed below sea level.
- The climate is so dry that there is no insulating snow cover during winter.
- There is no vegetation to insulate the ground from low SATs.
- The temperature curve reconstructed for the last glacial cycle (Figure 6-1), but without the presence of ice-sheets and submerged conditions, was employed for calculating ground surface temperatures.

This *severe permafrost case*, which is described in detail in SKB (TR-20-12, Section 5.5.3), represents an unlikely bounding case, whereby no ice sheet reaches the Forsmark area over the course of the glacial cycle. As with the reconstruction of the last glacial cycle, the severe permafrost simulations were performed for both a humid and a dry climate variant (Section 6.3.3). The resulting permafrost coverage and depth from these simulations are shown in Figure 6-7. The simulations suggest that Forsmark will experience more extensive permafrost if the ice sheet does not advance to the site. This result aligns with the permafrost variability projections in Section 6.5.1 (cf. Tables 6-2 and 6-3), which show significantly longer periods of periglacial conditions when ice coverage in Forsmark is limited ($\Delta T_{\text{threshold}} = -3.5$ °C, $T_{\text{per,lower}} = -16$ °C) compared to the case for which future ice coverage was calibrated against the conditions of the last glacial cycle ($\Delta T_{\text{threshold}} = -2.8$ °C, $T_{\text{per,lower}} = -14$ °C). When applying the SAT forcing of the last glacial cycle (Figure 6-1) without the presence of ice sheets, Forsmark experiences approximately 70 kyr of uninterrupted permafrost conditions (between 40 and 110 kyr) in the severe permafrost case (Figure 6-7). These prolonged permafrost periods result in greater permafrost depths compared to the Weichselian reconstruction. The maximum permafrost thickness at the location of the spent fuel repository, reaching nearly 400 m, occurs toward the end of this 70-kyr period, while the depth of perennially frozen ground over the repository location reaches approximately 350 m during this time (Figure 6-7).

Several sensitivity simulations were also conducted for the severe permafrost case to evaluate the importance of uncertainties in subsurface conditions in the simulations. The results indicate that permafrost could only extend to spent fuel repository depth under an extreme combination of parameters, including maximum thermal conductivity, minimum heat capacity for the subsurface, and the lowest assumed geothermal heat flow. However, this parameter combination is not considered realistic (see SKB TR-20-12, Section 5.5.3 for details).

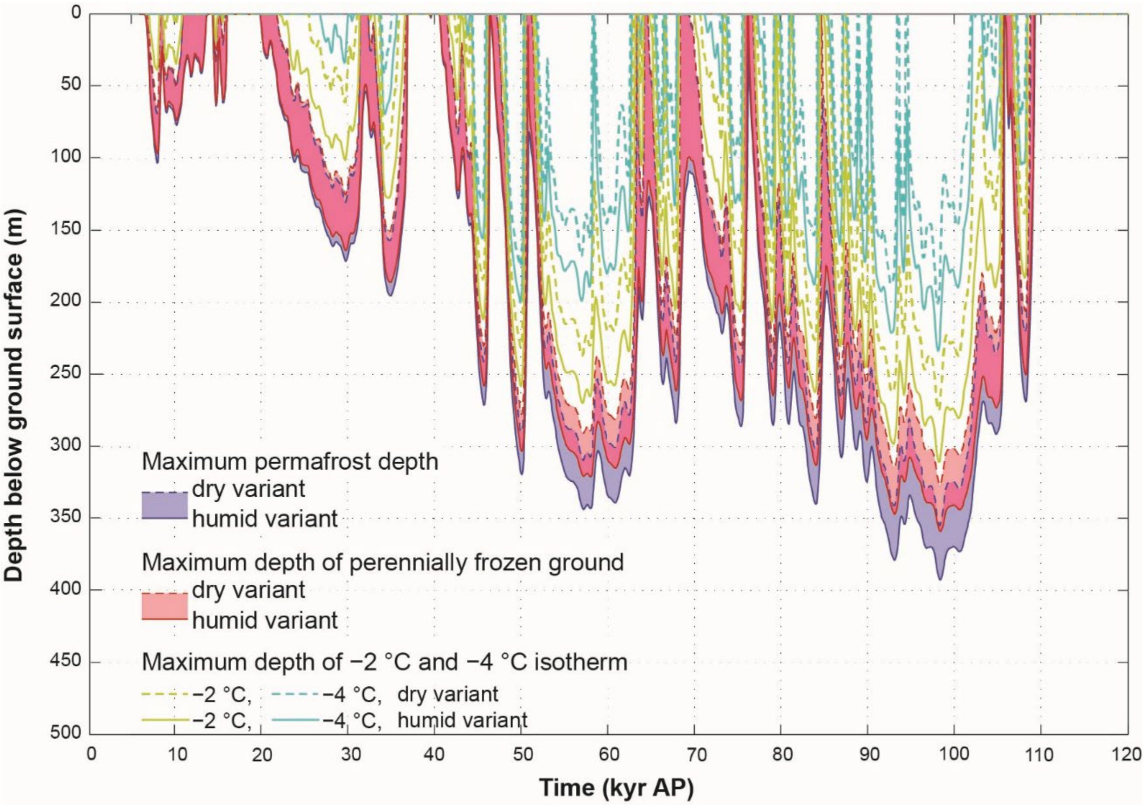

Figure 6-7. *Evolution of maximum permafrost depth, maximum depth of perennially frozen ground and maximum depth of −2 and −4 °C isotherms over the spent fuel repository for the severe permafrost case. The shaded area in blue and red represents the range when considering the dry and humid climate variants. The darker lilac colour indicates that the results for permafrost and perennially frozen ground overlap.*

Approach 2 – Permafrost depth projections based on climate simulations over the next 1 Myr

This approach uses the ensemble of 90 climate simulations (Williams et al. 2022) to assess the likelihood of permafrost and frozen ground at the characteristic depths of SFR and the spent fuel repository over the next 100 kyr and 1 Myr, respectively. Unlike the previous approach, which relied on reconstructed conditions from the last glacial cycle and modifications of that reconstruction to simulate a severe permafrost case, this method incorporates both projected changes in summer insolation and scenarios of anthropogenic carbon emissions.

A limitation with the climate simulations of Williams et al (2022) is that they only provide information about air temperature (i.e. the SAT), but not ground temperature. To convert the projected SATs from Williams et al. (2022) to bedrock temperatures at characteristic depths of SFR and spent fuel repository, and to estimate the time lag between temperature changes at the surface and those at repository depth, we use results from idealised permafrost simulations. These simulations calculate how permafrost evolves over the next 120 kyr at different depths under various fixed surface temperatures. Such simulations were first carried out with the 1D permafrost model (SKB TR-06-23, Section 3.4.4), evaluating the temporal evolution of permafrost depth at the location of the spent fuel repository in response to mean annual surface temperatures ranging from –20 °C to –2 °C (Figure 6-8). It is important to emphasise that Figure 6-8 is shows a sensitivity study illustrating an idealised permafrost development under a constant temperature forcing at the surface. In reality, the temperature at the surface will not be constant, but vary according to changes in climate over the next 1 Myr (see e.g. Figure 3-6). Similar idealised experiments were later conducted specifically for SFR using the 2D permafrost model (Brandefelt et al. 2013). In this exercise, potential permafrost formation at the depth of the spent fuel repository is estimated using results from the 1D model, while the 2D model is used for SFR.

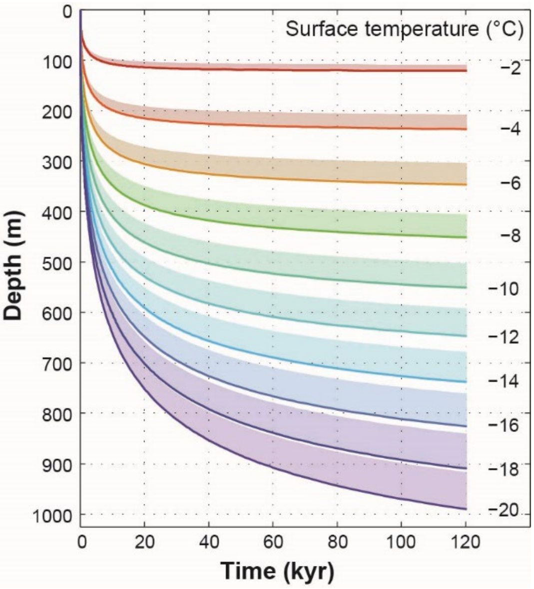

Figure 6-8. *Evolution of permafrost depth (thick lines) and related cryopegs (shadowed areas) for constant ground surface temperatures of −2, −4, ..., −20 °C at the spent fuel repository location using reference subsurface properties (for further information, see SKB TR-06-23, Section 3.4.4).*

Spent fuel repository

According to Figure 6-8, the mean annual ground surface temperature must be at least –8 °C for permafrost to reach the depth of the spent fuel repository (450 m). However, at this temperature, it takes a long time – about 120 kyr – for permafrost to reach this depth. If the surface temperature is lower, the time required for permafrost to reach repository depth decreases significantly. For example, at –10 °C, it takes 17 kyr years to reach 450 m, and at –12 °C, it takes only 7 kyr (Figure 6-8). However, these ground surface temperatures differ from the SATs provided by the climate projections. During periglacial conditions, permafrost modelling shows that the ground surface temperature is typically higher than the prevailing SAT (Hartikainen et al. 2010). To convert the SAT from the climate projections to ground surface temperatures, we assume – similar to the analysis about future periglacial variability (Section 6.5.1) – that the surface temperature is 1 °C higher than the SAT, implying that permafrost at the surface (0 °C) will form when SAT=–1 °C.

Furthermore, assessments of future ice-sheet and periglacial variability (Sections 4.5.2 and 6.5.1) suggest that Forsmark will be covered by an ice sheet once the SAT drops sufficiently low. Modelling indicates that when an ice sheet advances over an area with cold surface conditions, the permafrost depth tends to decrease (e.g. SKB TR-20-12, Figure 4-35). For simplicity, it is therefore assumed that permafrost at repository depth cannot exist when the repository location is covered by an ice sheet. This transition is parameterized by the same threshold value as in the analysis of future periglacial variability (Section 6.5.1), $T_{\text{per,lower}}$, below which ice coverage is assumed.

In conclusion, this means that permafrost is projected to form at spent fuel repository depth (450 m) when the Forsmark SAT, T_{Forsmark}, falls within the following ranges:

- $T_{\text{per,lower}} < T_{\text{Forsmark}} < –9$ °C for at least 120 kyr, or
- $T_{\text{per,lower}} < T_{\text{Forsmark}} <–11$ °C for at least 17 kyr, or
- $T_{\text{per,lower}} < T_{\text{Forsmark}} <–13$ °C for at least 7 kyr.

As shown in the analysis about future periglacial variability in Forsmark (Section 6.5.1), $T_{\text{per,lower}}$=–14 °C is considered to be a reasonable approximation for future glacial cycles with similar ice-sheet development to that of the last glacial cycle. $T_{\text{per,lower}}$=–16 °C was introduced as an unlikely bounding case featuring significantly less ice coverage and, therefore, longer periods of periglacial conditions, compared to the last glacial cycle. The likelihood of permafrost and frozen conditions at the spent fuel repository depth is examined for both of these thresholds.

Figures 6-9a and 6-10a show the percentage of the 90 simulations (per emission scenario) that yield permafrost formation (0 °C isotherm) at the depth of the spent fuel repository over the next 1 Myr for $T_{\text{per,lower}}$=–14 °C and $T_{\text{per,lower}}$=–16 °C, respectively.

For the case of $T_{\text{per,lower}}$=–14 °C, permafrost is projected to form at spent fuel repository depth during relatively short time intervals, particularly around ~200 kyr, ~300 kyr, ~450 kyr and ~870 kyr, in a limited number of simulations with anthropogenic emissions of 1500 Pg C or less. However, permafrost at repository depth is not projected by the majority of simulations (>50 %) at any point over the next 1 Myr for the case of $T_{\text{per,lower}}$=–14 °C (Figure 6-9a).

In the less likely case of $T_{\text{per,lower}}$=–16 °C, the number of projected periods of permafrost at repository depth increases significantly compared to the $T_{\text{per,lower}}$=–14 °C case (Figure 6-10a). This increase is primarily due to longer durations of individual periglacial periods (see $d_{\text{per,ave}}$ and $d_{\text{per,ind}}$ in Tables 6-2 and 6-3), providing more time for the permafrost to grow thick enough to reach repository depth. The majority of simulations (>50 %) project permafrost at repository depth during seven time intervals. Before 200 kyr, these intervals only occur for climate scenarios with low anthropogenic emissions (400 Pg C or less). However, after 200 kyr and 500 kyr, they are also projected for the 1500 Pg C and 5500 Pg C scenarios, respectively (Figure 6-10a).

Figures 6-9a and 6-10a only show the potential development of permafrost (i.e., the 0 °C isotherm) at the spent fuel repository depth. However, a more relevant question for post-closure safety – especially for assessing the potential for buffer freezing (Section 6.1.2) – is how cold the conditions around the repository could become, specifically, what the minimum temperature at repository depth could be over the next 1 million years. Unfortunately, idealised permafrost simulations, like those shown in Figure 6-8, are not available for isotherms below 0 °C at 450 m depth. Therefore, to estimate the minimum temperature at repository depth, we assume that any temperature change at the surface will be the same at depth. This is a very crude approximation because temperature anomalies that propagate from the surface to deeper bedrock layers will be mitigated by the geothermal heat flux, which transfers heat from the Earth's interior to the surface (Section 6.2.2). In Forsmark, the geothermal heat flux at the surface is estimated to be approximately 60 mW/m² (Sundberg et al. 2009). As a result, any cold anomaly at the surface gradually decreases as it moves deeper into the bedrock. Therefore, assuming that surface cooling will be fully preserved at depth significantly *overestimates* the potential cooling at repository depth. Consequently, the following analysis should be considered a maximum estimate of the possible cooling at repository depth over the next 1 Myr rather than a realistic one.

Based on this simplification, Figures 6-9b-e and 6-10b-e show the percentage of simulations that yield temperatures lower than –1 °C, –2 °C, –3 °C and –4 °C at the spent fuel repository depth over the next 1 Myr for $T_{\text{per,lower}}$=–14 °C and $T_{\text{per,lower}}$=–16 °C, respectively. In the case of $T_{\text{per,lower}}$=–14 °C, no simulations project temperatures lower than –1 °C at repository depth (Figure 6-9b), regardless of emission scenario. In the more extreme case of $T_{\text{per,lower}}$=–16 °C, a temperature of –1 °C at repository depth is projected in several simulations for most of the time intervals that also project permafrost (Figure 6-10b). However, projections of lower temperatures at repository depth are rare, even in the case of $T_{\text{per,lower}}$=–16 °C. A temperature of –2 °C is projected by more than 10 % of the simulations only during three periods, while –3 °C is projected in only a few individual simulations, and temperatures as low as –4 °C are not projected at all (Figure 6-10c-e). Given that these results are based on assumptions that very likely overestimate cooling at repository depth – namely, that (i) the cooling at the surface will be the same at repository depth, and that (ii) $T_{\text{per,lower}}$=–16 °C, which implies significantly longer periods of periglacial conditions compared to the last glacial cycle – projecting a minimum temperature of –3 °C at repository depth over the next 1 Myr can be considered a pessimistic estimate. The most likely scenario based on this analysis is that permafrost will not develop at all at the repository depth over the next 1 Myr, and if it does, the temperature will remain above –1 °C.

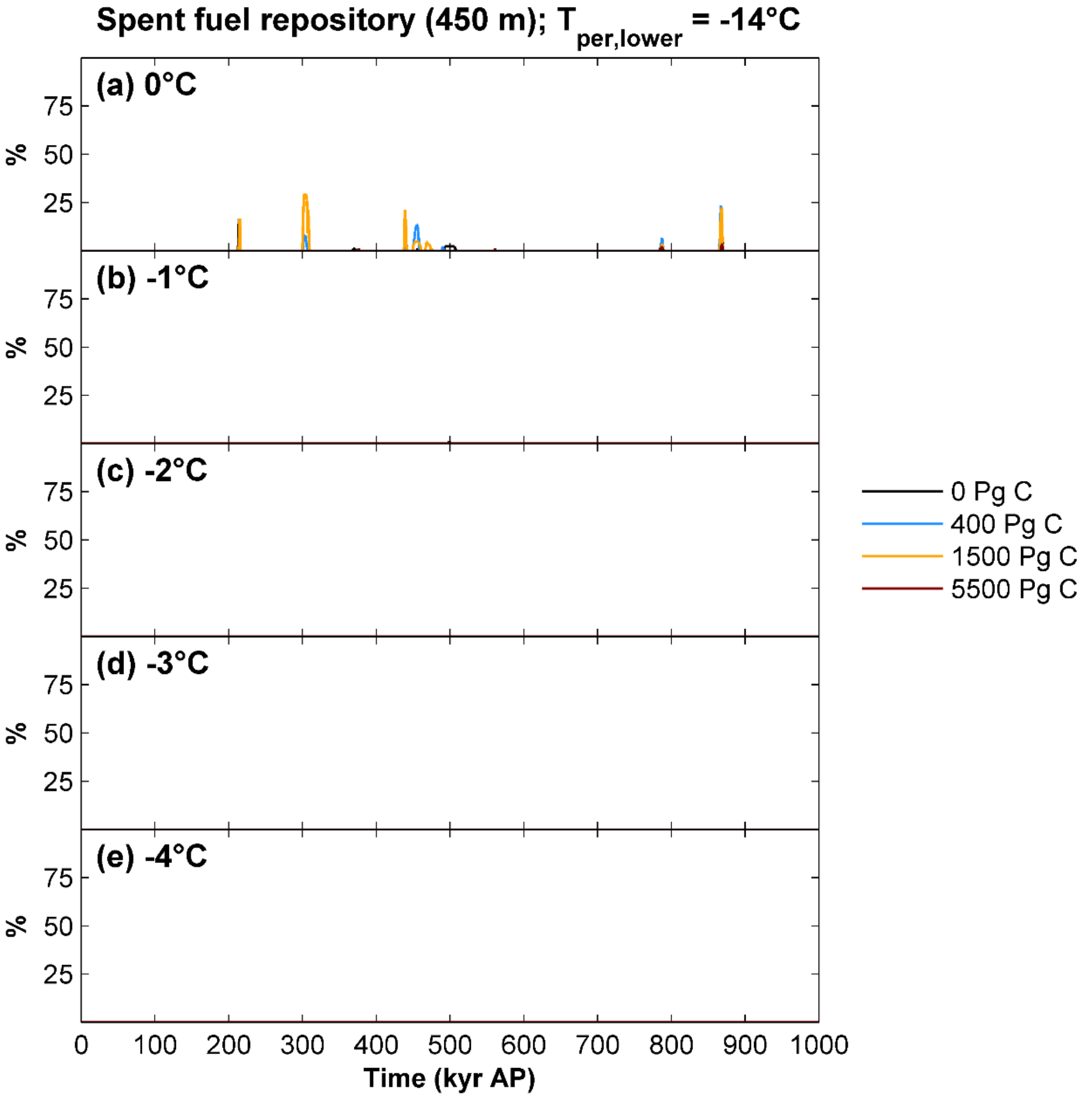

Figure 6-9. *Percentage of the 90 climate simulations (Williams et al. 2022) per emission scenario (see legend) that the give rise to the following low temperatures at spent fuel repository depth (450 m): (a) 0 °C (permafrost), (b) –1 °C, (c) –2 °C, (d) –3 °C and (e) –4 °C. The percentages have been calculated using a lower SAT threshold for periglacial conditions in Forsmark of* $T_{per,lower,}$*=–14 °C. See further Section 6.5.1 on the definition of this threshold.*

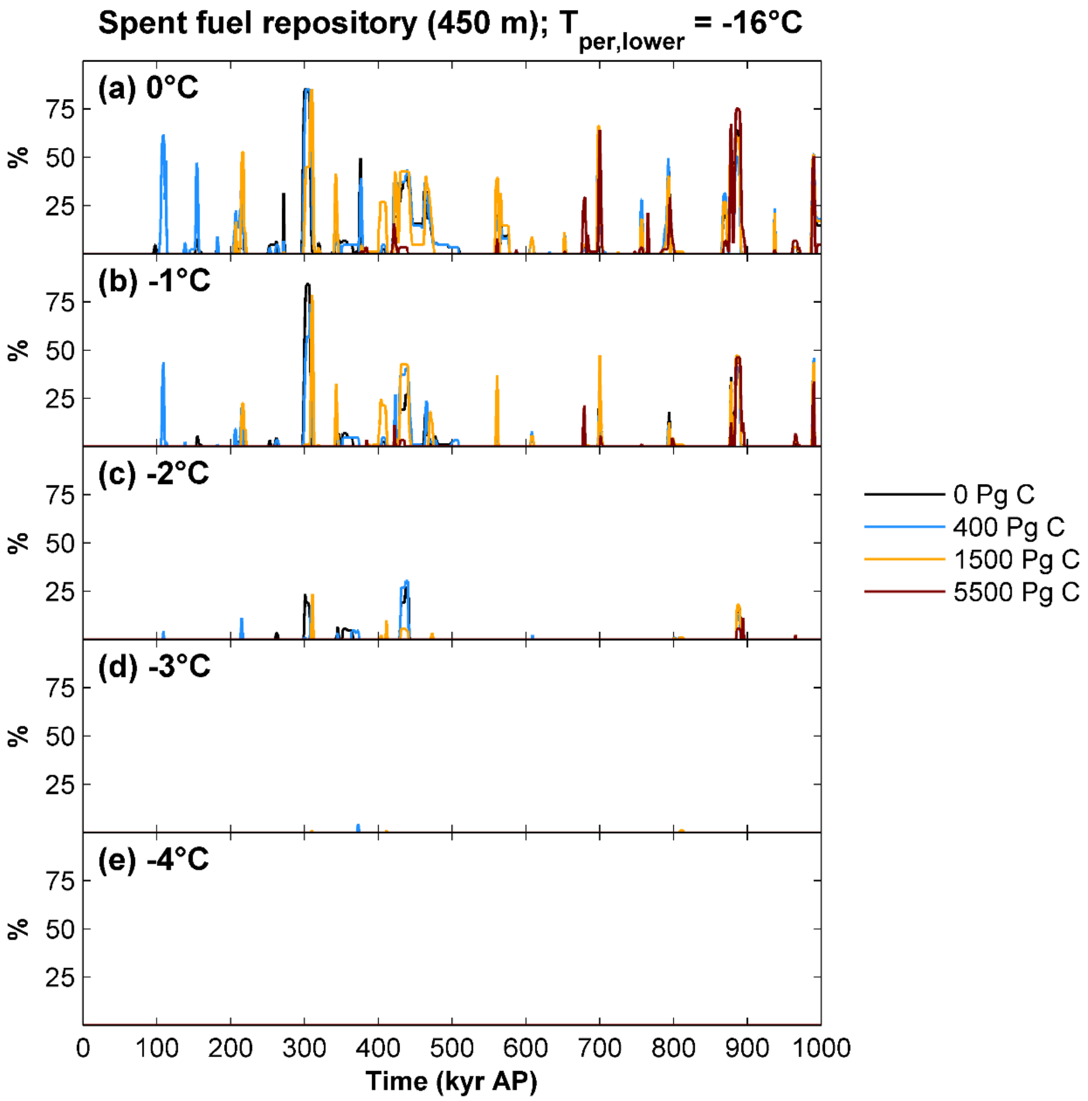

Figure 6-10. *Same as Figure 6-9, but using a bounding value of $T_{per,lower,}=-16$ °C, which results in longer periods of periglacial conditions compared to $T_{per,lower,}=-14$ °C, see further Section 6.5.1.*

SFR

In constrast to the spent fuel repository, post-closure safety assessment of SFR extends only 100 kyr into the future (Section 1.2.3). SFR is located at depths of approximately 60 m (SFR1) and 120 m (SFR3) (Section 1.2.1). Brandefelt et al. (2013) investigated the SAT decrease required for permafrost (0 °C isotherm) to reach these depths, using climate modelling and 2D permafrost simulations. Their results suggested that for the 0 °C isotherm to reach SFR1 and SFR3, the annual mean SAT would need to be at least −1 °C and −3 °C, respectively, sustained over approximately 2000 years.

These criteria are used to determine the percentage of 90 climate simulations (Williams et al. 2022) that result in permafrost conditions at the depths of SFR1 and SFR3 over the next 100 kyr. The results, shown in Figure 6-11, are based on the lower SAT threshold for periglacial conditions, $T_{\text{per,lower}}=-14$ °C. Using $T_{\text{per,lower}}=-16$ °C instead would have limited impact on the results, as the first 100 kyr are projected to be relatively warm, keeping the SAT above −14 °C for nearly the entire period.

Figure 6-11 shows that none of the simulations predict permafrost formation at SFR depths for anthropogenic emissions of 1500 Pg C or higher. This is expected since the same projections show that Forsmark will continue to have a temperate climate over the next 100 kyr under these higher emissions (Sections 3.5.4 and 3.6.1). In the zero-emissions scenario (0 Pg C), nearly all simulations indicate that the first permafrost formation at SFR depth occurs around 60 kyr AP, followed by a second period centred around 87 kyr AP (Figure 6-11). For low emissions (400 Pg C), most simulations suggest permafrost formation at SFR depth before about 90 kyr AP. However, unlike the 0 Pg C scenario, only about 10 % of simulations project permafrost at SFR1 after 60 kyr, and even less than that for SFR3 (Figure 6-11).

Interestingly, the majority of simulations under the 400 Pg C scenario project permafrost at SFR depth towards the end of the 100 kyr-period, while this is not the case for most simulations under the 0 Pg C scenario. This difference is primarily due to the timing of the first ice-sheet advance over the site, which is projected to occur before 100 kyr AP in the 0 Pg C scenario but after 100 kyr AP in the 400 Pg C scenario (Section 4.5.2). However, given SFR's relatively shallow depth, permafrost could persist around the repository for some time even after an ice-sheet advance. Therefore, the likelihood of permafrost around 100 kyr AP in the 0 Pg C scenario is probably higher than Figure 6-11 suggests.

All in all, the results in Figure 6-11 confirm the conclusions in Brandefelt et al. (2013) and in the latest (PSAR) post-closure safety assessment for SFR (SKB TR-23-05, Section 5.2.3) that the first future period of permafrost and frozen conditions at SFR depth could occur earliest around 60 kyr AP under realistic climate and surface conditions (see also Section 3.6.1). The new result in this report is that permafrost after 60 kyr is only likely in the absence of anthropogenic emissions. Even for low emission scenarios (400 Pg C), which is lower than the ~700 Pg C humanity has already emitted (Section 2.4), the earliest period of future permafrost at SFR depth is projected to occur later, between 80 and 90 kyr AP in most simulations.

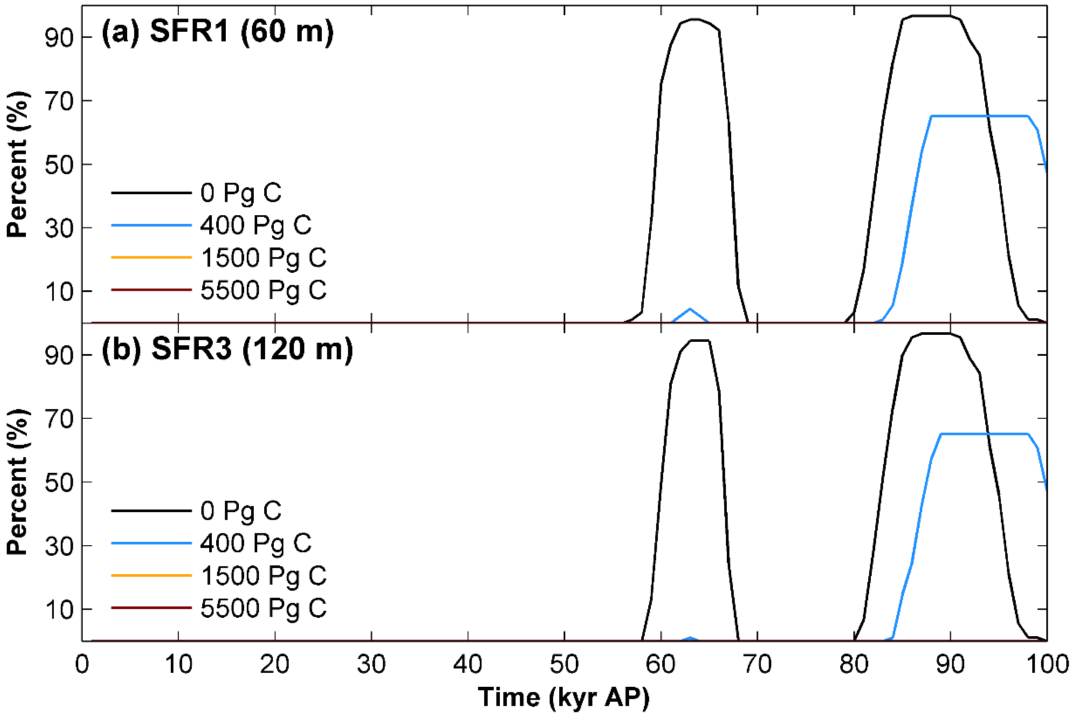

Figure 6-11. Percentage of the 90 climate simulations (Williams et al. 2022) per emission scenario (see legends) that the give rise to permafrost (0 °C) at characteristic depths of SFR1 and SFR3 (60 and 120 m).

Discussion and concluding remarks

This section presented two methods for estimating future maximum permafrost depth, with the key difference being the selection of SAT forcing used in the simulations. In the first approach, the SAT record from the past 120 kyr, derived from a Greenland ice core, was used as forcing. This method assumes that the last glacial cycle represents a typical glacial cycle and, as a result, that similar cycles will occur also in the future. By combining this SAT curve with information on reconstructed periods of ice-coverage in Forsmark (Section 4.3) and subsequent submerged periods (Section 5.3), the simulations estimate a maximum permafrost and freezing depth at Forsmark during such a typical glacial cycle of approximately 250 m and 230 m, respectively. A more severe permafrost case was also considered, in which the last glacial cycle SATs were modified to assume no ice coverage, no submerged periods, and the absence of insulating snow cover or vegetation. Under these conditions, the maximum permafrost and freezing depths increased to approximately 420 m and 370 m, respectively. Only in an extreme simulation – where the uncertainties in all parameters were set to promote permafrost development – did the permafrost depth reach 450 m, which corresponds to the depth of the spent fuel repository. However, even in this extreme simulation, freezing did not occur at 450 m depth. Thus, the overall conclusion from the simulations based on historical SAT forcing suggest that freezing of the groundwater at repository depth of the spent fuel repository is unlikely over the next 1 Myr.

The second approach combined results from idealised permafrost simulations, driven by a constant surface temperature forcing, with 90 projections of future SAT evolution based on predicted insolation changes and scenarios of anthropogenic carbon emissions (Lord et al. 2019, Williams et al. 2022). The projected SAT from the climate simulations was combined with permafrost depths from the idealised simulations to assess the likelihood of permafrost formation at the depths of the spent fuel repository and SFR. Unlike the first approach, which relied on historical data to derive SAT forcing, this second method uses projected future SAT, and thus also provides insights into the potential timing of future permafrost events.

The second approach generally highlights the possibility of deeper permafrost compared to the method of repeating the last glacial cycle. While the latter yields a maximum permafrost depth of approximately 250 m over the spent fuel repository, some more than 10 % of the future projections suggest that permafrost could even reach repository depth (450 m) for short periods (order 10 kyr) at least four times over the next 1 Myr, under the assumption that future glaciations resembles the last glacial cycle. If the climate projections assume a more limited ice cover, permafrost formation at repository depth is not just possible but a likely outcome, as permafrost reaches 450 m depth in the majority of simulations during seven different periods over the next 1 Myr. This scenario can be compared to the severe permafrost case, where the maximum permafrost depth at the repository location reached approximately 400 m.

Why does the second approach, based on future climate projections, result in deeper permafrost compared to the first approach, which is based on the conditions of the last glacial cycle? One possible reason is that insolation changes over the next 1 Myr may differ from those of the past 120 kyr in a way that promotes permafrost development in Forsmark. However, a more likely explanation relates to the temporal variability of the SAT forcing, as discussed in Section 6.3.4. Specifically, the sudden warming events (DO-events) present in the SAT curve of the last glacial cycle likely inhibited deep permafrost formation in Forsmark. Since these warming events are projected to be less intense in Forsmark compared to Greenland (Section 6.3.4), their impact is likely overestimated in the reconstructed SAT curve, leading to an underestimation of maximum permafrost depth.

On the other hand, the simplified design of the future climate simulations used in this study (Lord et al. 2019, Williams et al. 2022) excludes potential SAT fluctuations on sub-Milankovitch timescales. One reason for this is due to the long timesteps (1000 years) used in the simulations. This means that any future ice-climate interactions that could influence local climate conditions in Forsmark are not accounted for. As a result, once SAT drops below freezing in the simulations, it tends to remain low for several tens of thousands of years, in contrast to the more variable SAT record from Greenland.

This prolonged cold period promotes deeper permafrost expansion in Forsmark. Therefore, the climate simulations likely underestimate future SAT variability, suggesting that the projected permafrost depths may be overestimated. Given these uncertainties, the most realistic estimate of maximum permafrost depth over the next 1 Myr is likely somewhere between the depth predicted by repeating last glacial cycle conditions and the depth projected by the future climate simulations.

For post-closure safety assessments of the spent fuel repository, a more relevant question than whether or not permafrost and frozen conditions will reach repository depth is how cold it could become at repository depth (Section 6.1.2).

This question was examined for the spent fuel repository over the next 1 Myr using the idealised permafrost simulations combined with the 90 climate projections. We found that the minimum temperature at repository depth will remain above −1 °C over the next 1 Myr if future ice-sheet variability mirrors that of the last glacial cycle. In the unlikely case of much more limited ice coverage than the last glacial cycle (Section 4.5.2), our estimates suggest that temperatures at repository depth will not drop below −3 °C over the next 1 Myr. However, the estimates of minimum temperature at repository depth are likely too low for two reasons: (i) the climate projections likely overestimate permafrost depth and thus cooling in the bedrock due to a lack of variability, as discussed earlier, and (ii) we assume that any cold anomaly at the surface will be preserved at repository depth, which is a very crude simplification. In reality, cooling at repository depth is expected to be considerably less than at the surface due to geothermal heat flux.

Based on idealised permafrost simulations (Brandefelt et al. 2013) and the 90 climate projections, we found that the first potential future period during which SFR could be affected by permafrost occurs around 60 kyr AP, followed by a second period around 80–90 kyr AP. This result aligns with the conclusions in PSAR SFR (e.g. SKB TR-23-05, Section 5.2.3), as well as with the assessment that permafrost in Forsmark will not occur in response to the weak insolation minimum after 17 kyr (Section 3.6.1). A key new finding in this analysis is that permafrost at SFR depth after 60 kyr is only likely in the absence of anthropogenic emissions (0 Pg C). Under a low-emission scenario (400 Pg C), the first permafrost period at SFR depth is projected to occur after 80–90 kyr in most simulations. For emissions of 1500 Pg C or higher, no simulations project permafrost at repository depth.

7 Denudation

7.1 Introduction

7.1.1 Definitions

Denudation is a geological process that refers to the wearing away of the Earth's surface by various weathering and erosion processes. Weathering can be defined as mechanical and/or chemical break down/alteration of rock to form regolith through the cumulative effects of physical, chemical and biological processes operating at or near the ground surface (e.g. Reiche 1950, Selby 1993). Erosion can be defined as the removal and transport of bedrock and earth materials by a moving natural agent, such as air, water or ice.

Denudation is the sum of the processes that results in the wearing away or modifications of the *topographic relief* (variations in land elevation). The topographic relief in Fennoscandia is generally low outside the Scandinavian mountains (e.g. Lidmar-Bergström and Näslund 2005). This is because the resistance to denudation of the Precambrian rocks that dominate in Fennoscandia is rather uniform, as compared with, for example, the variation between the Caledonian bedrock types in the Scandinavian mountains. Along significant portions of the Baltic Sea coastline of southern and south–central Sweden, including the Forsmark area, the relief is exceptionally low (up to a few tens of metres), due to the *sub-Cambrian peneplain*. This peneplain is interpreted as a denudation surface formed in crystalline rock down to sea level prior to the Cambrian period, i.e. prior to 540 Myr BP (cf. Rudberg 1954, Lidmar-Bergström 1995). Following geologically recent exposure from overlying sedimentary strata, the peneplain surface in the Forsmark region has been somewhat modified by denudation, but still exhibits a very low relief (Hall et al. 2019a). Over the past 1 Myr, glacial erosion has been the most significant denudation process in Fennoscandia, including Forsmark (Hall et al. 2019a). This process involves the transport and removal of bedrock and Quaternary sediments by ice sheets.

7.1.2 Importance for post-closure safety

Since glacial erosion is considered the most significant denudation process in Fennoscandia, and glaciations are not expected in the region before 100 kyr from now (Section 4.5.2), denudation poses a greater concern for the spent fuel repository, which has an assessment period of 1 Myr, compared to SFR, whose assessment period is limited to 100 kyr (Section 1.2). For SFR, potential effects of denudation over the next 100 kyr are not analysed in the safety assessment because the total denudation of crystalline bedrock during this period is projected to be very small (<1 m; see SKB TR-23-05, Section 2.4.6).

For the spent fuel repository, denudation becomes more relevant for post-closure safety toward the end of the 1 Myr assessment period, following repeated glaciations in the Forsmark area. These glaciations progressively reduce the repository depth, potentially increasing the risk of freezing within the repository structures (SKB TR-20-12, Section 5.5.4). They can also influence the topographic relief, which in turn affects hydrogeological and stress conditions in the bedrock.

7.1.3 Previous documentation

Key processes contributing to total denudation in Forsmark, as well as estimates of past and future denudation, have been thoroughly described in the PSAR climate reports for the spent fuel repository (SKB TR-20-12, Section 3.5) and SFR (SKB TR-23-05, Section 2.4). This chapter will briefly summarise the information compiled in these reports; for a more comprehensive review, readers are referred to the aforementioned PSAR reports.

This chapter focuses on new developments and findings since the preparation of the PSAR reports. It covers results from recent denudation studies, including the analysis and quantification of a newly identified erosion process called glacial ripping (e.g. Krabbendam et al. 2022). Additionally, it examines the possibility that an area about 25 km southeast of the spent fuel repository, known for stronger past erosion than at the Forsmark site, could migrate toward the repository area within the next 1 Myr (Hall et al. 2022).

Furthermore, projections of potential future denudation in the PSAR were based on projections of future ice-covered periods from Lord et al. (2019). These projections have been updated in this report (Section 4.5.2), requiring corresponding revisions to the denudation projections.

7.2 Controlling variables and conditions

Denudation is the result of weathering and erosion. The general characteristics of these processes are described in the following.

7.2.1 Weathering

Weathering occurs when minerals/rocks are exposed to temperatures, pressures and moisture conditions characteristic of the atmosphere and hydrosphere, i.e. in a near-surface environment that differs significantly from the conditions at depth in which most igneous and metamorphic rocks, as well as lithified sedimentary rocks, were formed. In this way, the alteration of rocks by weathering forms new materials (minerals) that are in near-equilibrium with conditions at or near the Earth's surface.

Weathering is generally divided into physical-, chemical- and biological components, of which physical and chemical weathering are typically the most important. Physical weathering occurs when volumetric expansion or other stresses lead to failure and disintegration of the rock. For example, volume changes due to decreased overburden load can result in the creation of new fractures at various scales. Crystallisation and volumetric alteration of salt crystals, freezing of water and freeze-thaw effects, as well as thermal fatigue due to repeated (diurnal) heating and cooling, may also cause physical weathering.

Chemical weathering comprises reactions between water and rock minerals. Examples are dissolution of minerals, carbonation, hydrolysis, hydration, and oxidation and reduction. Common to chemical weathering processes is that they depend on water composition, for example pH, salinity, CO_2 and redox potential. The prevailing temperature is another important parameter determining the type and efficiency of chemical weathering.

The degree of weathering depends on the availability of weathering agents such as salt, moisture, and on the microclimatic conditions to which the rock is exposed. Weathering occurs in all climates, but high temperatures and humid conditions increase weathering rates. In areas where frost and/or permafrost occur, freezing and freeze-thaw effects are important geomorphic processes. However, weathering in periglacial environments is also affected by salt (in combination with freezing), wetting and drying, thermal fatigue and biological agents (French 2007).

Under present temperate climate conditions in Sweden, weathering occurs slowly where bedrock is exposed. Swantesson (1992) estimated the postglacial weathering of bare bedrock surfaces in southern Sweden to be less than 0.02 m during the Holocene. Weathering rates of soils in tropical climates range between 2 and 48 m Myr^{-1} (Thomas 1994).

For a description of climatological, hydrological and geological factors affecting weathering, see e.g. Olvmo (2010, Section 3.3.3).

7.2.2 Erosion

There are various types of erosion, classified by the agents that remove bedrock and earth materials: wind (aeolian erosion), ocean (marine erosion), rivers (fluvial erosion), and ice (glacial erosion). This section provides a brief overview of the main mechanisms behind each type of erosion. It concludes with a summary discussing the relative importance of these erosion processes under different climate conditions.

Aeolian erosion

Erosion of weathered rock or sediments by wind, i.e. aeolian erosion, is most important in environments with sparse or non-existent vegetation, a loose and/or non-cohesive substrate of sufficiently fine texture, sufficiently deep groundwater tables and strong winds, for example semi-arid and/or arid periglacial regions Particle movement is achieved due to wind shear stress and atmospheric turbulence. The mass flux of particles is related to the wind shear velocity, abrasion and the impact of particles moved by saltation and creep. The latter mobilise fine-grained material affected by cohesion but easily carried by the wind. Thus, the transport rate is limited both by wind shear velocity and the supply of particles.

Marine erosion

Marine erosion is largely limited to the reworking of sediment in the shore zone. In regions with post-glacial uplift, such as in the Forsmark region, it is very low in solid rock because a shoreline at a given elevation is exposed to marine erosion for a relatively short period of time. Furthermore, the smooth, previously glaciated bedrock surfaces generally lack loose, fractured rock that can be exploited by wave action. Also, the wave energy in the Baltic Sea is relatively low, reducing the efficiency of marine erosion further.

Fluvial erosion

Fluvial erosion is controlled by the flow velocity. To generate water flow, a water supply and a flow gradient are required. Therefore, fluvial erosion occurs on slopes, in ditches, and in brooks and rivers. Fluvial erosion at the base of slopes releases material that is transported to brooks and rivers, and into lakes and the sea. When rivers reach the sea, the flow velocity decreases, erosion ceases and the sediment load is deposited. Erosion by water on a slope increases with increased intensity of rain or snowmelt, increased inclination and length of the slope and decreased resistance to erosion of the soil. As for wind erosion, the presence of vegetation may strongly reduce the erosion rate. For more information on fluvial erosion, see e.g. Olvmo (2010, Section 4.1) and references therein.

Fluvial erosion may also be sensitive to transitions between temperate and periglacial conditions. Mechanisms like permafrost thaw and increased runoff collectively increase the erosive force of rivers and decrease the erosional resistance. During a warming phase, increased discharge and thawing soils contribute to bank erosion, sediment supply, and lateral channel migration. Meanwhile, the switch from a stable cold period to a dynamic warm period can leave river systems unstable, causing incision and subsequent terrace formation (e.g. Vandenberghe 2008).

The sea level acts as the base-level for fluvial erosion, i.e. fluvial erosion cannot cut deeper than sea level. Therefore, a deep dissection of the landscape in Forsmark cannot occur by fluvial erosion under present conditions because the area is located just a few m above the Baltic Sea level. Because of the bathymetry in the southern part of the Baltic Sea, this inland sea transforms into a lake per definition if the sea level drops below 18 m (Section 5.2.4). This value provides, together with the altitude of the ground surface above the repository (today a few metres), an order-of-magnitude estimate of a couple of tens of metres to the potential maximum amount of future fluvial erosion at the planned spent fuel repository site.

Glacial erosion

Glacial erosion has been the dominant process of erosion in and around the Baltic Sea basin over at least the last 1 Myr (e.g. Hall and van Boeckel 2020). Glacial erosion is a complex process as it depends on material properties of ice and rocks, ice thermodynamics, friction and lubrication at the ice-sheet bed, chemical effects and subglacial hydrology and topography. In addition, glacial erosion in bedrock is enhanced by pre-glacial sub-aerial weathering processes.

In recent years, interpretations of geomorphological features (e.g. Kleman et al. 1997, 2008), measurements of cosmogenic radionuclides (e.g. Stroeven et al. 2002, Blomdin et al. 2016, Hall et al. 2019a) and ice-sheet modelling (e.g. Näslund et al. 2003) have identified the high variability of glacial erosion over Fennoscandia. In some areas, over time dominated by basal frozen conditions, glacial erosion has been limited, whereas in other areas, where basal melting and sliding have occurred, erosion has been more pronounced.

Glacial erosion is traditionally divided into two components; *plucking* and *abrasion*. Plucking is the process by which rock fragments of different size are loosened, entrained and transported away from the glacier bed by ice. Plucking is responsible for the characteristic irregular and fractured surfaces of lee sides of bedrock bumps and small hills in formerly glaciated areas. Abrasion is the grinding of the substrate by rock fragments held in basal ice sliding over the substrate (e.g. Sugden and John 1976, Benn and Evans 1998). Abrasion scours the bedrock by debris carried in the basal layers of the glacier (e.g. Sugden and John 1976, Drewry 1986). The process leads to striation and polishing of bedrock surfaces (cf. Benn and Evans 1998) and is typical of the stoss side of rock bumps in formerly glaciated terrain.

Yet another process of glacial erosion, *glacial ripping*, has been proposed in Hall et al. (2020). This process invokes disruption of bedrock by dilation of near-surface pre-existing sub-horizontal bedrock fractures under high hydrostatic pressures beneath the ice (hydraulic jacking). Traction from the overriding ice-sheet causes disintegration of the lifted rock surface that is ripped apart into blocks. The blocks are transported away from the in-situ location and are subsequently being deposited by the ice, today forming till areas with large and abundant blocks. Glacial ripping, described in detail in Krabbendam et al. (2022), is shown to be more spatially localised than plucking and abrasion. However, the potential erosion depth due to glacial ripping is comparable to that of abrasion and plucking.

In addition to abrasion, plucking and ripping, glacial meltwater erosion may also be an effective agent of erosion along meltwater routeways both in subglacial and proglacial environments. The sediment concentrations of glacial meltwater streams are often high, and the flow is often very rapid and turbulent during ice melt seasons, which means that highly fluctuating flows, including debris flows, can occur (Benn and Evans 1998). The controlling mechanisms behind glacial meltwater erosion are the same as for fluvial erosion.

The magnitude of glacial erosion by ice sheets differs widely both in time and space. At a continental scale, the large-scale pattern of glacial erosion is controlled by ice-sheet thermal regime and topography of the subglacial landscape. For example, Sugden (1977, 1978) found that the reconstructed thermal regime of the Laurentide ice sheet, with an inner warm-based area and an outer cold-bed area, broadly corresponds to the pattern of glacial erosion indicated by the distribution of erosional landforms. Other studies have indicated that basal sliding distance, i.e. the accumulated length of ice that has passed over the landscape by basal sliding, can be used as a broad-scale proxy for glacial erosion (Näslund et al. 2003, Staiger et al. 2005), indicating that glacial erosion has a great variation in space and time. This great spatial and temporal variation has also been observed for the Forsmark region, as described further in Hall et al. (2019a) (see also further Sections 7.3 and 7.5).

An approach to estimate average glacial erosion is presented by Hallet et al. (1996) who made a comprehensive review of glacial erosion rates based on sediment yields. They found that rates of glacial erosion vary by many orders of magnitude from 0.01 mm yr^{-1} for polar glaciers and thin temperate plateau glaciers on crystalline bedrock, to 0.1 mm yr^{-1} for temperate valley glaciers also on resistant crystalline bedrock in Norway, to 1.0 mm yr^{-1} for small temperate glaciers on diverse bedrock in the Swiss Alps, and to 10–100 mm yr^{-1} for large and fast-moving temperate valley glaciers in the tectonically active ranges of southeast Alaska. These major differences highlight the importance of the glacial basal thermal regime, glacial dynamics and topographic relief on the rates of glacial erosion. Estimated historical and projected future glacial erosion rates for the Forsmark region are presented in Sections 7.3 and 7.5, respectively.

Summary

Under temperate climate conditions, fluvial erosion is the dominant denudation process. In periglacial climates, where the environment is typically drier with sparse vegetation, aeolian erosion can also become significant. During spring snowmelt, erosion of sediments in the active layer may occur in periglacial permafrost areas. Especially at the transition between temperate and periglacial climate domains, the landscape can become unstable leading to denudation. Under glaciated conditions, glacial erosion is the dominant process, influenced by the thermal, hydrological and physical conditions at the ice-sheet/substrate interface. Where the ice is frozen to the bed, it preserves the subsurface with little to no erosion. However, in areas of basal melting, erosion of bedrock and sediments is likely, with a faster ice flow generally resulting in more erosion. Significant erosion can also occur in sub-glacial tunnels as meltwater flows toward the ice-sheet margin, affecting both loose sediments and bedrock.

7.3 Historical evolution

The long-term denudation history of Fennoscandia is interesting for two reasons. Firstly, it may help to understand the denudation rate through time in the Forsmark area. Secondly, it is important because the different landforms and surfaces that have been recognised, such as the sub-Cambrian peneplain mentioned Section 7.1.1, may be used as reference surfaces to understand the magnitude and patterns of denudation and glacial erosion, at least on a regional scale (e.g. Hall et al. 2019a). This is an important issue with respect to the time perspective of the safety assessment.

Some examples from Sweden of calculated long-term denudation rates are available, most of them using ancient smooth bedrock denudation surfaces as reference surface. In southestern Sweden, the maximum denudation of the tectonically uplifted sub-Cambrian peneplain is approximately 100 m. Once overlying sedimentary cover rocks had been removed, denudation and removal of the denudation products would have required a period of between 2 and 50 Myr (Lidmar-Bergström et al. 1997). On the Swedish west coast, a so-called *Sub-Cretaceous etch surface* has been incised into the sub-Cambrian peneplain by weathering. In some places, it has resulted in a maximum bedrock lowering of around 140 m. The time required for this amount of denudation has been suggested to be between 3 and 68 Myr (Lidmar-Bergström et al. 1997), with the denudation occurring during the Jurassic-Early Cretaceous (around 200–100 Myr ago). Finally, saprolite thicknesses of 50 m in Skåne were interpreted to have been produced by weathering over a time interval of 1–25 Myr (Lidmar-Bergström et al. 1997).

The examples above clearly show that the evolution of the sub-Cambrian peneplain in southern Sweden into a younger incised landscape has been a slow process, and that the total amount of material removed from the crystalline bedrock has not been large considering the very long time periods involved. The total maximum denudation of bedrock in areas of Precambrian crystalline basement in southern Sweden during the last 540 Myr is on the order of a few hundred metres. A significant part of this denudation took place during Mesozoic (250–65 Myr) tropical climate conditions, considerably more favourable for chemical deep weathering than for instance a climate similar to the current one. More detailed accounts of the long-term landform development and associated denudation in southern Sweden are given in Olvmo (2010) and Hall et al. (2019b).

7.3.1 Quaternary glacial cycles

During the Quaternary glacial cycles, ice-sheets have repeatedly covered parts or the whole of Fennoscandia (Section 4.3), producing glacial erosional landforms in bedrock (e.g. Rudberg 1954) and moulding loose surficial deposits to form different glacial depositional or erosional landforms (e.g. Kleman et al. 1997, 2008). Glacial erosion is usually regarded as the dominant erosion process in Fennoscandia during this period. However, as large parts of Fennoscandia were not covered by ice during significant portions of the Quaternary (Porter 1989), including the last glacial cycle (Section 4.3.1), other denudation processes must also be considered in quantifying the total denudation budget (e.g. Lidmar-Bergström 1997).

In the PSAR (SKB TR-20-12, Section 3.5), quantification of denudation in the Forsmark area over the past 100 kyr and 1 Myr were based on a comprehensive study documented mainly in Hall et al. (2019a). The prerequisites for the methodology used in Hall et al. (2019a) were investigated in Hall et al. (2019b) and Goodfellow et al. (2019). The aim of the study was to quantify the total denudation at the Forsmark site, including glacial erosion, as well as related questions such as bedrock surface stability, by employing a range of methodologies. To this end, Hall et al. (2019a) used a combination of (i) cosmogenic (radio-)nuclide analysis, (ii) geomorphological analysis of bedrock landforms and landforms in Quaternary deposits, (iii) bedrock fracture analysis, and (iv) shallow bedrock stress modelling, with the overall purpose to quantify the amount of denudation over the past 100 kyr and 1 Myr as well as for the coming 1 Myr (the latter of which is summarised in Section 7.5).

The cosmogenic nuclide methodology builds on the production of nuclides in quartz in rock surfaces that are exposed to cosmic rays (Hall et al. 2019a, Section 5.1). To this end, it is used to estimate the exposure age of the bedrock surface. Because the quartz in rock surfaces is only exposed to cosmic rays during ice-free periods and when the site is not covered by the sea, the cosmogenic analysis must be used in combination with datasets of past ice-cover periods and relative sea-level change. The cosmogenic nuclide that is most widely-applied in the field of Earth-surface processes is ^{10}Be, and it has a half-life of 1.39 Myr. Another commonly used isotope produced in quartz is ^{26}Al, with a half-life of 705 kyr. These isotopes are often measured together because their different half-lives allow a comparison of processes over different timescales, and because they can both be extracted using the same laboratory procedures. The production rates of these isotopes in quartz are well-constrained.

In Hall et al. (2019a), quartz in 32 surface bedrock samples and three boulder samples were collected at the Forsmark site and in neighbouring areas of the Uppland province (Figure 7-1). Two of the samples were located in the spent fuel repository footprint area (Figure 7-1). These samples were subsequently analysed for paired cosmogenic ^{10}Be and ^{26}Al nuclide concentrations. Erosion rates and depths were then simulated based on the cosmogenic nuclide data, along with reconstructions of past ice-free and terrestrial periods.

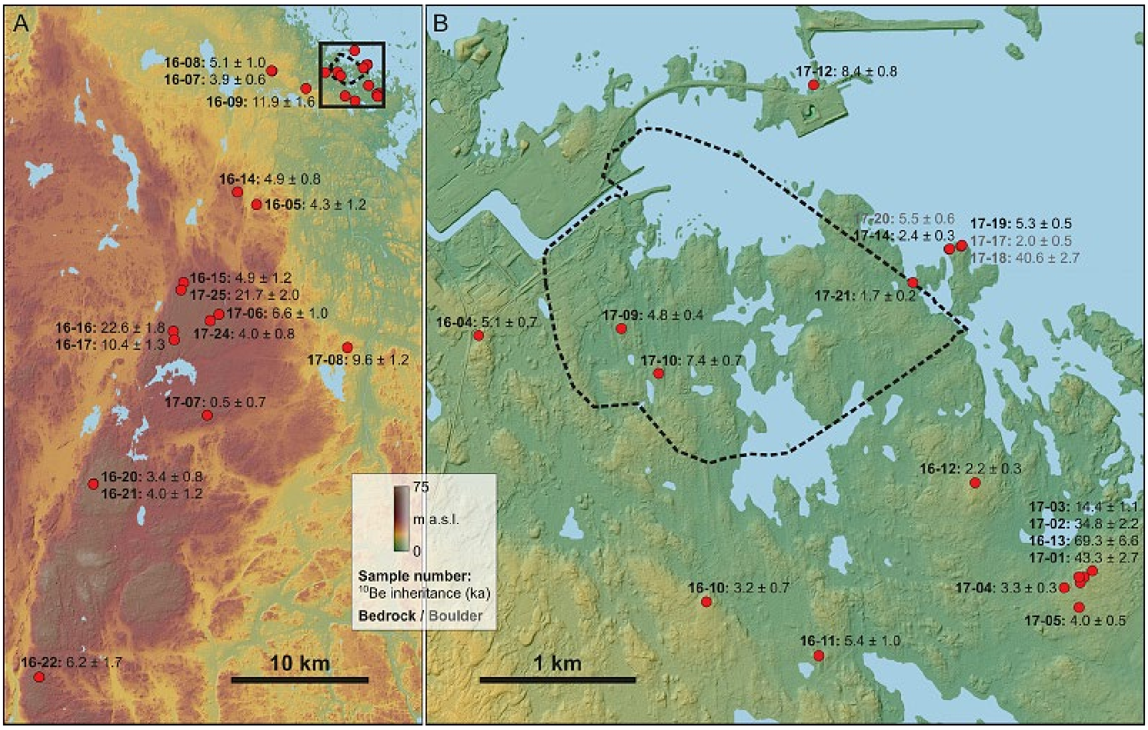

Figure 7-1. *Topographic maps of the investigation area around Forsmark including the distribution of cosmogenic nuclide samples with sample names and calculated ^{10}Be inheritance (defined as the difference between simple exposure age (Stroeven et al. 2016) and the reconstructed postglacial exposure history/shoreline displacement (SKB TR-20-12 and Goodfellow et al. 2024). A) Distribution of cosmogenic nuclide sample locations across the wider study area, from the planned repository location (black box; right panel) and along an NNE–SSW directed ridge. B) The repository footprint area (dashed line) and cosmogenic nuclide sample locations within and immediately beyond this area. From Hall et al. (2019a).*

The geomorphological analysis by Hall et al. (2019a) aimed to estimate the difference between the reconstructed summit envelope surface, representing the sub-Cambrian peneplain, and the present land surface.

The main results of Hall et al. (2019a) with regard to past denudation are as follows (see SKB TR-20-12, Section 3.5.4 for further details):

- The bedrock in the Forsmark area has a very low topographic relief and the rock type is crystalline bedrock. Also, the location of the planned spent fuel repository is not situated in a major fracture zone or topographic depression. This results in a setting not prone to effective glacial erosion and denudation.
- The geomorphological analysis shows that the average past denudation of crystalline basement rock over the Forsmark site, since (an estimated) re-exposure of basement 1.1 Myr ago, has been ~22 m, with a corresponding average denudation over the repository footprint area of ~18 m.
- The corresponding minimum and maximum denudation identified in the geomorphological analysis range from 10 to 50 m within the Forsmark site and from 10 to 33 m within the spent fuel repository footprint area.
- The typical denudation depths based on the cosmogenic analysis (25 % and 75 % percentiles across all samples within the Forsmark site) over the last 100 kyr was 1.6–3.5 m for the Forsmark site, whereas the full range (0 % and 100 % percentiles) was 0–8.6 m. The corresponding denudation within the spent fuel repository footprint area over the last 100 kyr was 1.0–5.6 m. Most of this denudation was caused by glacial erosion.
- The total range of denudation of basement rock over the past 1 Myr based on cosmogenic nuclide analysis across all samples in the Uppland province (Figure 7-1) is between 2 and 61 m.

The range in total denudation found in Hall et al. (2019a) shows that the amount of erosion has, as expected, varied over the site. This reflects spatial variations in dominant erosion processes and fracture control, the latter mainly in topographic lows. However, the overall conclusion in Hall et al. (2019a) is that the denudation and glacial erosion in Forsmark has been limited in the past. This conclusion aligns with the results obtained in the more restricted study by Olvmo (2010) used in the SR-Site safety assessment. The results are also in line with conclusions in Lidmar-Bergström (1997), who estimated a total amount of glacial erosion by all Late Cenozoic ice-sheets in lowland terrain in Sweden to be ~ 10 m (Hall and van Boeckel 2020).

Since the PSAR, additional studies have been performed to address remaining uncertainties or factors that were not fully considered in Hall et al. (2019a). These uncertainties and factors are summarised in the following.

1. **Uncertainty in the cosmogenic nuclide and geomorphological analysis.** Since the bedrock surface is only exposed to cosmic rays when the area is not submerged beneath the sea, it is essential to consider past shoreline changes in the cosmogenic nuclide analysis. Hall et al. (2019a) used SKB's current Holocene shoreline reconstruction for this purpose (Section 5.3). This reconstruction, based mainly on radiocarbon dating of organic material, carries some inherent uncertainty. To assess this uncertainty, Goodfellow et al. (2023, 2024) developed an independent Holocene shoreline displacement curve using in-situ ^{14}C in quartz. Their curve was found to be very similar to SKB's reconstruction (Section 5.3), suggesting that the uncertainty in SKB's model is likely small and that Hall et al. (2019a)'s earlier interpretations of cosmogenic nuclide data therefore are valid. Additionally, a study by Hall et al. (2023) and Krabbendam et al. (2023) estimated glacial erosion depth using cosmogenic nuclide and geomorphological analyses, respectively. The studies included five additional samples from the Forsmark site that were not included in Hall et al. (2019a). The estimated denudation depths from cosmogenic nuclide and geomorphological analyses of these samples ranged from 0.2 to 2.1 m, thus similar to the values reported in Hall et al. (2019a).

2. **Potential of headward erosion.** From a geomorphological perspective, the Forsmark region can be divided into distinct areas with varying relief: (i) a central area, which includes the Forsmark site, characterised by a topographic relief of less than 20 m of crystalline basement rock; (ii) the coastal region of the Öregrund archipelago, southeast of Forsmark, marked by coast-parallel lineaments; (iii) a southern area with more pronounced relief, featuring east–west trending fault scarps; and (iv) a hilly region in the northwest (Olvmo 2010). The low relief in the central area, including the Forsmark site, is characteristic of areas where the present bedrock surface has not been significantly lowered from that of the sub-Cambrian peneplain. In contrast, the coastal landscape of the Öregrund archipelago, approximately 25 km southeast of Forsmark, is more dissected, with topographic depressions that are 10–50 meters deeper than those to the west and south. This suggests that glacial erosion has been more intense in this area. Hall et al. (2022) investigated the factors contributing to this enhanced glacial erosion and the potential for further extension of the topographic depressions toward Forsmark through headward erosion. Their findings indicate that it would take at least 1 Myr for headward erosion from the Öregrund archipelago to reach Forsmark. However, due to the expected shortening, or even absence of, glacial cycles over the next several 100 kyr – partially driven by anthropogenic emissions – these timescales could extend well beyond 1 Myr.
3. **Effect of glacial ripping.** The recently highlighted erosion process glacial ripping (Section 7.2.2) was not explicitly included in the erosion projections by Hall et al. (2019a). The effect of glacial ripping was studied in detail in Krabbendam et al. (2022). In their study, glacial ripping is described as a sequence of three subglacial processes: (i) hydraulic jacking of surface near bedrock using pre-existing sub-horizontal fractures, (ii) rock mass disintegration of the uplifted bedrock, and (iii) boulder transport and deposition into boulder spreads (boulder fields). Evidence for this glacial-ripping sequence in eastern Sweden comes from three types of features (Krabbendam et al. 2022): (i) open, dilated sub-horizontal fractures, locally filled with sediment, and disruption or brecciation of the uppermost (top 1–13 m) rock mass indicating hydraulic jacking by subglacial groundwater; (ii) disrupted roches moutonnées, locally with fracture caves, that show further disintegration of the upper rock mass below the ice sheet, as well as variable damage on low-relief rock surfaces; and (iii) boulder spreads of large, angular boulders, with limited transport distances (usually less than 100 m, and not more than a few kilometres).
4. Near Forsmark, evidence of glacial ripping has been found in the form of disrupted rock surfaces and roches moutonnées (Hall et al. 2019a; Krabbendam et al. 2022), primarily located northwest and southwest of the nuclear power plant (Figure 7-2). The depths of rock mobilised or disintegrated by glacial ripping ranges from 1 to 4 m – similar to the depth of erosion during the Late Weichselian glaciation, as indicated by cosmogenic nuclide data (Hall et al. 2019a). Importantly, no evidence of glacial ripping has been found in the footprint area of the spent fuel repository (Krabbendam et al. 2022). The occurrence of near-surface hydraulic jacking and glacial ripping at the Forsmark site is influenced by distribution of subglacial water at overpressure, bedrock fracture patterns, local topography and till cover. Since many of these factors are locally confined, similar patterns and depths of glacial ripping can be expected at Forsmark during future glaciations (see further Section 7.5.2).

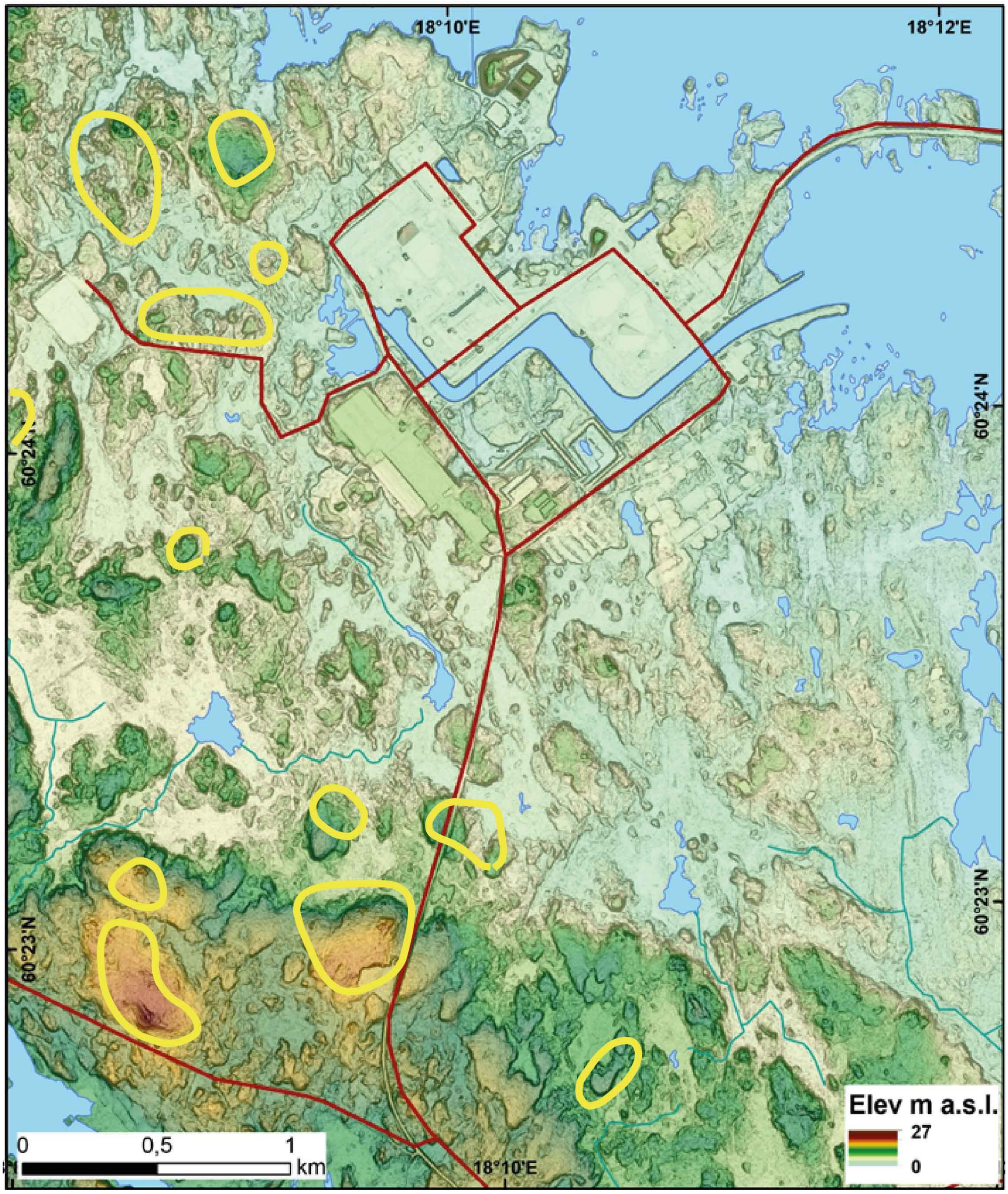

Figure 7-2. Bedrock elevation map of part of the Forsmark site showing the main areas with damage from glacial ripping, indicated by yellow lines. Modified from Krabbendam et al. (2022).

7.4 Present-day conditions and trends

Owing to the lack of ice sheets and large rivers in the Forsmark area, present-day denudation is mainly dominated by low rates of weathering and fluvial erosion along streams. Present-day denudation rates in the area are minimal and not of importance for post-closure safety.

7.5 Future evolution

In this section, projections of denudation at the Forsmark site over the next 100 kyr and 1 Myr are presented. The assessment of future denudation emanates from the assessment in the PSAR (SKB TR-20-12, Section 3.5.4), which is briefly summarised in Section 7.5.1. The PSAR projections are thereafter updated using new ice-sheet variability projections presented in Section 4.5.2; these are presented in Section 7.5.2.

7.5.1 Assessment in the PSAR

In the PSAR, estimates of total denudation over the next 100 kyr and 1 Myr were primarily based on the cosmogenic nuclide analysis by Hall et al. (2019a). This analysis simulated site-specific glacial erosion using observed concentrations of ^{10}Be and ^{26}Al in quartz in surficial bedrock samples (Section 7.3.1). In Hall et al. (2019a), the glacial erosion simulations based on these cosmogenic data were run in two modes, representing different ways in which glacial erosion may operate: (i) constant erosion rate (denoted E_r) and (ii) constant erosion depth (E_d). In the constant erosion-rate mode, the depth of erosion during each period of ice coverage scales with the duration of that coverage. In the constant erosion-depth mode, the depth of erosion remains the same for each ice coverage period, regardless of its duration, and instead scales with the number of ice coverage periods. The first mode may represent the effects of wet-bed glaciation, while the second may reflect glaciations dominated by dry-bed conditions, with erosion occurring mainly during wet-bed deglaciation phases (Kleman 1992, Harbor et al. 2006, Sugden et al. 2019). Although useful for the present assessment, this is a simplified view of natural conditions beneath ice sheets. In reality, conditions favouring either mode of erosion could coexist or switch on and off during a single glaciation event.

For the E_r mode, Hall et al. (2019a) estimated glacial erosion rates to range from 40 to 89 mm kyr^{-1} in the 25th to 75th percentile range, and from 16 to 144 mm kyr^{-1} in the 5th to 95th percentile range. For the E_d mode, the corresponding values were 39 to 109 cm per glaciation and 14 to 166 cm per glaciation (see Hall et al. 2019a, Section 5.4.5 for details). These uncertainty ranges primarily reflect spatial variations in erosion across the study area, as indicated by differences in erosion across the 32 cosmogenic nuclide samples (Figure 7-1). In addition to these glacial erosion estimates, Hall et al. (2019a) also considered subaerial denudation, assuming it occurs at a constant rate throughout the area during ice-free periods. The assumption of a uniform subaerial denudation rate is reasonable given the low-relief landscape of the Forsmark region.

To estimate the glacial erosion depth over the next 100 kyr and 1 Myr, the projected erosion rates and depths were combined with projections of future durations of ice-sheet coverage (for the E_r mode) and the number of ice-sheet coverage periods (for the E_d mode) (Hall et al. 2019b). These projections were derived from Lord et al. (2019) under the same emission scenarios (0, 400, 1500, and 5500 Pg C[28]) as used in the updated ice-sheet variability projections presented in this report (see Section 4.5.2). Unlike the current report, which features projections of future ice-sheet coverage using 90 calibrated model configurations with varying parameterisations, Lord et al. (2019) projected ice-sheet variability based on only one single calibrated model. This model was run 1 Myr into the future for each emission scenario, providing two projections of ice-sheet coverage periods: (1) a high-confidence projection, and (2) a low-confidence projection. The high-confidence projection included only those ice-sheet periods that were deemed likely based on comparisons with historical data (i.e., corresponding to low values of the glaciation threshold, $\Delta T_{\text{threshold}}$, in Section 4.5.2). The low-confidence projection included additional potential periods of ice-sheet coverage with lower likelihood (i.e., corresponding to higher $\Delta T_{\text{threshold}}$ values). Hall et al. (2019a) based their erosion projections solely on the high-confidence ice-sheet coverage periods from Lord et al. (2019).

Based on these ice-sheet coverage projections, Hall et al. (2019a) estimated that the mean total bedrock denudation (glacial and aeolian erosion) over the next 100 kyr will be less than 1 m, regardless of the emissions scenario. Over the next 1 Myr, assuming a constant erosion rate (E_r), the projected total denudation at the Forsmark site ranged from 5 to 28 m for the mid-range (25th–75th percentiles) and from 2 to 43 m for the wider range (5th–95th percentiles) across all emission scenarios. When assuming constant erosion depths (E_d), the denudation projections were similar but slightly lower at the high end. Specifically, the mid-range denudation over the next 1 Myr was projected to be 5 to 24 meters, with a wider range of 2 to 35 m across all scenarios. Based on these projections, the maximum possible denudation over the next 1 Myr was pessimistically set to 50 meters in the PSAR (SKB TR-20-12, Section 3.5.6).

---

[28] These scenarios were referred to as the "natural", "RCP2.6", "RCP4.5" and "RCP8.5" scenarios in Lord et al. (2019).

7.5.2 Assessment in the present work

Since the PSAR, the methodology for projecting future periods of ice coverage in Forsmark has been updated, leading to new results on future ice-sheet variability (Section 4.5.2). In this section, the erosion projections based on cosmogenic nuclide analysis are revised to reflect the updated projections of total duration of ice-sheet coverage duration ($d_{glac,\mathrm{tot}}$) and the number of glaciations (n_{glac}) presented in Section 4.5.2. Furthermore, this section includes a discussion of potential future erosion caused by the process of glacial ripping.

Updated erosion projections based on cosmogenic nuclide analysis

Approach

In the updated erosion projections, the same emissions scenarios as in Hall et al. (2019a) are used. Future periods of ice-sheet coverage are estimated based on when the simulated global-mean SAT drops below a certain threshold ($\Delta T_{\mathrm{threshold}}$; see Section 4.5.2). A best-estimate threshold was found to be $\Delta T_{\mathrm{threshold}} = -2.8$ °C, with an uncertainty range of potential alternative thresholds between –3.5 °C and –2.1 °C. For the following analysis, two thresholds are considered; the best estimate threshold, $\Delta T_{\mathrm{threshold}} = -2.8$ °C, and a higher threshold of $\Delta T_{\mathrm{threshold}} = -2.1$ °C. The best-estimate threshold was calibrated based on the conditions during the Weichselian, implying that future ice-sheet coverage over Forsmark will be associated with similar global cooling as during that glacial period. This threshold is similar to the high-confidence threshold used in Lord et al. (2019), which was also derived from the Weichselian conditions. $\Delta T_{\mathrm{threshold}} = -2.1$ °C represents a more cautious low-probability scenario, leading to longer periods of ice cover. In the most extreme case, $\Delta T_{\mathrm{threshold}} = -2.1$ °C could result in Forsmark being glaciated for nearly half of the next 1 Myr (Section 4.5.2).

For each emission scenario and $\Delta T_{\mathrm{threshold}}$ value, new probability distributions are calculated for both the E_{r} and E_{d} modes. In the E_{r} mode, the probability distribution is determined by multiplying the estimated erosion rates by the total ice-sheet coverage duration ($d_{glac,\mathrm{tot}}$). In the E_{d} mode, it is calculated by multiplying the estimated erosion depths by the number of glaciations (n_{glac}). The probabilities for each erosion rate and depth are based on data from Hall et al. (2019a), while the probabilities for $d_{glac,\mathrm{tot}}$ and n_{glac} are assumed to be evenly distributed across all 90 ice-sheet variability projections.

As in Hall et al. (2019a), subaerial denudation during ice-free periods is assumed to occur at a rate of 0–5 mm kyr^{-1}. This rate is applied to the new probability distribution in a simplified way: first, it is assumed that all percentiles above 50 have a subaerial denudation rate of 5 mm kyr^{-1}, while those below 50 have zero denudation. Second, the duration of ice-free conditions for each emission scenario and $\Delta T_{\mathrm{threshold}}$ value is estimated by averaging $d_{glac,\mathrm{tot}}$ across all 90 simulations, rather than considering each simulation individually. These simplifications are justified because the impact of subaerial denudation is typically an order of magnitude smaller than that of glacial erosion, meaning any potential errors from these approximations are minor in comparison to the projected glacial erosion over the next 1 Myr.

Results

The onset of the next glaciation in Forsmark is projected to occur around 100 kyr AP or later in all ice-sheet projections (see Table 4-3 and Figure 4-14). This means that denudation during the first 100 kyr will be virtually entirely driven by subaerial processes, which contributes with, at most, 0.5 m of total denudation during this period. Therefore, consistent with the conclusion in the PSAR, it is concluded here that total denudation over Forsmark during the next 100 kyr will be less than 1 m.

Over the next 1 Myr, recurrent glaciations are projected to lead to significantly higher denudation in Forsmark compared to the coming 100 kyr. Tables 7-1 and 7-2 present the projected mid-range (25th–75th percentiles) and wide-range (5th–95th percentiles) total denudation at the Forsmark site over the next 1 Myr for each erosion mode (E_{r} or E_{d}) and emissions scenario. The only difference between the tables is the applied $\Delta T_{\mathrm{threshold}}$ value: Table 7-1 uses $\Delta T_{\mathrm{threshold}} = -2.8$ °C, while Table 7-2 uses $\Delta T_{\mathrm{threshold}} = -2.1$ °C. A comparison with PSAR across all emissions scenarios and erosion modes is provided in Table 7-3. The key findings of the updated denudation projections over the Forsmark site for the next 1 Myr are summarised in the following.

- Using $\Delta T_{\mathrm{threshold}}$ = –2.8 °C, the projected mid-range total denudation depth at the Forsmark site is estimated to be between 2 and 23 m across all emissions scenarios (Table 7-1). This range is considered the most likely denudation outcome for Forsmark over the next 1 Myr.
- The projected denudation at the Forsmark site using $\Delta T_{\mathrm{threshold}}$ = –2.8 °C are generally slightly lower than in the PSAR. For example, in the 0 Pg C scenario, the 75th and 95th percentile denudation projections after 1 Myr are both about 5 m lower than the corresponding projections in the PSAR. Similarly, the total denudation at 5th and 25th percentile are projected to be similar or a couple of metres lower than in the PSAR. These differences can be attributed to lower average projections of $d_{glac,\mathrm{tot}}$ and n_{glac} in the simulations used here.
- Using $\Delta T_{\mathrm{threshold}}$ = –2.1 °C results in similar denudation depths at the Forsmark site compared to $\Delta T_{\mathrm{threshold}}$ = –2.8 °C when applying the E_{d} erosion mode (cf. Tables 7-1 and 7-2). This similarity can be attributed to the fact that this mode of erosion scales with n_{glac}, which shows low sensitivity to $\Delta T_{\mathrm{threshold}}$ (Figure 4-14). Using the E_{r} mode, the 5th and 25th percentile denudation projections at the Forsmark site also remain low, 5 metres or less. However, the highest percentiles are found to be more sensitive to the value of $\Delta T_{\mathrm{threshold}}$ when using the E_{r} mode. Specifically, the total denudation at the 75th and 95th percentiles are consistently 20–30 m higher than the corresponding projections for $\Delta T_{\mathrm{threshold}}$ = –2.8 °C (cf. Tables 7-1 and 7-2). These differences arise because total denudation in the E_{r} mode scales with $d_{glac,\mathrm{tot}}$, which increases almost linearly with the value of $\Delta T_{\mathrm{threshold}}$ (Figure 4-14). Consequently, the average duration of ice-sheet coverage over the next 1 Myr using $\Delta T_{\mathrm{threshold}}$ = –2.1 °C is approximately doubled compared to the case with $\Delta T_{\mathrm{threshold}}$ = –2.8 °C.

The highest projected denudation within the Forsmark site over the coming 1 Myr using the E_{r} mode is 71 m. This value reflects areas within the site that were more eroded, relatively speaking, in the past. Importantly, however, these areas are *not* located within the footprint area of the spent fuel repository. Hall et al. (2019b) found that the maximum past denudation within the footprint area is considerably lower than the maximum denudation over the entire site. Specifically, over the last 100 kyr, the estimated maximum denudation above the repository area was 5.6 m (Section 7.3.1), which is ~35 % lower than the maximum denudation over the entire Forsmark site (8.6 m). Applying this adjustment to the calculations, and over the full 1 Myr period, the projected 95th percentile denudation (using $\Delta T_{\mathrm{threshold}}$ = –2.1 °C) within the footprint area amounts to 51 m over the coming 1 Myr. This estimate is similar to the maximum denudation of 50 m used in the PSAR for the entire site (SKB TR-20-12, Section 3.5.6). It should be emphasized that the 51 m of denudation over the footprint area is based on the unlikely scenario that there will be nearly 500 kyr of ice-sheet coverage (a result of using $\Delta T_{\mathrm{threshold}}$ = –2.1 °C). Therefore, this value is considered to be an unlikely cautious upper bound rather than a realistic estimate. The unlikely nature of this number is also reflected by the fact that the maximum denudation of crystalline rock within the footprint area over the last 1.1 Myr was estimated to be 33 m based on geomorphological analysis (Section 7.3.1).

In summary, based on cosmogenic nuclide data, the likely total denudation within the footprint area of the spent fuel repository as well as the Forsmark site amounts to 2–23 m over the next 1 Myr. This range assumes that future erosion rates and periods of ice coverage will be similar to those of the past. It encompasses both possible modes of glacial erosion (E_{r} and E_{d}) as well as all considered scenarios of anthropogenic carbon emissions, which affect the timing of the next glacial inception. The maximum possible denudation above the spent fuel repository over the next 1 Myr, considering all relevant processes (abrasion, plucking and subaerial denudation) except glacial ripping, is very cautiously set to 50 m. The potential additional contribution of glacial ripping is further described in the following.

Table 7-1. Projected total denudation over the Forsmark site within the coming 1 Myr based on the E_r and E_d erosion modes (Hall et al. 2019a) and projected future ice-cover periods using $\Delta T_{threshold}$ = –2.8 °C (Section 4.5.2)

$\Delta T_{threshold}$ = –2.8 °C	Mid-range (25th – 75th percentile) denudation depth		Wide range (5th – 95th percentile) denudation depth	
Emission scenario (Pg C)	**Glacial erosion rate (E_r mode): 39–89 mm kyr^{-1}**	**Glacial erosion depth (E_d mode): 38–110 cm per glaciation**	**Glacial erosion rate (E_r mode): 36–145 mm kyr^{-1}**	**Glacial erosion depth (E_d mode): 14 – 167 cm per glaciation**
0	7–23 m	6–22 m	3–39 m	2–34 m
400	6–21 m	5–21 m	2–35 m	2–33 m
1500	5–17 m	4–18 m	2–29 m	1–28 m
5500	2–12 m	2–14 m	1–18 m	1–20 m

Table 7-2. Same as Table 7-1, but for $\Delta T_{threshold}$ = –2.1 °C

$\Delta T_{threshold}$ = –2.1 °C	Mid-range (25th – 75th percentile) denudation depth		Wide range (5th – 95th percentile) denudation depth	
Emission scenario (Pg C)	**Glacial erosion rate (E_r mode): 39–89 mm kyr^{-1}**	**Glacial erosion depth (E_d mode): 38–110 cm per glaciation**	**Glacial erosion rate (E_r mode): 36–145 mm kyr^{-1}**	**Glacial erosion depth (E_d mode): 14 – 167 cm per glaciation**
0	16–41 m	6–22 m	5–71 m	2–34 m
400	14–38 m	6–21 m	5–66 m	2–34 m
1500	12–34 m	5–20 m	4–60 m	2–31 m
5500	7–23 m	3–15 m	2–39 m	1–24 m

Table 7-3. Estimates of total denudation across all emissions scenarios and erosion modes in the PSAR and in this report (for $\Delta T_{threshold}$ = –2.8 °C and –2.1 °C)

	PSAR Table 3-15 in SKB TR-20-12	This report $\Delta T_{threshold}$ = –2.8 °C	This report $\Delta T_{threshold}$ = –2.1 °C
Mid-range (25th – 75th percentile) denudation depth	5–28 m	2–23 m	3–41 m
Wide range (5th – 95th percentile) denudation depth	2–43 m	1–39 m	1–71 m

Effects of glacial ripping

The cosmogenic nuclide inventories used in the erosion projections above and in Hall et al. (2019a) were primarily sampled from high points on smooth and undisturbed whalebacks and roches moutonnées. Therefore, the erosion depths obtained from the cosmogenic nuclide analysis likely reflect mainly abrasion. At the Forsmark site, it has been shown that Late Weichselian abration contributed with 0.2-1.5 m of erosion whereas block removal (plucking) contributed with another 0-1.6 m over the same period (Krabbendam et al. 2023). In contrast to these processes acting over time, glacial ripping is a process that causes extensive disintegration of rock hills and surfaces, producing numerous boulders in a localised area at the same time (Section 7.2.2). As noted by Krabbendam et al. (2022), this process locally removed 2–4 meters of rock just before the Late Weichselian deglaciation, comparable to the total erosion caused by abrasion and plucking throughout the entire Late Weichselian (see also Section 7.3.1). Glacial ripping is a highly localized process, both in time and space, affecting approximately 10-20 % of the Forsmark site during the last glacial cycle (Krabbendam et al. 2022, 2023).

The *total* amount of glacial ripping of the crystalline bedrock over the Forsmark site by all Middle- to Late Quaternary glaciations is however assessed to be restricted, given that the site in general still retains a low bedrock relief and that the bedrock surface still is situated in close vertical proximity to the former Sub-Cambrian peneplain (Hall et al. 2019b).

Modelling by Krabbendam et al. (2022) suggests that glacial ripping is physically plausible under certain realistic glaciological and geological conditions, but impossible under other, also realistic conditions. Glaciological conditions that favour glacial ripping include moderately to fast-flowing ice and hydraulic overpressure events at the ice-bed interface. Geologically, ripping is more likely in areas with transmissive, continuous near-surface subhorizontal fractures. These geological factors suggest that areas affected by ripping in the past are also likely to be vulnerable to this process in the future. In the Forsmark area, evidence of glacial ripping during the Weichselian has primarily been found northeast and southwest of the planned location of the spent fuel repository (Figures 7-1 and 7-2). Importantly, however, no evidence of ripping has been found *directly* over the repository footprint. Therefore, it is reasonable to expect that glacial ripping will not occur in the repository footprint area in the future. Thus, while it cannot be entirely ruled out, the most likely scenario is that glacial ripping over the spent nuclear fuel repository is negligible over the next 1 Myr.

Nevertheless, to provide a pessimistic upper-bound estimate of the amount of glacial ripping within the spent fuel repository footprint area over the next 1 Myr, it is assumed that the probability of ripping is uniform across the Forsmark site. As argued above, this is not the case since certain glaciological and geological conditions make some areas more prone to ripping than others. Nevertheless, this approach offers insight into the potential impact of ripping above the repository if this area were more susceptible to this process than historical data suggests. According to Krabbendam et al. (2022), 10–20 % of the ice-sheet bed was affected by glacial ripping during the last period of ice coverage in Forsmark. Assuming that the extent of ripping during future glaciations will be in the middle of this range, i.e. 15 %, and further assuming that there will be 20 periods of ice coverage over the next 1 Myr (which for this purpose is a cautious estimate; see Section 4.5.2), each location within the Forsmark site would be affected by glacial ripping 3 times within the next 1 Myr. Since each past ripping event typically eroded 2–4 m, the total contribution of future glacial ripping, assuming equal spatial probability across the area and an equal amount of erosion per glacial period, would range from 6 to 12 m. A pessimistic upper-bound estimate of the contribution of glacial ripping above the spent fuel repository over the next 1 Myr is for simplicity set to 10 m.

For SFR, the issue of glacial ripping is not relevant, partly because the next glaciation in Forsmark is projected to occur around 100 kyr AP (Section 4.5.2). However, even in the unlikely event that a glaciation in Forsmark would occur well before 100 kyr AP, in conjunction with the 54 kyr AP insolation minimum (Section 3.6.1), the possible contribution from ripping is small compared to the repository depth, and thus not considered significant.

Summary

In this section, projected denudation over the next 100 kyr and 1 Myr over the Forsmark site has been updated based on (i) new projections of future ice-covered periods (Section 4.5.2) and (ii) estimated contributions of the glacial ripping process (Krabbendam et al. 2022). Similar to the results of the PSAR, the maximum total denudation is projected to be less than 1 m within the Forsmark site over the next 100 kyr. These low denudation depths result from the fact that the Forsmark site is projected to remain ice-free for virtually the entire next 100 kyr, even if atmospheric CO_2 level would return to pre-industrial levels (Section 4.5.2).

Over the next 1 Myr, the likely denudation within the Forsmark site as well as the footprint area of the spent fuel repository, accounting for all processes except glacial ripping (abrasion, block removal and subaerial denudation), amount to 2–23 m (Table 7-4). This range is slightly lower compared to the corresponding range in the PSAR (5–28 m, see TR-20-12, Section 3.5.4). The difference is explained by, on average, shorter periods of ice coverage in the updated projections (Section 4.5.2) compared to those used in the PSAR.

Accounting for uncertainties in future ice coverage and basal conditions of future ice sheets, the denudation within the footprint area may be slightly higher than the likely range of 2–23 m over the next 1 Myr. In the most extreme case, which assumes (i) that the Forsmark site will be ice covered for nearly half of the time of the next 1 Myr and (ii) that the ice sheet will be warm-based, and hence erosive, for the entire time, the maximum total denudation within the footprint area due to abrasion, plucking and subaerial denudation is approximately 50 m (Table 7-4). This value constitutes an unlikely cautious upper bound rather than a realistic estimate. Over other areas of the Forsmark site, which are more prone to glacial erosion, this extreme value may reach 70 m.

If adding the potential contribution of glacial ripping to the total denudation over the next 1 Myr, it is also important to make distinctions between different areas within the Forsmark site. This is because, as mentioned above, glacial ripping is a highly localised process that can only occur under certain glaciological and geological conditions. These conditions, in turn, mean that areas that were exposed to glacial ripping in the past will likely also be so in the future. Consequently, since no glacial ripping has been observed within the footprint area of the spent fuel repository in the past (Krabbendam et al. 2022), this process will likely have a negligible contribution at this location also in the future (Table 7-4). A high-end pessimistic estimate of glacial ripping over the repository area is provided by assuming that all areas within the Forsmark site are equally likely to be affected by this process. This assumption results in ~10 m of glacial ripping over the footprint area within the next 1 Myr (Table 7-4).

All in all, adding all denudation processes (abrasion, plucking, subaerial denudation and ripping) results in a likely denudation of 2–23 m over the spent fuel repository within the next 1 Myr. An unlikely high-end value of the maximum possible denudation over the repository within this time frame is estimated by adding the pessimistic maximum contribution from abrasion, plucking and subaerial denudation (~50 m) with a pessimistic contribution from glacial ripping (~10 m). This results in that the total maximum possible denudation above the spent fuel repository within the next 1 Myr, accounting for all relevant denudation processes, is set to ~60 m (Table 7-4).

Table 7-4. Summary of likely and maximum possible denudation depths above the spent fuel repository over the next 1 Myr. The maximum estimates are a result of several cautious and pessimistic assumption and therefore have an extremely low likelihood of occurrence

Process contributing to the total denudation	Likely range	Maximum estimate
Abrasion, plucking and subaerial denudation	2–23 m	~50 m
Glacial ripping	~0 m	~10 m
Total	2–23 m	~60 m

8 Examples of Forsmark climate evolutions over the next 1 Myr

Chapters 2–7 summarise the current state of knowledge on climate and climate-related processes in Forsmark, with particular emphasis on analyses updated since the PSAR climate reports. Notable additions include 1-Myr projections of ice cover, permafrost, and denudation in Forsmark, along with associated uncertainties, based on the climate modelling studies of Lord et al. (2019) and Williams et al. (2022). This concluding chapter integrates some of these projections and illustrates them as potential climate evolutions in Forsmark over the next 1 Myr.

The climate evolutions presented in this chapter are based on the climate projections for Forsmark conducted by Williams et al. (2022) (see further Sections 3.5.3, 3.5.4 and 6.5.1) and the simple isostatic LLRA model (Section 5.5.3). The simulations of Williams et al. (2022) provide 90 SAT projections for Forsmark over the next 1 Myr for four different cumulative anthropogenic carbon emissions: 0 Pg C, 400 Pg C, 1500 Pg C and 5500 Pg C (Section 2.5.2).

Frequency and duration of ice sheets in Forsmark over the next 1 Myr was calculated using the conceptual global model (CGM) of Lord et al. (2019) (see further Section 4.5.2). This model was run 1000 times with different parameter combinations. A total of 90 of these 1000 simulations were retained after calibration with paleo proxy-data. Based on these 90 simulations, thresholds in the global SAT change, $\Delta T_{\text{threshold}}$, were derived; when the future projected global SAT fell below this threshold, Forsmark was assumed to be covered by an ice sheet, while ice-free conditions prevailed when it was above this threshold. The value of $\Delta T_{\text{threshold}}$ was constrained by the drop in simulated global SAT change during reconstructed periods of Weichselian glaciations in Forsmark. Accounting for the uncertainty in future ice-sheet variability a range of $\Delta T_{\text{threshold}}$ was derived. Within this range, three $\Delta T_{\text{threshold}}$ values were then further propagated to the ice-sheet variability analysis:

- **$\Delta T_{\text{threshold}} = -2.8$ °C**. A best-estimate, rendering a future ice-sheet variability in Forsmark similar to that used for model calibration (i.e. the Weichselian).
- **$\Delta T_{\text{threshold}} = -3.5$ °C**. A low-end estimate, rendering a significantly reduced ice coverage in Forsmark compared to the Weichselian.
- **$\Delta T_{\text{threshold}} = -2.1$ °C**. A high-end estimate, rendering a significantly increased ice coverage in Forsmark compared to the Weichselian.

The examples provided in this chapter are presented as evolutions of climate domain (Section 1.2.3), i.e. as transitions between temperate, periglacial and glacial climate conditions in Forsmark. Furthermore, periods of submerged conditions following ice coverage in Forsmark is estimated. For each of the three thresholds listed above, the conversion from projected Forsmark SAT in the 90 Williams et al. (2022) simulations, T_{Forsmark}, to climate domains is carried out according to Table 8-1. The motivation for using the local SAT to compute transitions between the climate domains is discussed in further detail Section 6.5.1, and the LLRA model is described in Section 5.5.3.

In sum, the 90 simulations of Williams et at (2022) (for each emissions scenario) represents modelling uncertainty, whereas the four emissions scenarios and the three $\Delta T_{\text{threshold}}$ values represents scenario uncertainty. The total uncertainty in the Forsmark climate over the next 1 Myr, based on these datasets, is represented by a total of 1080 (90 × 4 × 3) climate evolutions representing both anticipated and extreme (bounding-case) evolutions. In the following, a handful of these evolutions are shown.

Table 8-1. Projected Forsmark mean annual SAT (Williams et al. 2022), T_{Forsmark}, corresponding to each climate domain for each of the considered global SAT thresholds for Forsmark glaciation

Climate domain	Global SAT threshold for Forsmark glaciation		
	$\Delta T_{\text{threshold}} = -2.8$ °C	$\Delta T_{\text{threshold}} = -3.5$ °C	$\Delta T_{\text{threshold}} = -2.1$ °C
Temperate	$T_{\text{Forsmark}} \geq -1$ °C		
Periglacial	-14 °C < T_{Forsmark} < -1 °C	-16 °C < T_{Forsmark} < -1 °C	-11 °C < T_{Forsmark} < -1 °C
Glacial	$T_{\text{Forsmark}} \leq -14$ °C	$T_{\text{Forsmark}} \leq -16$ °C	$T_{\text{Forsmark}} \leq -11$ °C
Submerged	Calculated with the LLRA model in response to periods with glacial climate domain. Assumed local ice thickness = 2500 m.		

8.1 Anticipated climate evolutions

These are defined as evolutions with ice-sheet variabilities similar to the past observed ones (i.e. only evolutions which assume $\Delta T_{\text{threshold}} = -2.8$ °C). Simulations forced by cumulative emissions of 1500 Pg C are considered the most likely under current developments (Section 2.6.1) as these approximately correspond to business-as-usual scenarios. However, simulations with cumulative emissions of 400 Pg C are also shown in this section. These broadly represent future developments by which the targets agreed upon within the Paris climate agreement have been met.

Based on these criteria, Figures 8-1 to 8-4 illustrate four examples of anticipated climate evolutions in Forsmark over the next 1 Myr. In all of these examples, the evolution of climate domains at Forsmark over the next 1 Myr is dominated by glacial cycles similar to the Weichselian. An exception to this cyclic behaviour is found during the initial ~150 kyr and ~80 kyr which remain temperate under the 1500 Pg C (Figures 8-1 and 8-2) scenario and the 400 Pg C scenario (Figures 8-3 and 8-4), respectively. This long initial temperate period is primarily explained by a low summer insolation variability during the first 50 kyr (see further Section 3.5.3).

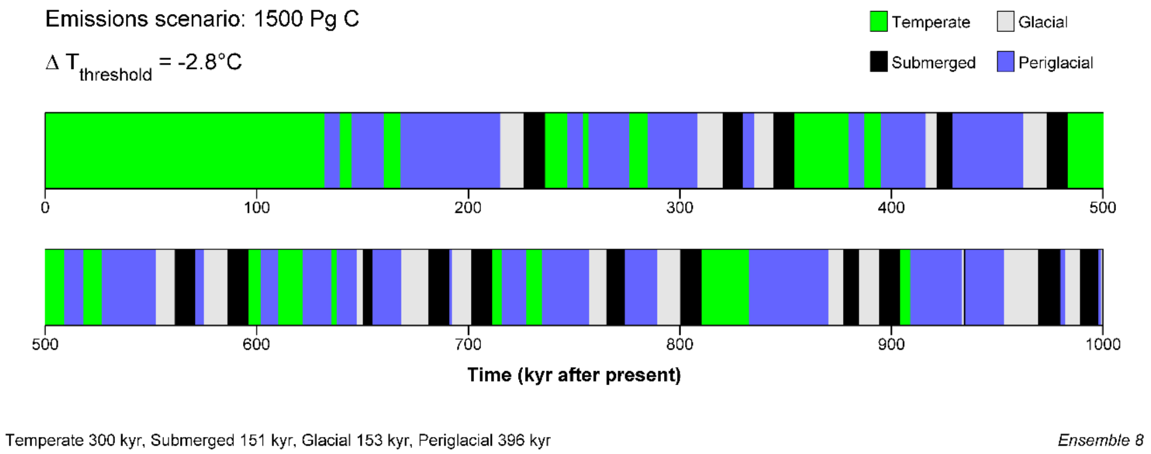

Figure 8-1. *Example of a climate evolution in Forsmark over the next 1 Myr based on climate modelling of Williams et al. (2022), the analysis of future ice-sheet variability in Forsmark (Section 4.5.2) and estimates of submerged periods using the LLRA model (Section 5.5.3). The evolutions are shown as transitions between climate domains. The projected mean annual SAT for Forsmark in the Williams simulations corresponding to these transitions are shown in Table 8-1. This example shows the evolution of ensemble number 8 from the Williams et al. (2022) simulations, forced by cumulative emissions of 1500 Pg C. Furthermore, it is assumed that* $\Delta T_{\text{threshold}} = -2.8$ *°C.*

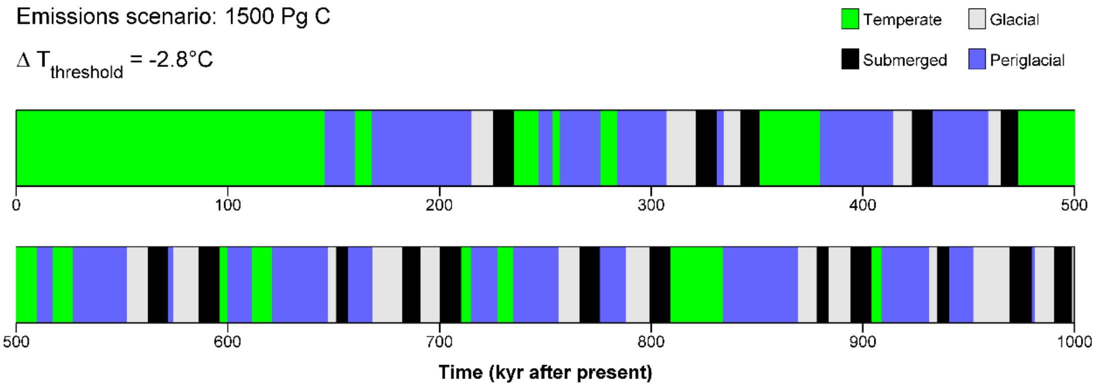

Temperate 311 kyr, Submerged 154 kyr, Glacial 167 kyr, Periglacial 368 kyr *Ensemble 31*

Figure 8-2. *Same as Figure 8-1 but for ensemble number 31.*

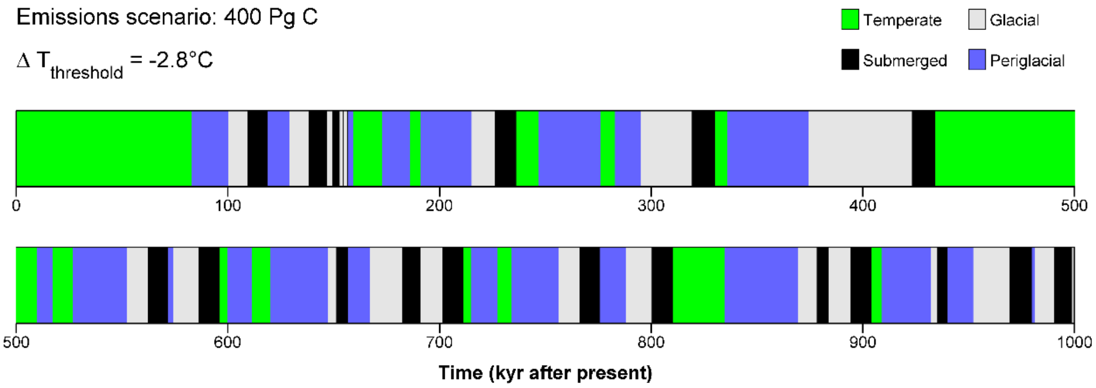

Temperate 266 kyr, Submerged 163 kyr, Glacial 228 kyr, Periglacial 343 kyr *Ensemble 1*

Figure 8-3. *Same as Figure 8-1 but for ensemble number 1 forced by cumulative emissions of 400 Pg C.*

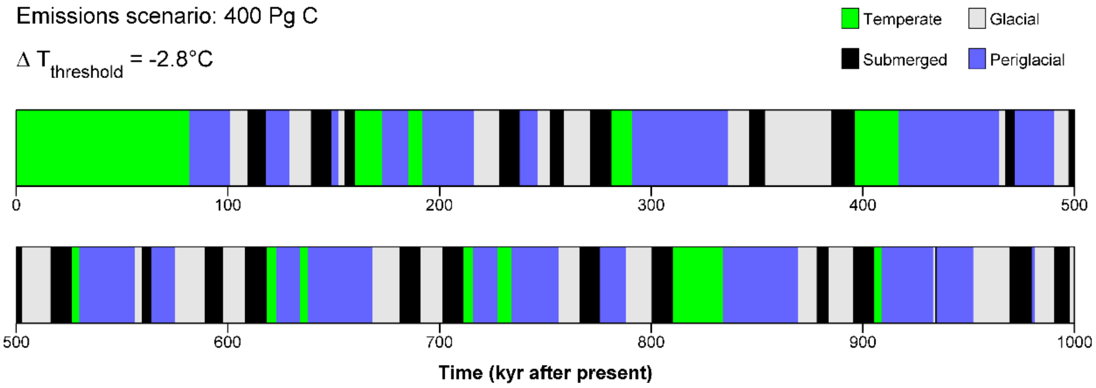

Temperate 186 kyr, Submerged 191 kyr, Glacial 236 kyr, Periglacial 387 kyr *Ensemble 81*

Figure 8-4. *Same as Figure 8-3 but for ensemble number 81.*

8.2 Extreme climate evolutions

In this section, amongst the most extreme evolution found in the 1080 ensemble are presented. Thus, they comply to end-member emission scenarios (0 Pg C or 5500 Pg C) and $\Delta T_{threshold}$ values, or a combination of both. While the occurrence of these Forsmark evolutions cannot be ruled out, they are considered unlikely in light of the current knowledge of future climate evolution.

Temperate-dominated evolutions

The most temperate-dominated evolutions in Forsmark are found amongst the simulations forced by the highest anthropogenic emissions (5500 Pg C), because they may potentially lead to a substantial delay of the next glacial inception (Section 3.5.3). Two examples of such developments, with more than 500 kyr of initial temperate conditions at Forsmark, are shown in Figures 8-5 and 8-6.

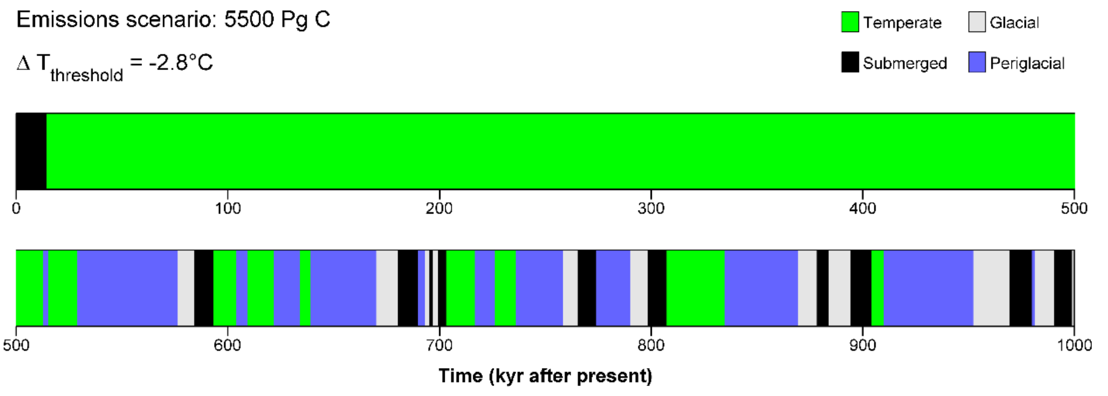

Temperate 600 kyr, Submerged 93 kyr, Glacial 83 kyr, Periglacial 224 kyr *Ensemble 6*

Figure 8-5. *Same as Figure 8-1 but for ensemble number 6 forced by cumulative emissions of 5500 Pg C.*

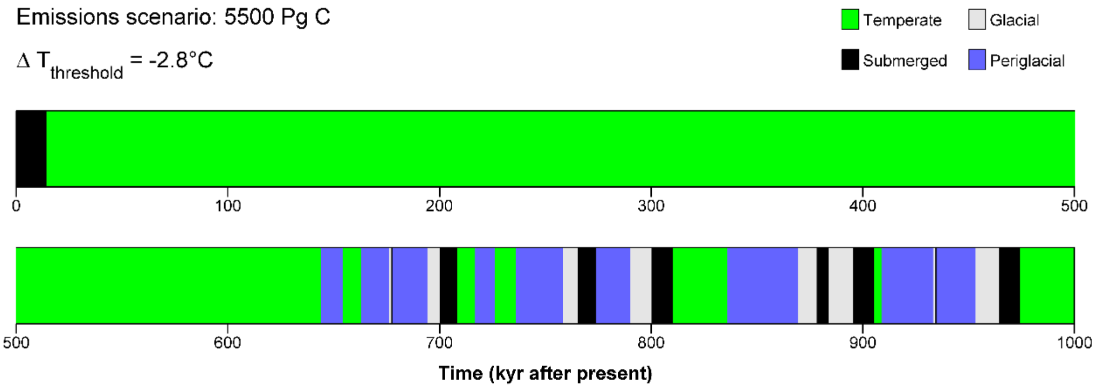

Temperate 714 kyr, Submerged 69 kyr, Glacial 56 kyr, Periglacial 161 kyr *Ensemble 89*

Figure 8-6. *Same as Figure 8-5 but for ensemble number 89.*

Ice-dominated evolutions

These evolutions assume that Fennoscandia will experience more frequent and prolonged glaciations than during the Weichselian cycle. Accordingly, a threshold value of $\Delta T = -2.1$ °C is applied. Cumulative anthropogenic emissions are further assumed to be zero. Examples of such ice-dominated evolutions for Forsmark over the next 1 Myr are shown in Figures 8-7 and 8-8. A particularly notable development, illustrated in Figure 8-8, is the uninterrupted sequences of glacial and submerged conditions between ~90 and ~240 kyr, and between ~550 and ~720 kyr.

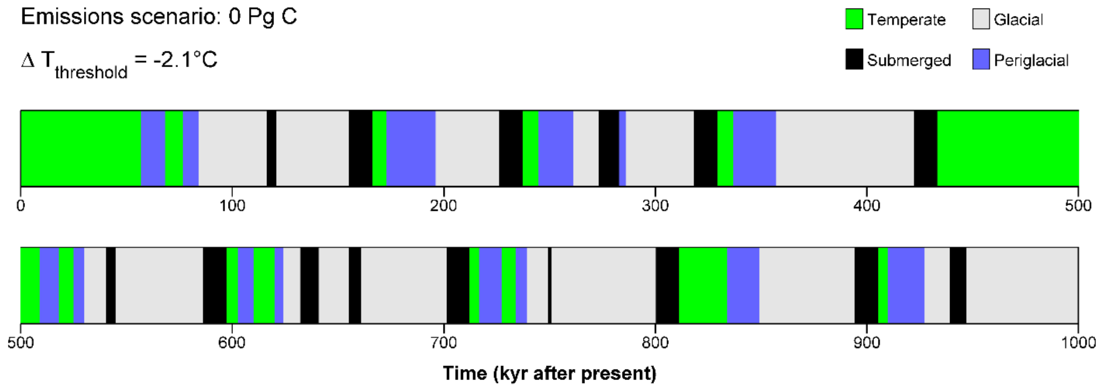

Temperate 228 kyr, Submerged 133 kyr, Glacial 487 kyr, Periglacial 152 kyr *Ensemble 34*

Figure 8-7. *Same as Figure 8-1 but for ensemble 34, 0 Pg C cumulative emissions and $\Delta T_{threshold}$ = –2.1 °C.*

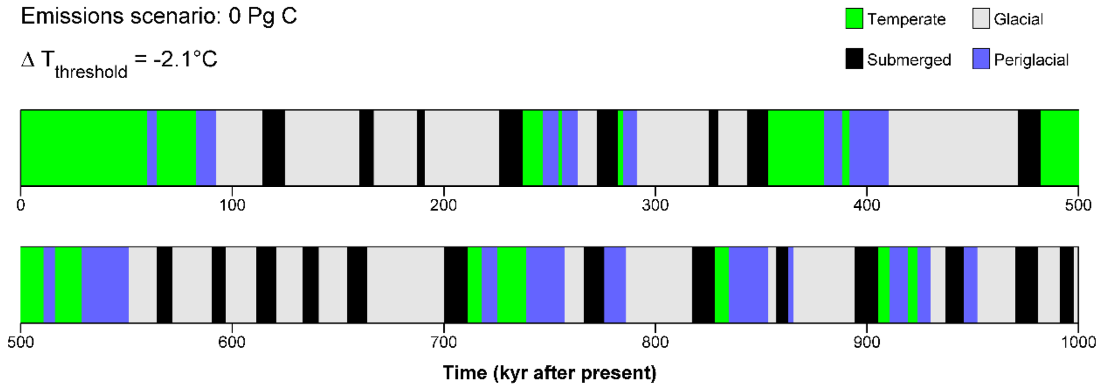

Temperate 206 kyr, Submerged 188 kyr, Glacial 445 kyr, Periglacial 161 kyr *Ensemble 68*

Figure 8-8. *Same as Figure 8-7 but for ensemble 68.*

Permafrost-dominated evolutions

These evolutions assume that Fennoscandia will be glaciated less frequently and for shorter periods than during the Weichselian glacial cycle (i.e. we assume that $\Delta T_{threshold}$ = –3.5 °C), resulting in a greater domination of permafrost during colder periods. Furthermore, it is assumed that cumulative anthropogenic emissions are zero. Examples of such permafrost-dominated evolutions for Forsmark over the next 1 Myr are shown in Figures 8-9 and 8-10. In both of these evolution, more than half of the coming 1 Myr is characterised by permafrost coverage in Forsmark.

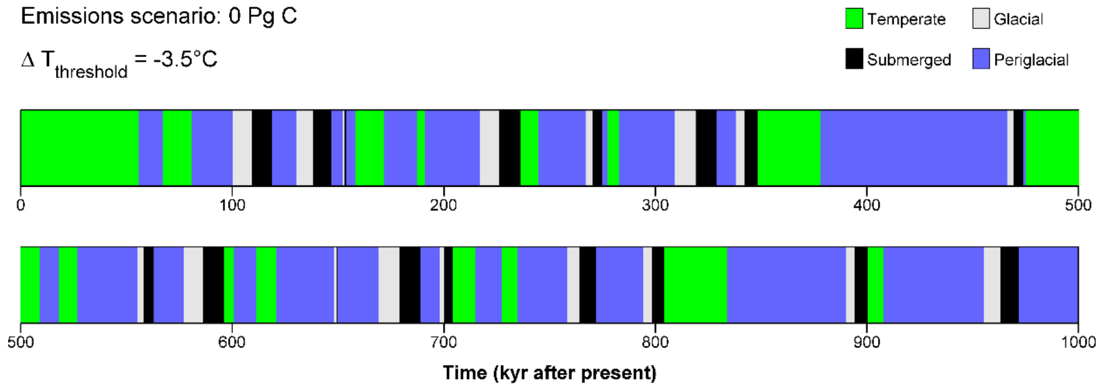

Temperate 248 kyr, Submerged 115 kyr, Glacial 94 kyr, Periglacial 543 kyr *Ensemble 3*

Figure 8-9. *Same as Figure 8-1 but for ensemble 3, 0 Pg C cumulative emissions and $\Delta T_{threshold}$ = –3.5 °C.*

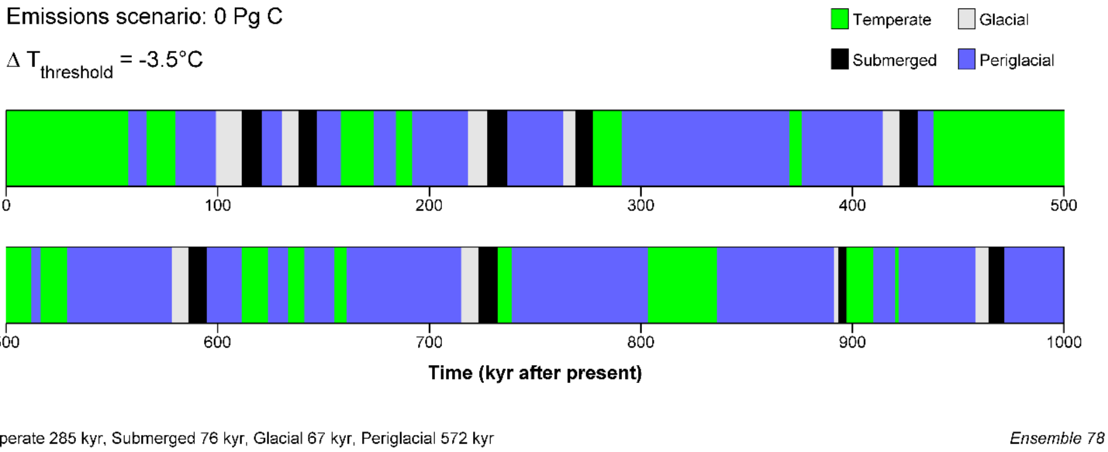

Figure 8-10. *Same as Figure 8-9 but for ensemble 78.*

References

SKB's (Svensk Kärnbränslehantering AB) publications can be found at www.skb.com/publications. SKBdoc documents will be submitted upon request to document@skb.se.

Abe-Ouchi A, Segawa T, Saito F, 2007. Climatic conditions for modelling the Northern Hemisphere ice sheets throughout the ice age cycle. Clim. Past 3, 423-438.

Abe-Ouchi A, Saito F, Kawamura K, Raymo M E, Okuno J, Takahashi K, Blatter H, 2013. Insolation-driven 100,000-year glacial cycles and hysteresis of ice-sheet volume. Nature 500, 190–193.

Abraham J, Wesström I, Grusson Y, 2018. Beräknat framtida bevattningsbehov för svenskt jordbruk under en 30-års period; 2021-2050. In: Jordbrukets behov av vattenförsörjning. Rapport 2018:18, Jordbruksverket (in Swedish).

Agha Karimi A, Bagherbandi M, Horemuz M, 2021. Multidecadal sea level variability in the Baltic Sea and its impact on acceleration estimations. Frontiers in Marine Science, 1111.

Archer D, Ganopolski A, 2005. A movable trigger: Fossil fuel CO2 and the onset of the next glaciation. Geochemistry, Geophysics, Geosystems 6, Q05003. doi:10.1029/2004GC000891

Archer D, Eby M, Brovkin V, Ridgwell A, Cao L, Mikolajewicz U, Caldeira K, Matsumoto K, Munhoven G, Montenegro A, Tokos K, 2009. Atmospheric lifetime of fossil fuel carbon dioxide. Annual Review of Earth and Planetary Sciences 37, 117–134.

Árnadóttir T, Lund B, Jiang W, Geirsson H, Björnsson H, Einarsson P, Sigurdsson T, 2009. Glacial rebound and plate spreading: results from the first countrywide GPS observations in Iceland. Geophysical Journal International 177, 691–716.

Armstrong E, Izumi K, Valdes P, 2023. Identifying the mechanisms of DO-scale oscillations in a GCM: a salt oscillator triggered by the Laurentide ice sheet. Climate Dynamics 60, 3983-4001.

Aschwanden A, Bartholomaus T C, Brinkerhoff D J, Truffer M, 2021. Brief communication: A roadmap towards credible projections of ice sheet contribution to sea-level. The Cryosphere 15, 5705–5715.

Astakhov V, 2004. Middle Pleistocene glaciations of the Russian North. Quaternary Science Reviews, Quaternary Environments of the Eurasian North (QUEEN) 23, 1285–1311.

Bakker P, Schmittner A, Lenaerts J T M, Abe-Ouchi A, Bi D, van den Broeke M R, Chan W-L, Hu A, Beadling R L, Marsland S J, Mernild S H, Saenko O A, Swingedouw D, Sullivan A, Yin J, 2016. Fate of the Atlantic Meridional Overturning Circulation: Strong decline under continued warming and Greenland melting. Geophysical Research Letters 43, 12-252.

Bamber J L, Oppenheimer M, Kopp R E, Aspinall W P, Cooke R M, 2022. Ice sheet and climate processes driving uncertainty in projections of future sea level rise: Findings from a structured expert judgment approach. Earth's Future 10, e2022EF002772. https://doi.org/10.1029/2022EF002772

Batchelor C L, Margold M, Krapp M, Murton D K, Dalton A S, Gibbard P L, Stokes C R, Murton J B, Manica A, 2019. The configuration of Northern Hemisphere ice sheets through the Quaternary. Nature communications 10, 3713.

Bellomo K, Angeloni M, Corti S, von Hardenberg J, 2021. Future climate change shaped by inter-model differences in Atlantic meridional overturning circulation response. Nature Communications 12, 3659.

Benn D I, Evans D J A, 1998. Glaciers & glaciation. London: Arnold.

Bennett M R, 2003. Ice streams as the arteries of an ice sheet: their mechanics, stability and significance. Earth-Science Reviews 61, 309-339.

Berger A, 1978. Long-term variations of caloric insolation resulting from the Earth's orbital elements. Quaternary research 9, 139-167.

Berger A, Mélice J L, Loutre M F, 2005. On the origin of the 100-kyr cycles in the astronomical forcing. Paleoceanography 20.

Białas J, Sośnica K, 2024. Changes in the water surface level of the Baltic Sea from satellite altimetry and gravity missions. Artificial Satellites: Journal of Planetary Geodesy, 59.

Björkqvist J-V, Lukas I, Alari V, van Vledder G P, Hulst S, Pettersson H, Behrens A, Männik A, 2018. Comparing a 41-year model hindcast with decades of wave measurements from the Baltic Sea, Ocean Eng., 152, 57–71.

Blomdin R, Fu P, Goodfellow B W, Gribenski N, Heyman J, Newall J C, Stroeven A (Eds), 2016. Third Nordic Workshop on cosmogenic nuclide techniques. Celebrating 30 years of counting cosmogenic atoms. Svensk Kärnbränslehantering AB, 73 p.

Booth B B, Harris G R, Murphy J M, House J I, Jones C D, Sexton D, Sitch S, 2017. Narrowing the range of future climate projections using historical observations of atmospheric CO2. Journal of Climate 30, 3039–3053.

Bosmans J H C, Hilgen F J, Tuenter E, Lourens L J, 2015. Obliquity forcing of low-latitude climate. Climate of the Past 11, 1335-1346.

Bosson E, Gustafsson L-G, Sassner M, 2008. Numerical modelling of surface hydrology and near-surface hydrogeology at Forsmark. Site descriptive modelling. SDM-Site Forsmark. SKB R-08-09, Svensk Kärnbränslehantering AB.

Boulton G S, Kautsky U, Morén L, Wallroth T, 2001. Impact of long-term climate change on a deep geological repository for spent nuclear fuel. SKB TR-99-05, Svensk Kärnbränslehantering AB.

Brandefelt J, Näslund J-O, Zhang Q, Hartikainen J, 2013. The potential for cold climate conditions and permafrost in Forsmark in the next 60,000 years. SKB TR-13-04, Svensk Kärnbränslehantering AB.

Broecker W S, 1991. The great ocean conveyor. Oceanography 4, 79–89.

Brydsten L, 2009. Sediment dynamics in the coastal areas of Forsmark and Laxemar during an interglacial. SKB TR-09-07, Svensk Kärnbränslehantering AB.

Brydsten L, Engqvist A, Näslund J-O, Lindborg T, 2009. Expected extreme sea levels at Forsmark and Laxemar-Simpevarp up until year 2100. SKB TR-09-21, Svensk Kärnbränslehantering AB.

Buckley M W, Marshall J, 2016. Observations, inferences, and mechanisms of the atlantic meridional overturning circulation: A review. Reviews of Geophysics 54, 5–63.

Byrne, M P, O'Gorman P A, 2013. Land–Ocean Warming Contrast over a Wide Range of Climates: Convective Quasi-Equilibrium Theory and Idealized Simulations. Journal of Climate, 26(12), 4000–4016.

Byrne M P, O'Gorman P A, 2018. Trends in continental temperature and humidity directly linked to ocean warming. Proceedings of the National Academy of Sciences 115, 4863–4868.

Calvez M, Brulhet J, de Noblet N, Paillard D, Degnan P, Becker A, Cortes A, Pinedo P, Recreo F, Aguero A, Ruiz C, Lomba L, Torres T, Lucini M, Ortiz J E, Laciok A, Berger A, Loutre M-F, Yearsley R, Reynard N, Goodess C, Palutikof J, Watkins B, Egan M, 2001. Deliverable D3: Global climatic features over the next million years and recommendation for specific situations to be considered. Work Package 2, Simulation of the future evolution of the biosphere system using the hierarchical strategy. Modelling Sequential Biosphere Systems under Climate Change for Radioactive Waste Disposal (BIOCLIM). URL: https://www.andra.fr/mini-sites/bioclim/pdf/d3.pdf

Canadell J G, Monteiro P M S, Costa M H, Cotrim da Cunha L, Cox P M, Eliseev A V, Henson S, Ishii M, Jaccard S, Koven C, Lohila A, Patra P K, Piao S, Rogelj J, Syampungani S, Zaehle S, Zickfeld K, 2021. Global Carbon and other Biogeochemical Cycles and Feedbacks. In Climate Change 2021: The Physical Science Basis. Contribution of Working Group I to the Sixth Assessment Report of the Intergovernmental Panel on Climate Change. Cambridge University Press, Cambridge, United Kingdom and New York, NY, USA, pp. 673–816.

Chen D, Rojas M, Samset B H, Cobb K, Diongue Niang A, Edwards P, Emori S, Faria S H, Hawkins E, Hope P, Huybrechts P, Meinshausen M, Mustafa S K, Plattner G-K, Tréguier A-M, 2021. Framing, Context, and Methods. In Climate Change 2021: The Physical Science Basis. Contribution of Working Group I to the Sixth Assessment Report of the Intergovernmental Panel on Climate Change. Cambridge University Press, Cambridge, United Kingdom and New York, NY, USA, pp. 147–286, doi:10.1017/9781009157896.003.

Christensen O B, Kjellström E, Dieterich C, Gröger M, Meier H E M, 2022. Atmospheric regional climate projections for the Baltic Sea Region until 2100, Earth System Dynamics 13, 133–157.

Clark P, Clague J, Curry B, Dreimanis A, Hicock S, Miller G, Berger G, Eyles N, Lamothe M, Miller B, Mott R, Oldale R, Stea R, Szabo J, Thorleifson L, Vincent J, 1993. Initiation and development of the Laurentide and Cordilleran ice sheets following the last interglaciation, Quaternary Sci. Rev. 12, 79–114.

Clark P U, Shakun J D, Marcott S A, Mix A C, Eby M, Kulp S, Levermann A, Milne G A, Pfister P L, Santer B D, Schrag D P, Solomon S, Stocker T F, Strauss B H, Weaver A J, Winkelmann R, Archer D, Bard E, Goldner A, Lambeck K, Pierrehumbert R T, Plattner G-K, 2016. Consequences of twenty-first-century policy for multi-millennial climate and sea-level change. Nature Climate Change 6, 360–369.

Climate Action Tracker, 2023. 2100 warming projections. Available at: https://climateactiontracker.org/global/temperatures/ [22 Jan 2024]

Cohen-Corticchiato D, Zwinger T, 2021. Modelling permafrost evolution at Olkiluoto for the next 120,000 years. Posiva Working Report 2021-14, Posiva Oy.

Colbourn G, Ridgwell A, Lenton T M, 2015. The time scale of the silicate weathering negative feedback on atmospheric CO2. Global Biogeochemical Cycles 29, 583-596.

Colleoni F, 2009. On the Late Saalian glaciation (160–140 ka): a climate modeling study. PhD thesis. Laboratoire de Glaciologie et de Géophysique de l'Environnement, Université Grenoble I.

Colleoni F, Liakka J, 2020. Transient simulations of the Eurasian ice sheet during the Saalian glacial cycle. SKB TR-19-17, Svensk Kärnbränslehantering AB.

Colleoni F, Krinner G, Jakobsson M, Peyaud,V, Ritz C, 2009. Influence of regional parameters on the surface mass balance of the Eurasian ice sheet during the peak Saalian (140 kya). Global and Planet. Change 68, 132–148.

Colleoni F, Wekerle C, Masina S, 2014. Long-term safety of a planned geological repository for spent nuclear fuel in Forsmark – estimate of maximum ice-sheet thicknesses. SKB TR-14-21, Svensk Kärnbränslehantering AB.

Collins M, Knutti R, Arblaster J M, Dufresne J-L, Fichefet T, Friedlingstein P, Gao X, Gutowski W J, Johns T, Krinner G, Shongwe M, Tebaldi C, Weaver A J, Wehner M, 2013. Long term climate change: projections, commitement and irreversibility. In Stocker T F, Qin D, Plattner G-K, Tignor M, Allen S K, Boschung J, Nauels A, Xia Y, Bex V, Midgley P M (eds). Climate change 2013: the physical science basis: Working Group I Contribution to the Fifth Assessment Report of the Intergovernmental Panel on Climate Change. Cambridge: Cambridge University Press, 1029–1136.

Copernicus, 2022. Sea level daily gridded data from satellite observations for the global ocean from 1993 to present [Data set]. DOI:10.5285/77B64C55-7166-4A06-9DEF-2E400398E452

Dansgaard W, Johnsen S J, Clausen H B, Dahl-Jensen D, Gundestrup N S, Hammer C U, Hvidberg C S, Steffensen J P, Sveinbjörnsdottir A E, Jouzel J, Bond G, 1993. Evidence for general instability of past climate from a 250-kyr ice-core record. Nature 364, 218–220.

Darvill C M, Menounos B, Goehring B M, Lian O B, Caffee M W. 2018. Retreat of the western Cordilleran ice sheet margin during the last deglaciation. Geophysical Research Letters 45(18), 9710-9720.

DeConto R M, Pollard D, 2016. Contribution of Antarctica to past and future sea-level rise, Nature 531, 591–597.

DeConto R M, Pollard D, Alley R B, Velicogna I, Gasson E, Gomez N, Sadai S, Condron A, Gilford D M, Ashe E L, Kopp R E, Li D, Dutton A. 2021. The Paris Climate Agreement and future sea-level rise from Antarctica, Nature 593, 83–89.

Ditlevsen P, Ditlevsen S, 2023. Warning of a forthcoming collapse of the Atlantic meridional overturning circulation. Nature Communications 14, 4254.t

Donohoe A, Battisti D S, 2011. Atmospheric and surface contributions to planetary albedo. Journal of Climate 24, 4402-4418.

Drewry D, 1986. Glacial geologic processes. London: Arnold.

Edwards T L, Brandon M A, Durand G, Edwards N R, Golledge N R, Holden P B, Nias I J, Payne A J, Ritz C, Wernecke A, 2019. Revisiting Antarctic ice loss due to marine ice-cliff instability. Nature 566, 58–73.

Edwards T L, Nowicki S, Marzeion B, Hock R, Goelzer H, Seroussi H, Jourdain N C, Slater D A, Turner F E, Smith C J, McKenna C M, Simon E, Abe-Ouchi A, Gregory J M, Larour E, Lipscomb W H, Payne A J, Shepherd A, Agosta C, Alexander P, Albrecht T, Anderson B, Asay-Davis X, Aschwanden A, Barthel A, Bliss A, Calov R, Chambers C, Champollion N, Choi Y, Cullather R, Cuzzone J, Dumas C, Felikson D, Fettweis X, Fujita K, Galton-Fenzi B K, Gladstone R, Golledge N R, Greve R, Hattermann T, Hoffman M J, Humbert A, Huss M, Huybrechts P, Immerzeel W, Kleiner T, Kraaijenbrink P, Le Clec'h S, Lee V, Leguy G R, Little C M, Lowry D P, Malles J-H, Martin D F, Maussion F, Morlighem M, O'Neill J F, Nias I, Pattyn F, Pelle T, Price S F, Quiquet A, Radić V, Reese R, Rounce D R, Rückamp M, Sakai A, Shafer C, Schlegel N-J, Shannon S, Smith R S, Straneo F, Sun S, Tarasov L, Trusel L D, Van Breedam J, van de Wal R, van den Broeke M, Winkelmann R, Zekollari H, Zhao C, Zhang T, and Zwinger T, 2021. Projected land ice contributions to twenty-first-century sea level rise, Nature 593, 74–82.

Ekman M, 1991. A concise history of postglacial land uplift research (from its beginning to 1950). Terra Nova 3, 358–365.

Eriksson B, 1981. Den “potentiella” evapotranspirationen i Sverige. Norrköping, Sweden: SMHI. (SMHI rapporter, Hydrology and oceanography 27) (In Swedish.)

Etminan M, Myhre G, Highwood E J, Shine K P, 2016. Radiative forcing of carbon dioxide, methane, and nitrous oxide: A significant revision of the methane radiative forcing. Geophysical Research Letters 43, 12-614.

Eyring V, Bony S, Meehl G A, Senior C A, Stevens B, Stouffer R J, Taylor K E, 2016. Overview of the Coupled Model Intercomparison Project Phase 6 (CMIP6) experimental design and organization. Geoscientific Model Development 9, 1937–1958.

Fastook J L, 1994. Modeling the Ice Age: the finite-element method in glaciology. Computing Science and Engineering 1, 55–67.

Fastook J L, Chapman J E, 1989. A map plane finite-element model: three modeling experiments. Journal of Glaciology 35, 48–52.

Fastook J L, Prentice M, 1994. A finite-element model of Antarctica: sensitivity test for meteorological mass-balance relationship. Journal of Glaciology 40, 167–175.

Fjeldskaar W, 1994. The amplitude and decay of the glacial forebulge in Fennoscandia. Norsk Geologisk Tidsskrift 74, 2–8.

Flato G, 2011. Earth system models: an overview. WIREs Climate Change 2, 783–800.

Flato G, Marotzke J, Abiodun B, Braconnot P, Chou S C, Collins W, Cox P, Driouech F, Emori S, Eyring V, Forest C, Gleckler P, Guilyardi E, Jakob C, Kattsov V, Reason C, Rummukainen M, 2013. Evaluation of Climate Models. In: Climate Change 2013: The Physical Science Basis. Contribution of Working Group I to the Fifth Assessment Report of the Intergovernmental Panel on Climate Change. Cambridge University Press, Cambridge, United Kingdom and New York, NY, USA, pp. 741–866.

Forster P, Storelvmo T, Armour K, Collins W, Dufresne J-L, Frame D, Lunt D J, Mauritsen T, Palmer MD, Watanabe M, Wild M, Zhang H, 2021. The Earth's Energy Budget, Climate Feedbacks, and Climate Sensitivity. In Climate Change 2021: The Physical Science Basis. Contribution of Working Group I to the Sixth Assessment Report of the Intergovernmental Panel on Climate Change. Cambridge University Press, Cambridge, United Kingdom and New York, NY, USA, pp. 923–1054, doi:10.1017/9781009157896.009.

Fotiev S M, 1997. Permafrost groundwater Russian Literature Review. In Haldorsen S, Liebman M, Nelson G, van Everdingen R O, Boike J. State-of-the-art report on saturated water movement in permafrost areas. Report No 4/97 (lnr 54), Norges landbrukshøgskole, Norway.

Fox-Kemper B, Hewitt H T, Xiao C, Aðalgeirsdóttir G, Drijfhout S S, Edwards T L, Golledge N R, Hemer M, Kopp R E, Krinner G, Mix A, Notz D, Nowicki S, Nurhati I S, Ruiz L, Sallée JB, Slangen A B A, Yu Y, 2021. Ocean, Cryosphere and Sea Level Change. In Climate Change 2021: The Physical Science Basis. Contribution of Working Group I to the Sixth Assessment Report of the Intergovernmental Panel on Climate Change. Cambridge University Press, Cambridge, United Kingdom and New York, NY, USA, pp. 1211–1362, doi:10.1017/9781009157896.011.

Frajka-Williams E, Ansorge I J, Baehr J, Bryden H L, Chidichimo M P, Cunningham S A, Danabasoglu G, Dong S, Donohue K A, Elipot S, Heimbach P, Holliday N P, Hummels R, Jackson L C, Karstensen J, Lankhorst M, Bras I A L, Lozier M S, McDonagh E L, Meinen C S, Mercier H, Moat B I, Perez R C, Piecuch C G, Rhein M, Srokosz M A, Trenberth K E, Bacon S, Forget G, Goni G, Kieke D, Koelling J, Lamont T, McCarthy G D, Mertens C, Send U, Smeed D A, Speich S, van den Berg M, Volkov D, Wilson C, 2019. OceanObs19: Atlantic meridional overturning circulation: Observed transports and variability, Front. Mar. Sci. 6, 260, https://doi.org/10.3389/fmars.2019.00260

French H M, 2007. The periglacial environment. 3rd ed. Chichester: Wiley.

Fredén C (ed), 2002. Sveriges nationalatlas. Berg och Jord. Stockholm: SNA publishing. (In Swedish.)

Fretwell P, Pritchard H D, Vaughan D G, Bamber J L, Barrand N E, Bell R, Bianchi C, Bingham R G, Blankenship D D, Casassa G, Catania G, Callens D, Conway H, Cook A J, Corr H F J, Damaske D, Damm V, Ferraccioli F, Forsberg R, Fujita S, Gim Y, Gogineni P, Griggs J A, Hindmarsh R C A, Holmlund P, Holt J W, Jacobel R W, Jenkins A, Jokat W, Jordan T, King E C, Kohler J, Krabill W, Riger-Kusk M, Langley K A, Leitchenkov G, Leuschen C, Luyendyk B P, Matsuoka K, Mouginot J, Nitsche F O, Nogi Y, Nost O A, Popov S V, Rignot E, Rippin D M, Rivera A, Roberts J, Ross N, Siegert M J, Smith A M, Steinhage D, Studinger M, Sun B, Tinto B K, Welch B C, Wilson D, Young D A, Xiangbin C, Zirizzotti A, 2013. Bedmap2: improved ice bed, surface and thickness datasets for Antarctica, The Cryosphere 7, 375–393.

Friedlingstein P, Meinshausen M, Arora V K, Jones C D, Anav A, Liddicoat S K, Knutti R, 2014. Uncertainties in CMIP5 climate projections due to carbon cycle feedbacks. Journal of Climate 27, 511–526.

Friedlingstein P, O'Sullivan M, Jones M W, Andrew R M, Gregor L, Hauck J, Le Quéré C, Luijkx I T, Olsen A, Peters G P, Peters W, Pongratz J, Schwingshackl C, Sitch S, Canadell J G, Ciais P, Jackson R B, Alin S R, Alkama R, Arneth A, Arora V K, Bates N R, Becker M, Bellouin N, Bittig H C, Bopp L, Chevallier F, Chini L P, Cronin M, Evans W, Falk S, Feely R A, Gasser T, Gehlen M, Gkritzalis T, Gloege L, Grassi G, Gruber N, Gürses Ö, Harris I, Hefner M, Houghton R A, Hurtt G C, Iida Y, Ilyina T, Jain A K, Jersild A, Kadono K, Kato E, Kennedy D, Klein Goldewijk K, Knauer J, Korsbakken J I, Landschützer P, Lefèvre N, Lindsay K, Liu J, Liu Z, Marland G, Mayot N, McGrath M J, Metzl N, Monacci N M, Munro D R, Nakaoka S-I, Niwa Y, O'Brien K, Ono T, Palmer P I, Pan N, Pierrot D, Pocock K, Poulter B, Resplandy L, Robertson E, Rödenbeck C, Rodriguez C, Rosan T M, Schwinger J, Séférian R, Shutler J D, Skjelvan I, Steinhoff T, Sun Q, Sutton A J, Sweeney C, Takao S, Tanhua T, Tans P P, Tian X, Tian H, Tilbrook B, Tsujino H, Tubiello F, van der Werf G R, Walker A P, Wanninkhof R, Whitehead C, Willstrand Wranne A, Wright R, Yuan W, Yue C, Yue X, Zaehle S, Zeng J, Zheng B, 2022. Global Carbon Budget 2022, Earth Syst. Sci. Data 14, 4811–4900.

Fujimori S, Hasegawa T, Masui T, Takahashi K, Herran D S, Dai H, Hijioka Y, Kainuma M, 2017. SSP3: AIM implementation of shared socioeconomic pathways. Global Environmental Change 42, 268–283.

Galbraith D, Levy P E, Sitch S, Huntingford C, Cox P, Williams M, Meir P, 2010. Multiple mechanisms of Amazonian forest biomass losses in three dynamic global vegetation models under climate change. New Phytologist 187, 647–665.

Galeotti S, DeConto R, Naish T, Stocchi P, Florindo F, Pagani M, Barrett P, Bohaty S M, Lanci L, Pollard D, Sandroni S, Talarico F M, Zachos J C, 2016. Antarctic Ice Sheet variability across the Eocene-Oligocene boundary climate transition, Science 352, 76–80, https://doi.org/10.1126/science.aab0669

Ganopolski A, Calov R, 2011. The role of orbital forcing, carbon dioxide and regolith in 100 kyr glacial cycles, Clim. Past 7, 1415–1425, https://doi.org/10.5194/cp-7-1415-2011.

Ganopolski A, Brovkin V, 2017. Simulation of climate, ice sheets and CO2 evolution during the last four glacial cycles with an Earth system model of intermediate complexity, Clim. Past 13, 1695–1716, https://doi.org/10.5194/cp-13-1695-2017.

Ganopolski A, Winkelmann R, Schellnhuber H J, 2016. Critical insolation–CO2 relation for diagnosing past and future glacial inception. Nature 529, 200–203.

Gasson E, Lunt D J, DeConto R, Goldner A, Heinemann M, Huber M, LeGrande A N, Pollard D, Sagoo N, Siddall M, Winguth A, Valdes P J, 2014. Uncertainties in the modelled CO_2 threshold for Antarctic glaciation. Climate of the Past 10, 451-466.

Gent P R, Danabasoglu G, Donner L J, Holland M M, Hunke E C, Jayne S R, Lawrence D M, Neale R B, Rasch P J, Vertenstein M, Worley P H, Yang Z-L, Zhang M, 2011. The Community Climate System Model Version 4. Journal of Climate 24, 4973–4991.

Gidden M J, Riahi K, Smith S J, Fujimori S, Luderer G, Kriegler E, van Vuuren D P, van den Berg M, Feng L, Klein D, Calvin K, Doelman J C, Frank S, Fricko O, Harmsen M, Hasegawa T, Havlik P, Hilaire J, Hoesly R, Horing J, Popp A, Stehfest E, Takahashi, K, 2019. Global emissions pathways under different socioeconomic scenarios for use in CMIP6: a dataset of harmonized emissions trajectories through the end of the century, Geosci. Model Dev. 12, 1443–1475, https://doi.org/10.5194/gmd-12-1443-2019

Gilford D M, Ashe E L, DeConto R M, Kopp R E, Pollard D, Rovere A, 2020. Could the Last Interglacial Constrain Projections of Future Antarctic Ice Mass Loss and Sea-Level Rise?, J. Geophys. Res.-Earth 125, e2019JF005418, https://doi.org/10.1029/2019JF005418

Girod B, Wiek A, Mieg H, Hulme M, 2009. The evolution of the IPCC's emissions scenarios. Environmental science & policy 12, 103-118.

Glen J W, 1955. The creep of polycrystalline ice. Proceedings of the Royal Society of London, Series A 228, 519–538.

Global Registry of Fossil Fuels, 2022. Emissions and fossil fuel reserves. Available at: https://fossilfuelregistry.org/reserves [25 July 2023]

Goodfellow B W, Stroeven A P, Martel S J, Heyman J, Rossi M, Caffee M W, 2019. Exploring alternative models for the formation of conspicuously flat basement surfaces in southern Sweden. SKB TR-19-22, Svensk Kärnbränslehantering AB.

Goodfellow B W, Stroeven A P, Lewerentz A, Hippe K, Heyman J, Lifton N A, Caffee M W, 2023. Evaluation of shoreline displacement and glacial erosion at Forsmark using in situ 14C in quartz. SKB TR-23-17, Svensk Kärnbränslehantering AB.

Goodfellow B W, Stroeven A P, Lifton N A, Heyman, J, Lewerentz A, Hippe K, Näslund J-O, Caffee M W, 2024. Last ice sheet recession and landscape emergence above sea level in east-central Sweden, evaluated using in situ cosmogenic 14C from quartz, Geochronology 6, 291–302, https://doi.org/10.5194/gchron-6-291-2024.

Govaerts J, Beerten K, ten Veen, J, 2016. Weichselian permafrost depth in the Netherlands: a comprehensive uncertainty and sensitivity analysis. The Cryosphere 10, 2907-2922.

Greve R, 1997. Application of a Polythermal Three-Dimensional Ice Sheet Model to the Greenland Ice Sheet: Response to Steady-State and Transient Climate Scenarios, J. Climate 10, 901–918.

Greve R, 2001. Glacial isostasy: Models for the response of the Earth to varying ice loads. In: Continuum Mechanics and Applications in Geophysics and the Environment (pp. 307-325). Berlin, Heidelberg: Springer Berlin Heidelberg.

Grinsted A, Jevrejeva S, Riva R E, Dahl-Jensen D, 2015. Sea level rise projections for northern Europe under RCP8.5. Climate Research 64, 15–23.

Grolander S, 2013. Biosphere parameters used in radionuclide transport modelling and dose calculations in SR-PSU. SKB R-13-18, Svensk Kärnbränslehantering AB.

Gräwe U, Klingbeil K, Kelln J and Dangendorf S, 2019. Decomposing Mean Sea Level Rise in a Semi-Enclosed Basin, the Baltic Sea, J. Climate 32, 3089–3108.

Gulev S K, Thorne P W, Ahn J, Dentener F J, Domingues C M, Gerland S, Gong D, Kaufman D S, Nnamchi H C, Quaas J, Rivera J A, Sathyendranath S, Smith S L, Trewin B, von Schuckmann K, Vose R S, 2021. Changing State of the Climate System. In Climate Change 2021: The Physical Science Basis. Contribution of Working Group I to the Sixth Assessment Report of the Intergovernmental Panel on Climate Change. Cambridge University Press, Cambridge, United Kingdom and New York, NY, USA, pp. 287–422, doi:10.1017/9781009157896.004.

Gustafsson D, 2022. Potential evapotranspiration in boreal forests. An assessment of different calculation methods. SKB R-22-03, Svensk Kärnbränslehantering AB.

Gutiérrez J M, Jones R G, Narisma G T, Alves L M, Amjad M, Gorodetskaya I V, Grose M, Klutse N A B, Krakovska S, Li J, Martínez-Castro D, Mearns L O, Mernild S H, Ngo-Duc T, van den Hurk B, Yoon J-H, 2021. Atlas. In Climate Change 2021: The Physical Science Basis. Contribution of Working Group I to the Sixth Assessment Report of the Intergovernmental Panel on Climate Change. Cambridge University Press, Cambridge, United Kingdom and New York, NY, USA, pp. 1927–2058. Interactive Atlas available from http://interactive-atlas.ipcc.ch/

Hall A, van Boeckel M, 2020. Origin of the Baltic Sea basin by Pleistocene glacial erosion. GFF 142, 237–252.

Hall A M, Ebert K, Goodfellow B W, Hättestrand C, Heyman J, Krabbendam M, Moon S, Stroeven A P, 2019a. Past and future impact of glacial erosion in Forsmark and Uppland. Final Report. SKB TR-19-07, Svensk Kärnbränslehantering AB.

Hall A M, Krabbendam M, van Boeckel M, Hättestrand C, Ebert K, Heyman J, 2019b. The sub-Cambrian unconformity in Västergötland, Sweden: Reference surface for Pleistocene glacial erosion of basement. SKB TR-19-21, Svensk Kärnbränslehantering AB.

Hall A M, Krabbendam M, van Boeckel M, Goodfellow B W, Hättestrand C, Heyman J, Palamakumbara R N, Stroeven A P, Näslund J-O, 2020. Glacial ripping: geomorphological evidence from Sweden for a new process of glacial erosion. Geografiska Annaler, Series A. doi:10.1080/04353676.2020.1774244

Hall A M, Krabbendam M, van Boeckel M, 2022. Glacial erosion in the Öregrund archipelago. Potential for headward erosion towards Forsmark in future glaciations? SKB TR-22-08, Svensk Kärnbränslehantering AB.

Hall A M, Heyman J, Hein A, 2023. Glacial erosion rates at Forsmark derived from Terrestrial Cosmogenic Nuclides - additional results. SKB TR-23-21, Svensk Kärnbränslehantering AB.

Hallet B, Hunter L, Bogen J, 1996. Rates of erosion and sediment evacuation by glaciers: a review of field data and their implications. Global and Planetary Change 12, 213–235.

Harbor J, Stroeven A P, Fabel D, Clarhäll A, Kleman J, Li Y, Elmore D, Fink D, 2006. Cosmogenic nuclide evidence for minimal erosion across two subglacial sliding boundaries of the late glacial Fennoscandian ice sheet. Geomorphology 75, 90–99.

Harris I, Osborn T J, Jones P, Lister D, 2020. Version 4 of the CRU TS monthly high-resolution gridded multivariate climate dataset. Scientific data 7, 109.

Hartikainen J, 2004. Permafrost modeling in DECOVALEX III for BMT3. In Eloranta E (ed). DECOVALEX III, 1999–2003. An international project for the modelling of coupled thermo-hydromechanical processes for spent fuel disposal. Finnish national contributions. STUK-YTO-TR 209, Finnish Centre for Radiation and Nuclear Safety (STUK), Helsinki.

Hartikainen J, 2013. Simulations of permafrost evolution at Olkiluoto. Posiva Working Report, 2012-34, Posiva Oy.

Hartikainen J, 2018. Continuum thermodynamic modelling of porous medium with application to ground freezing. PhD thesis. Aalto University.

Hartikainen J, Kouhia R, Wallroth T, 2010. Permafrost simulations at Forsmark using a numerical 2D thermo-hydro-chemical model. SKB TR-09-17, Svensk Kärnbränslehantering AB.

Hartikainen J, Näslund J O, Liakka J, Claesson Liljedahl L, Kolisoja P, Kouhia R, 2022. Evaluation of the SR-Site and SR-PSU permafrost models against GAP site bedrock temperatures. SKB TR-21-08, Svensk Kärnbränslehantering AB.

Haskins R K, Oliver K I, Jackson L C, Drijfhout S S, Wood R A, 2019. Explaining asymmetry between weakening and recovery of the AMOC in a coupled climate model. Climate dynamics 53, 67-79.

Hausfather 2019. CMIP6: the next generation of climate models explained. Carbon Brief. Available at: https://www.carbonbrief.org/cmip6-the-next-generation-of-climate-models-explained/

Hedenström A, Risberg J, 2003. Shore displacement in northern Uppland during the last 6500 calender years. SKB TR-03-17, Svensk Kärnbränslehantering AB.

Held I M, Soden B J, 2000. Water vapor feedback and global warming. Annual review of energy and the environment 25, 441-475.

Helmens K F, 2009. Climate, vegetation and lake development at Sokli (northern Finland) during early MIS 3 at ~ 50 kyr: Revising earlier concepts on climate, glacial and vegetation dynamics in Fennoscandia during the Weichselian. SKB TR-09-16, Svensk Kärnbränslehantering AB.

Helmens K, 2013. The last interglacial–glacial cycle (MIS 5–2) re-examined based on long proxy records from central and northern Europe. SKB TR-13-02, Svensk Kärnbränslehantering AB.

Helmens K F, 2019. The last 130000 years in Fennoscandia reconstructed based on a long and fossil-rich sediment sequence preserved at Sokli, northern Finland: new evidence for highly dynamic environmental and climate conditions. SKB TR-18-04, Svensk Kärnbränslehantering AB.

Helmens K F, Katrantsiotis C, Kuosmanen N, Luoto T P, Salonen J S, Väliranta M, 2021. Prolonged interglacial warmth during the Last Glacial in northern Europe. Boreas 50: 331-350.

Helmens K F, Engels S, Salonen J S, Väliranta M, 2024. The late Quaternary of Fennoscandia revisited. 15 years of collaborative research at Sokli in northern Finland - a complete overview. SKB TR-23-28, Svensk Kärnbränslehantering AB.

Hersbach H, Bell B, Berrisford P, Hirahara S, Horányi A, Muñoz-Sabater J, Nicolas J, Peubey C, Radu R, Schepers D, Simmons A, Soci C, Abdalla S, Abellan X, Balsamo G, Bechtold P, Biavati G, Bidlot J, Bonavita M, De Chiara G, Dahlgren P, Dee D, Diamantakis M, Dragani R, Flemming J, Forbes R, Fuentes M, Geer A, Haimberger L, Healy S, Hogan R J, Hólm E, Janisková M, Keeley S, Laloyaux P, Lopez P, Lupu C, Radnoti G, de Rosnay P, Rozum I, Vamborg F, Villaume S, Thépaut J-N, 2020. The ERA5 global reanalysis. Quarterly Journal of the Royal Meteorological Society 146, 1999-2049.

Hieronymus M, Kalén O, 2020. Sea-level rise projections for Sweden based on the new IPCC special report: The ocean and cryosphere in a changing climate, Ambio, 49, 1587–1600.

Holgate S J, Matthews A, Woodworth P L, Rickards L J, Tamisiea M E, Bradshaw E, Foden P R, Gordon K M, Jevrejeva S, Pugh J, 2013. New data systems and products at the Permanent Service for Mean Sea Level. Journal of Coastal Research 29, 493–504.

Holland P R, Bracegirdle T J, Dutrieux P, Jenkins A, Steig E J, 2019. West Antarctic ice loss influenced by internal climate variability and anthropogenic forcing. Nature Geoscience, 12 718-724.

Holmlund P, Fastook J, 1995. A time dependent glaciological model of the Weichselian ice-sheet. Quaternary International 27, 53–58.

Holmlund P, Jansson P, 2003. Glaciologi. Stockholm: Stockholm University and the Swedish Research Council. (In Swedish.)

Houmark-Nielsen M, Kjær K H, 2003. Southwest Scandinavia, 40–15 kyr BP: palaeogeography and environmental change. Journal of Quaternary Science 18, 769–786.

Hubau W, Lewi, S L, Phillips O L, Affum-Baffoe K, Beeckman H, Cuní-Sanchez A, Daniels A K, Ewango C E N, Fauset S, Mukinzi J M, Sheil D, Sonké B, Sullivan M J P, Sunderland T C H, Taedoumg H, Thomas S C, White L J T, Abernethy K A, Adu-Bredu S, Amani C A, Baker T R, Banin L F, Baya F, Begne S K, Bennett A C, Benedet F, Bitariho R, Bocko Y E, Boeckx P, Boundja P, Brienen R J W, Brncic T, Chezeaux E, Chuyong G B, Clark C J, Collins M, Comiskey J A, Coomes D A, Dargie G C, de Haulleville T, Djuikouo Kamdem M N, Doucet J-L, Esquivel-Muelbert A, Feldpausch T R, Fofanah A, Foli E G, Gilpin M, Gloor E, Gonmadje C, Gourlet-Fleury S, Hall J S, Hamilton A C, Harris D J, Hart T B, Hockemba M B N, Hladik A, Ifo S A, Jeffery K J, Jucker T, Kasongo Yakusu E, Kearsley E, Kenfack D, Koch A, Leal M E, Levesley A, Lindsell J A, Lisingo J, Lopez-Gonzalez G, Lovett J C, Makana J-R, Malhi Y, Marshall A R, Martin J, Martin E H, Mbayu F M, Medjibe V P, Mihindou V, Mitchard E T A, Moore S, Munishi P K T, Bengone N N, Ojo L, Ondo F E, Peh K S-H, Pickavance G C, Dalberg Poulsen A, Poulsen J R, Qie L, Reitsma J, Rovero F, Swaine M D, Talbot J, Taplin J, Taylor D M, Thomas D W, Toirambe B, Mukendi J T, Tuagben D, Umunay P M, van der Heijden G M F, Verbeeck H, Vleminckx J, Willcock S, Wöll H, Woods J T, Zemagho L, 2020. Asynchronous carbon sink saturation in African and Amazonian tropical forests. Nature 579, 80–87.

Hudson T S, Kufner S K, Brisbourne A M, Kendall J M, Smith A M, Alley R B, Arthern R, Murray T, 2023. Highly variable friction and slip observed at Antarctic ice stream bed. Nature Geoscience 16, 612-618.

Hutter K, 1983. Theoretical glaciology: material science of ice and the mechanics of glaciers and ice-sheets. Dordrecht: Reidel.

IEA, 2019. World energy outlook 2019. Paris: IEA. Available at: https://www.iea.org/reports/world-energy-outlook-2019

IEA, 2022. World energy outlook 2022. Paris: IEA. Available at: https://www.iea.org/reports/world-energy-outlook-2022

IIASA, 2018. International Institute for Applied Systems Analysis. SSP Database (Shared Socioeconomic Pathways) - Version 2.0. Available at: https://tntcat.iiasa.ac.at/SspDb/dsd?Action=htmlpage&page=10 [26 July 2023]

Imbrie J, Berger A, Boyle E A, Clemens S C, Duffy A, Howard W R, Kukla G, Kutzbach J, Martinson D G, McIntyre A, Mix A C, Molfino B, Morley J J, Peterson L C, Pisias N G, Prell W L, Raymo M E, Shackleton N J, Toggweiler J R, 1993. On the structure and origin of major glaciation cycles 2. The 100,000-year cycle. Paleoceanography 8, 699-735.

IPCC, 1990. Climate Change—The IPCC Scientific Assessment. Cambridge University Press, Cambridge.

IPCC, 2018. Summary for Policymakers. In: Global Warming of 1.5°C. An IPCC Special Report on the impacts of global warming of 1.5°C above pre-industrial levels and related global greenhouse gas emission pathways, in the context of strengthening the global response to the threat of climate change, sustainable development, and efforts to eradicate poverty. Cambridge University Press, Cambridge, UK and New York, NY, USA, pp. 3-24. https://doi.org/10.1017/9781009157940.001.

IPCC, 2019. IPCC special report on the ocean and cryosphere in a changing climate. [Pörtner H-O, Roberts D C, Masson-Delmotte V, Zhai P, Tignor M, Poloczanska E, Mintenbeck K, Alegría A, Nicolai M, Okem A, Petzold J, Rama B, Weyer N M (eds)]. Cambridge University Press.

IPCC, 2021a. Climate Change 2021: The Physical Science Basis. Contribution of Working Group I to the Sixth Assessment Report of the Intergovernmental Panel on Climate Change[Masson-Delmotte, V., P. Zhai, A. Pirani, S.L. Connors, C. Péan, S. Berger, N. Caud, Y. Chen, L. Goldfarb, M.I. Gomis, M. Huang, K. Leitzell, E. Lonnoy, J.B.R. Matthews, T.K. Maycock, T. Waterfield, O. Yelekçi, R. Yu, and B. Zhou (eds.)]. Cambridge University Press, Cambridge, United Kingdom and New York, NY, USA, In press, doi:10.1017/9781009157896.

IPCC, 2021b. Annex III: Tables of historical and projected well-mixed greenhouse gas mixing ratios and effective radiative forcing of all climate forcers. In Climate Change 2021: The Physical Science Basis. Contribution of Working Group I to the Sixth Assessment Report of the Intergovernmental Panel on Climate Change. Cambridge University Press, Cambridge, United Kingdom and New York, NY, USA, pp. 2139–2152, doi:10.1017/9781009157896.017.

Iturbide M, Gutiérrez J M, Alves L M, Bedia J, Cerezo-Mota R, Cimadevilla E, Cofiño A S, Di Luca A, Faria S H, Gorodetskaya I V, Hauser M, Herrera S, Hennessy K, Hewitt H T, Jones R G, Krakovska S, Manzanas R, Martínez-Castro D, Narisma G T, Nurhati I S, Pinto I, Seneviratne S I, van den Hurk B, Vera C S, 2020. An update of IPCC climate reference regions for subcontinental analysis of climate model data: definition and aggregated datasets, Earth System Science Data 12, 2959–2970.

Iturbide M, Fernández J, Gutiérrez J M, Bedia J, Cimadevilla E, Díez-Sierra J, Manzanas R, Casanueva A, Baño-Medina J, Milovac J, Herrera S, Cofiño A S, San Martín D, García-Díez M, Hauser M, Huard D, Yelekci Ö, 2021. Repository supporting the implementation of FAIR principles in the IPCC-WG1 Atlas. Zenodo, DOI: 10.5281/zenodo.3691645. Available from: https://github.com/IPCC-WG1/Atlas

Izumi K, Armstrong E, Valdes P, 2023. Global footprints of dansgaard-oeschger oscillations in a GCM. Quaternary Science Reviews 305, 108016.

Jackson L C, 2013. Shutdown and recovery of the AMOC in a coupled global climate model: the role of the advective feedback. Geophysical Research Letters 40, 1182-1188.

Jackson L C, Kahana R, Graham T, Ringer M A, Woollings T, Mecking J V, Wood R A, 2015. Global and European climate impacts of a slowdown of the AMOC in a high resolution GCM. Climate dynamics 45, 3299-3316.

Jacob D, Goettel H, Jungclaus J, Muskulus M, Podzun R, Marotzke J, 2005. Slowdown of the thermohaline circulation causes enhanced maritime climate influence and snow cover over Europe. Geophysical research letters 32.

Jakobsson M, Stranne C, O'Regan M, Greenwood S L, Gustafsson B, Humborg C and Weidner E, 2019. Bathymetric properties of the Baltic Sea, Ocean Sci. 15, 905–924.

Jansen D, Sandhäger H, Rack W, 2005. Model experiments on large tabular iceberg evolution: ablation and strain thinning. Journal of Glaciology 51, 363-372.

Jenkins A, Shoosmith D, Dutrieux P, Jacobs S, Kim T W, Lee S H, Ha H K, Stammerjohn S, 2018. West Antarctic Ice Sheet retreat in the Amundsen Sea driven by decadal oceanic variability. Nature Geoscience, 11, 733-738.

Johansson J, 2016. Total and Regional Runoff to the Baltic Sea. Available at: https://helcom.fi/wp-content/uploads/2020/07/BSEFS-Total-and-Regional-Runoff-to-the-Baltic-Sea-2015.pdf

Johnson J, Fastook J L, 2002. Northern Hemisphere glaciation and its sensitivity to basal melt water, Quaternary Int. 95–96, 65–74.

Joughin I, Abdalati W, Fahnestock M, 2004. Large fluctuations in speed on Greenland's Jakobshavn Isbræ glacier. Nature 432, 608–610.

Jupp T E, Cox P M, Rammig A, Thonicke K, Lucht W, Cramer W, 2010. Development of probability density functions for future South American rainfall. New Phytologist 187, 682–693.

Kachuck S B, Martin D F, Bassis J N, Price S F, 2020. Rapid Viscoelastic Deformation Slows Marine Ice Sheet Instability at Pine Island Glacier. Geophysical Research Letters, 47, e2019GL086446.

Kageyama M Charbit S, Ritz C, Khodri, M, Ramstein G, 2004. Quantifying ice-sheet feedbacks during the last glacial inception. Geophys. Res. Lett., 31, L24203, DOI:10.1029/2004GL021339.

Karabil S, Zorita E, Hünicke B, 2018. Contribution of atmospheric circulation to recent off-shore sea-level variations in the Baltic Sea and the North Sea. Earth System Dynamics 9, 69-90.

Khatiwala S, Schmittner A, Muglia J, 2019. Air-sea disequilibrium enhances ocean carbon storage during glacial periods. Science advances 5, eaaw4981.

Kjellström E, Strandberg G, Brandefelt J, Näslund J-O, Smith B, Wohlfarth B, 2009. Climate conditions in Sweden in a 100,000-year time perspective. SKB TR-09-04, Svensk Kärnbränslehantering AB.

Kleman J, 1992. The palimpsest glacial landscape in northwestern Sweden: Late Weichselian deglaciation landforms and traces of older west-centered ice sheets. Geografiska Annaler: Series A, Physical Geography 74, 305–325.

Kleman J, Hättestrand C, Borgström I, Stroeven A, 1997. Fennoscandian palaeoglaciology reconstructed using a glacial geological inversion model. Journal of Glaciology 43, 283–299.

Kleman J, Stroeven A, Lundqvist J, 2008. Patterns of Quaternary ice-sheet erosion and deposition in Fennoscandia and a theoretical framework for explanation. Geomorphology 97, 73–90.

Kleman J, Jansson K, De Angelis H, Stroeven A P, Hättestrand C, Alm G, Glasser N, 2010. North American Ice Sheet build-up during the last glacial cycle, 115–21 kyr. Quaternary Science Reviews 29, 2036-2051.

Kleman J, Fastook J, Ebert K, Nilsson J, Caballero R, 2013. Pre-LGM Northern Hemisphere ice sheet topography. Climate of the Past, 9(5), 2365-2378.

Kniebusch M, Meier H M, Radtke H, 2019. Changing Salinity Gradients in the Baltic Sea As a Consequence of Altered Freshwater Budgets. Geophysical Research Letters 46, 9739–9747.

Kopp R E, Mitrovica J X, Griffies S M, Yin J, Hay C C, Stouffer R J, 2010. A partially coupled analysis of dynamic and static equilibrium effects. Climate Change 103, 619–625.

Kopp R E, Horton R M, Little C M, Mitrovica J X, Oppenheimer M, Rasmussen D, Strauss B H, Tebaldi C, 2014. Probabilistic 21st and 22nd century sea-level projections at a global network of tide-gauge sites. Earth’s Future 2, 383–406.

Krabbendam M, Hall A M, Palamakumbura R, Finlayson A, Diogardi F, Arnhardt C, 2022. Glacial ripping as a significant erosion mechanism in eastern Sweden – Field evidence and modelling. SKB TR-22-09, Svensk Kärnbränslehantering AB.

Krabbendam M, Finlayson A, Palamakumbura R, Hall A M, 2023. Quantifying the contribution of abrasion versus block removal to subglacial erosion on basement rocks. Very-high resolution DSM analysis at Forsmark, east Sweden. SKB TR-23-27, Svensk Kärnbränslehantering AB.

Kuhlbrodt T, Rahmstorf S, Zickfeld K, Vikebø F B, Sundby S, Hofmann M, Link P, Bondeau A, Cramer W, Jaeger C, 2009. An integrated assessment of changes in the thermohaline circulation. Climatic Change 96, 489-537.

Källén E, Crafoord C, Ghil M, 1979. Free oscillations in a climate model with ice-sheet dynamics. Journal of Atmospheric Sciences 36, 2292-2303.

Köppen W, 1884. Die Wärmezonen der Erde, nach der Dauer der heissen, gemässigten und kalten Zeit und nach der Wirkung der Wärme auf die organische Welt betrachtet. Meteorologische Zeitschrift 1, 215–226.

Lai C Y, Kingslake J, Wearing M G, Chen P C, Gentine P, Li H, Spergel J, van Messem J M, 2020. Vulnerability of Antarctica's ice shelves to meltwater-driven fracture, Nature 584, 574–578.

Lambeck K, 1995. Late Devensian and Holocene shorelines of the British Isles and North Sea from models of glacio-hydroisostatic rebound. Journal of the Geological Society 152, 437–448.

Lambeck K, Smither C, Johnston P, 1998. Sea-level change, glacial rebound and mantle viscosity for northern Europe. Geophysical Journal International 134, 102–144.

Lambeck K, Purcell A, Funder S, Kjær K H, Larsen E, Möller P, 2006. Constraints on the Late Saalian to early Middle Weichselian ice-sheet of Eurasia from field data and rebound modelling. Boreas 35, 539–575.

Lambeck K, Rouby H, Purcell A, Sun Y, Sambridge M, 2014. Sea level and global ice volumes from the Last Glacial Maximum to the Holocene. Proceedings of the National Academy of Sciences 111, 15296-15303.

Lampinen A, 2025. Baseline Forsmark – Hydrological and hydrogeological modelling using MIKE SHE, DHI Sverige AB. SKBdoc 2082885 ver 1.0, Svensk Kärnbränslehantering AB.

Laskar J, Robutel P, Joutel F, Gastineau M, Correia A C M, Levrard B, 2004. A long-term numerical solution for the insolation quantities of the Earth. Astronomy & Astrophysics 428, 261–285.

Laurian A, Drijfhout S S, Hazeleger W, van den Hurk B J J M, 2010. Response of the Western European climate to a collapse of the thermohaline circulation. Climate Dynamics 34, 689-697.

Le Meur E, Huybrechts P, 1996. A comparison of different ways of dealing with isostasy: examples from modelling the Antarctic ice sheet during the last glacial cycle. Annals of glaciology 23, 309-317.

Lee J-Y, Marotzke J, Bala G, Cao L, Corti S, Dunne J P, Engelbrecht F, Fischer E, Fyfe J C, Jones C, Maycock A, Mutemi J, Ndiaye O, Panickal S, Zhou T, 2021. Future Global Climate: Scenario-Based Projections and Near-Term Information. In Climate Change 2021: The Physical Science Basis. Contribution of Working Group I to the Sixth Assessment Report of the Intergovernmental Panel on Climate Change. Cambridge University Press, Cambridge, United Kingdom and New York, NY, USA, pp. 553–672, doi:10.1017/9781009157896.006.

Leppäranta M and Myrberg K, 2009. Physical oceanography of the Baltic Sea, Springer-Praxis books in geophysical sciences, Springer/Praxis Pub., Berlin, Chichester, UK, 2009.

Levermann A, Clark P U, Marzeion B, Milne G A, Pollard D, Radic V, Robinson A, 2013. The multimillennial sea-level commitment of global warming. Proceedings of the National Academy of Sciences 110, 13745–13750.

Levermann A, Winkelmann R, Albrecht T, Goelzer H, Golledge N R, Greve R, Huybrechts P, Jordan J, Leguy G, Martin D, Morlighem M, Pattyn F, Pollard D, Quiquet A, Rodehacke C, Seroussi H, Sutter J, Zhang T, Van Breedam J, Calov R, DeConto R, Dumas C, Garbe J, Gudmundsson G H, Hoffman M J, Humbert A, Kleiner T, Lipscomb W H, Meinshausen M, Ng E, Nowicki S M J, Perego M, Price S F, Saito F, Schlegel N-J, Sun S, van de Wal R S W, 2020. Projecting Antarctica's contribution to future sea level rise from basal ice shelf melt using linear response functions of 16 ice sheet models (LARMIP-2), Earth System Dynamics 11, 35–76.

Li C, Born A, 2019. Coupled atmosphere-ice-ocean dynamics in Dansgaard-Oeschger events. Quaternary Science Reviews 203, 1-20.

Liakka J, Näslund J O, Brandefelt J, 2021. Timing of future glacial inception. In Haeberli W, Whiteman C (eds). Snow and ice-related hazards, risks and disasters. 2nd ed. Oxford: Elsevier, Chapter 11.2.

Liakka J, Lord N S, Kennedy-Asser A, Lunt D J, Williams C J, Näslund J O, 2024. Assessing future ice-sheet variability for long-term safety of deep geological repositories. Advances in Geosciences 65, 71-81.

Lidberg M, Johansson J M, Scherneck H-G, Milne G A, 2010. Recent results based on continuous GPS observations of the GIA process in Fennoscandia from BIFROST. Journal of Geodynamics 50, 8–18.

Lidmar-Bergström K, 1995. Relief and saprolites through time on the Baltic shield. Geomorphology 12, 45–61.

Lidmar-Bergström K, 1997. A long-term perspective on glacial erosion. Earth Surface Processes and Landforms 22, 297–306.

Lidmar-Bergström K, Näslund J-O, 2005. Major landforms and bedrock. In Seppälä M (ed). The physical geography of Fennoscandia, Oxford: Oxford University Press.

Liu J, Milne G A, Kopp R E, Clark P U, Shennan, I, 2016. Sea-level constraints on the amplitude and source distribution of Meltwater Pulse 1A, Nature Geoscience 9, 130-134.

Liu W, Xie S P, Liu Z, Zhu J, 2017. Overlooked possibility of a collapsed Atlantic Meridional Overturning Circulation in warming climate. Science Advances 3, e1601666. doi:10.1126/sciadv.1601666

Lisiecki L E, Raymo M E, 2005. A Pliocene-Pleistocene stack of 57 globally distributed benthic d18O records. Paleoceanography 20. doi:10.1029/2004PA001071

Lohmann J, Ditlevsen P D, 2021. Risk of tipping the overturning circulation due to increasing rates of ice melt. Proceedings of the National Academy of Sciences, 118(9), e2017989118, doi:10.1073/pnas.2017989118

Lokrantz H, Sohlenius G, 2006. Ice-marginal fluctuations during the Weichselian glaciation inFennoscandia, a literature review. SKB TR-06-36, Svensk Kärnbränslehantering AB.

Lord N S, Ridgwell A, Thorne M C, Lunt D J, 2016. An impulse response function for the "long tail" of excess atmospheric CO2 in an Earth system model. Global Biogeochemical Cycles 30, 2–17.

Lord N S, Lunt D, Thorne M, 2019. Modelling changes in climate over the next 1 million years. SKB TR-19-09, Svensk Kärnbränslehantering AB.

Lunardini V J, 1978. Theory of n-factors and correlation of data. In Proceedings of the 3rd International Conference on Permafrost. Edmonton, Alta, 10–13 July 1978. Ottawa: National Research Council of Canada, Vol 1, 40–46.

Lund B, Schmidt P, Hieronymus C, 2009. Stress evolution and fault stability during the Weichselian glacial cycle. SKB TR-09-15, Svensk Kärnbränslehantering AB.

Lundqvist J, Wohlfarth B, 2000. Timing and east–west correlation of south Swedish ice-marginal lines during the Late Weichselian. Quaternary Science Reviews 20, 1127–1148.

Lunkka J P, Johansson P, Saarnisto M, Sallasmaa O, 2004. Glaciation of Finland. In Ehlers J, Gibbard P L (eds). Quaternary glaciations: extent and chronology. Part I: Europe. Amsterdam: Elsevier. (Developments in Quaternary Science 2), 93–100.

Lüthi D, Le Floch M, Bereiter B, Blunier T, Barnola J-M, Siegenthaler U, Raynaud D, Jouzel J, Fischer H, Kawamura K, Stocker T F, 2008. High-resolution carbon dioxide concentration record 650,000–800,000 years before present. Nature 453, 379–382.7

Madsen K S, Høyer J L, Suursaar Ü, She J, Knudsen P, 2019. Sea Level Trends and Variability of the Baltic Sea From 2D Statistical Reconstruction and Altimetry, Front. Earth Sci. 7, 67, https://doi.org/10.3389/feart.2019.00243, 2019a.

Mahowald N, Kohfeld K, Hansson M, Balkanski Y, Harrison S P, Prentice I C, Schulz M, Rodhe H, 1999. Dust sources and deposition during the last glacial maximum and current climate: A comparison of model results with paleodata from ice cores and marine sediments. J. Geophys. Res., 104, 15 895–15 916, doi:10.1029/1999JD900084.

Matthäus W, Franck H, 1992. Characteristics of major Baltic inflows – a statistical analysis, Cont. Shelf Res. 12, 1375–1400.

McGuffie K, Henderson-Sellers A, 2014. The climate modelling primer. John Wiley & Sons.

McKee Smith J, Sherlock A R, Resio D T, 2001. STWAVE: Steady-State Spectral Wave Model. User's manual for STWAVE, Version 3.0. Coastal and Hydraulics Laboratory U.S. Army Engineer Research and Development Center.

Meier H E M, Kauker F, 2003. Modeling decadal variability of the Baltic Sea: 2. Role of freshwater inflow and large-scale atmospheric circulation for salinity. J. Geophys. Res. 108, 3368, https://doi.org/10.1029/2003JC001799

Meier H E M, Dieterich C, Gröger M, Dutheil C, Börgel F, Safonova K, Christensen O B, Kjellström E, 2022. Oceanographic regional climate projections for the Baltic Sea until 2100, Earth Syst. Dynam. 13, 159–199.

Meinshausen M, Nicholls Z R, Lewis J, Gidden M J, Vogel E, Freund M, Beyerle U, Gessner C, Nauels A, Bauer N, Canadell J G, Daniel J S, John A, Krummel P B, Luderer G, Meinshausen N, Montzka S A, Rayner P J, Reimann S, Smith S J, van den Berg M, Velders G J M, Vollmer M K, Wang R H J, 2020. The shared socio-economic pathway (SSP) greenhouse gas concentrations and their extensions to 2500. Geoscientific Model Development 13, 3571-3605.

Mikolajewicz U, Gröger M, Maier-Reimer E, Schurgers G, Vizcaíno M, Winguth A M E, 2007. Long-term effects of anthropogenic CO_2 emissions simulated with a complex earth system model. Climate Dynamics 28, 599–633.

Milne G A, 1998. Refining models of the glacial isostatic adjustment process. PhD thesis. University of Toronto.

Milne G A, Mitrovica J X, 1998. Postglacial sea-level change on a rotating Earth. Geophysical Journal International 133, 1–19.

Milne G A, Mitrovica J X, Davis J L, 1999. Near-field hydro-isostasy: the implementation of a revised sea-level equation. Geophysical Journal International 139, 464–482.

Mitrovica J X, Hay C C, Kopp R E, Harig C, Latychev K, 2018. Quantifying the sensitivity of sea level change in coastal localities to the geometry of polar ice mass flux. Journal of Climate 31, 3701–3708.

Mohrholz V, 2018. Major Baltic Inflow Statistics – Revised, Front. Mar. Sci., 5, 280, https://doi.org/10.3389/fmars.2018.00384

Morlighem M, Seroussi H, Larour E, Rignot E, 2013. Inversion of basal friction in Antarctica using exact and incomplete adjoints of a higher-order model. Journal of Geophysical Research, Earth Surface 118, 1746–1753

Moss R H, Edmonds J A, Hibbard K A, Manning M R, Rose S K, van Vuuren D P, Carter T R, Emori S, Kainuma M, Kram T, Meehl G A, Mitchell J F B, Nakicenovic N, Riahi K, Smith S J, Stouffer R J, Thomson A M, Weyant J P, Wilbanks T J, 2010. The next generation of scenarios for climate change research and assessment. Nature 463, 747–756.

Myhre G, Highwood E J, Shine K P, Stordal F, 1998. New estimates of radiative forcing due to well mixed greenhouse gases. Geophysical Research Letters 25, 2715–2718.

NASA, 2023. National Aeronautics and Space Administration. Solar System Temperatures. Available at: https://science.nasa.gov/resource/solar-system-temperatures/ [24 Jan 2024].

National Snow and Ice Data Center, 2024. Ice sheets. Available at: https://nsidc.org/learn/partscryosphere/ice-sheets [29 Apr 2024]

NOAA, 2023. National Oceanic and Atmospheric Administration. Trends in Atmospheric Carbon Dioxide. Available at: https://gml.noaa.gov/ccgg/trends/data.html [25 July 2023].

North G R, Stevens M J, 2006. Energy-balance climate models. In Kiehl J T and Ramanathan V (eds). Frontiers of Climate Modeling. Cambridge: Cambridge University Press 52–72.

Nummelin A, Li C, Hezel P J, 2017. Connecting ocean heat transport changes from the midlatitudes to the Arctic Ocean. Geophysical Research Letters 44, 1899–1908.

Näslund J-O, Rodhe L, Fastook J L, Holmlund P, 2003. New ways of studying ice-sheet flow directions and glacial erosion by computer modelling – examples from Fennoscandia. Quaternary Science Reviews 22, 245–258.

Näslund J-O, Jansson P, Fastook J L, Johnson J, Andersson L, 2005. Detailed spatially distributed geothermal heat-flow data for modeling of basal temperatures and meltwater production beneath the Fennoscandian ice-sheet. Annals of Glaciology 40, 95–101.

Näslund J-O, Brandefelt J, Claesson Liljedahl L, 2013. Climate considerations in long-term safety assessments for nuclear waste repositories. Ambio 42, 393–401.

Oerlemans J, 1980. Model experiments on the 100,000-yr glacial cycle. Nature 287, 430-432.

Oerlemans J, 2005. Extracting a climate signal from 169 glacier records. Science 308, 675-677.

Oerlemans J, van der Veen C J, 1984. Ice sheets and climate (Vol. 21, No. 7). Dordrecht: Reidel.

Olvmo M, 2010. Review of denudation processes and quantification of weathering and erosion rates at a 0.1 to 1 Ma time scale. SKB TR-09-18, Svensk Kärnbränslehantering AB.

O'Neill B C, Tebaldi C, van Vuuren D P, Eyring V, Friedlingstein P, Hurtt G, Knutti R, Kriegler E, Lamarque J F, Lowe J, Meehl G A, Moss R, Riahi K, Sanderson B M, 2016. The Scenario Model Intercomparison Project (ScenarioMIP) for CMIP6. Geoscientific Model Development 9, 461–482.

Otto-Bliesner B L, Brady E C, Zhao A, Brierley C M, Axford Y L, Capron E, Govin A, Hoffman J S, Isaacs E, Kageyama M, Scussolini P, Tzedakis P C, Williams C J R, Wolff E, Abe-Ouchi A, Braconnot P, Ramos Buarque S, Cao J, de Vernal A, Guarino M V, Guo C, LeGrande A N, Lohmann G, Meissner K J, Menviel L, Morozova P A, Nisancioglu K H, O'ishi R, Salas y Melia D, Shi X, Sicard M, Sime L, Stepanek C, Tomas R, Volodin E, Yeung N K H, Zhang Q, Zhang Z, Zheng W, 2021. Large-scale features of Last Interglacial climate: results from evaluating the lig127k simulations for the Coupled Model Intercomparison Project (CMIP6)-Paleoclimate Modeling Intercomparison Project (PMIP4). Climate of the Past 17, 63-94.

PAGES, 2016. Interglacials of the last 800,000 years. Reviews of Geophysics 54, 162-219.

Paillard D, 1998. The timing of Pleistocene glaciations from a simple multiple-state climate model. Nature 391, 378–381.

Paillard D, 2010. Climate and the orbital parameters of the Earth. Comptes Rendus Geoscience 342, 273-285.

Pan L, Powell E M, Latychev K, Mitrovica J X, Creveling J R, Gomez N, Hoggard M J, Clark P U, 2021. Rapid postglacial rebound amplifies global sea level rise following West Antarctic Ice Sheet collapse. Science Advances 7, 1–9.

Passaro M, Müller F L, Oelsmann J, Rautiainen L, Dettmering D, Hart-Davis M G, Abulaitijiang A, Andersen O B, Høyer J L, Madsen K S, Ringgaard I M, Särkkä J, Scarrott R, Schwatke C, Seitz F, Tuomi L, Restano M, Benveniste J, 2021. Absolute Baltic Sea Level Trends in the Satellite Altimetry Era: A Revisit, Front. Mar. Sci. 8, 7, https://doi.org/10.3389/fmars.2021.647607

Patton H, Hubbard A, Andreassen K, Winsborrow M, Stroeven A P, 2016. The build-up, configuration, and dynamical sensitivity of the Eurasian ice-sheet complex to Late Weichselian climatic and oceanic forcing. Quaternary Science Reviews, 153, 97-121.

Patton H, Hubbard A, Andreassen K, Auriac A, Whitehouse P L, Stroeven A P, Shackleton C, Winsborrow M, Heyman J, Hall A M, 2017. Deglaciation of the Eurasian ice sheet complex. Quaternary Science Reviews, 169, 148-172.

Pattyn F, Ritz C, Hanna E, Asay-Davis X, DeConto R, Durand G, Favier L, Fettweis X, Goelzer H, Golledge N R, Munneke P K, Lenaerts J T M, Nowicki S, Payne A J, Robinson A, Seroussi H, Trusel L D, van den Broeke M, 2018. The Greenland and Antarctic ice sheets under 1.5 C global warming, Nature Climate Change 8, 1053–1061.

Peel M C, Finlayson B L, McMahon T A, 2007. Updated world map of the Köppen-Geiger climate classification. Hydrology and earth system sciences 11, 1633-1644.

Pellikka H, Rauhala J, Kahma K K, Stipa T, Boman H, Kangas A, 2014. Recent observations of meteotsunamis on the Finnish coast, Nat. Hazards 74, 197–215.

Pellikka H, Särkkä J, Johansson M, Pettersson H, 2020. Probability distributions for mean sea level and storm contribution up to 2100 AD at Forsmark, Sweden. SKB TR-19-23, Svensk Kärnbränslehantering AB.

Peltier W R, 2004. Global glacial isostasy and the surface of the ice-age Earth: the ICE-5G (VM2) model and GRACE. Annual Review of Earth and Planetary Science 32, 111–149.

Peltier W R, Argus D F, Drummond R, 2015. Space geodesy constrains ice age terminal deglaciation: The global ICE-6G_C (VM5a) model. Journal of Geophysical Research: Solid Earth 120, 450-487.

Pereira A R, Pruitt W O, 2004. Adaptation of the Thornthwaite scheme for estimating daily reference evapotranspiration. Agricultural Water Management 66, 251–257.

Petit J R, Jouzel J, Raynaud D, Barkov N I, Barnola J M, Basile I, Bender M, Chappellaz J, Davis M, Delaygue G, Delmotte M, Kotlyakov V M, Legrand M, Lipenkov V Y, Lorius C, Pepin L, Ritz C, Saltzman E, Stievenard M, 1999. Climate and atmospheric history of the past 420,000 years from the Vostok ice core, Antarctica. Nature 399, 429–436.

Pimenoff N, Venäläinen A, Järvinen H, 2011. Climate scenarios for Olkiluoto on a time-scale of 120,000 years. Posiva 2011-04, Posiva Oy, Finland.

Pimenoff N, Venäläinen A, Järvinen H, 2012. Climate and sea level scenarios for Olkilouto for the next 10,000 years. Posiva 2012-26, Posiva Oy, Finland.

Pollard D, 1982. A simple ice sheet model yields realistic 100 kyr glacial cycles. Nature 296, 334-338.

Porter S C, 1989. Some geological implications of average Quaternary glacial conditions. Quaternary Research 32, 245–261.

PSMSL, 2022. "Tide Gauge Data", Retrieved 1 Oct 2022 from http://www.psmsl.org/data/obtaining/.

Proudman J, 1929. The effects on the sea of changes in atmospheric pressure. Geophysical Journal International 2, 197–209.

Påsse T, 2001. An empirical model of glacio-isostatic movements and shore-level displacement in Fennoscandia. SKB R-01-41, Svensk Kärnbränslehantering AB.

Påsse T, Daniels J, 2015. Past shore-level and sea-level displacements. Uppsala: Geological Survey of Sweden. (Rapporter och meddelanden 137)

Quaas J, Jia H, Smith C, Albright A L, Aas W, Bellouin N, Boucher O, Doutriaux-Boucher M, Forster P M, Grosvenor D, Jenkins S, Klimont Z, Loeb N G, Ma X, Naik V, Paulot F, Stier P, Wild M, Myhre G, Schulz M, 2022. Robust evidence for reversal of the trend in aerosol effective climate forcing, Atmos. Chem. Phys. 22, 12221–12239.

Quiquet A, Colleoni F, Masina S, 2016. Long-term safety of a planned geological repository for spent nuclear fuel in Forsmark, Sweden and Olkiluoto, Finland. Phase 2: impact of ice-sheet dynamics, climate forcing and multi-variate sensitivity analysis on maximum ice-sheet thickness. SKB TR-16-02, Svensk Kärnbränslehantering AB.

Rahmstorf S, 2006. Thermohaline ocean circulation. Encyclopedia of quaternary sciences 5.

Rammig A, Jupp T, Thonicke K, Tietjen B, Heinke J, Ostberg S, Lucht W, Cramer W, Cox P, 2010. Estimating the risk of Amazonian forest dieback. New Phytologist 187, 694–706.

Ranganathan M, Minchew B, Meyer C R, Gudmundsson G H, 2021. A new approach to inferring basal drag and ice rheology in ice streams, with applications to West Antarctic Ice Streams. Journal of Glaciology 67, 229-242.

Reiche P, 1950. Survey of weathering processes and products. University of New Mexico publications in geology 3

Riahi K, van Vuuren D P, Kriegler E, Edmonds J, O'Neill B C, Fujimori S, Bauer N, Calvin K, Dellink R, Fricko O, Lutz W, Popp A, Cuaresma J C, KC S, Leimbach M, Jiang L, Kram T, Rao S, Emmerling J, Ebi K, Hasegawa T, Havlik P, Humpenöder F, Da Silva L A, Smith S, Stehfest E, Bosetti V, Eom J, Gernaat D, Masui T, Rogelj J, Strefler J, Drouet L, Krey V, Luderer G, Harmsen M, Takahashi K, Baumstark L, Doelman J C, Kainuma M, Klimont Z, Marangoni G, Lotze-Campen H, Obersteiner M, Tabeau A, Tavoni M, 2017. The Shared Socioeconomic Pathways and their energy, land use, and greenhouse gas emissions implications: an overview. Global Environmental Change 42, 153–168.

Ritz C, Rommelaere V, Dumas C, 2001. Modeling the evolution of Antarctic ice-sheet over the last 420000 years: Implications for altitude changes in the Vostok region. Journal of Geophysical Research 106, 31943–31964.

Robson J, Hodson D, Hawkins E, Sutton R, 2013. Atlantic overturning in decline? Nature Geosciences 7, 2–3.

Rohling E J, Hibbert F D, Williams F H, Grant K M, Marino G, Foster G L, Hennekam R, de Lange G J, Roberts A P, Yu J, Webster J M, Yokoyama Y, 2017. Differences between the last two glacial maxima and implications for ice-sheet, δ18O, and sea-level reconstructions. Quaternary Science Reviews 176, 1–28

Rudberg S, 1954. Västerbottens berggrundsmorfologi: ett försök till rekonstruktion av preglaciala erosionsgenerationer i Sverige. PhD thesis. Uppsala University. Geographica 25.

Ruddiman W F, 2001. Earth's Climate: past and future. Macmillan.

Ruddiman W F, 2013. The anthropocene. Annual Review of Earth and Planetary Sciences, 41, 45-68.

Rutgersson A, Jaagus J, Schenk F, Stendel M, 2014. Observed changes and variability of atmospheric parameters in the Baltic Sea region during the last 200 years, Clim. Res., 61, 177–190.

Samuelsson M and Stigebrandt A, 1996. Main characteristics of the long-term sea level variability in the Baltic sea, Tellus A 48, 672–683.

Schenk F, Wohlfarth B, 2019. The imprint of hemispheric-scale climate transitions on the European climate during the last deglaciation (15.5 ka to 9 ka BP). SKB TR-18-05, Svensk Kärnbränslehantering AB.

Schmidt G A, Ruedy R A, Miller R L, Lacis A A, 2010. Attribution of the present-day total greenhouse effect. Journal of Geophysical Research: Atmospheres, 115(D20).

Schäfer M, Zwinger T, Christoffersen P, Gillet-Chaulet F, Laakso K, Pettersson R, Pohjola V A, Strozzi T, Moore J C, 2012. Sensitivity of basal conditions in an inverse model: Vestfonna ice cap, Nordaustlandet/Svalbard. The Cryosphere 6, 771–783

Selby M J, 1993. Hillslope materials and processes. 2nd ed. Oxford: Oxford University Press.

Seneviratne S I, Zhang X, Adnan M, Badi W, Dereczynski C, Di Luca A, Ghosh S, Iskandar I, Kossin J, Lewis S, Otto F, Pinto I, Satoh M, Vicente-Serrano S M, Wehner M, Zhou B, 2021. Weather and Climate Extreme Events in a Changing Climate. In Climate Change 2021: The Physical Science Basis. Contribution of Working Group I to the Sixth Assessment Report of the Intergovernmental Panel on Climate Change. Cambridge University Press, Cambridge, United Kingdom and New York, NY, USA, pp. 1513–1766, doi:10.1017/9781009157896.013.

Serreze M C, Barry R G, 2011. Processes and impacts of Arctic amplification: A research synthesis. Global and Planetary Change 77, 85–96.

SKB TR-06-23. SKB 2006. Climate and climate-related issues for the safety assessment SR-Can. Svensk Kärnbränslehantering AB.

SKB TR-10-09. SKB 2010. Biosphere assessment of SR-Site Forsmark – synthesis and summary of results. Svensk Kärnbränslehantering AB.

SKB TR-10-49. SKB 2010. Climate and climate-related issues for the safety assessment SR-Site. Svensk Kärnbränslehantering AB.

SKB TR-11-01. SKB 2011. Long-term safety for the final repository for spent nuclear fuel at Forsmark. Main report of the SR-Site project. Svensk Kärnbränslehantering AB.

SKB TR-13-05. SKB 2014. Climate and climate-related issues for the safety assessment SR-PSU. Svensk Kärnbränslehantering AB.

SKB TR-14-01. SKB 2015. Safety analysis for SFR. Long-term safety. Main report for the safety assessment SR-PSU. Revised edition. Svensk Kärnbränslehantering AB.

SKB TR-19-04. SKB 2019. Climate and climate-related issues for the safety evaluation SE-SFL. Svensk Kärnbränslehantering AB.

SKB TR-20-12. SKB 2020. Post-closure safety for the final repository for spent nuclear fuel at Forsmark. Climate and climate-related issues, PSAR version. Svensk Kärnbränslehantering AB.

SKB TR-21-01. SKB 2022. Post-closure safety for the final repository for spent nuclear fuel at Forsmark. Main report, PSAR version. Svensk Kärnbränslehantering AB.

SKB TR-21-04. SKB 2022. Post-closure safety for the final repository for spent nuclear fuel at Forsmark – Geosphere process report, PSAR version. Svensk Kärnbränslehantering AB.

SKB TR-23-01. SKB 2023. Post-closure safety for SFR, the final repository for short-lived radioactive waste at Forsmark. Main report, PSAR version. SKB TR-23-01, Svensk Kärnbränslehantering AB.

SKB TR-23-05. SKB 2023. Post-closure safety for SFR, the final repository for short-lived sradioactive waste at Forsmark. Climate and climate-related issues, PSAR version. SKB TR-23-05, Svensk Kärnbränslehantering AB.

SKB TR-23-06. SKB 2023. Post-closure safety for SFR, the final repository for short-lived radioactive waste at Forsmark. Biosphere synthesis report, PSAR version. Svensk Kärnbränslehantering AB.

SKB TR-23-09. SKB 2023. Post-closure safety for SFR, the final repository for short-lived radioactive waste at Forsmark. Radionuclide transport and dose calculations, PSAR version. SKB TR-23-09, Svensk Kärnbränslehantering AB.

Smeed D A, McCarthy G D, Cunningham S A, Frajka-Williams E, Rayner D, Johns W E, Meinen C S, Baringer M O, Moat B I, Duchez A, Bryden H L, 2014. Observed decline of the Atlantic meridional overturning circulation 2004–2012. Ocean Sci. 10, 29–38.

Smeed D A, Josey S A, Beaulieu C, Johns W E, Moat B I, Frajka-Williams E, McCarthy G D, 2018. The North Atlantic Ocean is in a state of reduced overturning. Geophysical Research Letters 45, 1527–1533.

SMHI 2014. Air pressure and sea level. Available at: https://www.smhi.se/en/theme/air-pressure-and-sea-level-1.12266

SMHI, 2022. Climate indicator – Length of the vegetation period. Available at: https://www.smhi.se/en/climate/climate-indicators/climate-indicators-length-of-vegetation-period-1.91482

Smith C, Nicholls Z R J, Armour K, Collins W, Forster P, Meinshausen M, Palmer M D, Watanabe M, 2021. The Earth's Energy Budget, Climate Feedbacks, and Climate Sensitivity Supplementary Material. In Climate Change 2021: The Physical Science Basis. Contribution of Working Group I to the Sixth Assessment Report of the Intergovernmental Panel on Climate Change. Available from https://www.ipcc.ch/.

Snyder C W, 2016. Evolution of global temperature over the past two million years. Nature 538, 226-228.

Spada, G, Olivieri M, Galassi G, 2014. Anomalous secular sea-level acceleration in the Baltic Sea caused by isostatic adjustment. Annals of Geophysics 57, S0432-S0432.

SSMFS 2008:21. Strålsäkerhetsmyndighetens föreskrifter och allmänna råd om säkerhet vid slutförvaring av kärnämne och kärnavfall (Regulations concerning safety in connection with the disposal of nuclear material and nuclear waste). Stockholm: Swedish Radiation Safety Authority. (In Swedish.)

SSMFS 2008:37. Strålsäkerhetsmyndighetens föreskrifter och allmänna råd om skydd av människors hälsa och miljön vid slutligt omhänder-tagande av använt kärnbränsle och kärnavfall (Regulations on the protection of human health and the environment in connection with the final management of spent nuclear fuel and nuclear waste). Stockholm: Swedish Radiation Safety Authority. (In Swedish.)

Staiger J K W, Gosse J C, Johnson J V, Fastook J, Gray J T, Stockli D F, Stockli L, Finkel R, 2005. Quaternary relief generation by polythermal glacier ice. Earth Surface Processes and Landforms 30, 1145–1159.

Stroeven A P, Fabel D, Hättestrand C, Harbor J, 2002. A relict landscape in the centre of Fennoscandian glaciation: cosmogenic radionuclide evidence of tors preserved through multiple glacial cycles. Geomorphology 44, 145–154.

Stroeven A P, Hättestrand C, Kleman J, Heyman J, Fabel D, Fredin O, Goodfellow B W, Harbor J M, Jansen J D, Olsen L, Caffee M W, Fink D, Lundqvist J, Rosqvist G C, Strömberg B, Jansson K N, 2016. Deglaciation of Fennoscandia. Quaternary Science Reviews 147, 91–121.

Sugden D E, 1977. Reconstruction of the morphology, dynamics and thermal characteristics of the Laurentide ice-sheet at its maximum. Arctic and Alpine Research 9, 27–47.

Sugden D E, 1978. Glacial erosion by the Laurentide ice-sheet. Journal of Glaciology 20, 367–391.

Sugden D E, John B S, 1976. Glaciers and landscape: a geomorphological approach. London: Arnold.

Sugden D E, Hall A M, Phillips W M, Stewart M A, 2019. Plucking enhanced beneath ice sheet margins: evidence from the Grampian Mountains, Scotland. Geografiska Annaler: Series A, Physical Geography 101, 34–44.

Sundberg J, 1988. Thermal properties of soils and rocks. PhD thesis. Chalmers University of Technology, Sweden. (Geologiska institutionen publ. A 57)

Sundberg J, Back P-E, Ländell M, Sundberg A, 2009. Modelling of temperature in deep boreholes and evaluation of geothermal heat flow at Forsmark and Laxemar. SKB TR-09-14, Svensk Kärnbränslehantering AB.

Svendsen J I, Alexanderson H, Astakhov V I, Demidov I, Dowdeswell J A, Funder S, Gataullin V, Henriksen M, Hjort C, Houmark-Nielsen M, Hubberten H W, Ingólfsson O, Jakobsson M, Kjær K H, Larsen E, Lokrantz H, Lunkka J P, Lyså A, Mangerud J, Matiouchkov A, Murray A, Moller P, Niessen F, Nikolskaya O, Polyak L, Saarnisto M, Siegert C, Siegert M J, Spielhagen R F, Stein R, 2004. Late Quaternary ice-sheet history of northern Eurasia. Quaternary Science Reviews 23, 1229–1271.

Swantesson J O H, 1992. Recent micro-weathering phenomena in southern and central Sweden. Permafrost and Periglacial Processes 3, 275–292.

Södling J, Nerheim S, 2017. Statistisk metodik för beräkning av extrema havsvattenstånd, Oceanografi 124, SMHI. Available at: https://www.smhi.se/polopoly_fs/1.165622!/Oceanografi_124%20Statistisk%20metodik%20f%C3%B6r%20ber%C3%A4kning%20av%20extrema%20havsvattenst%C3%A5nd.pdf

Talento S, Ganopolski A, 2021. Reduced-complexity model for the impact of anthropogenic CO2 emissions on future glacial cycles. Earth System Dynamics 12, 1275-1293.

The IMBIE Team, 2021. Antarctic and Greenland Ice Sheet mass balance 1992–2020 for IPCC AR6 (Version 1.0) [Data set]. UK Polar Data Centre, Natural Environment Research Council, UK Research & Innovation, doi:10.5285/77B64C55-7166-4A06-9DEF-2E400398E452.

Thomas M F, 1994. Geomorphology in the tropics: a study of weathering and denudation in low latitudes. Chichester: Wiley.

Thomas M D, Fedorov A V, 2019. Mechanisms and impacts of a partial AMOC recovery under enhanced freshwater forcing. Geophysical Research Letters 46, 3308-3316.

Thornthwaite C W, 1948. An approach toward a rational classification of climate. Geographical Review 38, 55–94.

Thölix L, Korhonen H, Ruosteenoja K, 2019. Climate projections for Olkiluoto. Technical report 2018-09, Posiva Oy.

Tian H, Xu R, Canadell J G, Thompson R L, Winiwarter W, Suntharalingam P, Davidson E A, Ciais P, Jackson R B, Janssens-Maenhout G, Prather M J, Regnier P, Pan N, Pan S, Peters G P, Shi H, Tubiello F N, Zaehle S, Zhou F, Arneth A, Battaglia G, Berthet S, Bopp L, Bouwman A F, Buitenhuis E T, Chang J, Chipperfield M P, Dangal S R S, Dlugokencky E, Elkins J W, Eyre B D, Fu B, Hall B, Ito A, Joos F, Krummel P B, Landolfi A, Laruelle G G, Lauerwald R, Li W, Lienert S, Maavara T, MacLeod M, Millet D B, Olin S, Patra P K, Prinn R G, Raymond P A, Ruiz D J, van der Werf G R, Vuichard N, Wang J, Weiss R F, Wells K C, Wilson C, Yang J, Yao Y, 2020. A comprehensive quantification of global nitrous oxide sources and sinks, Nature 586, 248–256.

Turney C S, Jones R T, McKay N P, Van Sebille E, Thomas Z A, Hillenbrand C D, Fogwill C J, 2020. A global mean sea surface temperature dataset for the Last Interglacial (129–116 ka) and contribution of thermal expansion to sea level change. Earth System Science Data 12, 3341-3356.

Tylmann K, Rinterknecht V R, Woźniak P P, Guillou V, ASTER Team, 2022. Asynchronous dynamics of the last Scandinavian Ice Sheet along the Pomeranian ice-marginal belt: A new scenario inferred from surface exposure 10Be dating. Quaternary Science Reviews 294, 107755.

Tzedakis P C, Channell J E T, Hodell D A, Kleiven H F, Skinner L C, 2012. Determining the natural length of the current interglacial. Nature Geoscience 5, 138-141.

UNFCCC, 2015. United Nations Framework Convention on Climate Change. Adoption of the Paris Agreement. Conference of the Parties, Twenty-first session, Paris, 30 November – 11 December 2015. Paris: United Nations.

UNEP-CCAC, 2022. United Nations Environment Programme/Climate and Clean Air Coalition. Global Methane Assessment: 2030 Baseline Report. Nairobi.

Van Breedam J, Goelzer H, Huybrechts P, 2020. Semi-equilibrated global sea-level change projections for the next 10 000 years. Earth System Dynamics 11, 953-976.

van de Wal R S W, Nicholls R J, Behar D, McInnes K, Stammer D, Lowe J A, Church J A, DeConto R, Fettweis X, Goelzer H, Haasnoot M, Haigh I D, Hinkel J, Horton B P, James T S, Jenkins A, LeCozannet G, Levermann A, Lipscomb W H, Marzeion B, Pattyn F, Payne A J, Pfeffer W T, Price S F, Seroussi H, Sun S, Veatch W, White K, 2022. A High-End Estimate of Sea Level Rise for Practitioners, Earth's Future, 10, e2022EF002 751, https://doi.org/https://doi.org/10.1029/2022EF002751

van der Veen, C J, 2013. Fundamentals of glacier dynamics. CRC press.

van Vuuren D P, Edmonds J, Kainuma M L T, Riahi K, Thomson A, Hibbard K, Hurtt G C, Kram T, Krey V, Masui T, Lamarque J-F, Meinshausen M, Nakicenovic N, Smith S J, Rose S K, 2011. Representative concentration pathways: An overview. Climatic Change 109, 5. doi:10.1007/s10584-011-0148-z

Vandenberghe J, 2008. The fluvial cycle at cold–warm–cold transitions in lowland regions: a refinement of theory. Geomorphology 98, 275-284.

Vellinga M, Wood R A, 2002. Global climatic impacts of a collapse of the Atlantic thermohaline circulation. Climatic change 54, 251-267.

Vellinga M, Wood R A, 2008. Impacts of thermohaline circulation shutdown in the twenty-first century. Climatic Change 91, 43-63.

Vestøl O, Ågren J, Steffen H, Kierulf H, Tarasov L, 2019. NKG2016LU: a new land uplift model for Fennoscandia and the Baltic Region. Journal of Geodesy 93, 1759–1779.

Vidstrand P, Follin S, Zugec N, 2010. Groundwater flow modelling of periods with periglacial and glacial conditions – SR-Site Forsmark. SKB R-09-21, Svensk Kärnbränslehantering AB.

Vikberg E, Thunholm B, Thorsbrink M, Dahné J, 2015. Grundvattennivåer i ett förändrat klimat – nya klimatscenarier. SGU-rapport 2015:19, Sveriges Geologiska Undersökning.

Waelbroeck C, Labeyrie L, Michel E, Duplessy J C, McManus J, Lambeck K, Balbon E, Labracherie M, 2002. Sea-level and deep water temperature changes derived from benthic foraminifera isotopic records, Quaternary Sci. Rev. 21, 295–305.

Wang S, Foster A, Lenz E A, Kessler J D, Stroeve J C, Anderson L O, Turetsky M, Betts R, Zou S, Liu W, Boos W R, Hausfather Z, 2023. Mechanisms and impacts of Earth system tipping elements. Reviews of Geophysics 61, e2021RG000757.

Washburn A L, 1979. Geocryology: a survey of periglacial processes and environments. 2nd ed. London: Arnold.

Watanabe Y, Abe-Ouchi A, Saito F, Kino K, O'ishi R, Ito T, Kawamura K, Chan W-L, 2023. Astronomical forcing shaped the timing of early Pleistocene glacial cycles, Communications Earth & Environment 4.

Weertman J, 1976. Milankovitch solar radiation variations and ice age ice sheet sizes. Nature 261, 17–20.

Weisse R, Dailidienė I, Hünicke B, Kahma K, Madsen K, Omstedt A, Parnell K, Schöne T, Soomere T, Zhang W, and Zorita E, 2021. Sea level dynamics and coastal erosion in the Baltic Sea region, Earth System Dynamics 12, 871–898.

Werner K, Norville J, Öhman J, 2014. Meteorological, hydrological and hydrogeological monitoring data from Forsmark – compilation and analysis for the SR-PSU project. SR-PSU Biosphere. SKB R-13-20, Svensk Kärnbränslehantering AB.

Whitehouse P, 2009. Glacial isostatic adjustment and sea-level change. State of the art report. SKB TR-09-11, Svensk Kärnbränslehantering AB.

Willeit M, Ganopolski A, 2018. The importance of snow albedo for ice sheet evolution over the last glacial cycle. Climate of the Past 14, 697-707.

Williams P J, Smith M W, 1989. The frozen earth: fundamentals of geocryology. Cambridge: Cambridge University Press.

Williams C J R, Lunt D J, Kennedy-Asser A T, Lord N S, 2022. Uncertainties in modelled climate changes at Forsmark over the next 1 million years. SKB TR-22-02, Svensk Kärnbränslehantering AB.

Willmott C J, Rowe C M, Mintz Y, 1985. Climatology of the terrestrial seasonal water cycle. Journal of Climatology 5, 589–606.

Winsor P, Rodhe J, Omstedt A, 2001. Baltic Sea ocean climate: An analysis of 100 yr of hydrographic data with focus on the freshwater budget, Clim. Res. 18, 5–15.

Wise M G, Dowdeswell J A, Jakobsson M, Larter R D, 2017. Evidence of marine ice-cliff instability in Pine Island Bay from iceberg-keel plough marks, Nature 550, 506-510.

Wohlfarth B, 2009. Ice-free conditions in Fennoscandia during Marine Oxygen Isotope Stage 3? SKB TR-09-12, Svensk Kärnbränslehantering AB.

Wohlfarth B, 2013. A review of Early Weichselian climate (MIS 5d–a) in Europe. SKB TR-13-03, Svensk Kärnbränslehantering AB.

Wolski T, Wisniewski B, 2020. Geographical diversity in the occurrence of extreme sea levels on the coasts of the Baltic Sea, J. Sea Res., 159, 101890, https://doi.org/10.1016/j.seares.2020.101890

Wübber C, Krauss W, 1979. The two dimensional seiches of the Baltic Sea, Oceanol. Acta 2, 435–446.

Yershov E D, 1998. General Geocryology. Cambridge: Cambridge University Press.

Young N E, Briner J P, Miller G H, Lesnek A J, Crump S E, Thomas E K, Pendleton S L, Cuzzone J, Lamp J, Zimmerman S, Caffee M, Schaefer J M, 2020. Deglaciation of the Greenland and Laurentide ice sheets interrupted by glacier advance during abrupt coolings. Quaternary Science Reviews 229, 106091.

Zickfeld K, Eby M, Weaver A J, 2008. Carbon-cycle feedbacks of changes in the Atlantic meridional overturning circulation under future atmospheric CO2. Global Biogeochemical Cycles 22.

Zickfeld K, Eby M, Weaver A J, Alexander K, Crespin E, Edwards N R, Eliseev A V, Feulner G, Fichefet T, Forest C E, Friedlingstein P, Goosse H, Holden P B, Joos F, Kawamiya M, Kicklighter D, Kienert H, Matsumoto K, Mokhov I I, Monier E, Olsen S M, Pedersen J O P, Perrette M, Philippon-Berthier G, Ridgwell A, Schlosser A, Schneider Von Deimling T, Shaffer G, Sokolov A, Spahni R, Steinacher M, Tachiiri K, Tokos K S, Yoshimori M, Zeng N, Zhao F, 2013. Long-term climate change commitment and reversibility: An EMIC intercomparison. Journal of Climate 26, 5782–5809.

Appendix A – Supplementary information to Chapter 3 Climate evolution

A1 Possibility and potential consequence of an AMOC collapse

In this appendix, the possibility and potential consequence at Forsmark of an AMOC collapse is discussed. These issues add to the uncertainty in the climate evolution during operational and early post-closure phase of SKB's repositories.

In the analysis of climate change until 2100 AD (Section 3.5.1), it was concluded that projected warming in northern Europe is slightly lower than other land regions of comparable latitude, and that this reduced warming is a consequence of a projected AMOC weakening in the CMIP6 models. However, it is highly uncertain how much AMOC will decrease in response to anthropogenic warming. This uncertainty is, for example, reflected by a wide range of projected AMOC weakenings across CMIP6 models (Bellomo et al. 2021). Thus, it is possible that AMOC will weaken more, or less, than the average across the CMIP6 models. In addition, it cannot be excluded that the AMOC will undergo a complete collapse, i.e. that the circulation strength diminishes to almost zero over a relatively short period of time, as a result of the increased flux of freshwater to the North Atlantic surface waters from higher precipitation and melting of the Greenland ice sheet (Section 3.2.4). It is unclear how much freshwater is required to induce a complete collapse, but a greater likelihood of such an event is expected as the freshwater forcing increases (e.g. Wang et al. 2023). Thus, the likelihood of a collapse is expected to increase with each degree of warming. As the threshold for an AMOC collapse is unknown, it is also unclear when such an event might occur. Whilst the overall assessment by the IPCC AR6 is that a collapse of the AMOC will not occur before 2100 AD under any SSP scenario, recent studies have raised concerns that an AMOC collapse can be induced by smaller freshwater forcing than previously anticipated, such that it may occur within the next few decades under business-as-usual emissions (corresponding to SSP2-4.5) (Lohmann and Ditlevsen 2021, Ditlevsen and Ditlevsen 2023).

The largest cooling following a collapse would occur in the North Atlantic region. Based on back-of-the-envelope calculations of SAT decreases due to heat loss to high latitudes in the North Atlantic, it is estimated that the maximum cooling in the North Atlantic region would be about 5 °C, resulting in sea surface temperatures similar to those in the Pacific region at comparable latitudes (Rahmstorf 2006). This cooling may further be reinforced by increased sea-ice cover in the area (Rahmstorf 2006) and/or mitigated by changes in the atmospheric circulation (Jackson et al. 2015). In sum, AMOC-impact studies suggest that the maximum average cooling in the North Atlantic region is in the range of 3–8 °C following a collapse (Wang et al. 2023 and references therein). Studies have also demonstrated that the cooling signal in the North Atlantic will gradually decline towards the east; however, the rate of this decline varies between the studies. Whilst a limited number of studies suggest that the cooling in the Forsmark region resulting from an AMOC collapse could be as high as 5–6 °C (Vellinga and Wood 2008, Jackson et al. 2015), the majority of these studies project a reduced cooling, ranging from 2 °C or lower (Vellinga and Wood 2002, Jacob et al. 2005, Kuhlbrodt et al. 2009, Laurian et al. 2010) to 3–4 °C (Mikolajewicz et al. 2007, Zickfeld et al. 2008, Pimenoff et al. 2012, Liu et al. 2017). Thus, the overall assessment is that an AMOC collapse would cool the Forsmark climate by 2–6 °C relative to the pre-industrial climate, which featured a stable AMOC unaffected by anthropogenic forcing.

The Forsmark SAT under the assumption of an AMOC collapse can be estimated using the 2–6 °C cooling range together with the present-day Forsmark SAT (Table 3-2) and future SAT projections for Forsmark until 2100 AD under the SSP2-4.5, SSP3-7.0 and SSP5-8.5 scenarios. Since the 2–6 °C cooling range is defined relative to an unchanged AMOC, it is important that the SAT projections until 2100 AD do not include the effect of a weakened AMOC. To estimate the anthropogenic warming at Forsmark in absence of a weakened AMOC, it is assumed that the warming in the region is 1.5 times the global mean (median estimate from the climate emulator, see Table 3-6), as opposed to 1.1–1.2 found in the CMIP6 models (Section 3.5.1). The factor 1.5 approximately corresponds to the average warming-amplification at 60ºN across the CMIP6 models (Nummelin et al. 2017).

The resulting estimated Forsmark SAT after a potential AMOC collapse is shown in Table A-1. The mid-century (2061–2080) SAT at Forsmark following an AMOC collapse is relatively similar among the scenarios due to the small difference in mid-century warming between them (cf. Table 3-6). Specifically, if the AMOC were to undergo a mid-century collapse, the resulting Forsmark SAT is estimated to be 2–6 °C under SSP2-4.5 to 3–7 °C under SSP5-8.5 (Table A-1). For a late-century (2081-2100) collapse, larger differences between the emission scenarios are projected. Under the SSP2-4.5 scenario, the projected SAT at Forsmark following a late-century collapse is 3–7 °C (Table A-1). Under the SSP3-7.0 and SSP5-8.5 scenarios, the lowest possible SAT at Forsmark following a late-century collapse is similar to the pre-industrial (~5 °C) and present-day (~6.5 °C) SAT in the region, respectively. If the cooling induced by the collapsed AMOC is less pronounced, however, the SAT in these scenarios will be several degrees higher than at present towards the end of the century (Table A-1).

If the threshold for an AMOC collapse would be as high as assessed by IPCC AR6 (Fox-Kemper et al. 2021), i.e. that a collapse of the AMOC can only occur after 2100 AD, the resulting Forsmark SAT would be higher than that featured in Table A-1. This is because the warming at Forsmark is expected to continue after 2100 AD under all the investigated scenarios (Section 3.5.2).

It is important to note that the lowest estimated SAT presented in Table A-1 should be regarded as unlikely bounding cases rather than probable outcomes. These low-end estimates correspond to the largest possible cooling contributions and to a mid-century AMOC collapse, none of which conform to the overall consensus in the scientific literature. For example, most studies suggest that the impact of an AMOC collapse on the Forsmark SAT is less than 4 °C rather than the 6 °C that was assumed in the coldest estimates. If these studies are correct, pre-industrial or higher SAT can be expected at Forsmark, regardless of emission scenario.

It should also be noted that an anthropogenically-induced collapse of the AMOC is expected to have a relatively short duration, especially when considering the long timescales relevant to post-closure safety. The overall assessment in the scientific literature is that the AMOC will recover, at least partially, over centennial to millennial timescales following a strong weakening or a collapse (Jackson 2013, Zickfeld et al. 2013, Bakker et al. 2016, Haskins et al. 2019, Thomas and Fedorov 2019). The only exception found in the literature concerns scenarios with strong GHG forcing comparable to SSP5-8.5, under which the AMOC may remain in a persistent state during the time covered in the modelling (up to 1000 years) (Zickfeld et al. 2013, Bakker et al. 2016, Thomas and Fedorov 2019). Under those high emission scenarios, however, the GHG-induced warming at Forsmark is expected to exceed the cooling due to an AMOC collapse by several degrees, especially after 2100 AD.

Table A-1. Estimated Forsmark SAT after an AMOC collapse within this century

	Forsmark SAT due to a collapsed AMOC (ºC)	
Scenario	**2061–2080**	**2081–2100**
SSP2-4.5	2–6	3–7
SSP3-7.0	3–7	5–9
SSP5-8.5	3–7	6–10

A2 Methodology for estimating Forsmark SAT change over the next millennia: updates since PSAR SFR

The calculations of Forsmark SAT over multi-millennial timescales (Section 3.5.2) have undergone several updates in the present report compared to the analysis in the PSAR SFR climate report (SKB TR-23-05, Appendix B). In this appendix, these updates are motivated and described in detail.

In PSAR SFR, changes in the global-mean SAT over the next 10 000 years under different emission scenarios were estimated based on several parameters, namely (i) the projected SAT changes by 2100 AD, (ii) the maximum SAT increase within the next 10 000 years, (iii) the timing of the maximum SAT increase, and (iv) the SAT increase after 10 000 years. Uncertainty intervals of each of these parameters were defined based on predominately a literature review of recent multi-millennial climate change projections.

Three scenarios were considered representing low, medium and high emissions, labelled as RCP2.6, RCP4.5 and RCP8.5 in the report. Each scenario encompassed a certain range of future emissions, with RCP2.6 corresponding to <1000 Pg C, RCP4.5 to 1250–2500 Pg C and RCP8.5 to >5000 Pg C. The parameters describing the global-mean SAT evolution in PSAR SFR were thereafter converted to Forsmark conditions by the multiplication of a factor representing Arctic amplification.

Two major drawbacks related to the methodology of estimating future SAT in PSAR SFR have been identified; these are described in the following.

1. In PSAR SFR, the global-mean SAT increase was estimated based on results from several climate modelling studies, without any evaluation of, or discussion about, the climate sensitivity in each of the models. As a result, the projected SAT increase was never evaluated, or sense-checked, against the ECS estimated by the IPCC at the time, which is generally more well-constrained than results from individual models. This approach introduced a bias in the global-mean SAT increase as compared to the best estimate and likely ranges of ECS.
2. Representing each scenario by "emission ranges" was problematic for two reasons. First, this approach made it much more difficult to disentangle and evaluate the impact of different uncertainty sources on the future SAT change. For example, by using emission ranges, uncertainty in future emissions was included in the uncertainty intervals within each scenario (together with the uncertainty in climate sensitivity), in addition to being represented by the different (low, medium and high) scenarios. Second, the employment of the emission ranges also entailed that the scenarios representing low, medium and high emissions were somewhat inaccurately labelled as "RCP2.6", "RCP4.5" and "RCP8.5", respectively. The labelling of medium emissions (1250–2500 Pg C) as RCP4.5 was particularly confusing; according to the cumulative future emissions estimated for the SSP scenarios (Table 2-2), medium emissions (RCP4.5) in PSAR SFR represents the range between SSP2-4.5 and SSP3-7.0, and thus SAT increases due to actual RCP4.5 emissions were only represented by the lower range of SAT curve constructed for RCP4.5 in PSAR SFR. A potential reason for the mismatch in the labelling is that in some of the extended RCP scenarios, in contrast to the SSP scenarios (Section 2.5.1), did not reach net-zero emissions and, thus, no closure of the carbon budgets was achieved in the scenarios. Thus, in contrast to the SSP scenarios, calculating cumulative emissions from the RCP scenarios was not a straightforward task.

In light of these drawbacks with the previous methodology, the calculation of Forsmark SAT over the next millennia is updated for the present report. First, consistency with the most recent ECS estimates is ensured by that the projected global-mean SAT increase in the present report is calculated directly from the IPCC-estimated ECS ranges (Section 3.2.1) instead of relying on a literature review of multi-millennial climate change modelling projections. Second, the projected SAT change for each scenario is in the present report calculated based on the cumulative emissions provided by each SSP scenario (Table 2-2) rather than by emission ranges. This change is implemented to clarify the impact of the different uncertainty sources on the future SAT change, because it entails that the uncertainty in future emissions are provided by the different scenarios, whereas the uncertainty within each scenario represent that of the climate sensitivity.

Taken together, the updated methodology in the present report implies that the calculation of SAT is simplified and more straightforward as compared to PSAR SFR. A potential limitation of the updated methodology, in contrast to that of PSAR SFR, is that the timing of peak warming for different emission scenarios is not specifically evaluated. This is however considered to be an adequate simplification, as the exact timing of the peak warming is not of importance for post-closure safety. This is however considered to be an adequate simplification. To take the uncertainty in the exact timing of peak warming into account in the post-closure safety assessment, potential effects of the warming are evaluated assuming that peak warming persist during the entire assessment period (see e.g. SKB TR-23-06, Section 10.2.1).

A3 Effect of Greenland and Antarctic ice sheets on the global-mean SAT

The ECS is used as basis in the calculations of the global-mean and Forsmark SAT changes over the next millennia (Section 3.5.2). When establishing best-estimate as well as the likely and very likely ranges of ECS is that the Earth's ice sheets will remain the same as at present (Section 3.2.1). In the calculations of future SAT changes, it was assumed that the potential effect of growing/receding ice sheets on the climate is significantly smaller than that of the anthropogenic CO_2 forcing, and thus this effect was omitted in the SAT calculations. However, in light of the projected large disintegrations of the Antarctic and Greenland ice sheets under the SSP3-7.0 and SSP5-8.5 scenarios (Sections 3.5.2 and 5.5.2), it is important to quantify the effect of this simplification on the multi-millennial SAT projections.

In the calculations provided here, it is for simplicity assumed that the Greenland and Antarctic ice sheets have disappeared completely. If this were to occur, the magnitude of SAT increase (relative to present) would be the greatest over the areas that were previously covered by the ice sheets due to a lower local albedo and reduced surface elevation (e.g. Oerlemans and van der Veen 1984). Although the global-mean SAT will also increase in response to such event (due to a global-average increase of the planetary albedo), the regional SAT changes would be highly dependent on the ensuing changes in the atmosphere and ocean circulation. For example, it is reasonable to believe that a complete disintegration of the Greenland ice sheet would result in a complete collapse of the AMOC (Section 3.2.4) and, thus, at least temporarily, to lower SAT increases in northern Europe than for other regions (Appendix A1). However, in absence of regional climate projections after a potential recovery of such collapse, it is for simplicity assumed that the northern European SAT change in response to a complete disappearance of Earth's ice sheet will be similar to the global-mean SAT change.

The global-mean SAT is calculated using the zero-dimensional EBM (Equation 3-2). Following the methodology in Donohoe and Battisti (2011), the planetary albedo, α_p, can be described as the sum of the albedo contributions from the atmosphere and the surface ($\alpha_p = \alpha_{p,atmos} + \alpha_{p,surf}$), where:

$$\alpha_{p,atmos} = R$$

$$\alpha_{p,surf} = \alpha_s \frac{(1 - R - A)^2}{1 - \alpha_s R} \qquad \text{Equation A-1}$$

The atmospheric contribution to planetary albedo is defined as the percentage of reflection of solar radiation in the atmosphere (R), whereas the surface contribution to the planetary albedo depends on the surface reflection, or surface albedo (α_s), as well as on the atmospheric attenuation of the surface albedo (described by the factor $(1 - R - A)^2/(1 - \alpha_s R)$, where A is the percentage solar radiation absorbed in the atmosphere). Inserting values representative for the present-day global-mean conditions (α_s= 0.12, R = 0.26, A = 0.2; see Donohoe and Battisti 2011), yields $\alpha_p \approx 0.30$, with the surface contribution amounting to only 13 % of the planetary albedo ($\alpha_{p,surf}$= 0.04) due to the atmospheric attenuation. Substituting α_p into Equation 3-2, together with present-day estimates of the solar constant (S = 1360 W m^{-2}) and the effective emissivity (ε = 0.6) (see Section 3.2.1), yields an estimate of the global mean SAT of 16.2 °C.

To estimate the impact of the Greenland and Antarctic ice sheets on the global-mean SAT, it is here assumed that the present-day surface albedo over the Greenland and Antarctic ice sheets is 0.8, and that it would be 0.1 if the ice sheets disappeared. Taking the total land area covered by ice sheets in relation to Earth's area into account, it is estimated that the global-mean α_s would decrease to 0.10 as consequence of removing the ice sheets. Assuming for simplicity that global-mean R and A are not affected by the removal of the ice sheets, α_p decreases to ~0.29 and the global-mean SAT increases to 16.9 °C, thus only 0.7 °C above the present-day estimate.

The relatively modest effect on the planetary albedo and, consequently, the global-mean SAT of disappearance of the Greenland and Antarctic ice sheets can be explained by a significant atmospheric attenuation of the surface albedo. In other words, a relatively large portion of the incoming solar radiation will be reflected or absorbed through the atmosphere (both the downward and upward fluxes), such that only a small fraction is affected directly by the surface reflection. It is possible that atmospheric reflection and absorption could also change in response to disappearance of the ice sheets, e.g. due to changes in cloudiness and its spatial distribution. However, these changes and their possible impacts on the planetary albedo are difficult to constrain, in particular because contemporary models exhibit widely different responses in cloudiness to climate change (e.g. Donohoe and Battisti 2011). Therefore, the potential influence on the atmospheric reflection and absorption due to the disappearance is not account for in the present analysis.

In summary, the estimated impact on the global-mean SAT of the removal of Earth's ice sheets is substantially lower (about one order of magnitude) than the global-mean SAT increase under the highest emissions scenarios (which are the scenarios that could possibly result in a disappearance of all ice sheets). Thus, neglecting this effect in the calculation of future Forsmark SAT over the next millennia (Section 3.5.2) is considered to be a reasonable simplification.

A4 Identification of climate analogues

Climate analogues are regions with present-day conditions similar to the future projected SAT and precipitation at Forsmark. In addition to providing a broader context for the projected warming at Forsmark, climate analogues can also facilitate obtaining relevant data for parameterising the effect of a warmer climate on the surface systems in the safety assessments. An example of such data is irrigation demands of crops. As irrigation is primarily a summer phenomenon, the climate analogues are only computed for the summer season (JJA). Climate analogues for the Laxemar region in Kalmar County were introduced in the safety evaluation SE-SFL (SKB TR-19-04, Appendix C). In this report, analogues for Forsmark are calculated using a near-identical methodology to that in SE-SFL.

As the effect of future climate evolution on the surface systems is not relevant when the Forsmark area is submerged by the sea (Section 3.5.2), the climate analogues are calculated for the highest projected SAT at Forsmark when terrestrial conditions are possible. This is projected to occur around 2100 AD for SSP1-2.6, 2500 AD for SSP2-4.5, 7000 AD for SSP3-7.0 and 12 000 AD for SSP5-8.5 (Tables 3-4 and 3-10). The difference in projected SAT increase between the seasons is relatively modest (Table 3-7), and thus the projected annual-mean SAT increase in Tables 3-4 and 3-10 are considered to be representative also for the summer season. Precipitation in the summer season may either increase or decrease in response to anthropogenic warming; however, the median estimate is that it will remain the same as at present (Table 3-8).

To identify the climate analogues, the CRU TS 4.07 monthly gridded (0.5° × 0.5°) global land dataset from the Climate Research Unit (CRU) at the University of East Anglia (Harris et al. 2020) is used. In this dataset, the average JJA SAT and precipitation between the years 1995 and 2014 from the grid cell covering Forsmark is 16.2 °C and 179 mm, respectively. These estimates are similar to local meteorological measurements from the Forsmark region (Table 3-2). Following the approach in SE-SFL, the climate analogues are defined by requiring that the SAT is within ± 1 °C and that the precipitation is within ±10 % of the median (best estimate) projections for Forsmark. This results in a set of ranges for each emissions scenario (Table A-2) that can be used when searching for climate analogues.

Areas in Europe with a present-day summer climate within the search criteria in Table A-2 are shown in Figures A-1 to A-4. Light blue patches in the figures indicate regions where both SAT and precipitation are within the limits of the projected climate at Forsmark during terrestrial conditions. They show that regions with a present-day summer climate similar to the projected warm and terrestrial climate at Forsmark can all be found in France. Specifically, a summer climate comparable to that in Normandie can be expected under SSP1-2.6 (2100 AD), Paris region (Île-de-France) under SSP2-4.5 (2500 AD) and SSP5-8.5 (12 000 AD), and Toulouse region (Occitanie) under SSP3-7.0 (7000 AD).

Table A-2. Ranges of summer (JJA) SAT and precipitation representative of projected future climate at Forsmark during terrestrial conditions. These ranges are used to identify climate analogues

Scenario	Timing of projected climate at Forsmark	Summer SAT (ºC)	Summer precipitation (mm)
SSP1-2.6	2100 AD	16.7–18.7	161–197
SSP2-4.5	2500 AD	18.3–20.3	161–197
SSP3-7.0	7000 AD	20.7–22.7	161–197
SSP5-8.5	12 000 AD	18.9–20.9	161–197

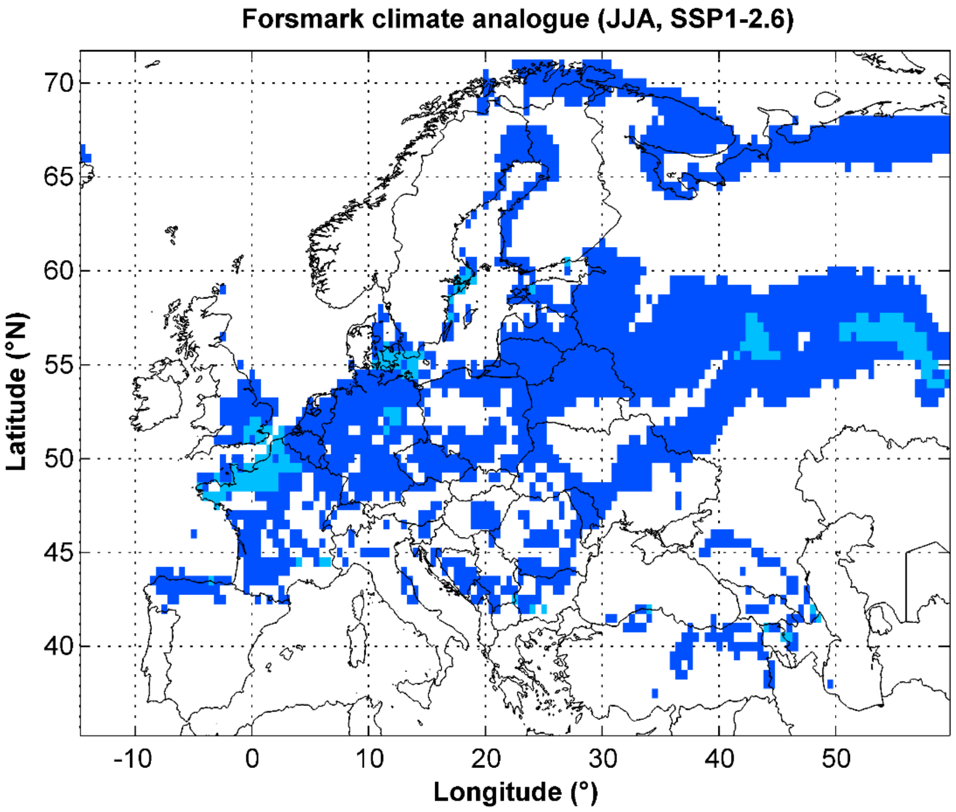

Figure A-1. Light blue: areas with both present-day summer (JJA) SAT and precipitation comparable to the projected climate at Forsmark around 2100 AD under SSP1-2.6 (Table A-2). Dark blue: areas with either SAT or precipitation comparable to that of the projected future at Forsmark.

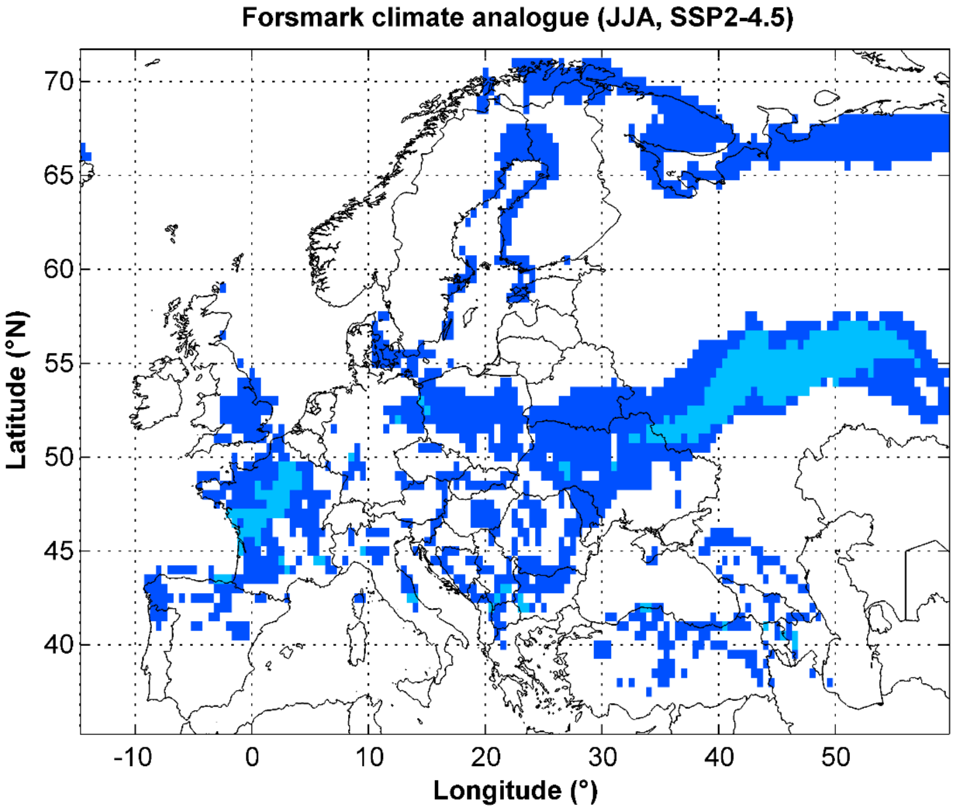

***Figure A-2**. Light blue: areas with both present-day summer (JJA) SAT and precipitation comparable to the projected climate at Forsmark around 2500 AD under SSP2-4.5 (Table A-2). Dark blue: areas with either SAT or precipitation comparable to that of the projected future at Forsmark.*

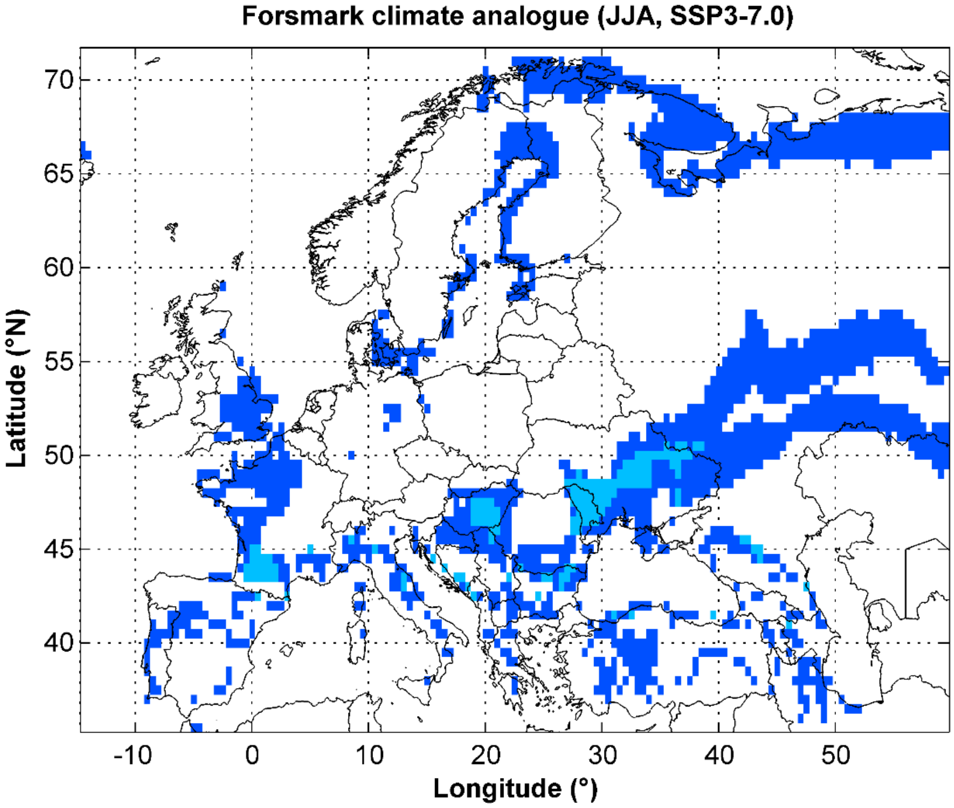

***Figure A-3**. Light blue: areas with both present-day summer (JJA) SAT and precipitation comparable to the projected climate at Forsmark around 7000 AD under SSP3-7.0 (Table A-2). Dark blue: areas with either SAT or precipitation comparable to that of the projected future at Forsmark.*

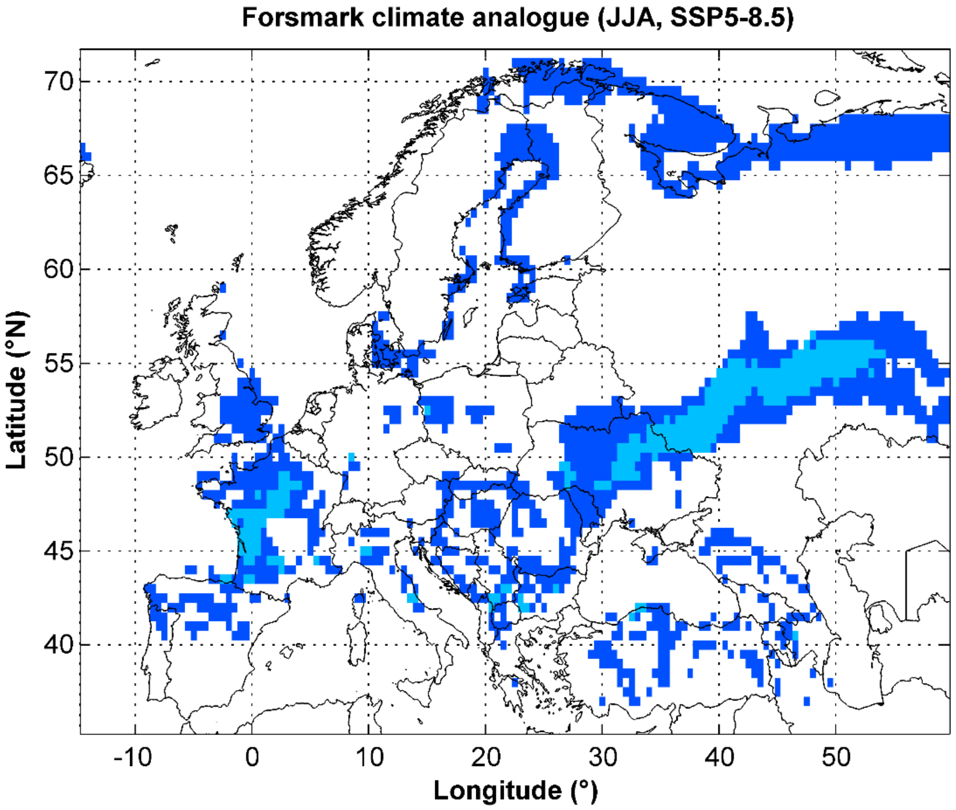

Figure A-4. *Light blue: areas with both present-day summer (JJA) SAT and precipitation comparable to the projected climate at Forsmark around 12 000 AD under SSP5-8.5 (Table A-2). Dark blue: areas with either SAT or precipitation comparable to that of the projected future at Forsmark.*

Appendix B – Supplementary information to Chapter 4 Ice-sheet development

B1 Conceptual model of ice-sheet time lag to climate forcing

The conceptual model that incorporates the lag effect of an ice sheet through a linear response equation (e.g., Oerlemans 2005), described by the following equation:

$$\frac{dL}{dt} = \frac{1}{\tau}\left(L_{eq}(t) - L\right). \qquad \text{Equation B-1}$$

L represents the length of the ice sheet, L_{eq} the length of the ice sheet when it is in equilibrium with the climate, and τ the characteristic time scale (in years) of ice-sheet dynamics in response to a climate perturbation. t represents time measured in years. In the model, L_{eq} is related to changes in climate by considering a simplified setup depicted in Figure B-1. In this setup, the northern margin of the ice sheet is assumed be located at the coast of the Arctic ocean, similar to past ice sheets in Eurasia (Section 4.3). It is further assumed that all ice accumulation that occurs north of the ice divide is removed by calving into the ocean, whereas the southern margin is located over land where melting is the dominant ablation process. Additionally, it is assumed that the local climate over the ice sheet is primarily controlled by the latitude, and that the surface mass balance decreases linearly with latitude. These assumptions result in a completely vertical ELA (E) that is located at exactly between the ice divide and the southern margin, i.e.:

$$E(t) = 3L_{eq}/4. \qquad \text{Equation B-2}$$

To first order, over glacial-interglacial timescales, E can be assumed to vary with the climate according Milankovitch theory (Section 2.2.1), here represented by a sinusoidal function:

$$E(t) = E_A \sin\left(\frac{2\pi t}{T}\right). \qquad \text{Equation B-3}$$

E_A represents the amplitude of the ELA variation, and T the characteristic period of the forcing variations. Substituting Equations 4-5 and 4-6 into Equation 4-4, the ice-sheet extent can be calculated in response to a given climate forcing. In the calculations, the characteristic timescale for ice-sheet dynamics, τ, is set to 6000 years.

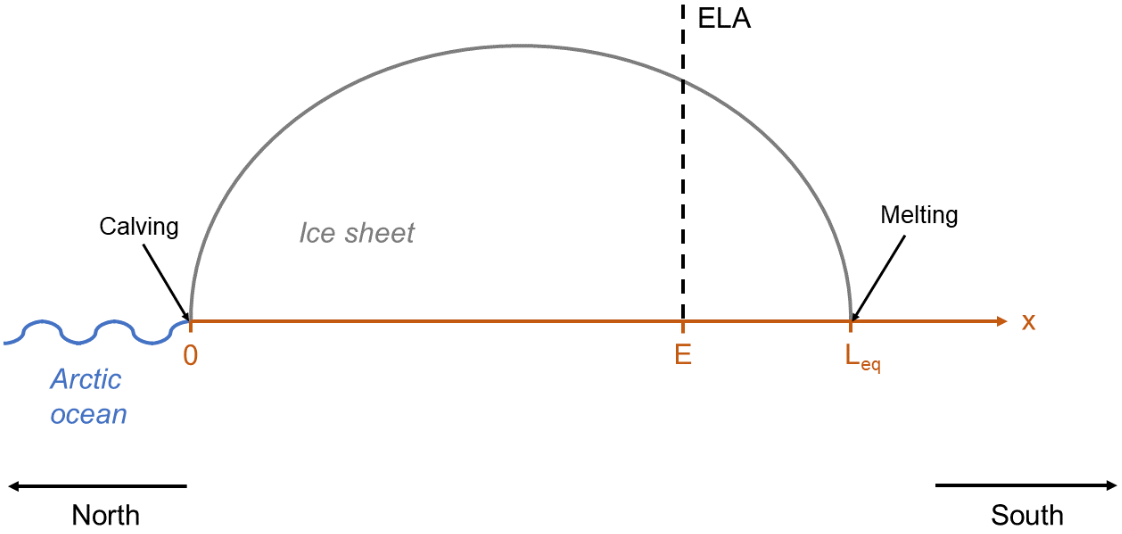

Figure B-1. *Illustration of the simplified model setup utilised to relate equilibrium ice-sheet extents (L_{eq}) to climate forcing (E_A).*

Appendix C – Supplementary information to Chapter 5 Relative sea-level change

C1 Sensitivity of present-day ASL trends at Forsmark to the spatial representation of satellite altimetry data

Satellite altimetry can make accurate measurements of ASL over large areas of open water. As the Baltic Sea contains several hundreds of thousands of islands and is covered by seasonally-varying sea ice, using altimetry to estimate current ASL trends may be challenging for certain parts of the basin (e.g. Weisse et al. 2021). Despite these limitations, it is possible to reconstruct the Forsmark RSL variability during the last decades using altimetry data from a grid cell close to Forsmark together with observationally-based GIA data from the semi-empirical model of Vestol et al (2019, see Section 5.4.1); the sum of these two datasets compares well with the RSL measured from tide-gauge data (Figure 5-4b). However, in light of the reported challenges of using altimetry data in the Baltic Sea, it is important to ensure that the calculated RSL trend featured in Figure 5-4b is not merely a consequence of selecting the "correct" grid cell from the altimetry data when estimating the ASL rise. Thus, if the estimated ASL rise inferred from adjacent grid cells is similar to the rise inferred from the grid cell used in Figure 5-4b, spatial uncertainties in the altimetry data can be considered to be small in the area outside of Forsmark.

Table C-1 shows the estimated ASL rise from altimetry data over the period 1993-2021 for 30 grid cells covering an area of approximately 1° × 1°, including the grid cell used in the analysis in Section 5.4.1. Two of the grid cells are defined as land points in the altimetry dataset, and are hence shown as "n/a" in Table C-1. Across the remaining 28 grid cells, ASL trends since 1993 range from 4.3 mm yr^{-1} and 4.5 mm yr^{-1}. This uncertainty range is significantly smaller than the difference in reported ASL trends between the Baltic Sea and the global mean or the adjacent North Atlantic (Section 5.4.1). Thus, the uncertainty in the altimetry data with regard to exact location outside Forsmark is small and does not alter any conclusions with regards to present-day RSL trends in Section 5.4.

Table C-1. Estimated ASL rise (mm yr^{-1}) between 1993 and 2021 for different grid cells in the satellite altimetry data. The value used for the analysis in Section 5.4 is indicated with bold font. n/a means "no value", thus it is defined as a land point in the altimetry data

	18.13°E	**18.38°E**	**18.63°E**	**18.88°E**	**19.13°E**	**19.38°E**
61.13°N	4.4	4.4	4.4	4.4	4.4	4.4
60.88°N	4.3	4.4	4.4	4.4	4.4	4.4
60.63°N	4.3	4.3	4.4	4.4	4.4	4.4
60.38°N	n/a	**4.4**	4.4	4.3	4.3	4.3
60.13°N	n/a	4.4	4.5	4.4	4.4	4.3

C2 Methodology for calculating the GIA and ASL evolutions at Forsmark over the next 10 000 years

Two approximations were made to estimate the RSL evolution at Forsmark over the next 10 000 years (Section 5.5.2). First, instead of using data directly from the GIA/empirical model (Section 5.3), the temporal evolution of GIA is simplified using an exponential function. This simplification is motivated by an ambition to achieve consistency with present-day GIA estimate (6.7 mm yr^{-1}), because present-day GIA is projected to be slightly slower than the observed rate (approximately 6.0 mm yr^{-1}) in the GIA/empirical model. Second, the results provided by the IPCC, which is used to estimate the ASL rise over the next 10 000 years at Forsmark (Figure 5-6), only includes ASL rise commitments for two points in time for each warming scenario, namely for 2000 and 10 000 years AP (Table 7-4). To enable estimation of the future RSL evolution at Forsmark of sufficient accuracy for handling in the safety assessments, a higher temporal resolution is needed. Thus, there is a need to connect the limited datapoints provided by the IPCC with an appropriate function representing the temporal evolution of the ASL rise until 12 000 AD.

Approximation of future RSL changes due to GIA

The evolution of GIA, f_{GIA} [m], with time, t [s], over the next 10 000 years and beyond is simplified using the following function:

$$f_{GIA}(t) = a_1 \exp(b_1 t) \qquad \text{Equation C-1}$$

The coefficients a_1 and b_1 are derived from the constraints that the present-day ($t = 0$) rate of GIA is 6.7 mm yr^{-1} (Vestøl et al. 2019) and that the remaining total contribution of the current post-glacial GIA is approximately 70 m (taken from the GIA modelling described in Section 5.3.1). The exponential simplification provides a GIA evolution that is very similar to the evolution taken directly from GIA/empirical modelling (Figure C-1).

A major uncertainty with regard to GIA is associated with the magnitude of the remaining contribution (69 m) as this value is only based on a deterministic simulation with the GIA/empirical model. However, as shown in Section 5.5.2, even if unrealistically assuming that the present-day GIA rate will prevail for the next millennia instead of becoming gradually slower, the shortest duration of submerged conditions in the area above SFR, which constitutes a key question for safety assessments for that repository (Section 5.1.2), is only shifted approximately 100 years earlier in time compared to when using the GIA approximation introduced here. Thus, the sensitivity of the shortest duration of submerged conditions to the exact representation of GIA within the coming millennia is relatively low.

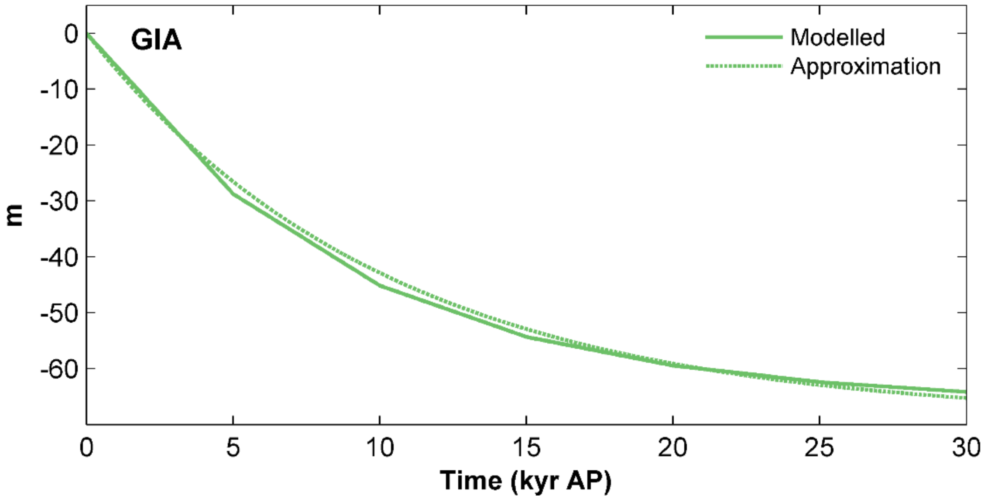

Figure C-1. *Temporal evolution of GIA over the next 30 000 years as predicted from the GIA/empirical model (solid line) and the exponential approximation provided by Equation A-1 (dotted line). The coefficients in Equation A-1 are set to the following values:* a_1*=69 m and* b_1*=-9.7 ×* 10^{-5} s^{-1}.

Temporal evolution of the ASL

Studies analysing the temporal evolution of ASL over multi-millennial timescales unequivocally shows a larger ASL increase for the first centuries after present than after several millennia when the atmospheric warming has stabilised (e.g. Clark et al. 2016, Van Breedam et al. 2020). For this reason, as in PSAR (SKB TR-23-05, Section 3.5), an arctan function is considered appropriate to represent the ASL rise behaviour over these timescales: the gradient of an arctan function, $1/(1+t^2)$, is the greatest at time $t = 0$ (here representing present-day) and it asymptotically approaches zero as $t \to \infty$ (here representing 12 000 AD and beyond). Thus, the multi-millennial ASL evolution, f_{ASL} [m], is here described by the following function:

$$f_{ASL}(t) = a_2 \arctan(b_2 t) \qquad \text{Equation C-2}$$

The coefficients a_2 and b_2 are estimated separately for each ASL curve in Figure 5-6 by minimising the distance to the ASL commitments provided by the IPCC (Table 7-4) using a least-square approach.

C3 The LLRA model

Description

The Local Lithosphere and Relaxing Asthenosphere (LLRA) model is a simple model of glacial isostasy, based on a plane, two-layer, lithosphere/asthenosphere system (Greve 2001). The underlying assumption is that the ice load causes a local steady-state vertical displacement of the lithosphere, $z_{ls}(x,y)$, at the location (x,y) beneath the ice. The value of z_{ls} is determined by the balance between the ice load and the buoyancy force acted on the lithosphere from the underlying viscous asthenosphere (the displacement is defined positive downwards):

$$\rho_a g z_{ls}(x,y) = \rho_i g H_i(x,y), \qquad \text{Equation C-3}$$

where ρ_a is the density of the asthenosphere, ρ_a the density of ice, g the gravitational constant and H_i the ice thickness. Thus, based on Equation A-3, the steady-state displacement of the lithosphere at a certain location (x,y) beneath the ice is governed by the density ratio between the ice and the asthenosphere and the ice thickness:

$$z_{ls}(x,y) = \frac{\rho_i}{\rho_a} H_i(x,y), \qquad \text{Equation C-4}$$

Due to the viscous properties of the asthenosphere, the lithosphere cannot be assumed to in the steady-state z_{ls} immediately following an ice load. Instead, the response is lagged, and the model parameterises this lag by a single time constant, τ_a. The evolution of the actual displacement, z_l, with time, t, is then determined by

$$\frac{\partial z_l}{\partial t} = -\frac{1}{\tau_a}(z_l - z_{ls}) \qquad \text{Equation C-5}$$

The model has been used in several pioneer modelling studies of terrestrial ice sheets, e.g. Oerlemans (1980) and Greve (1997).

Calibration

The average densities of ice (ρ_i) and the asthenosphere (ρ_a) are relatively well constrained, and are set to ρ_i = 910 kg m^{-3} and ρ_a = 3300 kg m^{-3} in the LLRA model (van der Veen 2013). The most unconstrained parameter of the LLRA model is the time constant, τ_a, representing the time lag caused by the viscous asthenosphere. Previous studies have found that an appropriate value of this parameter is typically within the range of 3000 – 10 000 years (Oerlemans 1980, Le Meur and Huybrechts 1996, Greve 1997, Greve 2001). In the present work, this time constant is used to calibrate the LLRA model to Forsmark conditions. To this end, we constrain this parameter using the Weichselian reconstruction, which featured two phases of ice coverage and ensuing submerged periods in Forsmark (Figure 5-2). For the Weichselian, the GIA and associated submerged periods were computed using a comprehensive GIA model which solves the sea-level equation (Section 5.3.1). This model suggests that the ongoing uplift in the Forsmark is completed after an additional ~70 m uplift compared to present-day (Appendix C2). Currently, the area above SFR is situated a few metres below sea level, whereas most of the footprint area of the planned spent fuel repository will be close to sea level. Therefore, the threshold for submerged conditions in Forsmark, z_{Fo}, is for simplicity set to 70 m. In the LLRA model, the submerged period is then determined by the time during which $z_l > z_{Fo}$ after an ice sheet retreats from the region.

Forcing the model with the reconstructed ice loads during the MIS 4 and LGM glaciations (Figure 5-2 and C-1), it is possible to compute the time of submerged conditions ($z_l < z_{Fo}$) after each glaciation. The results are shown in Table C-2 for different values of τ_a. These estimates are compared to the corresponding time of submerged conditions during the Weichselian, reconstructed using the more comprehensive GIA model. As can be seen in the table, the projected durations of the submerged periods using τ_a=5000 years shows the best agreement with the GIA model. For this time constant, the LLRA model yields only a few hundred years shorter durations of the post-glacial submerged period as the GIA model (Table C-2). The simulated temporal evolution of the lithosphere response to the MIS 4 and LGM ice loads using this time constant is shown in Figure C-2.

Table C-2. Estimated time of submerged conditions in Forsmark for different values of the time constant (see Equation A-5) after the MIS 4 and LGM glaciations. The results are compared with corresponding estimates using the more comprehensive GIA model, described in Section 5.3.1

Model	Time constant, τ_a (years)	Time of submerged conditions in Forsmark (years)	
		after MIS 4 ice sheet	after LGM ice sheet
LLRA	3000	5000	5700
	4000	6400	7900
	5000	7700	10 000
	6000	8800	12 000
	7000	9700	14 000
	8000	10 600	15 800
GIA (Section 5.3.1)	-	8000	10 500

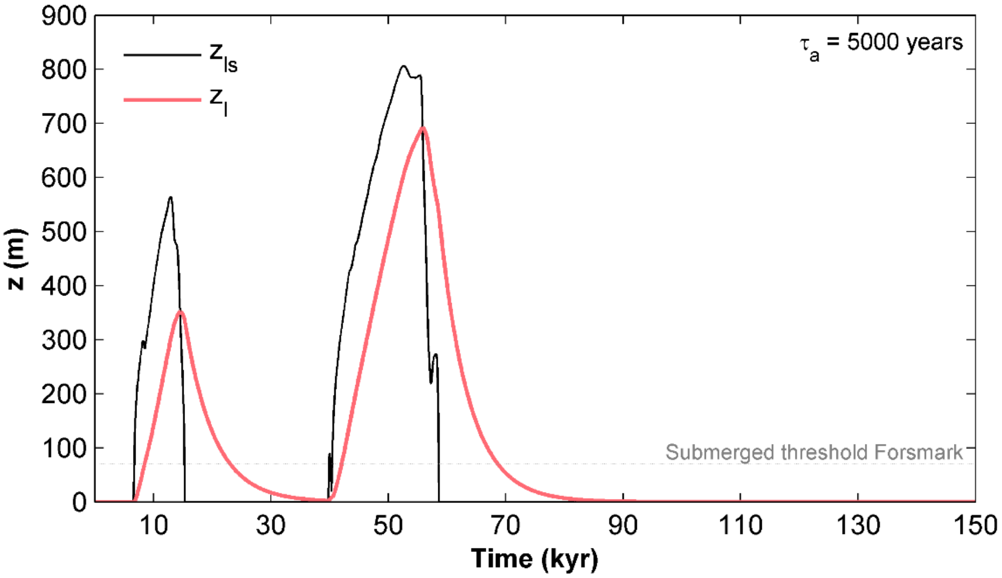

Figure C-2. *Simulated vertical displacement of the lithosphere (z_l) and the steady-state displacement (z_{ls}) caused by the reconstructed Forsmark ice load during the Weichselian (Section 4.3.1), using the LLRA model. The threshold for submerged conditions in Forsmark (z_{Fo}) is indicated by the grey dotted line. The area is submerged when the area is ice free and $z_l > z_{Fo}$.*